

Targeting Archean Orogenic Gold Mineralization Using Physical Properties and Integrated Geophysical Methods

by

DIANNE EDITH MITCHINSON

B.Sc., Memorial University of Newfoundland, 2001

M.Sc., Laurentian University, 2004

A DISSERTATION SUBMITTED IN PARTIAL FULFILLMENT OF
THE REQUIREMENTS FOR THE DEGREE OF

DOCTOR OF PHILOSOPHY

in

THE FACULTY OF GRADUATE STUDIES
(Geological Sciences)

THE UNIVERSITY OF BRITISH COLUMBIA
(Vancouver)
January 2009

© Dianne Edith Mitchinson, 2009

Abstract

Although Archean orogenic gold mineralization is not readily detected using geophysical methods, due to a lack of petrophysical contrast between typical low volumes of gold and hosting rocks, it is possible to use geophysics to detect other petrophysically distinct gold indicators. Geophysical inversion methods, in particular, make it possible to not only detect important gold-related rocks in the subsurface, but to map their distribution in three dimensions. The research presented examines the effectiveness of geophysical inversion as an exploration tool in the Archean orogenic gold environment through extensive physical property analysis, synthetic modeling, and inversion of various geophysical data over the Hislop gold deposit, Ontario.

As understanding rock properties is imperative to interpreting geophysical data, it was necessary to establish the physical property ranges of typical host rock types, hydrothermally-altered, and mineralized rocks in this deposit setting. Felsic dikes, known to be associated with gold at Hislop, have low magnetic susceptibility and density ranges that allow them to be distinguished from mafic and ultramafic rocks. Additionally, many potentially mineralized, carbonate-altered mafic and ultramafic rocks can be isolated from their least-altered equivalents using susceptibility.

Synthetic modeling showed that narrow, near-vertical felsic dikes, and sulfide-rich zones hosted by mafic and ultramafic volcanic rocks can be imaged up to ~350 m in the subsurface using inversion methods. It is necessary however, to focus on small areas, to have closely spaced measurements, and small inversion cell sizes. It was demonstrated that constraining inversions through addition of basic prior geologic and physical property information, yields models with improved physical property distribution, and estimates. Applying knowledge gained from physical property, and synthetic modeling work lent confidence to interpretations of inversion results for the Hislop area. At regional scales, susceptibility and density models reveal a steep southward dip for the gold-related Porcupine-Destor Deformation Zone, and a greenstone depth of approximately 7000 m. Fe-rich mafic rocks directly hosting the Hislop deposit are

complexly faulted and extend to 3000 m depth. At deposit-scales, model cells with combined low susceptibilities and high chargeabilities, occurring proximal to faults, felsic intrusions, and Fe-rich mafic rocks, highlight prospective areas for further investigation.

Table of Contents

Abstract	ii
Table of Contents	iv
List of Tables	viii
List of Figures	ix
Acknowledgements	xiv
Co-authorship Statement.....	xvi
Chapter 1: Introduction	1
1.1. Combining geology and geophysical inversion for mineral exploration.....	1
1.1.1. Geophysics and mineral exploration.....	1
1.1.2. Mineral Deposit Research Unit – Geophysical Inversion Facility project	2
1.1.3. Inversion in the Archean orogenic gold environment.....	3
1.2. Background to geophysical inversion.....	5
1.3. Archean orogenic gold - geologic and geophysical background	7
1.3.1. Background on Archean orogenic gold	7
1.3.2. The Hislop gold deposit.....	8
1.3.3. Geophysics and gold	9
1.4. Project objectives	10
References.....	13
Chapter 2: Physical properties of rocks in an Archean orogenic gold environment	17
2.1. Introduction.....	17
2.1.1 Rationale	17
2.1.2 Objectives	18
2.2. Background	19
2.2.1 Geology and geophysics of Archean orogenic gold deposits	19
2.2.2 Geology of the study area	20
2.3. Methodology	25
2.3.1 Field and mineralogical studies	25
2.3.2 Physical property measurements.....	26

2.4. Data and observations	29
2.4.1. Hislop deposit rock types, hydrothermal alteration, and associated mineralogy	29
2.4.2. Physical properties of the Hislop deposit.....	32
2.5. Interpretations	43
2.5.1. Effect of geological processes on physical properties at Hislop.....	43
2.6. Discussion	60
2.6.1. Exploration using physical properties.....	60
2.6.2. Comparison to analogous areas	67
2.7. Conclusions.....	75
References.....	77

Chapter 3: Detecting gold-related geology in Archean orogenic gold environments using geophysical inversion: a synthetic modeling study based on the Hislop gold

deposit, Ontario.....	86
3.1. Introduction.....	86
3.1.1. Rationale	86
3.1.2. Objectives	87
3.2. Background.....	88
3.2.1. Geology of the Hislop gold deposit and relationship to other Archean orogenic gold deposits	88
3.2.2. Physical Properties of rock types and alteration zones at Hislop	90
3.2.3. General forward modeling and inversion background.....	95
3.3. Methods.....	97
3.4. Synthetic modeling results.....	103
3.4.1. Potential fields modeling	103
3.4.2. DC resistivity and induced polarization modeling.....	112
3.4.3. Improving model results with basic constraints.....	120
3.4.4. Other solutions for improving model results	125
3.5. Conclusions.....	128
References.....	131

Chapter 4: 3D inversion of magnetic, gravity, DC resistivity, and induced polarization data over the Hislop gold deposit, south-central Abitibi greenstone belt	137
4.1. Introduction	137
4.1.1. Rationale	137
4.1.2. Geological background	138
4.1.3. Relationships between geophysics, physical properties, and geology	140
4.1.4. Inversion background	147
4.2. Inversion Approach	150
4.2.1. General strategy	150
4.2.2. Magnetic inversions	151
4.2.3. Gravity inversions	157
4.2.4. DC resistivity and IP inversions	158
4.2.5. Constraining magnetic inversions with reference models built in Modelbuilder	160
4.2.6. Inversion model display	162
4.3. Inversion results and analysis	165
4.3.1. Magnetic susceptibility models	165
4.3.2. Density model	175
4.3.3. Resistivity models	175
4.3.4. Chargeability models	180
4.4. Querying combined inversion results	181
4.4.1. Regional scale query (susceptibility and density)	182
4.4.2. Local scale query (susceptibility, chargeability)	184
4.4.3. Deposit scale query (susceptibility, chargeability)	186
4.5. Summary and discussion	188
References	192
Chapter 5: Summary and future work	198
5.1. Synthesis of research presented	198
5.2. Significance and contributions to the field	199

5.3. Limitations of the thesis research	200
5.4. Recommendations for continued work	202
5.5. Future directions of the field of study.....	204
References.....	207
Appendix 2A – List of Abbreviations.....	209
Appendix 2B - Hislop Drillcore Logs, Cross-sections, and Outcrop Maps.....	210
Appendix 2C - Detailed and Expanded Methods	222
Appendix 2D – X-ray Diffraction Analyses	231
Appendix 2E – Physical Properties of Hislop Deposit Rocks	233
Appendix 2F – Physical Properties – Descriptive Statistics.....	248
Appendix 2G – correlation coefficients for Physical Properties and XRD (Rietveld) - Derived mineral abundances.....	251
Appendix 3A - Observed versus Predicted Data for Synthetic Inversion Models.....	257
Appendix 4A - Hislop 3D Magnetic, 3D Gravity, 3D DC Resistivity, and 3D IP Inversion Results.....	257
Appendix 4B - 2D DC Resistivity and Induced Polarization Inversion Results for Hislop	257
Appendix 4C - Observed versus Predicted Data for Hislop Inversion Models	257

List of Tables

Table 2.1. Geophysical characteristics of Archean orogenic gold deposits	21
Table 2.2. Summary of the principal rock types found in the Hislop deposit area, and associated mineralogy.	30
Table 2.3. Ranges of resistivity and chargeability for rock types similar to those occurring in the Hislop deposit area (data from Telford et al., 1990).	42
Table 2.4. Densities of the common minerals in Hislop deposit rocks (from www.mindat.org).	49
Table 2.5. Statistical data for prospective rocks at Hislop, and cut-off values used for querying physical property data.	64
Table 2.6. Results from magnetic susceptibility and density queries of the Hislop physical property dataset.	65
Table 3.1. Characteristics of Archean orogenic gold deposits.	91
Table 3.2. Physical property values used in synthetic modeling.	96
Table 3.3. Synthetic survey parameters.	100
Table 3.4. Synthetic inversion parameters.	100
Table 3.5. Model differences calculated between recovered and true models (the lowest model differences for each geophysical method are highlighted with bold text).	102
Table 4.1. Typical and anomalous physical property ranges for principal rock types occurring in the Hislop deposit area.	142
Table 4.2. Survey parameters.	155
Table 4.3. Inversion parameters.	156
Table 4.4. GIFtools ModelBuilder options chosen for building Hislop reference models.	163

List of Figures

Figure 1.1. Flow chart illustrating the role of physical properties in the inversion process.	4
Figure 2.1. Approximate location of the Hislop study area in the Abitibi greenstone belt of the Superior Province.	22
Figure 2.2. Geology of the Hislop deposit area as interpreted by Power et al. (2004) from high resolution aeromagnetics.	24
Figure 2.3. Cross section looking northwest through the Hislop deposit.....	25
Figure 2.4. Geology, alteration, magnetic susceptibility, and gold grade logs.....	33
Figure 2.5. Magnetic susceptibility histograms for the five main rock types found in the Hislop deposit area.....	34
Figure 2.6. Magnetic susceptibility histograms showing susceptibility data for a) least- altered and altered ultramafic volcanic rocks, and b) least-altered and altered mafic volcanic rocks.	36
Figure 2.7. Magnetic susceptibility histograms showing susceptibility data for a) least- altered and altered intermediate dikes, b) least-altered and altered syenitic dikes, and c) least-altered and altered porphyritic rhyolite dikes.....	37
Figure 2.8. Density histograms for the five main rock types found in the Hislop deposit area.	38
Figure 2.9. Density histograms showing density data for a) least-altered and altered ultramafic volcanic rocks, and b) least-altered and altered mafic volcanic rocks.	39
Figure 2.10. Density histograms showing density data for a) least-altered and altered intermediate dikes, b) least-altered and altered syenitic dikes, and c) least-altered and altered porphyritic rhyolite dikes.	40
Figure 2.11. Resistivity histograms for Hislop deposit rocks.	42
Figure 2.12. Chargeability histograms for Hislop deposit rocks.	43
Figure 2.13. Positive correlation between modal magnetite in Hislop rock samples (as derived from XRD analysis) and magnetic susceptibility. For calculated correlation coefficients see Appendix 2G (all rock types).	44

Figure 2.14. Magnetite grains (reflective grains in lower image) are destroyed within a carbonate altered zone surrounding a carbonate vein in a mafic volcanic rock from Hislop.	45
Figure 2.15. Modal magnetite versus total Fe-rich carbonate abundance for all Hislop samples with measured quantities of these minerals.	46
Figure 2.16. Histograms showing distribution of susceptibility for fine- and medium-grained a) mafic volcanic rocks, and b) ultramafic volcanic rocks.	48
Figure 2.17. Density increases for Hislop rocks with an overall increase in the abundance of Fe-rich carbonate. For calculated correlation coefficients see Appendix 2G (all rock types).....	51
Figure 2.18. Measured versus calculated density for Hislop rocks.	52
Figure 2.19. Porosity of ultramafic volcanic rocks at Hislop decreases with carbonate-related hydrothermal alteration	53
Figure 2.20. No relationships are indicated between porosity and density for mafic volcanic rocks at Hislop.....	53
Figure 2.21. Resistivity versus magnetic susceptibility.....	56
Figure 2.22. Resistivity versus density.	57
Figure 2.23. A plot of porosity versus resistivity shows that annealing of ultramafic rocks due to precipitation of carbonate minerals during hydrothermal alteration brings about a decrease in porosity and a corresponding increase in resistivity.	58
Figure 2.24. A weak positive correlation exists between pyrite abundance and chargeability,.....	58
Figure 2.25. A negative correlation between chargeability and porosity	59
Figure 2.26. Magnetic susceptibility plotted against density for Hislop samples.	60
Figure 2.27. Carbonate-alteration destroys magnetite in a) mafic and b) ultramafic volcanic rocks	62
Figure 2.28. Magnetic susceptibility histograms comparing data from Hislop rocks, and equivalent rocks from surrounding regional areas.....	68
Figure 2.29. Density histograms comparing data from equivalent rock types from Hislop rocks, and equivalent rocks from surrounding regional areas.	69

Figure 2.30. A comparison of magnetic susceptibility data associated with least-altered and carbonate-altered mafic rocks from the Hislop deposit, and from the greater surrounding area.....	70
Figure 2.31. A comparison of density data associated with least-altered and carbonate-altered mafic rocks from the Hislop deposit, and from the greater surrounding area.	72
Figure 3.1. Cross-section looking northwest through the Hislop deposit.....	89
Figure 3.2. Plot of magnetic susceptibility versus density for major rock units at Hislop.	92
Figure 3.3. Plot of magnetic susceptibility versus density for variably altered mafic volcanic rocks, and variably altered ultramafic volcanic rocks from Hislop.	93
Figure 3.4. Resistivity histograms for Hislop deposit rocks.	94
Figure 3.5. Chargeability histograms for Hislop deposit rocks.	94
Figure 3.6. a) 3D geological model based on the geologic setting of the Hislop gold deposit. b-e) North-facing cross-sections through 3D physical property models generated from the geologic model	99
Figure 3.7. Starting model and unconstrained magnetic inversion result for the ‘Hislop-like’ magnetic susceptibility model.	104
Figure 3.8. Starting models and magnetic inversion results with changes made to geometry of the target body.	105
Figure 3.9. Magnetic inversion results for starting models with different physical property contrasts between the target and host rocks.	106
Figure 3.10. Starting model and unconstrained gravity inversion result for the ‘Hislop-like’ density contrast model.	108
Figure 3.11. Gravity inversion results with changes made to geometry of the target body.	108
Figure 3.12. Inversion results with different physical property contrasts between the target and host rocks.	110
Figure 3.13. Starting model and unconstrained DC resistivity inversion result (conductivity model) for the ‘Hislop-like’ resistivity model.	113
Figure 3.14. DC resistivity inversion results (conductivity models) with changes made to physical property contrasts, and to the geometry of the target body.	114

Figure 3.15. Starting model and unconstrained IP inversion result for the ‘Hislop-like’ chargeability model.....	116
Figure 3.16. IP inversion results with changes made to physical property contrasts and geometry of the target body.	117
Figure 3.17. Inversion results for the Hislop-like susceptibility model after constraints applied.....	122
Figure 3.18. Inversion results for the Hislop-like conductivity model after constraints applied.....	124
Figure 3.19. Inversion results for the Hislop-like susceptibility model with depth weightings reduced.	126
Figure 3.20. Comparison of a dipole-dipole electrode configuration and a Schlumberger configuration which resembles a Realsection array.....	127
Figure. 3.21. DC resistivity inversion result for resistivity data collected via a dipole-dipole survey.....	128
Figure 4.1. Geological map of the southwest Abitibi greenstone belt.....	139
Figure 4.2. Geology of the Hislop deposit area	140
Figure 4.3. Cross section looking Northwest through the Hislop deposit,	141
Figure 4.4. Magnetic susceptibility plotted against density for the major rock types at Hislop.....	143
Figure 4.5. Magnetic susceptibility plotted against density for a) mafic and b) ultramafic volcanic rocks from the Hislop deposit area.....	144
Figure 4.6. Resistivity histograms for Hislop deposit rocks.....	146
Figure 4.7. Chargeability histograms for Hislop deposit rocks.	148
Figure 4.8. Chargeability plotted against pyrite abundance for Hislop samples.	148
Figure 4.9. Chargeability versus porosity for mafic rock samples from Hislop.....	149
Figure 4.10. Extents of magnetic data used in the deposit-, local-, and regional-scale magnetic inversions	152
Figure 4.11. Data used in regional-scale magnetic inversion.	153
Figure 4.12. Data used in local-scale magnetic inversion.	154
Figure 4.13. Data used in deposit-scale magnetic inversion.....	154
Figure 4.14. Data used in regional-scale gravity inversion.	158

Figure 4.15. Location of DC resistivity and IP lines used for 3D DC resistivity and IP inversions. Local mine grid line numbers shown. See Figure 4.2 for geology legend. .	159
Figure 4.16. Extents of inversion model volumes, with cross-section location indicated.	164
Figure 4.17. North-south cross-section through the regional-scale unconstrained magnetic inversion result.....	166
Figure 4.18. Isosurface model from regional scale magnetic inversion results.....	167
Figure 4.19. North-south cross-sections through the local-scale a) unconstrained, and b) constrained magnetic inversion results	169
Figure 4.20. Isosurface model from local magnetic inversion results.	171
Figure 4.21. North-south cross-sections through the deposit-scale a) unconstrained, and b) constrained magnetic inversion results	172
Figure 4.22. Isosurface model from deposit-scale magnetic inversion results.....	174
Figure 4.23. North-south cross-section through the regional-scale gravity inversion result, inverted with non-located constraints.	176
Figure 4.24. Isosurface density model from regional-scale gravity inversion results. ..	177
Figure 4.25. North-south cross-section through the deposit-scale a) DC resistivity and b) IP inversion results.....	178
Figure 4.26. Isosurface models for deposit-scale a) conductivity, and b) chargeability results.	179
Figure 4.27. Result for a physical property query targeting low magnetic susceptibility-low density cells within the regional-scale common earth model.	183
Figure 4.28. Result for a physical property query targeting high magnetic susceptibility - high density cells within the regional-scale common earth model.	184
Figure 4.29. Result for a physical property query targeting low magnetic susceptibility - high density cells within the regional-scale common earth model.	185
Figure 4.30. Result for a physical property query targeting low magnetic susceptibility - high chargeability cells within the local-scale common earth model.	186
Figure 4.31. Result for a physical property query targeting low magnetic susceptibility - high chargeability cells within the deposit-scale common earth model.	187

Acknowledgements

Thanks to my supervisor Richard Tosdal for the always timely feedback and the numerous edits of my chapters, and for support during the course of the thesis research. Thanks to all the geologists and geophysicists who provided input through discussions and edits, including Claire Chamberlain, Shane Ebert, Rob Eso, Ken Hickey, Peter Lelievre, Doug Oldenburg, Nicolas Pizarro, and Victoria Sterritt. I am most especially gracious for all the geophysics help provided by Nigel Phillips and Nick Williams. Thanks for being so generous with your time, and for having so much patience.

The sponsors of the MDRU-GIF project, including Geoinformatics Exploration Inc., Anglo American, Anglo Gold Ashanti, Barrick, BHP Billiton, Kennecott Exploration, Teck, Vale Inco, and Xtrata are thanked. Additional funding was provided by an NSERC postgraduate scholarship. A Hugo Dummett Mineral Discovery Fund grant from the Society of Economic Geologists provided funding for XRD and physical property analyses.

Geologists and geophysicists at Geoinformatics Exploration Inc., and St. Andrew Goldfields Ltd., especially Darren Holden (Geoinformatics), and Wayne Reid (former exploration manager at St. Andrew Goldfields), are thanked for providing data, general information on the Hislop deposit and surrounding area, and use of the offices and core yard at Stock. Thanks to Brian Atkinson, Dave Truscott, and Ken Kryklywy for geological tours in and around Timmins.

Elisabetta Pani is thanked for XRD analyses, and Mati Raudsepp and Sasha Wilson for help on the SEM. Kelly Russell, Steve Quane, and Krista Michol, provided guidance for density and porosity data collection. Lisa Swinnard, Lorraine Tam, and Marcia Wilson, and were all thorough and well-organized in collecting density data. Arne Toma and Karie Smith are thanked respectively, for helping me deal with various computer, and financial matters.

Thanks to my friends at UBC. You are all so smart and inspiring. And you did an amazing job of decorating the office with a stunning array of wine bottles. To my legion of former officemates, you ladies always kept it fun and funny, and kept geological conversation at tolerable levels. To Victoria and Kirsten and Amber, thanks for listening to my ramblings, and hitting the slopes and the waves hard with me between stints in the office.

Thanks to my family for helping me to get back home once in a while, for their interest in my life, and of course for their constant encouragement. To Billy: thanks for helping me with core lifting and susceptibility measuring in Timmins, for cutting my rocks for me at UBC, for not (really) asking me if I am done yet, for being ok with me not having goals or plans, and for keeping everything together when I was too busy, i.e. almost all the time. Maybe you *are* the nicest person I will ever meet?

Co-authorship Statement

Chapters 2-4 were written as independent manuscripts that will be submitted for publication to journals focusing on applied uses of geophysics, for exploration or otherwise. Each chapter involved some input from others, in the form of instruction, discussion, editing of the work, or data collection. Those who played the largest roles in collaborating are to be recognized as co-authors on the submitted manuscripts. Their contributions are outlined below.

Chapter 2: Physical properties of rocks in an Archean orogenic gold environment

Authors: Dianne Mitchinson, Nigel Phillips, Elisabetta Pani, Richard Tosdal

Nigel Phillips, a former research associate at the Mineral Deposit Research Unit, of the Department of Earth and Ocean Sciences helped to interpret some of the physical property data, and edited parts of the manuscript, as well as related posters and abstracts. Elisabetta Pani, researcher in the Department of Earth and Ocean Sciences, collected X-ray diffraction data for the Hislop deposit suite of samples, and analyzed the data using Rietveld methods to yield mineral abundance data. My thesis supervisor Richard Tosdal contributed suggestions, and provided numerous edits of this chapter.

Chapter 3: Detecting gold-related geology in Archean orogenic gold environments using geophysical inversion: a synthetic modeling study based on the Hislop gold deposit, Ontario

Authors: Dianne Mitchinson, Nigel Phillips

Nigel Phillips initiated the idea of completing synthetic modeling to explore the capabilities of inversion in the studied geologic setting, and provided suggestions for

possible variations on starting models, and on inversion parameters. He provided guidance and instruction with respect to forward and inverse modeling techniques using the University of British Columbia Geophysical Inversion Facility (UBC-GIF) inversion codes. He also edited the work.

Chapter 4: 3D inversion of magnetic, gravity, DC resistivity, and induced polarization data over the Hislop gold deposit, south-central Abitibi greenstone belt

Authors: Dianne Mitchinson, Nigel Phillips, Nick Williams

Nigel Phillips familiarized me with inversion codes, and with the inversion modeling process in general. He helped to organize geophysical data, and provided guidance and suggestions throughout the 2D and 3D DC resistivity and induced polarization modeling. Nick Williams aided with the management and manipulation of the large datasets involved, instructed me on the use of his program ModelBuilder, and provided discussion on a number of the inversion model results.

Chapter 1: Introduction

1.1. COMBINING GEOLOGY AND GEOPHYSICAL INVERSION FOR MINERAL EXPLORATION

1.1.1. Geophysics and mineral exploration

Geophysical techniques are used regularly to aid or supplement geologic mapping in areas where outcrop is limited. In addition to delineating surface geology with geophysics, it is possible to investigate geology at depth, where otherwise subsurface geology must be inferred from maps and structural measurements, or by drilling. Geophysics has become an especially important tool in mineral exploration. Many mineral deposit targets produce strong geophysical signatures due to high abundances of oxides and sulfides, allowing them to be distinguished from their host rocks. Geophysics is so prolific in the field of mineral exploration because of the significant amount of information it can provide for low costs (Phillips et al., 2001). Regional geophysical data, usually magnetic and gravity data covering hundreds of kilometers of ground, is commonly available for free, or at an insignificant cost, from government geological surveys. From this data geology can be inferred, and large exploration targets spotted. With advanced stages of mineral exploration, an exploration company can have more fine-scale geophysical surveys completed for a higher cost, however, the price is minimal compared to the cost of drilling.

Traditionally, geophysical data collected at the surface or from boreholes is interpreted directly after standard filtering and corrections. Estimations of sizes and shapes of features are made based on known relationships between sources and the measurement location, and through forward modeling. The relatively recent development of robust geophysical inversion methods for calculation of 3-dimensional physical property models of the subsurface allows petrophysically distinct geological features to be located in 3D space, and their geometry to be delineated at significant depths of up to

thousands of meters. These methods are becoming a staple in the mineral exploration industry as it is thought that most near-surface mineral deposits have been discovered, and that future resources exist at depth.

1.1.2. Mineral Deposit Research Unit – Geophysical Inversion Facility project

This PhD project was completed alongside a number of others under the Mineral Deposit Research Unit – Geophysical Inversion Facility (MDRU-GIF) joint research initiative. The MDRU-GIF project was a collaborative project involving researchers and students from the University of British Columbia's (UBC) Mineral Deposit Research Unit, and the Geophysical Inversion Facility, in addition to ten mineral exploration industry sponsors. The formal project began in 2003, and ended in the spring of 2007. The overlying objective of the MDRU-GIF project was to enhance inversion-based exploration and generate more robust 3D subsurface models through effective combination of geology, physical properties, and geophysical information. A number of more specific themes were encompassed within this principal objective including: relating physical properties to geology and geological processes (Sterritt, 2006), scaling physical property data for use at larger scales of inversion (Pizarro, 2008), and developing methods of more effectively incorporating prior geological information into geophysical inversions to yield more geologically realistic models (Phillips et al., 2007; Lelievre et al., 2008; Williams, 2008). The MDRU-GIF projects were based on data from a range of mineral deposit types including kimberlitic diamond, magmatic sulfide, orogenic gold, volcanogenic massive sulfide, and porphyry deposits, and considered different stages in exploration from regional reconnaissance to deposit delineation. This PhD project focused on the application of geophysical inversion methods to exploration in the Archean orogenic gold environment, for a range of scales of exploration.

1.1.3. Inversion in the Archean orogenic gold environment

The Hislop deposit, a gold deposit in the south-central Abitibi greenstone belt, acted as a representative orogenic gold deposit for this work. Although the deposit is small, and was only mined for a short period, it was a good candidate for a case study deposit for this research for a number of reasons. Due to extensive exploration in the Hislop deposit area, and in nearby surrounding areas, there is a large amount of geophysical data available for use in geophysical inversions. There are numerous drillholes available for reconnaissance work on the local geology. Additionally, the area has been mapped and modeled recently (Berger, 1999 and 2002; Power et al., 2004; Reed, 2005; Mueller et al., 2006), and inversion results can be compared to known geology. Finally, it may be possible to apply concepts and results from this work to other areas, as the geology of the deposit is characteristic of other orogenic gold deposits both locally, and globally.

The intent of this PhD project was to apply knowledge of orogenic gold models, of local greenstone belt geology, and of the Hislop deposit, to optimize the inversion process for this specific mineral deposit setting. The desired outcome was to generate subsurface models that are consistent with known geology in order to be able to interpret results with confidence. The project is, in essence, a multi-faceted case study, which broaches many of the themes of the MDRU-GIF project, and covers a number of stages that comprise the inversion process. PhD research encompassed understanding physical property – geology relationships, completing synthetic modeling to determine inversion imaging capabilities, and carrying out unconstrained and constrained inversions of actual geophysical data collected over the Hislop deposit.

The role of physical properties in inversion is emphasized throughout this work, as they ultimately quantitatively link geology to geophysics (Fig. 1.1). Having an understanding of relationships between geology and physical properties is important for constraining geophysical inversions, determining if physical property values composing

model results are reasonable, and of course for interpreting geology from the recovered models.

The entire process represented by the work in this thesis should be analogous to the process that an exploration company might follow if embarking on completing inversion work for a prospect, or even a more well-understood deposit where continuations of ore zones or other nearby targets are sought.

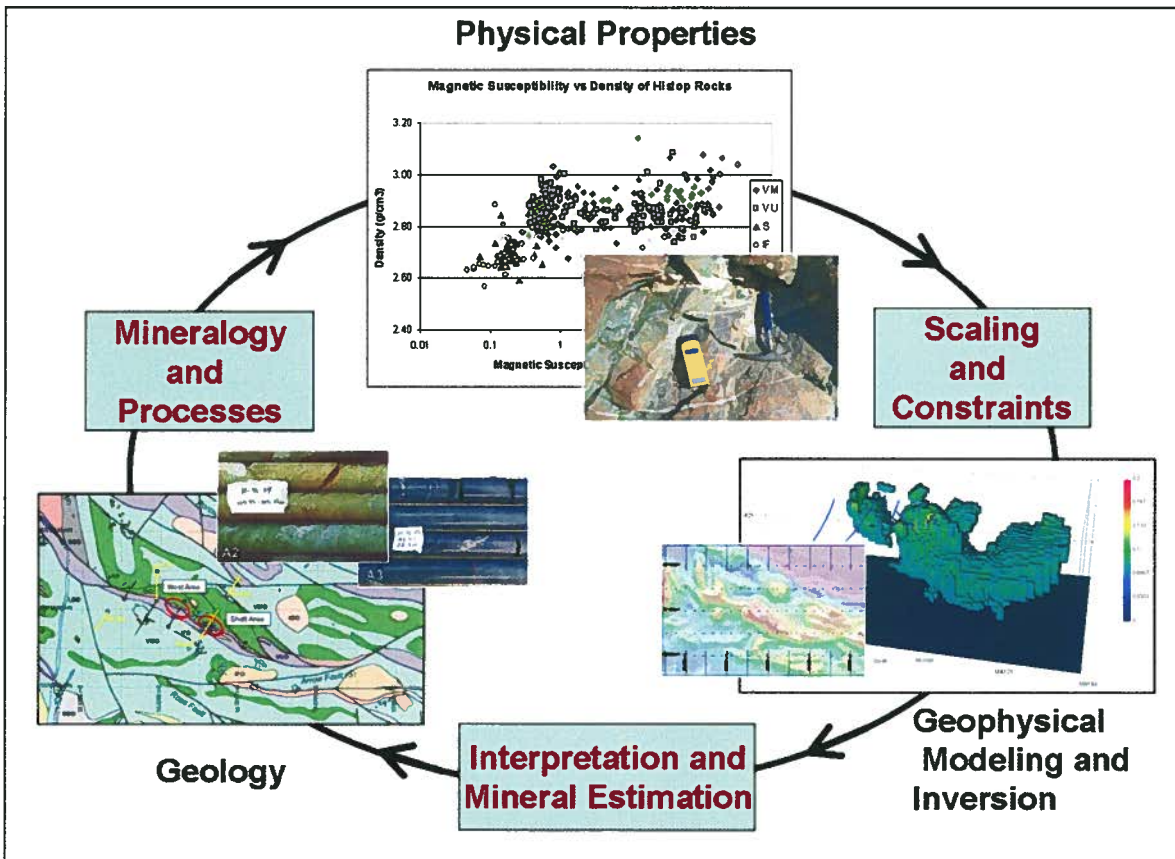


Figure 1.1. Flow chart illustrating the role of physical properties in the inversion process.

1.2. BACKGROUND TO GEOPHYSICAL INVERSION

The UBC-GIF inversion programs are primarily used as modeling and exploration tools in this project. This thesis does not go into detail regarding the mathematics behind the inversion codes. However, in order to understand how prior geologic information can be accommodated in the inversion, and in order to appreciate features and anomalies that are manifested in the inversion results, it is important to have a general knowledge of how the codes work.

Geophysical inversion can be considered the opposite process to forward modeling. Forward modeling involves generating data for a known subsurface physical property distribution. Forward modeling is sometimes used to determine the effect a specific source within the subsurface has on a measured geophysical signal. Geophysical inversion involves estimating a subsurface physical property distribution based on an observed geophysical dataset. In this case the data are known, and the location, and physical property value of the source must be calculated.

To calculate a 3D subsurface model, a volume representing the earth is discretized into many model cells. A reference model or starting physical property value is assigned to the earth and physical properties within cells are perturbed over numerous iterations to attempt to fit the observed geophysical data (either collected at surface or from boreholes). The user specifies a misfit, represented by Equation 1. The misfit is essentially a measure of the difference between the observed data, and the data predicted by the recovered inversion model. Because there are far more unknowns (model cells) than there are data, there are an infinite number of possible solutions to the inversion problem. This non-uniqueness is alleviated by the addition of more information to the problem. Results can be constrained by formulating the inversion to achieve a model with particular characteristics, based on prior geological knowledge. This information is incorporated into the problem through the model objective function.

$$\phi_d(m) = \sum_{i=1}^N \left(\frac{d_i^{obs} - d_i^{pred}}{\varepsilon_i} \right)^2$$

Equation 1. Where N is the number of geophysical data, d_i^{obs} is the observed data at location i , d_i^{pred} is the predicted data at location i , and ε_i is the standard deviation.

For default inversions, the model objective function specifies that the desired model is one that is close to a given reference or background model, and is smooth in all directions. The inversion is guided toward a result honoring these specifications. The model objective function is represented in Equation 2, showing only the function controlling closeness to the reference value, and the function controlling smoothness in the x direction. These default parameters can be modified when more specific information is known about the geology. The reference value can be modified and its degree of influence on the result can be manipulated (α_s), and directionality can be invoked by increasing smoothing in different directions by varying amounts (α_x). The resulting inversion model is only acceptable if, data generated when the model is forward modeled (the predicted data) is within error of the observed data.

In effect, there is no ‘best’ model, but likely a range of models that satisfy the model criteria and are geologically reasonable.

$$\phi_m = \alpha_s \int (m - m_0)^2 dx + \alpha_x \left(\frac{d}{dx} (m - m_0) \right)^2 dx \dots$$

Equation 2. Where α_s is the alpha weighting determining the degree of closeness to reference model, α_x determines smoothing in the x direction, m is the model, and m_0 is the reference model. In the full equation, functions in the same form as the x -smoothing function exist for the y and z directions.

Detailed inversion procedures and equations are found in Li and Oldenburg (1996, 1998, and 2000).

1.3. ARCHEAN OROGENIC GOLD - GEOLOGIC AND GEOPHYSICAL BACKGROUND

1.3.1. Background on Archean orogenic gold

Recent comprehensive summaries of orogenic gold deposits are given in Groves et al. (1998), Hagemann and Cassidy (2000), Goldfarb et al. (2005), and Robert et al. (2005), and characteristics significant to the thesis are generalized here. Orogenic gold deposits are epigenetic, structurally controlled gold deposits that are hosted in orogenic belts. They are generally accepted as having formed during late stages of continental collision. Most of the discovered orogenic gold deposits in the world occur in greenstone belts situated on Archean cratons in North America, Australia, and southern Africa.

Archean orogenic gold deposits typically occur proximal to large, crustal-scale faults, which are thought to represent the conduits that transported gold-bearing fluids to near-surface from depth. These deposits can occur in any host lithology, however there appears to be a common spatial relationship to felsic intrusive rocks, perhaps due to their brittle nature and ability to develop fractures, and to Fe-rich rocks, which may promote sulfidation causing gold precipitation. Hydrothermal fluids carrying gold are typically CO₂-rich and this is reflected in the carbonate-rich alteration mineral assemblages that accompany mineralization. Gold is most commonly hosted within or proximal to quartz-carbonate veins, but may also occur in association with disseminated sulfides in spatial proximity to faults or shear zones.

1.3.2. The Hislop gold deposit

The Hislop deposit is found in the gold and base-metal rich Abitibi greenstone belt of the Superior Province of Canada. It lies near the Porcupine Deseor Deformation Zone (PDDZ), a regionally important structure with respect to gold mineralization.

The general geology of the Hislop Township was mapped by Prest (1956), and more recently by Berger (1999). A geological map of the eastern Timmins area based predominantly on interpretation of high resolution aeromagnetic data, was compiled by Geoinformatics Exploration Inc. Geoinformatics also compiled an extensive database of geologic logs from drillcore derived from exploration programs run by the companies that have explored the Hislop property over the last 75 years. Berger (2002) completed an assessment on the geology and geochemistry of rocks along the eastern portion of Highway 101 (the 'Golden Highway'), which follows the PDDZ, that included an overview of the geologic setting of mineral deposits along this corridor. The most detailed work on the Hislop deposit was completed by geologists working at St. Andrew Goldfields Ltd at the time of mining. Some underground maps were made, and petrographic and lithogeochemical work completed. At the time of the commencement of this project, the Hislop mine was closed, and most of the geologists who had worked at the mine no longer were with St. Andrew Goldfields. Much of the data on the deposit that was collected, some in digital and some in hard copy form, was scattered and difficult to compile. An internal report with significant detail on the various mineralized zones on the Hislop property was provided for this project as a reference (Roscoe and Postle, 1998).

For this project, ten drillholes were re-logged, and a limited amount of geologic mapping was completed at the flooded Hislop West Area open pit, and on select outcrops in the vicinity.

In general, the Hislop deposit is hosted within a series of metamorphosed mafic and ultramafic volcanic rocks. The area is structurally complex with numerous tight folds

and faults paralleling the regional structural trend. Gold is spatially related to a contact between a syenite dike and an ultramafic volcanic unit. Gold is refractory within disseminated pyrite, and mineralization is associated with carbonate and muscovite alteration.

St. Andrew Goldfields Ltd. currently own the Hislop deposit property. The deposit is a relatively small gold deposit only mined for a few years total, producing just over 400 000 tonnes of ore, grading between 2.33 and 5.55 grams per tonne. Further gold potential has been indicated by recent drilling and sampling programs (www.standrewgoldfields.com).

1.3.3. Geophysics and gold

Geophysics constitutes a useful tool in greenstone-hosted gold settings since these environments are commonly characterized by scarce outcrop. In the area between the main Timmins gold camp and the Ontario-Quebec border, where the Hislop deposit is situated, there is minimal topography. The area is heavily forested, and covered with numerous lakes.

Although geophysics is heavily relied on for geologic mapping and exploration for a variety of mineral deposits in these settings, gold deposits are a notoriously elusive geophysical target. The deposits are typically low grade, and locally restricted, resulting in a poor petrophysical contrast between the target and its host rocks. Nonetheless, other geological features known to be spatially related to gold, such as host rocks, hydrothermal alteration, or sulfide mineralization, might provide petrophysically distinct targets.

The geophysical methods most successfully applied for gold exploration have been DC resistivity and induced polarization (IP) methods. These methods detect conductive and chargeable sulfides commonly associated with orogenic gold. Some

examples of the use of these methods in gold exploration are given in Seigel et al. (1984), Johnson et al. (1989), Doyle (1990), and Halloff and Yamashita (1990)

There are limited case studies using inversion in this mineral deposit environment. Some recent work includes that of Kowalczyk et al. (2002) *Mira Geoscience* (2005a and 2005b), and Mueller et al. (2005). It is hoped that the work completed for this PhD will contribute to an advanced understanding of the application of geophysical inversion techniques in the Archean orogenic gold setting.

1.4. PROJECT OBJECTIVES

The overlying goal of this research was to optimize the geophysical inversion process to explore for gold-related rocks in the Archean orogenic gold setting. The first step in achieving this goal was to identify relationships between geology, specifically gold-related geology, and physical properties, and to delineate the key geological processes that lead to these relationships. Secondly, synthetic modeling was used to determine if typical gold-related features can be regularly detected by inversion, and if inversion parameters can be modified to improve their detection. The final stage of the work involved applying prior geological and physical property knowledge to the inversion of four geophysical datasets covering the Hislop deposit area. The results of this PhD research are presented in three chapters that correlate with each of the three research stages. The thesis objectives are summarized here by chapter.

Chapter 2.

Initial research involved defining relationships between geology and physical properties. As mentioned, this information is critical to any geophysical or inversion work. It is obviously important with respect to interpreting results. However, it is also valuable for constraining inversions, for identifying if inversion results are sensible, and for building synthetic physical property models to test hypotheses. Magnetic susceptibility, density, resistivity, and chargeability data were collected for Hislop rock

samples. The goals of this initial physical property work were to outline the physical property ranges for the main rock types at Hislop, to understand any trends within physical property data, and to determine if prospective rocks could be distinguished from barren rocks based on physical properties. Additionally, to establish whether the results from this work can be applied to geophysical exploration in other areas, physical property data was compared to a large regional dataset, and data from greenstone belts in Australia.

Chapter 3.

Although physical property work might indicate that certain gold-related rocks have unique physical property ranges, allowing them to be distinguished from likely barren rocks, these targets may still be undetectable through inversion. This may be attributable to: geophysical survey design, data spacing, data errors, inversion discretization, inversion sensitivities, and smoothing typical in inversion results. Synthetic forward and inverse modeling tests the effectiveness of inversion to delineate desirable features in the subsurface at deposit-scales of exploration. A model based on the Hislop deposit is used, however, variations are made to the initial model and to the applied inversion parameters to explore outcomes. The research aimed to determine: whether desired targets can be imaged using inversion, whether inversion parameters could be manipulated to get a better result, which geophysical datasets yield the most useful information about the subsurface, which are best for detection of gold-related features, and what limitations exist for inversion in this setting.

Chapter 4.

Chapter 4 presents results from inversion of four geophysical datasets (magnetic, gravity, DC resistivity, and IP) over the Hislop deposit. Where prior physical property data is available, inversions are constrained locally and globally to generate models more consistent with known geology. The main goals of this work was to examine the subsurface geology of the Hislop deposit area, to attempt to image specific geologic units or packages of rock, to locate key geologic structures in the subsurface, and most importantly, to identify prospective areas for exploration. Geophysical datasets most

useful for mapping geology, and for isolating mineral exploration targets were identified. Knowledge gained from physical property work and from synthetic modeling was invoked to assess and interpret inversion results.

Chapters 2 to 4 form the basis for three manuscripts to be submitted to mineral exploration-related, or applied geophysical journals. As the three chapters represent three separate deliverables, there is some overlap in information between them.

REFERENCES

Berger, B.R., 1999, Geological investigations along Highway 101, Hislop Township: Ontario Geological Survey, Summary of Field Work and Other Activities 1999, Open File Report, 6000, p. 5-1 – 5-8.

Berger, B.R., 2002, Geological synthesis of the Highway 101 area, east of Matheson, Ontario: Ontario Geological Survey, Open File Report 6091, 124 p.

Doyle, H.A., 1990, Geophysical exploration for gold – a review: *Geophysics*, v. 55, p. 134-146.

Goldfarb, R. J., Baker, T., Dube, B., Groves, D.I., Hart, C.J.R., and Gosselin, P., 2005, Distribution, character, and genesis of gold deposits in metamorphic terranes: *in* Hedenquist, J.W., Thompson, J.F.H., Goldfarb, R.J., and Richards, J.P., eds., 100th Anniversary Volume, *Economic Geology*, v. 100, p. 407-450.

Groves, D.I., Goldfarb, R.J., Gebre-Mariam, M., Hagemann, S.G., and Robert, F., 1998, Orogenic gold deposits: a proposed classification in the context of their crustal distribution and relationship to other gold deposit types: *Ore Geology Reviews*, v. 13, p. 7-27.

Hagemann, S.G., and Cassidy, K.F., 2000. Archaean orogenic lode gold deposits, *in* Hagemann, S.G., and Brown, P.E., eds., *Gold in 2000*, Society of Economic Geologists, *Reviews in Economic Geology*, v. 13, p. 9-68.

Halloff, P.G., and Yamashita, M., 1990, The use of the IP method to locate gold-bearing sulfide mineralization, *in* Fink, J.B., Sternberg, B.K., McAlister, E.O., Weiduwilt, W.G., and Ward, S.H., eds., *Induced Polarization: applications and case histories*, Society of Exploration Geophysicists, Tulsa, Ok., p. 227-279.

Johnson, I., Webster, B., Matthews, R., and McMullen, S., 1989, Time-domain spectral IP results from three gold deposits in northern Saskatchewan: CIM Bulletin, v. 82, p. 43-49.

Kowalczyk, P., Thomas, S., and Visser, S., 2002, 3D inversion of resistivity and IP data, two case studies from mineral exploration:, SEG International Exposition and 72nd Annual Meeting extended abstract, 4 p.

Lelievre, P., Oldenburg, D., and Williams, N., 2008, Constraining geophysical inversions with geologic information: Society of Exploration Geophysicists, 2008 Annual Meeting, Las Vegas, extended abstract, p. 1223-1227.

Li, Y., and Oldenburg, D.W., 1996, 3D inversion of magnetic data: Geophysics v. 61, p. 394-408.

Li, Y., and Oldenburg, D.W., 1998, 3D inversion of gravity data: Geophysics, v. 63, p. 109-119.

Li, Y., and Oldenburg, D.W., 2000, 3D inversion of induced polarization data: Geophysics, v. 65, p.1931-1945.

Mira Geoscience Limited, 2005a, Detectability of mineral deposits with electrical resistivity and induced polarization methods: Ontario Geological Survey, Miscellaneous Release – Data 181.

Mira Geoscience Limited, 2005b, Detectability of mineral deposits with potential field methods: Ontario Geological Survey, Miscellaneous Release – Data 177.

Mueller, E.L., Reford, S.W., Dawson, D.J.W., Morrison, D.F., Pawluk, C., Grant, J., Spector, A., Rogers, D.S., and Savage, T., 2006, Acquisition, inversion and presentation of geophysical data for geoscientific profiles in the Timmins–Kirkland Lake area:

Discover Abitibi Initiative, Ontario Geological Survey, Open File Report 6189 , 28 p., 15 sheets.

Phillips, N., Oldenburg, D., Chen, J., Li, Y., and Routh, P., 2001, Cost effectiveness of geophysical inversions in mineral exploration: Applications at San Nicolas: The Leading Edge, v. 20, p. 1351-1360.

Phillips, N., Hickey, K., Lelievre, P., Mitchinson, D., Oldenburg, D., Pizarro, N., Shekhtman, R., Sterritt, V., Tosdal, D., and Williams, N., 2007, Applied strategies for the 3D integration of exploration data: KEGS Inversion Symposium, PDAC 2007, extended abstract, 9 p.

Pizarro, N., 2008, Magnetic susceptibility scaling of rocks using geostatistical analysis: an approach to geologic and geophysical model integration: Unpublished M.Sc. thesis, University of British Columbia, 177 p.

Power, W. L., Byrne, D., Worth, T., Wilson, P., Kirby, L., Gleeson, P., Stapleton, P., House, M., Robertson, S., Panizza, N., Holden, D. J., Cameron, G., Stuart, R., and Archibald, N. J., 2004, Geoinformatics evaluation of the eastward extension of the Timmins Gold Camp: Geoinformatics Exploration Inc., Unpublished report for St Andrew Goldfields Ltd.

Prest, V.K., 1956, Geology of the Hislop Township: Ontario Department of Mines, Annual Report, 1956, v. 65, pt. 5, 51 p.

Reed, L. E., 2005, Gravity and magnetic three-dimensional (3D) modeling: Discover Abitibi Initiative, Ontario Geological Survey, Open File Report 6163, 40 p., 4 sheets.

Robert, F., Poulsen, K.H., Cassidy, K.F., and Hodgson, C.J., 2005, Gold metallogeny of the Superior and Yilgarn Cratons, *in* Hedenquist, J.W., Thompson, J.F.H., Goldfarb, R.J.,

and Richards, J.P., eds., 100th Anniversary Volume, *Economic Geology*, v. 100, p. 407-450.

Roscoe and Postle Inc., 1998, Hislop Mine Property, Roscoe and Postle Associates Inc., unpublished St. Andrew Goldfields Ltd. internal report, p. 66-89.

Seigel, H.O., Johnson, I., and Hennessey, J., 1984, Geophysics the leading edge: *Geophysics: the Leading Edge of Exploration*, v. 3, p. 32-35.

Sterritt, V.A., 2006, Understanding physical property–mineralogy relationships in the context of geologic processes in the ultramafic rock-hosted mineral deposit environment: aiding interpretation of geophysical data: Unpublished M.Sc. thesis, The University of British Columbia, 172 p.

Williams, N.C., 2008, Geologically-constrained UBC–GIF gravity and magnetic inversions with examples from the Agnew-Wiluna greenstone belt, Western Australia: Unpublished Ph.D. Thesis, The University of British Columbia, 479 p.

Chapter 2: Physical properties of rocks in an Archean orogenic gold environment¹

2.1. INTRODUCTION

2.1.1 Rationale

In order for geophysical inversion to be knowledgeably interpreted, it is imperative to (1) have an understanding of the rock types, alteration, and mineralization that typify the geological environment, and (2) possess an understanding of the characteristic ranges of physical properties associated with this geology. Ideally, physical property studies should be conducted on the range of representative rock types from the geological environment of interest to try and understand how, why, and on what scales, physical properties in this environment vary. It is possible to refer to published datasets for typical physical properties of rock types in a specific environment, however this information is commonly limited and the effects of hydrothermal alteration on the protolith are rarely considered.

Once a clear understanding of the relationships between various physical properties and rock types, alteration, and mineralization are established, this information can be used to interpret and guide geophysical inversions. If unique relationships are present and can be statistically characterized, physical property model data generated from inversion can be queried for prospective ranges, or filtered to yield mineralogical information (Williams and Dipple, 2005). Knowledge of physical property ranges typical of a given geological environment can indicate whether an inversion has yielded realistic values. Additionally, the inversion algorithm can be manipulated to incorporate prior physical property information to drive the inversion toward a result more consistent with expected geology (Ellis and Oldenburg, 1994; Li and Oldenburg, 1996). Understanding physical property behavior, and having confidence in the data being used to constrain

¹ A version of this chapter will be submitted for publication. Mitchinson, D., Phillips, N., Pani, E., and Tosdal, D., 2009, Physical properties of rocks in an Archean orogenic gold environment.

inversions is critical; changing inversion parameters, or using reference models to constrain inversions, can change a model significantly (Phillips, 2002; Williams, 2006).

A physical property study of the Hislop deposit aims to provide a detailed investigation into physical property relationships within an Archean orogenic gold deposit environment. Physical properties considered are magnetic susceptibility, density, resistivity, and chargeability. An important goal of these studies is to identify the physical property datasets, alone, or in combination, which are most effective in detecting Archean orogenic gold-related mineralization or proxies to mineralization.

2.1.2 Objectives

The objectives of this research are to:

1. Review the key characteristics of Archean orogenic gold environments, and the geophysical methods commonly employed in exploration for them;
2. Characterize the principal host rocks, alteration characteristics, and styles of gold mineralization at Hislop;
3. Document relationships between physical properties and rocks at Hislop through petrographic work and mineral analyses;
4. Explain the controls on physical property variations;
5. Outline magnetic susceptibility, density, resistivity, and chargeability ranges that specifically characterize the host rocks, alteration mineral assemblages, and mineralization at Hislop;
6. Define the most useful physical properties for targeting potentially mineralized rocks at Hislop;
7. Assess whether physical property values are representative of Archean orogenic gold settings elsewhere.

2.2. BACKGROUND

2.2.1 Geology and geophysics of Archean orogenic gold deposits

Geological characteristics of Archean orogenic gold deposits

Orogenic gold deposits are epigenetic, structurally-controlled gold deposits hosted in metamorphosed orogenic belts (Groves et al., 1998). This work focuses specifically on the physical property analysis of rocks associated with orogenic gold deposits hosted within an Archean age greenstone belt setting. Although Archean orogenic gold deposits are not restricted to one particular rock type, spatial relationships to felsic intrusive rocks, and to Fe-rich mafic rocks are common (Hodgson and Troop, 1988; Hodgson, 1990; Groves and Foster, 1991; Goldfarb et al., 2005; Robert et al., 2005). Gold is thought to be transported in CO₂-rich fluids (Bohlke, 1989; Ridley and Diamond, 2000) and as such, mineralization is usually associated with carbonate-rich alteration mineral assemblages (Fyon and Crockett, 1983; Kishhida and Kerrich, 1987; Mueller and Groves, 1991; McCuaig and Kerrich, 1998). Gold occurs most commonly within quartz- and carbonate-filled vein systems, and occurs less frequently as disseminated replacement zones, or as stockwork mineralization (Roberts, 1988; Hodgson, 1993; Hagemann and Cassidy, 2000; Goldfarb et al., 2005). The Archean gold deposits considered in this study do not include Archean-age placer, or banded iron formation (BIF)-hosted gold deposits.

Archean orogenic gold deposits have for many years been an important source of gold in Australia, Africa, India, and North America (Goldfarb et al., 2005; Robert et al., 2005). With a rise in gold prices in recent years, there has been a revival in exploration for these types of deposits, and an initiative to improve exploration methods for their discovery.

Geophysical characteristics of orogenic gold deposits

Gold is notoriously difficult to detect using geophysics (Seigel et al., 1984; Doyle, 1990). Although gold itself is dense and conductive (19.3 g/cm^3 , and $5 \times 10^7 \text{ S/m}$, respectively; Doyle, 1990), it is usually only present in relatively small quantities in Archean orogenic gold deposits, in contrast to massive-style mineralization represented in volcanogenic massive sulfide deposits or nickel sulfide deposits, which form larger geophysical targets in distinct contrast to host rocks. Defining alternative targets, or indicators, with known relationships to gold, and sufficiently distinct physical property characteristics, is required to fully utilize geophysical tools (Seigel et al., 1984; Doyle, 1990).

Geophysical methods used to target gold-associated structures, host rocks, and alteration zones include magnetics, gravity, electrical methods (DC resistivity and induced polarization), and electromagnetic methods. Table 2.1 lists various geological features commonly related to gold mineralization, and examples of the geophysical methods that are most effective in targeting them. Ideally some combination of techniques can be employed to target a variety of gold-related features at a particular locality, in order to prioritize areas of interest. Magnetics and induced polarization (IP) are historically the most useful methods in delineating lithologies, structures, alteration, and sulfide distribution related to gold mineralization.

2.2.2 Geology of the study area

Regional geological setting

The Superior Province of the Canadian Shield is the largest Archean craton on earth. It is composed of a number of northeast-trending, amalgamated volcano-plutonic, granitic-gneissic, and sedimentary terranes (Card and Ciesielski, 1986). Boundaries of the terranes, or subprovinces, are structural or metamorphic zones that juxtapose contrasting

geological and geophysical terranes (Card and Ciesielski, 1986; Card, 1990; Williams et al., 1991). The study area for this project is located within the south-central Abitibi subprovince, or greenstone belt (Fig. 2.1).

Table 2.1. Geophysical characteristics of Archean orogenic gold deposits

Feature	Scale	Geophysical character	Methods of detection
1 Greenstone terranes	Regional 1000 kms	Overall low, but 'rough' magnetic character Granitoids commonly lower density than greenstone	Airborne magnetics Airborne gravity
2 Large scale faults	Regional to district 100 kms □	Low magnetic signature attributed to oxidation/alteration High/low resistivity zones dependant on degree of annealing	Airborne/ground magnetics DC resistivity
3 Lithological marker units	District 10 kms	Various depending on physical properties of rock type of interest	Various depending on rock type of interest
4 Hydrothermal alteration	Local 10 m	Magnetic lows resulting from destruction of magnetite; less commonly magnetic highs, due to influx of Fe-rich fluids High resistivity if silicification	Airborne/ground magnetics DC resistivity
5 Mineralization	Local 10 m	Disseminated sulfide association with gold - conductive and chargeable Magnetic pyrrhotite	DC resistivity and Induced Polarization Magnetics if pyrrhotite is main Fe-sulfide associated with gold

1) Grant, 1985; Isles et al., 1989; Doyle, 1990; Williams et al., 1991; Gunn and Dentith, 1997; 2) Henkel and Guzman, 1977; Boyd, 1984; Grant, 1985; Doyle, 1990; Coggon, 1984; 3) Doyle, 1990; Groves et al., 1984; Gunn and Dentith, 1997; Boyd, 1984; Grant, 1985; Hood et al., 1982; 4) Holsner and Schneer, 1961; Grant, 1985; Harron et al., 1987; Doyle, 1990; Williams, 1994; Lapointe et al., 1986; Johnson et al., 1989; Doyle 1990; 5) Johnson et al., 1989; Seigel et al., 1984, Doyle, 1990; Hallof and Yamashita, 1990; Dockery et al., 1984.

Many of the gold deposits in Abitibi greenstone belt gold camps, like the Timmins-Porcupine, and Kirkland Lake camps, are spatially related to prominent, large scale crustal structures, including the east-west trending Porcupine-Destor Deformation Zone and Larder-Lake-Cadillac Deformation Zone (Colvine et al., 1988; Kerrich, 1989;

Hodgson and Hamilton, 1990; Jackson and Fyon, 1991). Most gold deposits are not localized by these larger “first order” faults, but by secondary or tertiary splays (Kerrich, 1989; Robert, 1990; Hodgson, 1993; McCuaig and Kerrich, 1998; Hagemann and Cassidy, 2000).

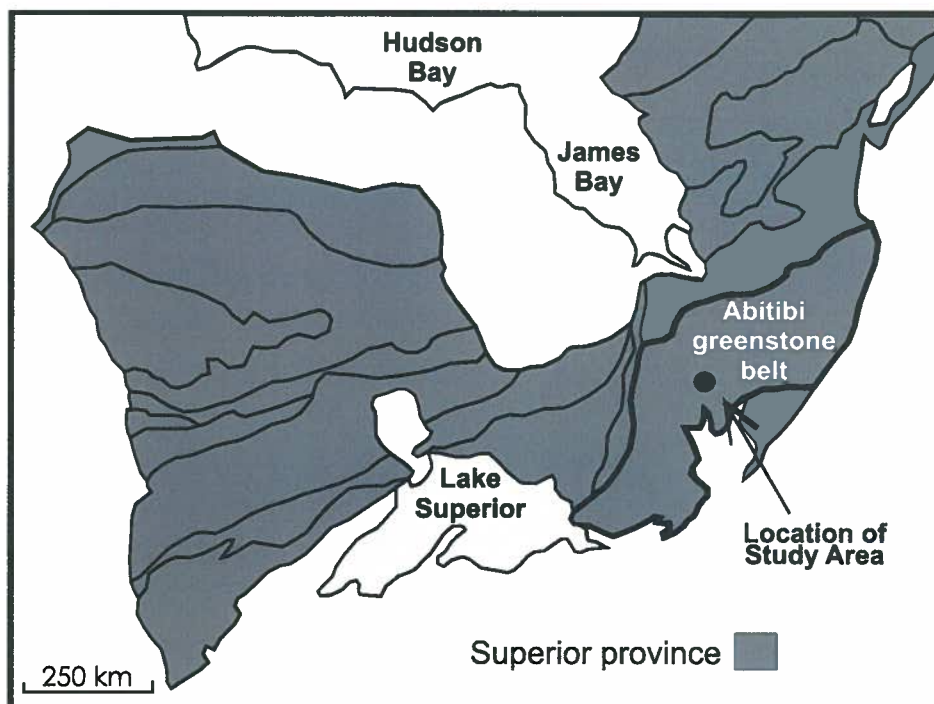


Figure 2.1. Approximate location of the Hislop study area in the Abitibi greenstone belt of the Superior Province. Modified after Card and Ciesielski (1986).

Hislop deposit geology and gold setting

The Hislop deposit area is underlain mainly by interlayered mafic and ultramafic volcanic rocks (Fig. 2.2). The volcanic rocks are complexly folded and are presently aligned northwest-southeast. They are intruded by coarse-grained syenites, fine-grained quartz-feldspar phyric rhyolite dikes, and dacitic to andesitic dikes, usually along northwest-southeast trending faults (Prest, 1956; Berger, 1999; Power et al., 2004).

Gold is localized near the northeast and southwest contacts of an elongate, approximately 30 m -100 m wide, northwest-trending syenite (Cooper, 1948; Prest, 1956; Roscoe and Postle, 1998; Berger, 1999 and 2002), as depicted in the cross-section in Fig. 2.3. The majority of gold at Hislop is associated with disseminated pyrite within, what is recorded in mine and geological survey documents as, “carbonate-breccia”, south of the syenite (Cooper, 1948; Prest, 1956; Roscoe and Postle, 1998). The carbonate breccia is predominantly a strongly carbonate-altered brecciated equivalent of an ultramafic unit at Hislop. Gold also occurs to a lesser extent within quartz veinlets, stockworks and fractures in mafic volcanic flows north of the syenite (Roscoe and Postle, 1998). Generally, there is little gold within the syenite, with the exception of weak mineralization occurring within a zone approximately 3 m from the southern contact with carbonate breccia. (Cooper, 1948). High gold grades at Hislop are also associated with rhyolite porphyries, which are found as narrow, discontinuous intrusive bodies in mafic and ultramafic units south of the syenite (Fig. 2.2).

A number of northeast-trending, sinistral separation cross-faults offset the syenite and bounding mafic and ultramafic flows in places (Cooper, 1948; Prest, 1956; Power et al., 2004). Gold-bearing zones widen, and gold grade commonly increases where these cross faults intersect mineralization along the syenite (Roscoe and Postle, 1998)

Two principal mineralized zones, the Shaft Area and the West Area (Fig. 2.2), were mined by St. Andrew Goldfields, Ltd., at Hislop over three separate intervals between 1990 and 2006. In 1990 and 1991, 215 990 tonnes of ore grading 5.55 g/t were mined, between 1999 and 2000, 185 100 tonnes of ore grading 3.4 g/t were mined, and recently in 2006, 10147 tonnes of ore grading 2.33 g/t were mined (www.standrewgoldfields.com).

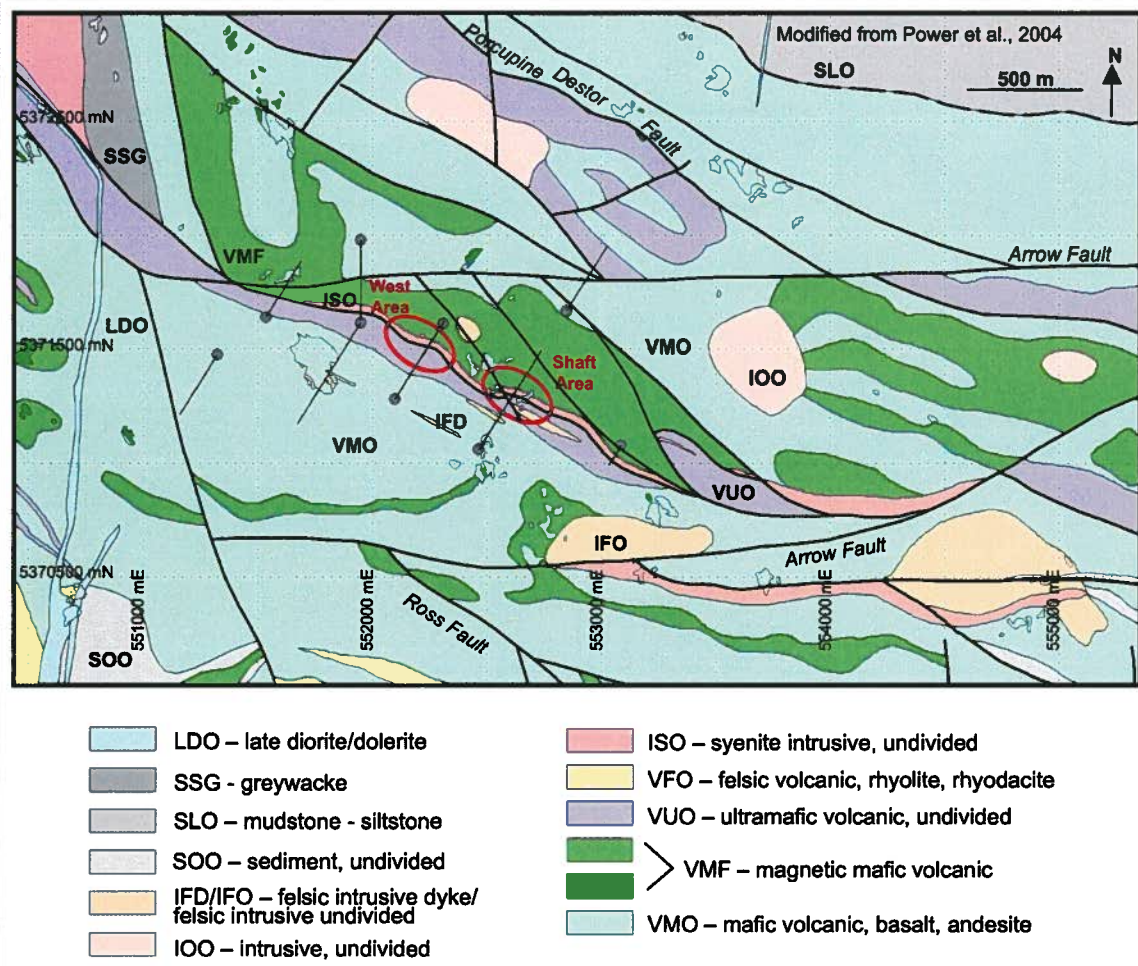


Figure 2.2. Geology of the Hislop deposit area as interpreted by Power et al. (2004) from high resolution aeromagnetics. Locations of two mined areas on the Hislop property (West Area open pit; Shaft Area underground) are outlined in red. Also shown are 10 drill holes (one overlapping) logged for this study. The cross-section shown in Figure 2.3 is based on core logging of three drill holes that were drilled in the West Area.

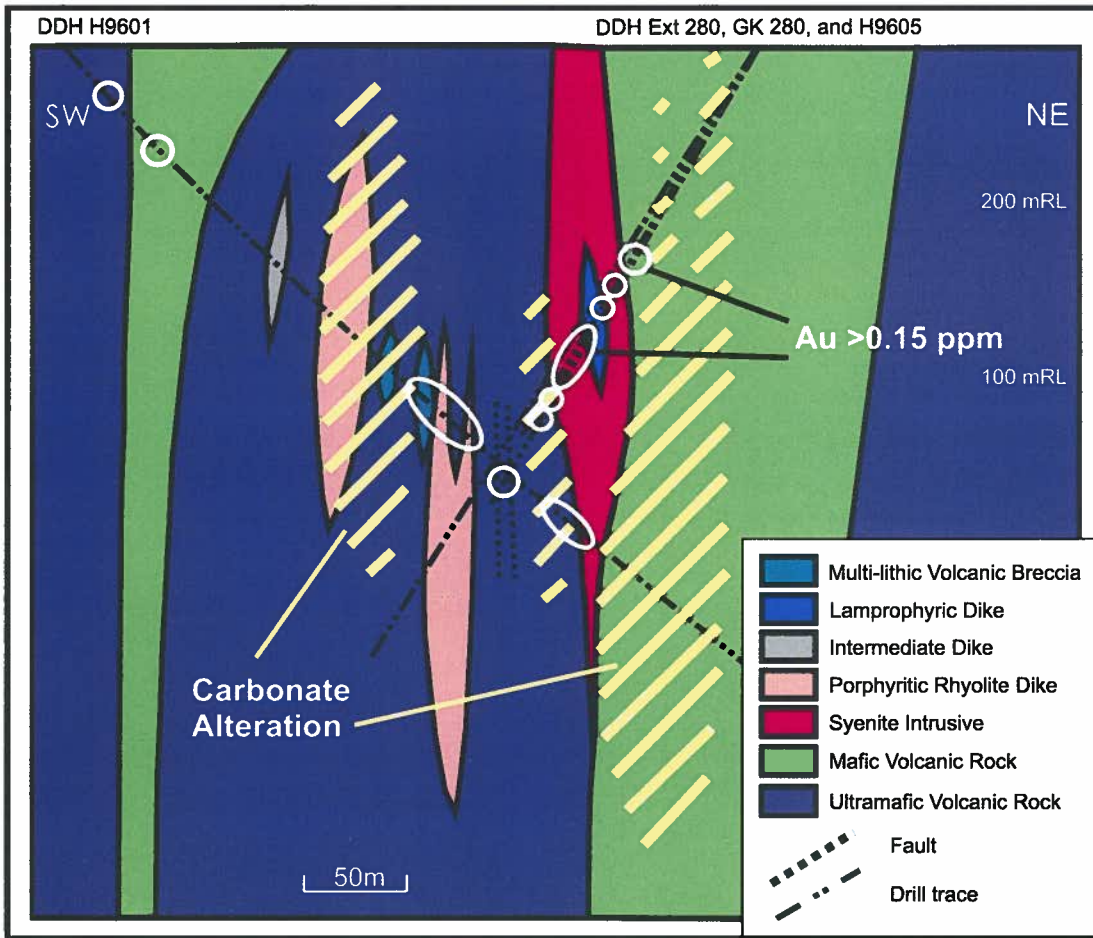


Figure 2.3. Cross section looking northwest through the Hislop deposit, showing locations of carbonate-dominated alteration and gold mineralization. Cross section interpreted from drill core logged from the West Area of the Hislop property.

2.3. METHODOLOGY

2.3.1 Field and mineralogical studies

Ten drill holes from the 1996 and 1997 St. Andrew Goldfields Ltd. drill programs were re-logged for this study. Geology, alteration and structure were recorded down-hole (Appendix 2B). Surface geology at the West Pit was mapped. Small areas, approximately

10 m by 10 m were mapped in detail for outcrop scale studies of magnetic susceptibility (Appendix 2B).

Petrographic, and mineralogical studies (scanning electron microscope and X-ray diffraction studies) allow for characterization of host rocks and alteration mineral assemblages within the Hislop deposit area. This work also constrains geological processes that control physical property variations. The presence, abundance, and composition of minerals, such as magnetite, pyrite, and carbonate, which have particularly significant influences on physical properties, were documented. Whereas petrographic and SEM work defines the minerals present in the various samples, quantitative XRD work using Rietveld refinement methods, described by Raudsepp and Pani (2003) and outlined in Appendix 2C, contributes relative mineral proportions for 37 samples at Hislop. This quantitative information is useful for comparisons to physical property data, and for calculations of density data.

2.3.2 Physical property measurements

Magnetic susceptibility

Magnetic susceptibility data from Hislop was recorded using a hand-held magnetic susceptibility meter, the Exploranium KT-9 Kappameter. Susceptibilities are reported in 10^{-3} SI Units. Magnetic susceptibility readings were taken every 5 m along drill core for all drill holes re-logged for this project. Measurements were made on all samples collected from drill core and from outcrop. Magnetic susceptibility readings were taken at 10 different points over each sample, and the average value was used in analyses of this data. Magnetic susceptibility readings were also collected systematically over six roughly 10 m^2 grids over mapped outcrops to understand controls on susceptibility at the surface at outcrop scale. Typically 2-5 readings were taken at each site and the average was used. In total magnetic susceptibility was determined for 432 samples. Greater than 1000 additional readings were collected from drill core and

outcrop. Corrections applied to susceptibility measurements to account for core diameter, and split core intervals are outlined in Appendix 2C. The magnetic susceptibility dataset represents the largest physical property dataset from the Hislop physical property study.

Density

Density measurements were made for 414 drill core and hand samples from Hislop using the buoyancy or hydrostatic method and calculations outlined by Johnson and Olhoeft (1984). To calculate grain density:

$$\rho_g = \rho_w * W_1 / (W_1 - W_2)$$

where ρ_g is grain density, W_1 is the mass of the oven-dried sample in air, and W_2 is the mass of the sample submerged in water. To obtain the mass of the sample in water, the sample is placed on a tray which is suspended from a weighing scale positioned above a small tank of water. The scale is tared with the tray hanging suspended in the water bath, and the sample is added to the submerged tray. ρ_w is the density of the water, which is assumed to be 1 g/cm³. Density is reported in g/cm³. Additional density measurements were made using an alternate method, the geometric method, to confirm data accuracy, and results are presented in Appendix 2C.

For grain density calculations, porosity is not considered. However, for later interpretations of some trends in the Hislop physical property data, it was of interest to calculate porosity. Porosity is calculated from dry and saturated rock masses. Isolated porosity (inaccessible to air or water) is not accounted for by this method. The equation used is (Cas and Wright, 1987):

$$\phi = 100 * (W_3 - W_1) / (W_3 - W_2)$$

where ϕ is porosity, W_1 is the mass of the oven-dried sample in air, W_2 is the mass of the sample submerged in water, and W_3 is the mass of the water-saturated sample in air (Cas and Wright, 1987). Porosity is reported as %.

Resistivity and chargeability

Resistivity and chargeability data for 67 representative drill core and hand samples were measured by Zonge Engineering and Research Organization, Inc. Resistivity and chargeability measurements are collected simultaneously after samples have been moisture-saturated. They are made in time-domain. A current is established between opposite ends of the samples using a constant current transmitter, which conducts currents as low as 100 nA. Resistivity is calculated based on the length, and cross-sectional area of the sample, the amplitude of the current, and the change in potential recorded across the sample. Resistivity is reported in Ohm-m. Conductivity can be calculated from resistivity by taking the inverse value. Conductivities are expressed in S/m. The chargeability of a sample is based on the rate of decay of the voltage after the applied current is turned off. For the Hislop samples, it was determined using an 8 second period, measured during the 0.45 – 1.1 seconds window after the current is turned off. The resultant value is the average chargeability value of a sample based on 16 cycles. Chargeability is reported in milliseconds (ms).

Large scale permeability, not necessarily exhibited in the drill core or hand sample, may control measurements made in the field. As such, measurements of resistivity taken on drill core or hand samples are commonly higher than measurements made in-situ (www.zonge.com/LabIP.html). This must be considered if sample-scale resistivity measurements are to be used to constrain geophysical inversions. Chargeability data collected from core or hand samples are thought to be sufficiently representative of larger scale measurements (www.zonge.com/LabIP.html).

2.4. DATA AND OBSERVATIONS

2.4.1. Hislop deposit rock types, hydrothermal alteration, and associated mineralogy

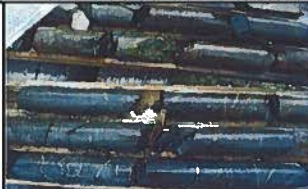
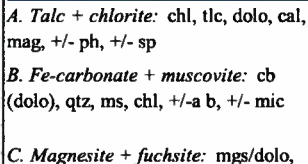
Rock Types

All rocks at Hislop have been metamorphosed to greenschist facies, however, for simplification purposes, the prefix meta- is herein ignored. The rock protoliths are recognizable based on textures and characteristic metamorphic mineral assemblages, and the protolith name is used hereafter. The five principal rock types at Hislop are, ultramafic volcanic rocks (predominantly komatiites), mafic volcanic rocks (tholeiitic basalts), intermediate (andesitic-basaltic) dikes, syenite intrusions, and feldspar (+/- quartz) porphyritic rhyolite dikes. Other rock types occurring less frequently in this area, which will not be discussed in detail, include mafic intrusions, lamprophyric dikes, and multi-lithic volcanic breccia units. Descriptions and typical mineralogy of the main Hislop rock types as determined through petrographic, scanning electron microscope, and X-ray diffraction work, are given in Table 2.2, and detailed results of XRD mineral abundance analyses are found in Appendix 2D.

Hydrothermal alteration

The most common hydrothermal alteration mineral assemblage at Hislop is a carbonate + muscovite rich assemblage that occurs predominantly in intermediate dikes, and mafic and ultramafic volcanic rocks. This is manifested as siderite or ankerite (grouped, and simplified herein as Fe-carbonate) + muscovite alteration in mafic volcanic rocks and intermediate dikes, and as either Fe/Mg-carbonate (ankerite to dolomite) + muscovite alteration, or magnesite (Mg-carbonate) + fuchsite (Cr-muscovite) alteration in ultramafic volcanic rocks. Carbonate + muscovite alteration was noted in drill core and outcrop to occur near faults and contacts, and in proximity to syenite and rhyolite

Table 2.2. Summary of the principal rock types found in the Hislop deposit area, and associated mineralogy.

	Ultramafic volcanic rocks	Mafic volcanic rocks	Intermediate dikes	Syenite dikes	Porphyritic rhyolite dikes
Least-altered					
Hand Sample Description	Dark black to brown (oxidized) in color; soft; commonly sheared; fine to medium grained textures; Qtz +/- cb veins; relict spinifex textures adjacent to margins of some flows; relict cumulate textures represent internal parts of the flow.	Dark grey-green to dark purple color; massive or pillowed (+/- variolites) flows up to 100 m thick; fine to medium grained rock; pillows are well-preserved with Qtz + cb filled amygdules increasing near margins; thin chl +/- ep altered selvages.	Dark grey to mauve in color; massive, homogeneous, and fine-grained; hbl-fsp phyrlic, hbl-phyric, or aphyric; phenocrysts approximately 1mm in length and euhedral; groundmass is very fine-grained and composed mainly of microlitic fsp.	Pink to mauve in color; massive; very coarse-grained; composed of mesoperthitic potassium fsp and ab; fsp crystals up to 3 cm; rare interstitial mafic minerals.	Massive; generally fsp (+/- Qtz) porphyritic; aphanitic grey to pink groundmass composed of very fine grained fsp and Qtz; fsp phenocrysts comprise 3% - 80% of the rock; Qtz phenocrysts make up 2 - 5% of the rock; minor mafic minerals.
Mineralogy	chl, dol, Qtz, +/- tlc, +/- hbl, +/- mag	ab, chl, aug, act, cal, Qtz, ep, ms, clzo, ulvo, mag	ab, cb, ms, Qtz, +/- chl, +/- mag, +/- py	ab, kspar, dol/ank/cal, py, +/- Qtz, +/- ms, +/- chl	ab, Qtz, mic, chl, +/- dol
Alteration	  	 	 	 	 
Alteration mineralogy	<i>A. Talc + chlorite:</i> chl, tlc, dolo, cal, mag, +/- ph, +/- sp <i>B. Fe-carbonate + muscovite:</i> cb (dolo), Qtz, ms, chl, +/- a b, +/- mic <i>C. Magnesite + fuchsite:</i> mgs/dolo, Qtz, ms (fuch), chl, +/- il, +/- cr -sp	<i>A. Fe-carbonate + muscovite - ank, ms, ab, sid, dol, Qtz, chl,</i> <i>B. Fe-carbonate + albite (+/-) quartz:</i> ab, dolo/ank, Qtz, mic, chl, mag	<i>A. Fe-carbonate + muscovite:</i> cb, ms, ab, Qtz, py <i>B. Fe/Mg-carbonate:</i> ab, cb, ms, py	<i>A. Muscovite:</i> ab, mic, ms, ank/dol, +/- py, <i>B. Fe-carbonate:</i> ab, mic, ank/dolo/sid, ms, +/- py, +/- chl	<i>A. Muscovite:</i> ab, Qtz, ms, cal, +/- py +/- py <i>B. Fe-carbonate:</i> ab, Qtz, ank, ms, +/- py <i>note: mineralogy based on 1 sample for each of A and B</i>

ab = albite; act = actinolite; ank = ankerite; aug = augite; cal = calcite; cb = carbonate; chl = chlorite; clzo = clinozoisite; cr-sl = Cr-spinel; dol = dolomite; ep = epidote; fu = fuchsite (Cr-muscovite); hbl = hornblende; il = ilmenite; mag = magnetite; mgn = magnesite; mic = microcline; ms = muscovite; ph = phlogopite; py = pyrite; Qtz = quartz; ser = sericite; sp = serpentine; sid = siderite; tlc = talc; ulv = ulvospinel; (Fe = iron; Mg = magnesium).

intrusions. Most of the mined Hislop ore came from an Fe-carbonate-altered ultramafic breccia, as such, carbonate-related alteration is considered an important vector to mineralization. Carbonate + muscovite alteration is commonly mapped as a distal, pervasive alteration surrounding Archean orogenic gold deposits, and this is the case for many gold deposits elsewhere in the Abitibi greenstone belt (Fyon and Crockett, 1983; Hodgson, 1990).

Fe-carbonate + albite alteration occurs at Hislop over narrow intervals within mafic volcanic rocks in drill core near some of the known high grade gold zones. Albite-rich alteration assemblages occur proximal to gold at other gold deposits in the Abitibi, including the Holloway deposit, near the Ontario-Quebec border (Ropchan et al., 2002) and the Kerr-Addison deposit in the Kirkland Lake district (Kishida and Kerrich, 1987).

Muscovite alteration is the predominant alteration affecting Hislop syenite intrusives and porphyritic rhyolite dikes. Fe-carbonate alteration affects these rocks to a lesser extent. The overall lack of Ca, Mg, and Fe in felsic rocks at Hislop hinders the formation of carbonate minerals when exposed to CO₂ rich fluids, as discussed in Roberts (1988).

Most prospective rock types and alteration at Hislop

From Archean orogenic gold deposit models (Roberts, 1988; Groves and Foster, 1991; Hodgson, 1993; Groves et al., 1998; Hagemann and Cassidy, 2000; Goldfarb et al., 2005), and from previous work done on nearby gold deposits (Moore, 1936; Prest, 1956; Troop, 1986; Berger 1999; Berger, 2002), and at Hislop (Roscoe and Postle, 1998; Power et al., 2004), it is possible to outline the prospective rocks at Hislop. Rock types known to have a close spatial relationship to gold at Hislop include Fe-rich volcanic rocks, syenite intrusive rocks, and porphyritic rhyolite dikes. Carbonate dominated hydrothermal alteration is frequently associated with gold in these deposits, and is known to be related to gold at Hislop.

2.4.2. Physical properties of the Hislop deposit

All physical property measurements made on Hislop deposit samples, including magnetic susceptibility, density, resistivity, chargeability, and porosity measurements, are compiled in Appendix 2E. Descriptive statistics, and correlation coefficients for physical properties and mineral abundances can be found in Appendices 2F and 2G, respectively.

Magnetic susceptibility

Magnetic susceptibility logs

Selected geology and susceptibility logs from various parts of the Hislop property illustrate the behavior of magnetic susceptibility associated with characteristic rock types and alteration styles at Hislop (Fig. 2.4). Most, but not all, unaltered or weakly altered (where alteration minerals are restricted to veins) mafic and ultramafic volcanic rocks are high susceptibility. Susceptibilities are also high where ultramafic rocks are characterized by talc-chlorite metamorphic mineral assemblages (depicted by the dark green color in Column 2 of the drill logs in Fig. 2.4).

There is a regular drop in magnetic susceptibility where Fe-carbonate + albite alteration, Fe-carbonate + muscovite alteration, or magnesite + fuchsite alteration has been superimposed on mafic and ultramafic volcanic rocks. Less pervasive, weakly fracture-focused alteration, such as an Fe-rich dolomite alteration that lends a pink color to some intermediate dikes and mafic volcanic rocks, do not appear to have a consistent effect on magnetic susceptibility values.

There are seemingly no obvious patterns between altered syenite intrusives and porphyritic rhyolite dikes and magnetic susceptibility. Other rock types generally occur as very narrow units, and susceptibility readings for these rocks are sporadic.

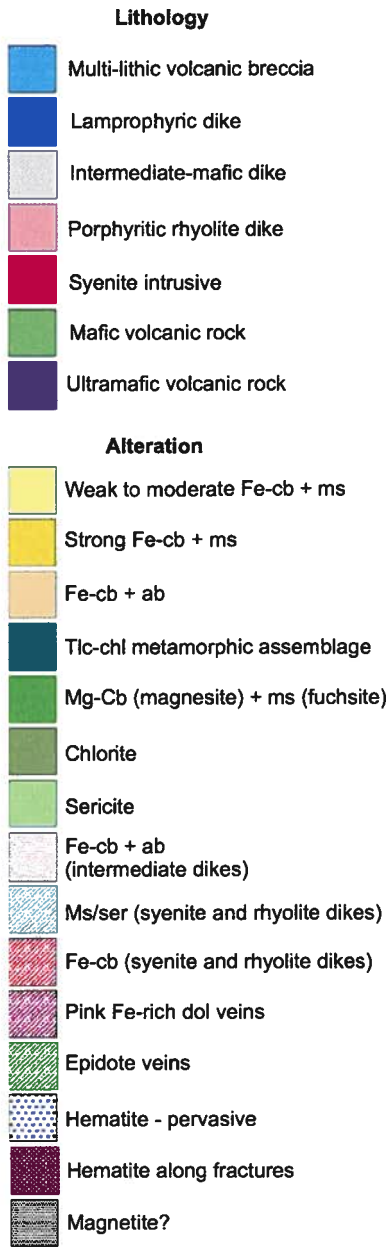
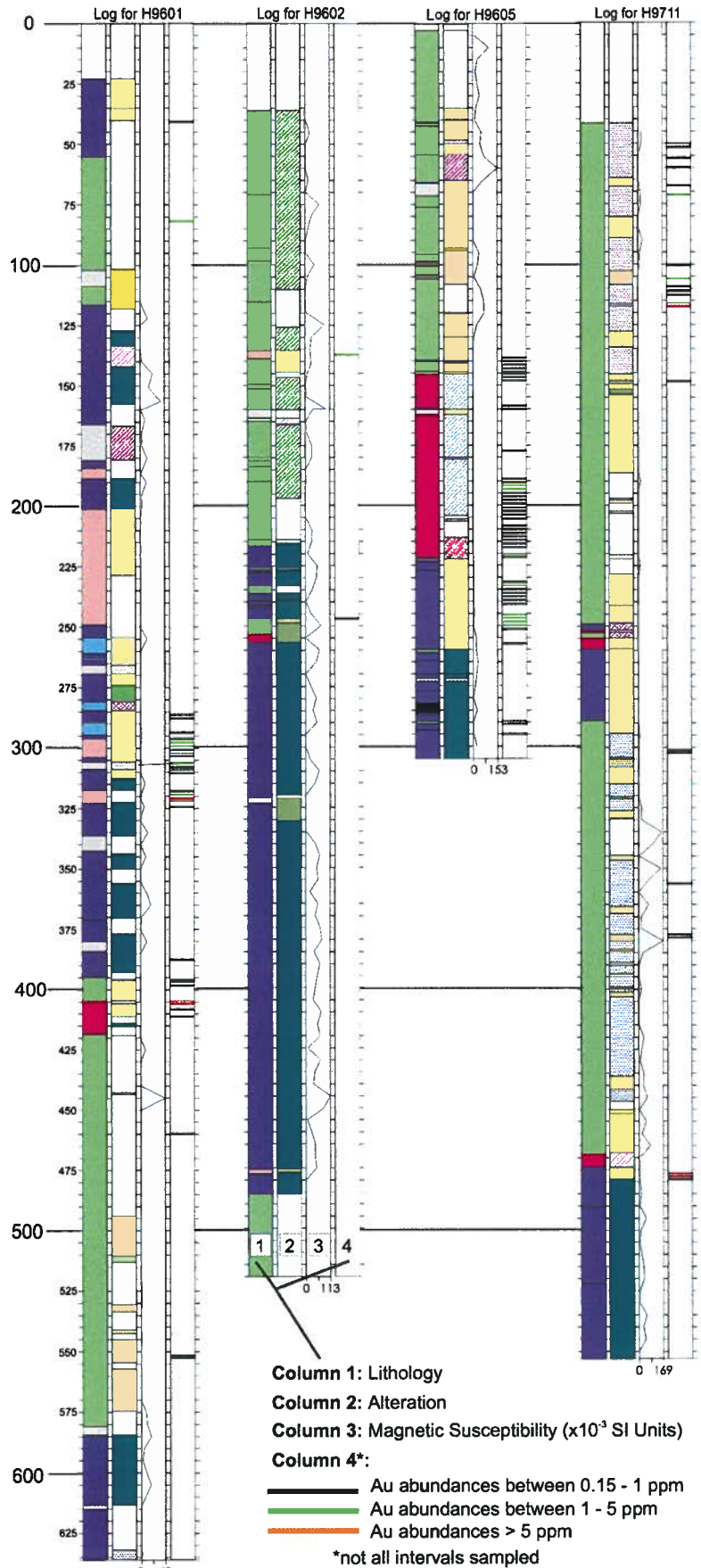


Figure 2.4. Geology, alteration, magnetic susceptibility, and gold grade logs for four Hislop drill holes logged for this study. The most consistent susceptibility trends include: low susceptibility of felsic intrusive rocks, high susceptibility of talc-chlorite assemblage ultramafic volcanic rocks, and some mafic volcanic rocks, and low susceptibility of carbonate-altered ultramafic and mafic volcanic rocks. For explanations of abbreviations in legend see bottom of Table 2.2.



Magnetic susceptibility data - all rock samples

Magnetic susceptibility data collected from drill core and hand samples are summarized in a series of histograms (Fig. 2.5). A wide range of susceptibilities, spanning 2 and 3 magnitudes, characterize the main rock types at Hislop. The histograms show a steady decrease in magnetic susceptibility values from ultramafic to felsic rocks.

Mafic and ultramafic rocks have distinct bimodal magnetic susceptibility distributions. Extended ranges of susceptibility for intermediate and felsic rocks may be attributed to a small number of outliers.

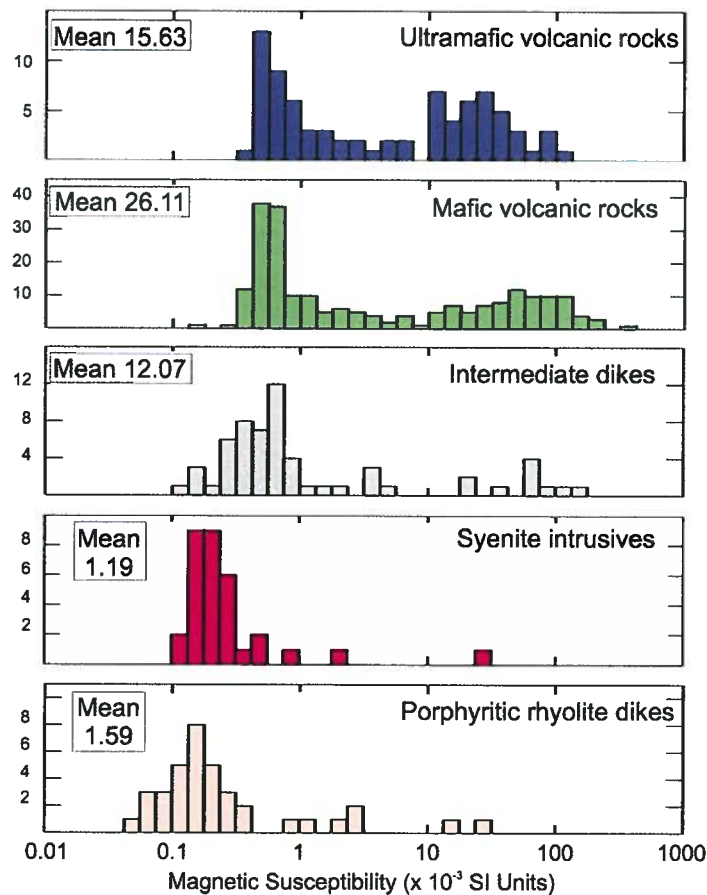


Figure 2.5. Magnetic susceptibility histograms for the five main rock types found in the Hislop deposit area. Mean values are given for general comparison, however the mean may not be an appropriate descriptor for populations with bimodal distributions.

Magnetic susceptibility data - least altered and altered rock samples

As was indicated in the magnetic susceptibility logs, some of the variation within ultramafic and mafic rock data may be attributed to effects of alteration. When magnetic susceptibility data for ultramafic and mafic rocks at Hislop is subdivided into least-altered, and carbonate-altered populations, it is apparent that the carbonate-altered populations have lower overall magnetic susceptibilities (Fig. 2.6). Intermediate dikes display a slight decrease in average magnetic susceptibility with Fe-carbonate, and Fe-carbonate + muscovite alteration (Fig. 2.7). Syenites and porphyritic rhyolite dikes, exhibit generally restricted ranges of magnetic susceptibility (Fig. 2.7). Alteration results in a minimal decrease in susceptibility for these intrusive rocks.

Density

Density data - all rock samples

From density histograms (Fig. 2.8), there is a decrease in density from ultramafic to felsic rocks. Narrow ranges in density characterize syenite intrusive rocks and porphyritic rhyolite dikes. Ultramafic and mafic rock densities span a larger range than density values for intermediate and felsic rocks

Density data - least altered and altered rock samples

Alteration of ultramafic rocks correlates with a slight increase in average density relative to least-altered ultramafic rocks. There is a minor decrease in average density for Fe-carbonate + albite altered mafic volcanic rocks (Fig. 2.9). Intermediate dikes undergo a marginal density increase with Fe-carbonate + muscovite alteration (Fig. 2.10). There are no significant changes in densities between unaltered and altered equivalents of syenites and rhyolite dikes at Hislop - data peaks are generally consistent between the subpopulations (Fig. 2.10).

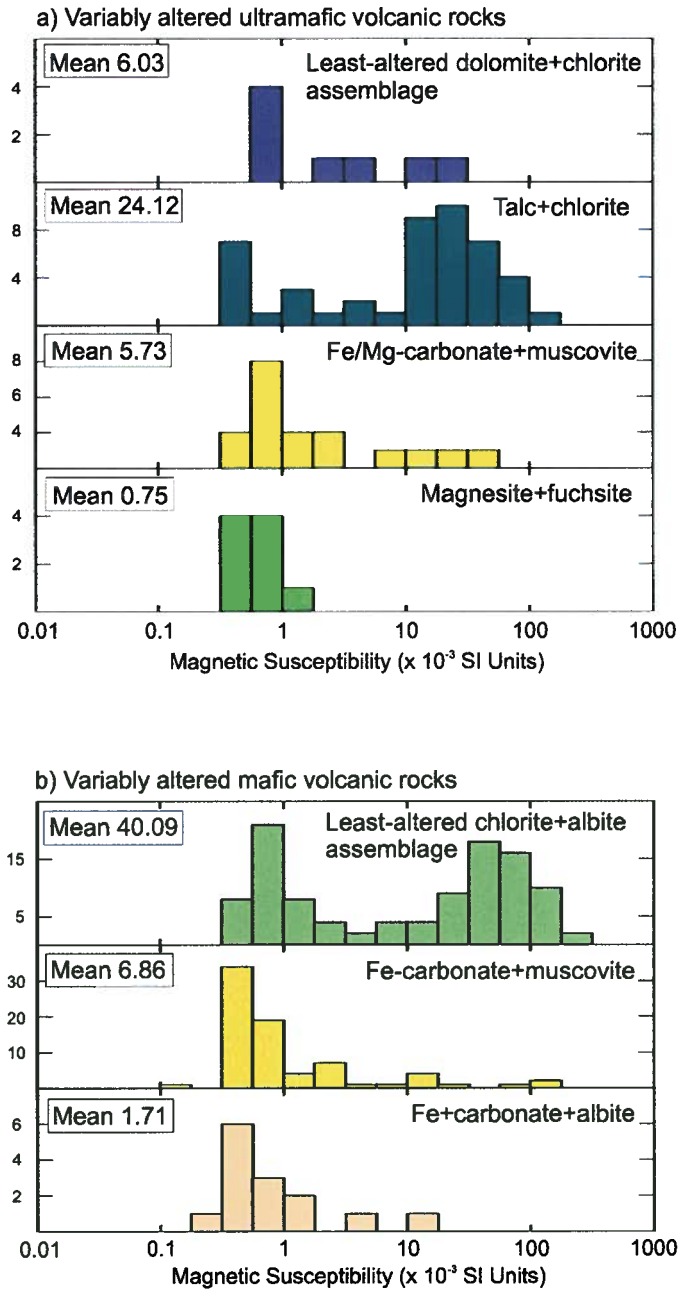


Figure 2.6. Magnetic susceptibility histograms showing susceptibility data for a) least-altered and altered ultramafic volcanic rocks, and b) least-altered and altered mafic volcanic rocks.

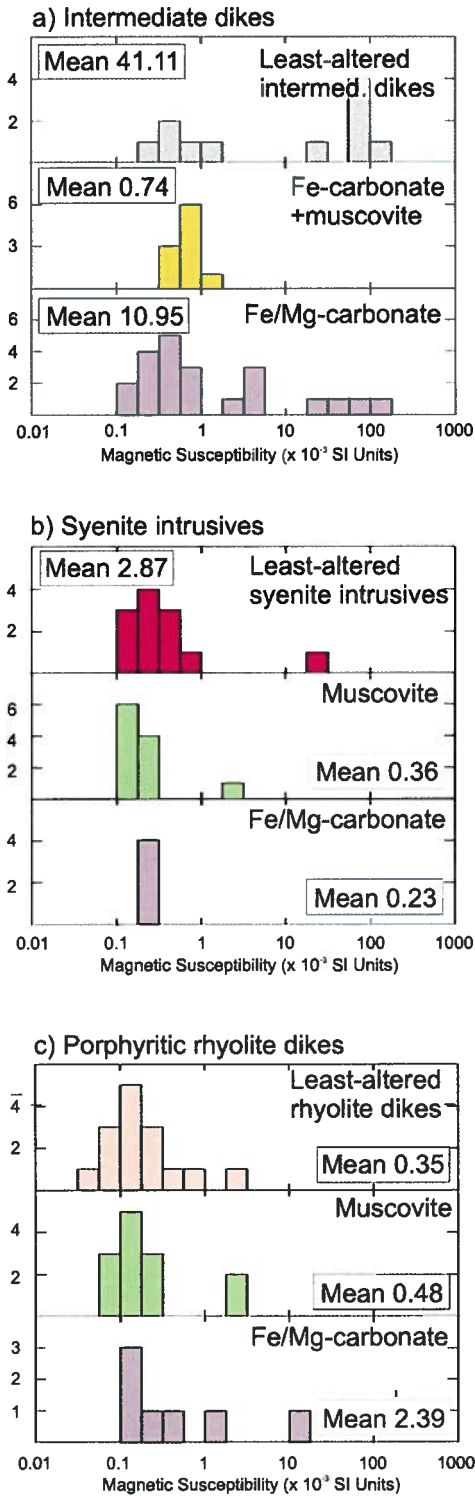


Figure 2 7. Magnetic susceptibility histograms showing susceptibility data for a) least-altered and altered intermediate dikes, b) least-altered and altered syenitic dikes, and c) least-altered and altered porphyritic rhyolite dikes.

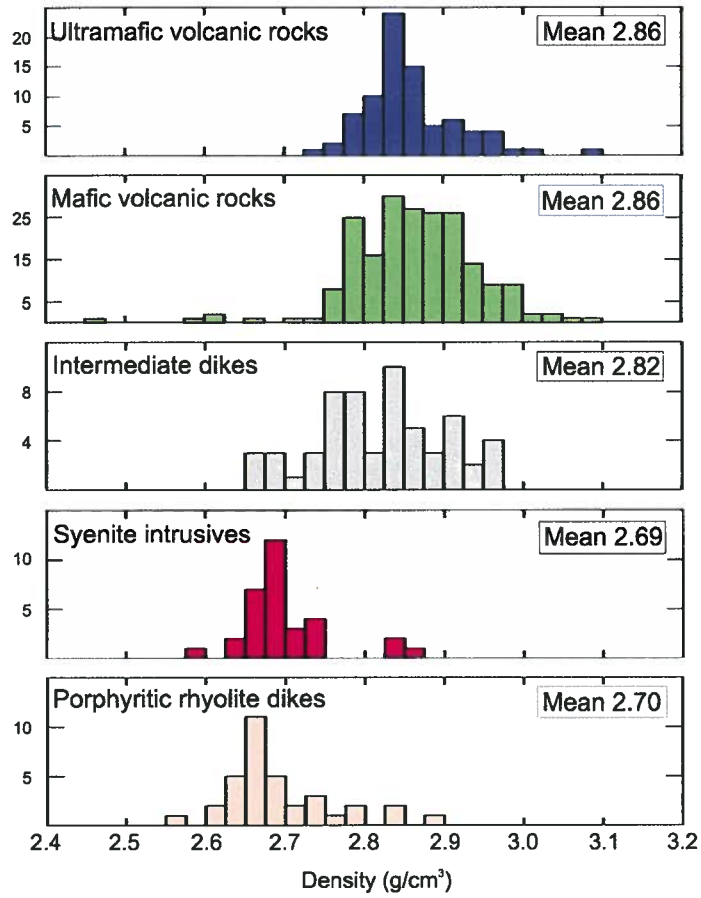


Figure 2.8. Density histograms for the five main rock types found in the Hislop deposit area.

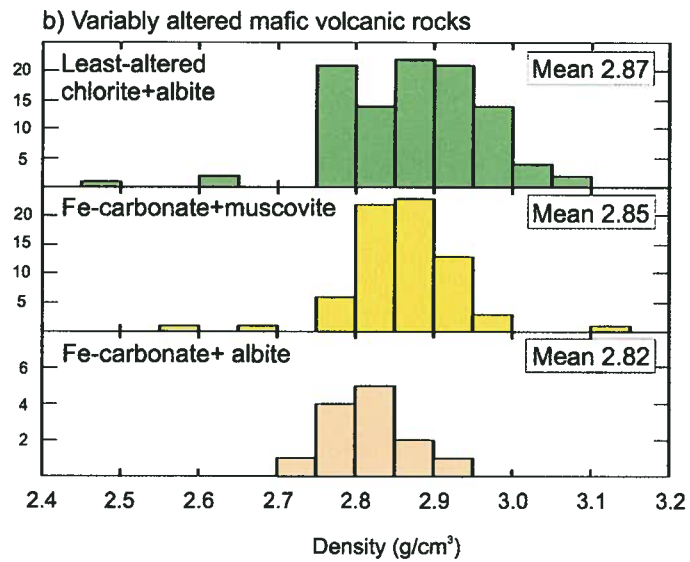
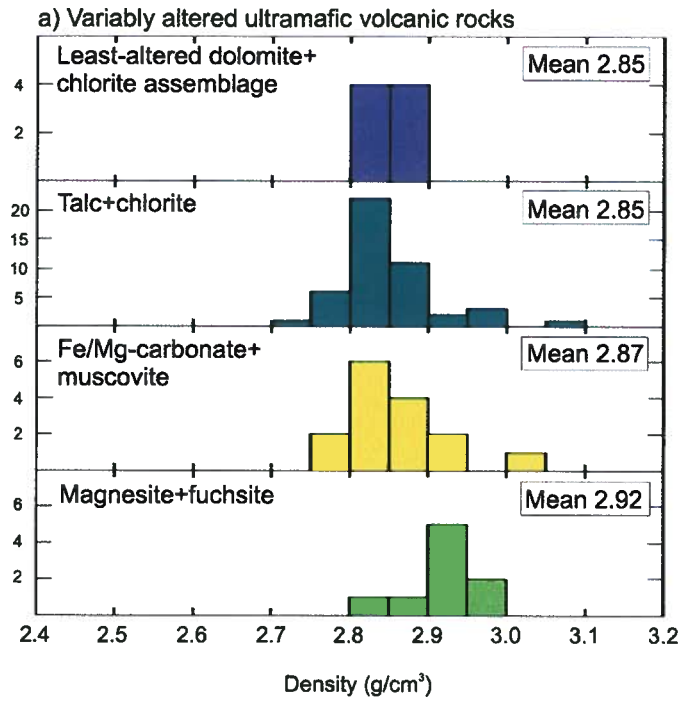


Figure 2.9. Density histograms showing density data for a) least-altered and altered ultramafic volcanic rocks, and b) least-altered and altered mafic volcanic rocks.

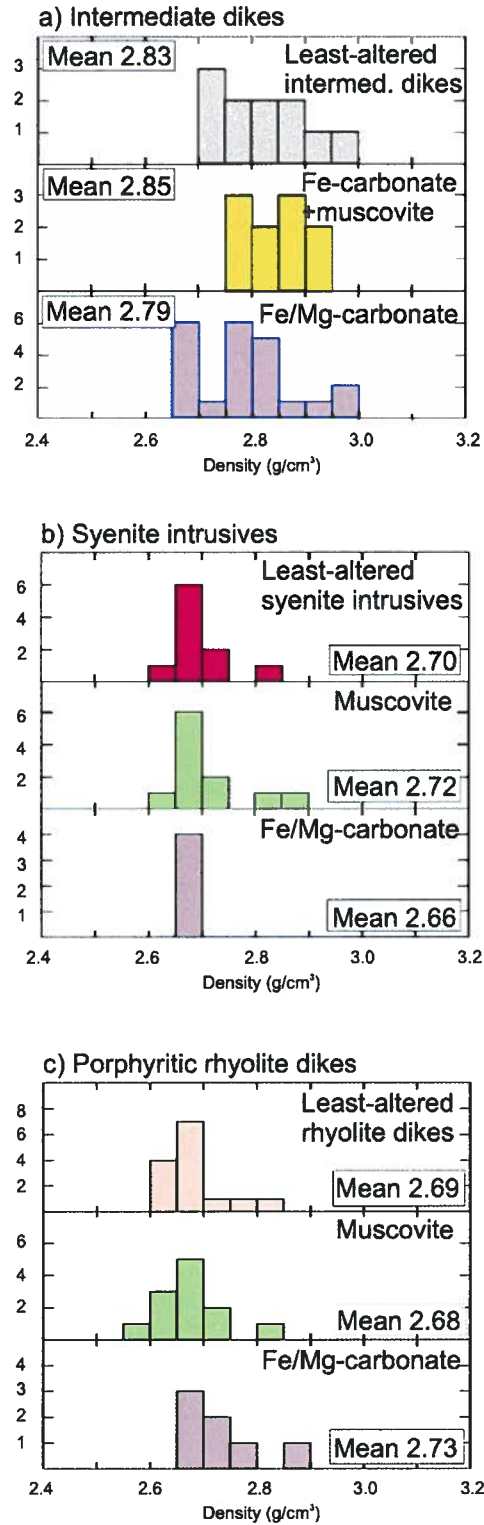


Figure 2.10. Density histograms showing density data for a) least-altered and altered intermediate dikes, b) least-altered and altered syenitic dikes, and c) least-altered and altered porphyritic rhyolite dikes.

Resistivity

Resistivity data - all rock samples

Ranges of resistivity for Hislop rocks are large and overlap one another significantly (Fig. 2.11). However, they are roughly comparable to published data for similar rock types (Tab. 2.3). From resistivity histograms, it is evident that ultramafic rocks have the lowest resistivities of the five main rock types at Hislop. Mafic volcanic rocks, intermediate dikes, syenite intrusives, and porphyritic rhyolite dikes have similar average resistivities. There was insufficient sample numbers to evaluate effects of hydrothermal alteration on the various rock types

Chargeability

Chargeability data - all rock samples

Ranges of chargeability values for the various Hislop rock types generally overlap one another, with some outliers (Fig. 2.12). Hislop chargeability data falls into the chargeability ranges considered to be characteristic of these rock types (Tab. 2.3), although many of these published chargeability ranges largely overlap. As with resistivity data, there were too few samples to compare the effects of alteration on chargeability values for the five rock types.

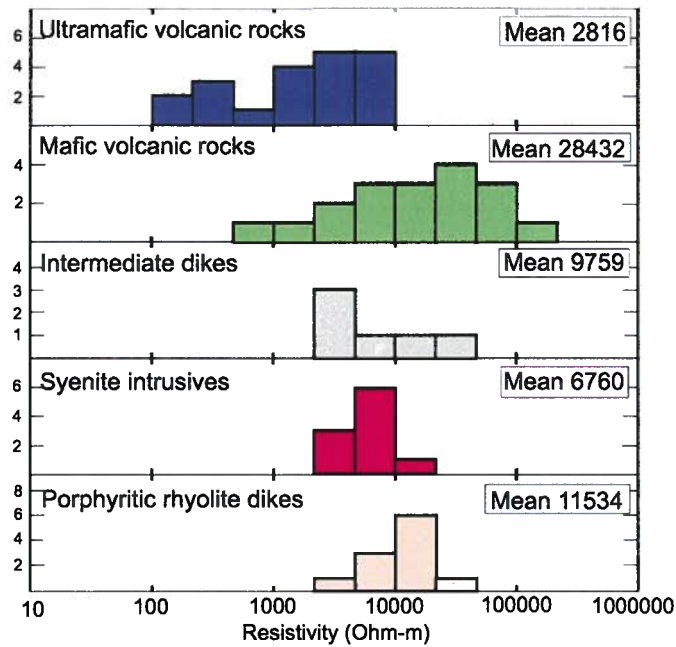


Figure 2.11. Resistivity histograms for Hislop deposit rocks. Data indicates lower overall resistivities for ultramafic volcanic rocks from Hislop.

Table 2.3. Ranges of resistivity and chargeability for rock types similar to those occurring in the Hislop deposit area (data from Telford et al., 1990).

Rock Type	Resistivity (Ohm-m)
feldspar porphyry	4×10^3 (wet)
porphyry (various)	$60 - 10^4$
syenite	$10^2 - 10^6$
andesite	1.7×10^2 (dry)
basalt	$10 - 1.3 \times 10^7$ (dry)
peridotite	6.5×10^3 (dry)
calcareous/mica schists	$20 - 10^4$
Rock Type	Chargeability (ms)
schists	5-20
precambrian volcanics	8-20
dense volcanic rocks	100-500
granites, granodiorites	10-50
2-8 % sulfides	500-1000
8-20% sulfides	1000-2000
20% sulfides	2000-3000

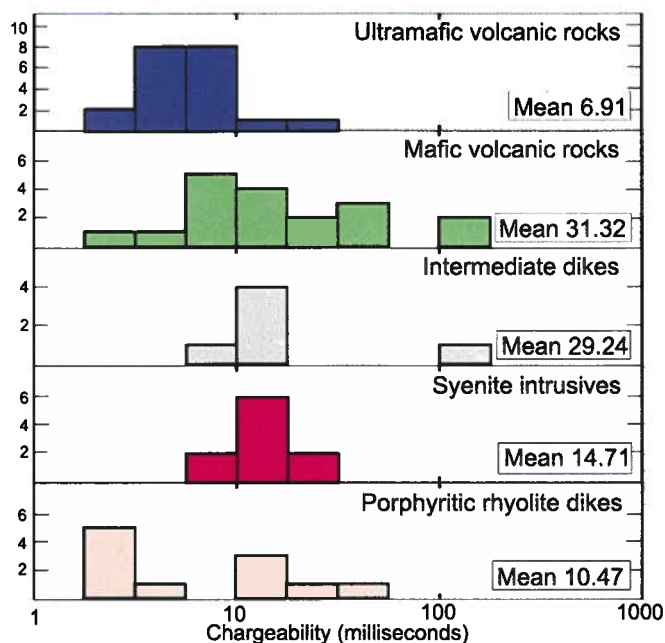


Figure 2.12. Chargeability histograms for Hislop deposit rocks. Chargeability ranges for the individual rock types overlap and are not unique.

2.5. INTERPRETATIONS

2.5.1. Effect of geological processes on physical properties at Hislop

Magnetic susceptibility

From petrographic, SEM, and XRD work, it was established that magnetite is the only significant magnetic mineral in the Hislop deposit rocks. The trend of decreasing magnetic susceptibility from ultramafic to felsic rocks observed at Hislop, reflects decreasing magnetite abundance. A plot of modal magnetite, as derived from XRD and Rietveld analyses, plotted against magnetic susceptibility (Fig. 2.13) shows a positive correlation between these data, supporting this interpretation.

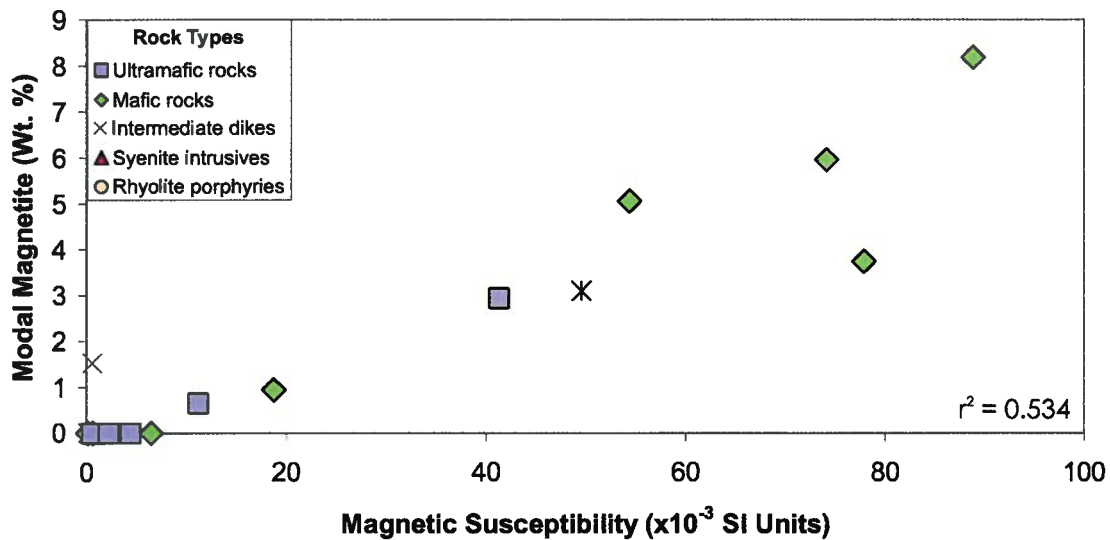


Figure 2.13. Positive correlation between modal magnetite in Hislop rock samples (as derived from XRD analysis) and magnetic susceptibility. For calculated correlation coefficients see Appendix 2G (all rock types).

Large susceptibility ranges for the major rock types at Hislop are not atypical and result from the broad range of mineralogy that can be encompassed under a given rock classification; classification schemes do not normally take into account oxide and sulfide accessory minerals, the minerals primarily controlling susceptibility (Clark, 1997). Bimodal populations are common in magnetic susceptibility data and are interpreted to represent distinct populations whereby Fe has partitioned mainly into paramagnetic minerals (weakly magnetic phases including silicates and carbonates) or into ferromagnetic minerals (strongly magnetic minerals, such as magnetite and pyrrhotite). A change in magma composition, or in oxidation state, may cause a rock to fall into one population or another (Clark, 1997).

Magnetite in mafic volcanic rocks, intermediate dikes, and felsic rocks at Hislop is primary igneous magnetite. Magnetite is not typically a primary igneous mineral in komatiitic rocks as chromite is the principal spinel that forms (Clark, 1997). Magnetite forms in ultramafic rocks usually as a product of serpentinization of olivine during early, retrograde metamorphism (Bucher and Frey, 2002).

In mafic rocks, the decrease in magnetic susceptibility with Fe-carbonate + muscovite, and Fe-carbonate + albite alteration is predominantly attributed to the conversion of magnetite in mafic rocks to Fe-carbonate upon exposure to CO₂-rich hydrothermal fluids (Roberts, 1988). Figure 2.14 shows this process occurring at Hislop, adjacent to a Fe-carbonate-filled fracture in a mafic volcanic rock. A negative correlation between modal magnetite and total Fe-rich carbonate abundance (ankerite + siderite + dolomite) further corroborates this relationship at Hislop (Fig. 2.15).

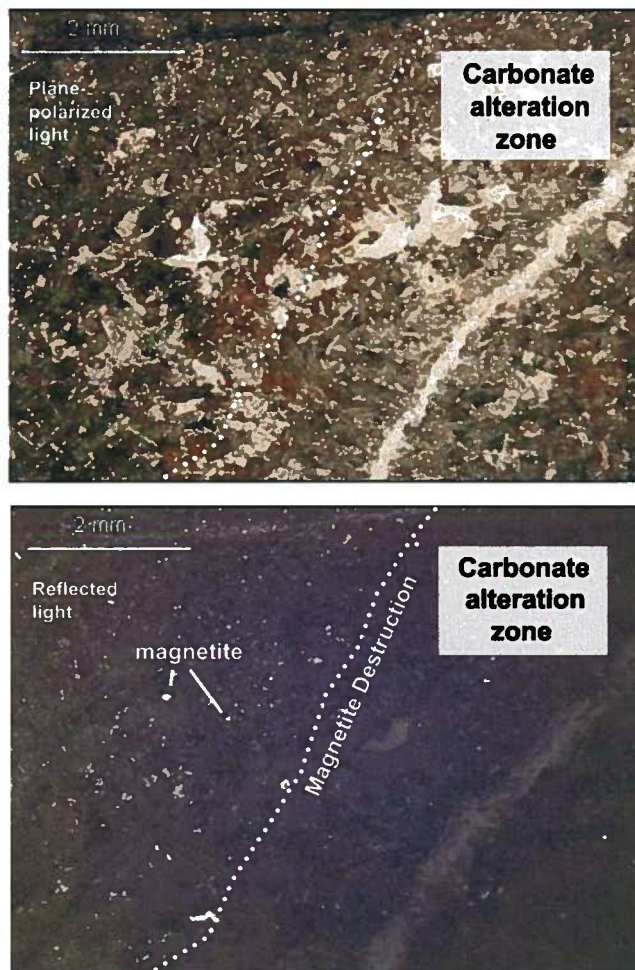


Figure 2.14. Magnetite grains (reflective grains in lower image) are destroyed within a carbonate altered zone surrounding a carbonate vein in a mafic volcanic rock from Hislop. Plane polarized and reflected light photomicrographs.

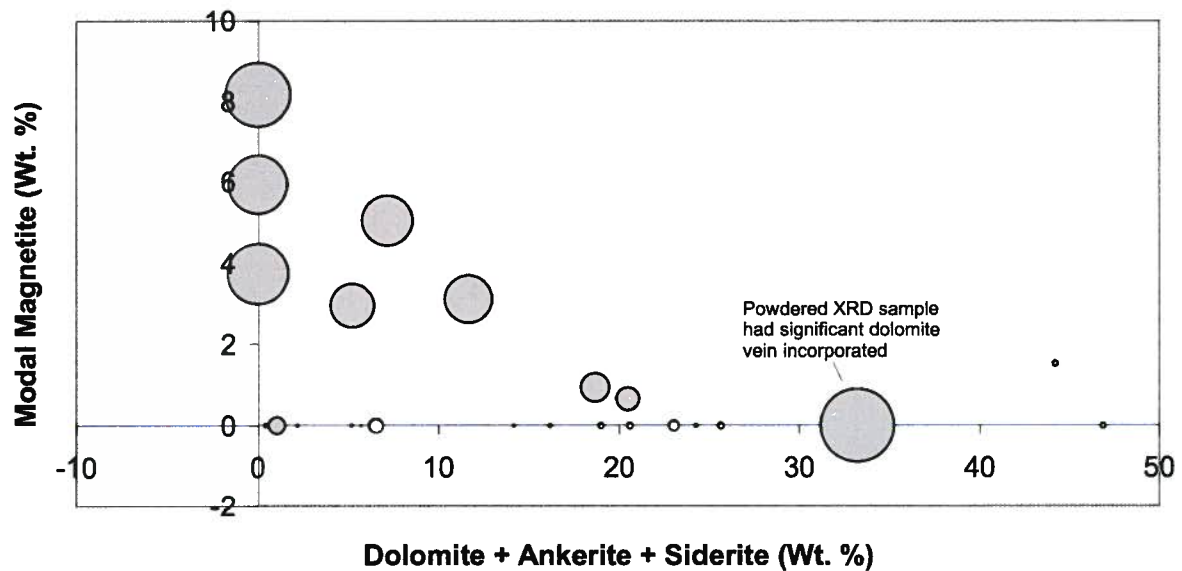


Figure 2.15. Modal magnetite versus total Fe-rich carbonate abundance for all Hislop samples with measured quantities of these minerals. Bubble size represents relative magnetic susceptibility. A decrease in susceptibility correlates with a decrease in modal magnetite and an increase in Fe-rich carbonate abundance.

Magnetite in ultramafic rocks formed during serpentinization is thought to be similarly affected by carbonate alteration. Clark (1997) explains that upon interaction with CO₂-rich fluids, magnetite is first redistributed in ultramafic rocks, and then is destroyed. Conversion of magnetite to Fe-rich carbonate was not directly observed in ultramafic rocks during petrographic or mineralogical work on Hislop rocks, however, the lack of magnetite in carbonate-altered ultramafic rocks compared to least-altered equivalents, is assumed to be due to alteration-related magnetite destruction.

Some intermediate dikes, porphyritic rhyolite dikes, and syenite intrusive rocks have low abundances of primary igneous magnetite, thus typically magnetite-destructive alteration does not affect magnetic susceptibility significantly (Fig. 2.10).

Hydrothermal alteration processes affecting mafic and ultramafic volcanic rocks do not explain all of the measured variation in magnetic susceptibility, as is indicated by additional heterogeneity in susceptibility readings from recorded unaltered intervals in drill core (Fig. 2.4). Variations in magnetic susceptibility in the absence of obvious

hydrothermal alteration could be related to a range of factors. Based on the rock types and mineralogy at Hislop, the most likely factors causing variable susceptibility in generally unaltered rocks at Hislop include an uneven distribution of primary or secondary magnetite, grain size, and irregular oxidation of magnetite to form hematite.

An uneven primary distribution of magnetite in mafic rocks, and uneven secondary distributions of magnetite in ultramafic rocks may explain non-alteration related magnetic susceptibility variations in these rocks. Some small scale variations must be expected, as rocks are not likely to be perfectly homogeneous in their modal mineralogy. Formation of magnetite in a mafic volcanic rock is dependant on many factors including the magma composition, the degree of differentiation, and the temperature and pressure conditions under which the rock is formed or metamorphosed (Clark, 1997). For ultramafic rocks, the formation of magnetite from olivine during serpentinization may be influenced by location of fluid pathways in the rock.

Small magnetite grain sizes are usually more susceptible than larger grain sizes as they do not easily retain remnant magnetism (Clark, 1997). To examine the role of visible grain size in non-alteration related variations in magnetic susceptibility, least-altered fine-grained and medium-grained samples are plotted separately. Magnetite grain size here is assumed to be consistent with the overall grain size of the samples. The resulting histograms (Fig. 2.16) illustrate that fine-grained, and medium-grained mafic and ultramafic rocks have similar ranges and distributions of magnetic susceptibility, and similar average susceptibilities. Thus, variations in magnetic susceptibility data for these rocks are not likely to be strongly controlled by grain size.

In some mafic and ultramafic rock samples, hematite rims magnetite grains indicating some oxidation of these rocks has occurred. A consistent pattern related to a particular alteration event, or having specific lithological or structural control, was not recognized during petrographic or mineralogical (SEM and XRD) analyses. Irregular oxidation of magnetite to hematite in mafic flows however, could contribute to decreases in magnetic susceptibility unrelated to hydrothermal alteration in mafic rock samples.

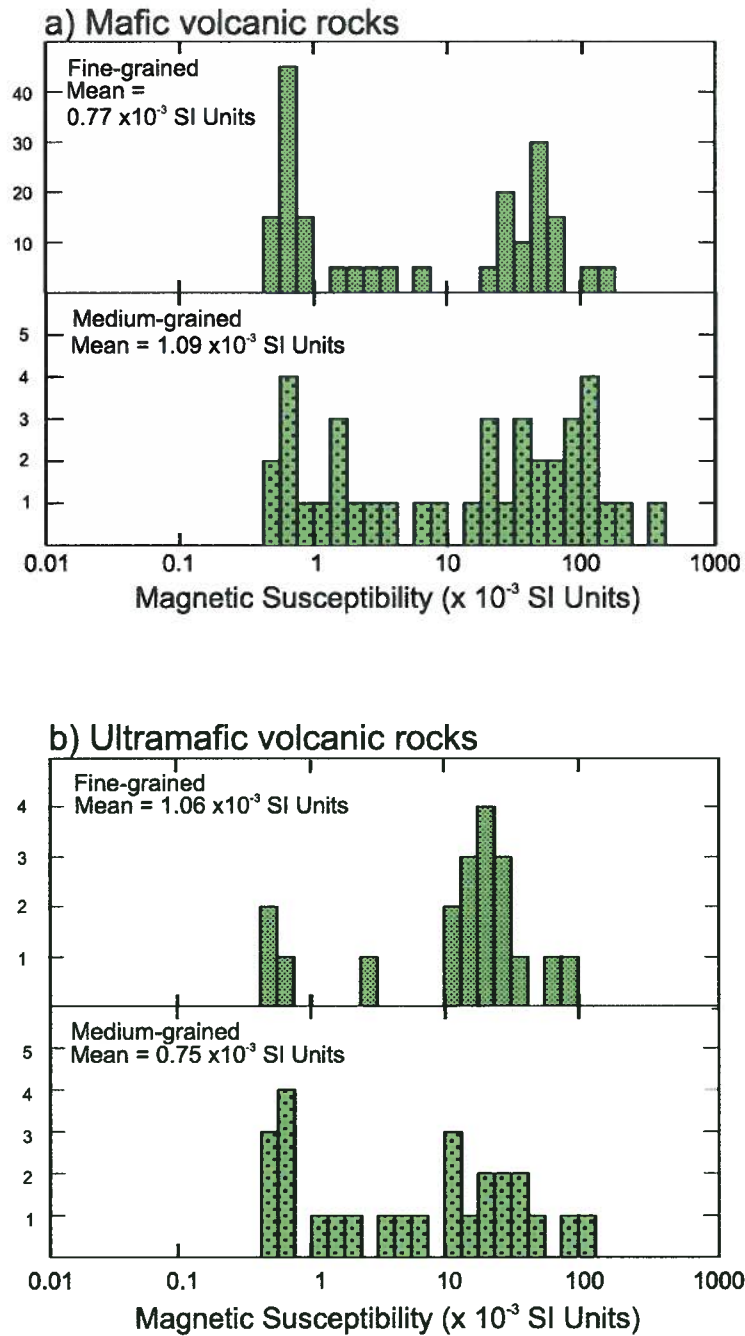


Figure 2.16. Histograms showing distribution of susceptibility for fine- and medium-grained a) mafic volcanic rocks, and b) ultramafic volcanic rocks. Similar distributions between fine- and medium-grained subsets indicates that grain size is not a major control on susceptibility at Hislop.

Density

Mineralogy and porosity are considered to be the main controls on density at Hislop. Both mineralogy and porosity are affected by geological processes including igneous fractionation/ differentiation, metamorphism, and hydrothermal alteration.

Mineralogy plays a significant role in determining rock densities. Igneous and volcanic rock densities generally decrease with increasing SiO₂ content (Johnson and Olhoeft, 1984; Telford et al., 1990), reflecting an increase in the abundance of low density felsic minerals, and a corresponding decrease in the abundance of higher density Fe- and Mg-rich mafic minerals. This is consistent for Hislop samples. From Table 2.4, it is apparent that minerals that typically characterize ultramafic and mafic rocks at Hislop are higher in density on average than those that characterize felsic rocks.

Table 2.4. Densities of the common minerals in Hislop deposit rocks (from www.mindat.org).

Mineral	Density (g/cm³)
Quartz	2.62
Microcline	2.56
Albite	2.62
Actinolite	3.04
Epidote	3.45
Augite	3.4
Chlorite	2.65
Muscovite	2.82
Calcite	2.71
Ankerite	3.05
Siderite	5
Dolomite	2.84
Magnesite	3
Talc	2.75
Serpentine	2.53
Pyrite	5.01
Magnetite	5.15
Hematite	5.3

The modal mineralogy of syenites and porphyritic rhyolite dikes brings about their narrow density ranges. They are dominated by a small number of similarly dense minerals, specifically quartz and feldspar. Densities of ultramafic and mafic rocks span a larger range of densities than those making up intermediate and felsic rocks which is a result of their more complex and varied mineralogy (refer to Tab. 2.2).

A slight increase in the average measured density of ultramafic volcanic rocks corresponds with Fe/Mg-carbonate + muscovite, and magnesite + fuchsite alteration. This relationship can be attributed to changes in mineralogy accompanying alteration. Based on published mineral densities (Tab. 2.4, mineral densities from www.mindat.org), a change in the bulk mineralogy of an ultramafic rock containing predominantly chlorite, plus carbonate, talc, quartz, and magnetite, to a rock composed of abundant Fe-rich and Mg-rich carbonate, plus muscovite, and quartz, should theoretically result in a denser rock. Carbonate minerals are expected to have a significant influence on rock density. On average, they are denser than those silicate minerals that dominate the mineralogy of igneous and volcanic rocks, Carbonates containing Fe would be especially influential, having densities as high as 5 g/cm^3 (e.g. siderite, Tab. 2.4). Figure 2.17 illustrates the correlation between increasing density values with increasing Fe-rich carbonate abundance in Fe-carbonate bearing Hislop deposit samples.

Minor variations in the density of mafic volcanic rocks from Hislop may be similarly attributable to alteration. The lower average density values for Fe-carbonate + albite altered samples, as compared to least-altered and Fe-carbonate + muscovite samples, is considered to be related to bulk mineralogy (Fig. 2.9). The increased relative abundances of low-density albite in rocks with Fe-carbonate and albite-dominated alteration assemblages has likely lowered the density.

Some changes in density for subpopulations of altered intermediate dikes (Fig. 2.10) are difficult to interpret due to irregular data populations that might have come about through oversimplified sample groupings. There is little change in density between the variably altered syenites and porphyritic rhyolites (Fig. 2.10). It is assumed that for

these rock types, bulk mineralogy changes do not add or subtract significant dense minerals, and thus alteration has little influence on the density of these rocks.

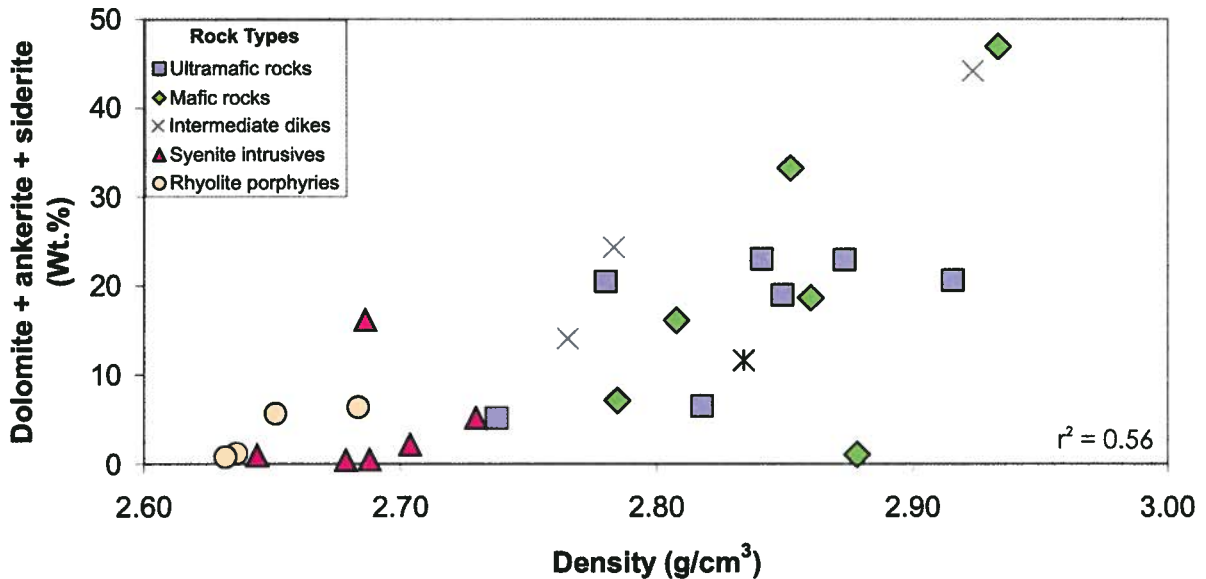


Figure 2.17. Density increases for Hislop rocks with an overall increase in the abundance of Fe-rich carbonate. For calculated correlation coefficients see Appendix 2G (all rock types).

Calculating densities from modal mineralogy as determined from XRD analysis and published mineral density data helps to determine what the densities of the rock should theoretically be, if the density is controlled solely by mineralogy. When compared to measured densities, discrepancies will indicate that there are factors aside from bulk mineralogy affecting the rock. Density is calculated simply by using volume concentrations of minerals (C) and their grain densities (ρ) as given in Johnson and Olhoeft (1984):

$$\rho = C_1 * \rho_1 + C_2 * \rho_2 + C_3 * \rho_3 \dots C_n * \rho_n$$

A lack of strong correlation between some of the measured and calculated densities for ultramafic and mafic rocks (Fig. 2.18), suggests that there may be other controls on density. Two possible explanations for the incongruity include not accounting for porosity in samples, and limitations in mineral identification using XRD methods.

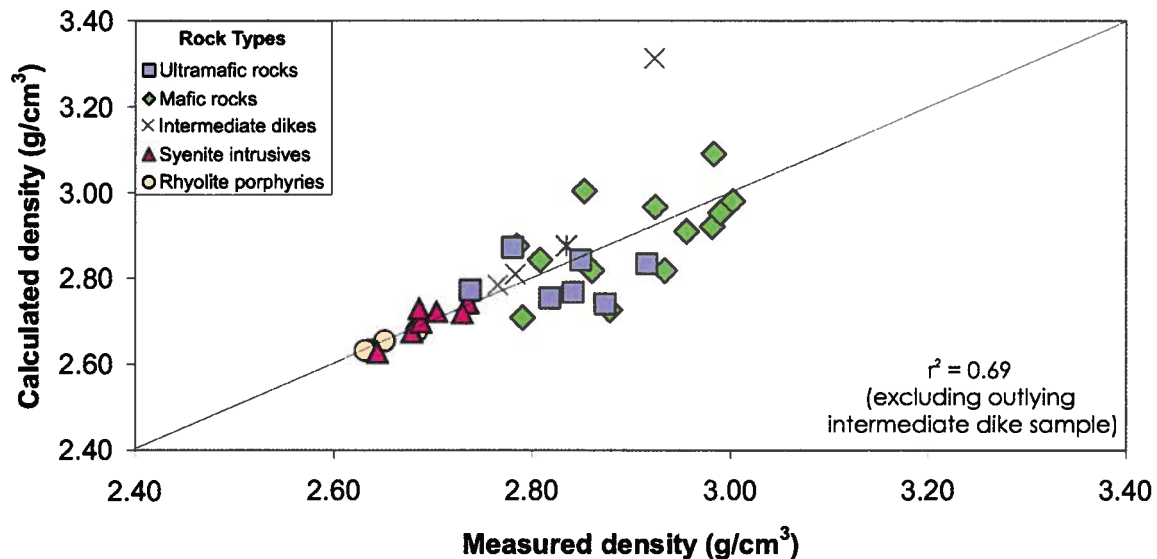


Figure 2.18. Measured versus calculated density for Hislop rocks. Discrepancies between the density values obtained from the two methods for ultramafic and mafic volcanic rocks could indicate that bulk mineralogy does not solely control density.

Density is known to decrease with increasing porosity (Telford et al., 1990; Johnson and Olhoeft, 1984), and porosity is thought to be a factor in some of the density variations at Hislop. To test the possible influence of porosity on the density of mafic and ultramafic rocks, a suite of samples in varying states of alteration were measured for porosity using the method described in section 3.2 Figure 2.19 shows that there is an overall negative correlation between density and porosity for ultramafic rocks at Hislop. Talc-chlorite assemblage rocks are most porous and least dense in accordance with their typically strong foliation. Strongly carbonate-altered samples have lower porosities and higher densities. Figure 2.20 indicates no obvious relationship between density and porosity for mafic volcanic rocks.

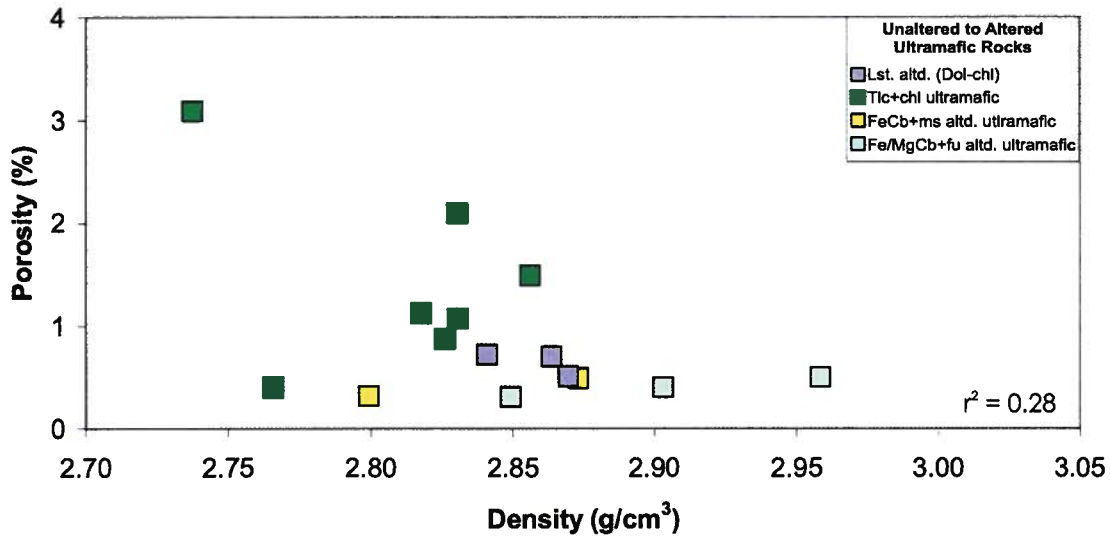


Figure 2.19. Porosity of ultramafic volcanic rocks at Hislop decreases with carbonate-related hydrothermal alteration, due to annealing of this commonly sheared rock. This brings about a corresponding increase in density. Abbreviations: Lst. altd. = least altered; dol+chl = dolomite + chlorite; tlc+chl = talc + chlorite; FeCb+ms = Fe-carbonate + muscovite; Fe/MgCb+fu = Fe(Mg)-carbonate + fuchsite. For calculated correlation coefficients see Appendix 2G (ultramafic rocks).

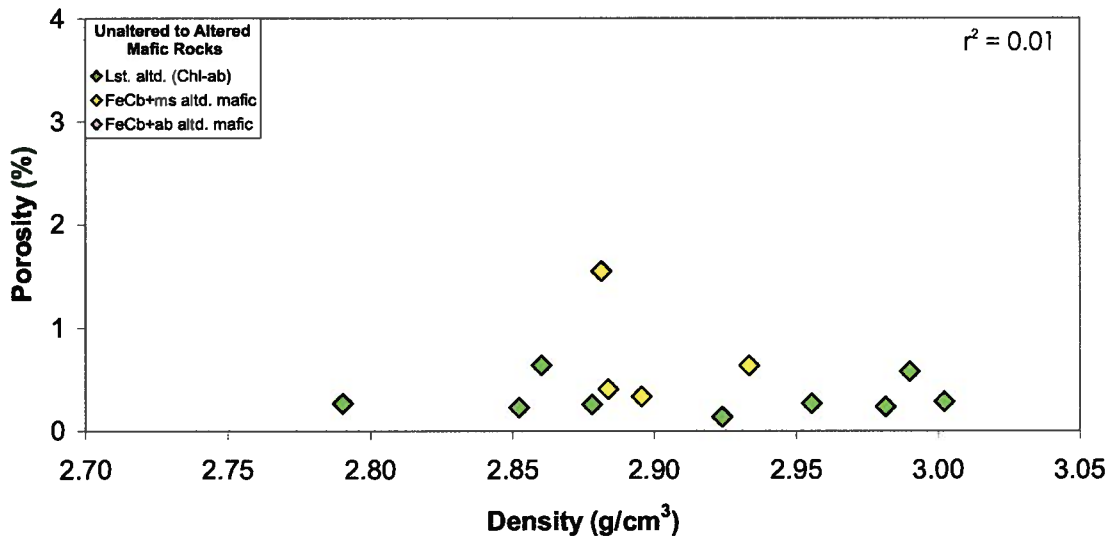


Figure 2.20. No relationships are indicated between porosity and density for mafic volcanic rocks at Hislop. Abbreviations: Lst. altd. = least altered; chl+ab = chlorite + albite; FeCb+ms = Fe-carbonate + muscovite; FeCb+ab = Fe-carbonate + albite. For calculated correlation coefficients see Appendix 2G (mafic rocks).

Discrepancies between measured and calculated density data could also be attributed to generalization of modal mineralogy during Rietveld analysis. For some minerals that exist as a solid solution, such as dolomite and ankerite, a proper name is not assigned for intermediate compositions. The density values for these end members differ significantly, and the resulting calculated density would be affected accordingly if one end member mineral classification was chosen over the other.

For intermediate and felsic intrusive rocks, calculated and measured density values match closely, indicating primarily mineralogical control on density. Changes in density between unaltered and altered versions of these rock types thus must be explained by relative additions or subtractions of more and less dense minerals.

Resistivity

Least-altered metamorphosed volcanic and igneous rocks at Hislop have resistivity ranges similar to published ranges for equivalent rocks types (Tab. 2.3). Published resistivity ranges for most minerals are very large and not as specific as density values for given minerals. This makes it difficult to assess the combined resistivity affects of minerals making up a rock. This being said, the role of mineralogy on resistivity at Hislop is thought to be minimal. The majority of minerals making up Hislop rocks are poor to intermediate conductors, or resistors ($> 1 \text{ Ohm-m}$; Telford et al., 1990). Most sulfides, and some oxides, are known to be good conductors (low resistivity, $<1 \text{ Ohm-m}$), and there is a small percentage of these minerals in Hislop samples.

Variations in resistivity at Hislop are interpreted to be primarily controlled by rock texture and porosity. Resistivity is known to drop considerably with increasing water content of rocks (Telford et al., 1990), thus to be related to the porosity of a rock (Haloff, 1992). As such, the low average resistivity of ultramafic rocks compared to the other Hislop rock types is interpreted to be a result of the relatively high porosities of

talc-chlorite assemblage ultramafic rocks, the most common ultramafic rock subpopulation sampled during this study.

Resistivity is plotted against magnetic susceptibility and density (Fig. 2.21 and Fig. 2.22), two properties shown to vary with alteration in ultramafic and mafic volcanic rocks at Hislop. In Figure 2.21a, the ultramafic samples are the only samples to outline a trend between resistivity and magnetic susceptibility. With ultramafic samples colored to represent their dominant alteration assemblages, it is obvious that the trend is related to alteration. This variation in resistivity is interpreted to be related specifically to alteration effects on porosity. Figure 2.23 demonstrates that a decrease in porosity of ultramafic rocks with carbonate alteration causes the rock to become more resistive. Thus, altered ultramafic samples are resistive and, as was indicated previously, are characterized by low magnetic susceptibilities due to magnetite destruction. When resistivity is compared with density (Fig. 2.22), again a weak correlation emerges only for ultramafic samples. When colored based on alteration, the relationship of increasing resistivities and densities with carbonate alteration is apparent for the majority of the samples, and is explained by a decrease in porosity for altered rocks.

Chargeability

The main control on the chargeability of Hislop rocks is thought to be the presence of disseminated sulfides. Disseminated sulfides in rocks are readily chargeable where subjected to an induced current, due to the chargeable nature of the metallic grains coupled with the large surface area provided by a disseminated texture (Telford et al., 1990). Other known controls on chargeability include presence of clay minerals and graphite, both of which are absent from Hislop rocks.

A positive relationship between pyrite abundance based on XRD analyses, and chargeability for syenites and porphyritic rhyolites is indicated in Figure 2.24. However, there is not a similarly convincing relationship indicated for other Hislop rock types.

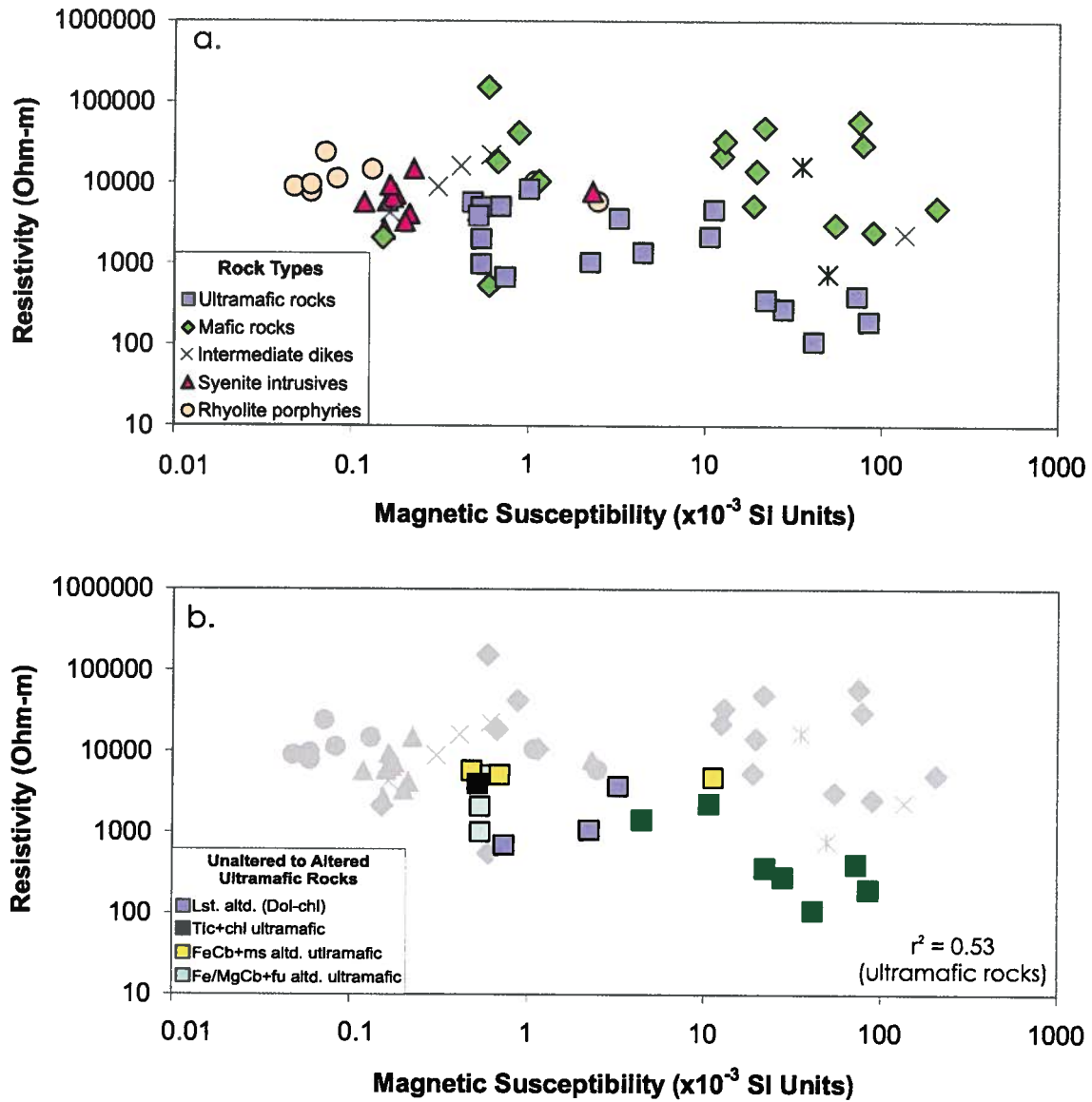


Figure 2.21. Resistivity versus magnetic susceptibility. a) Ultramafic volcanic rock samples indicate a trend between these physical properties, whereas variations in resistivity and magnetic susceptibility are more irregular for other rock types. b) When data points are colored to represent the various ultramafic alteration assemblages, it is apparent that the relationship between resistivity and susceptibility is controlled in part by carbonate alteration. For abbreviations, see Fig. 2.19. For calculated correlation coefficients see Appendix 2G (ultramafic rocks).

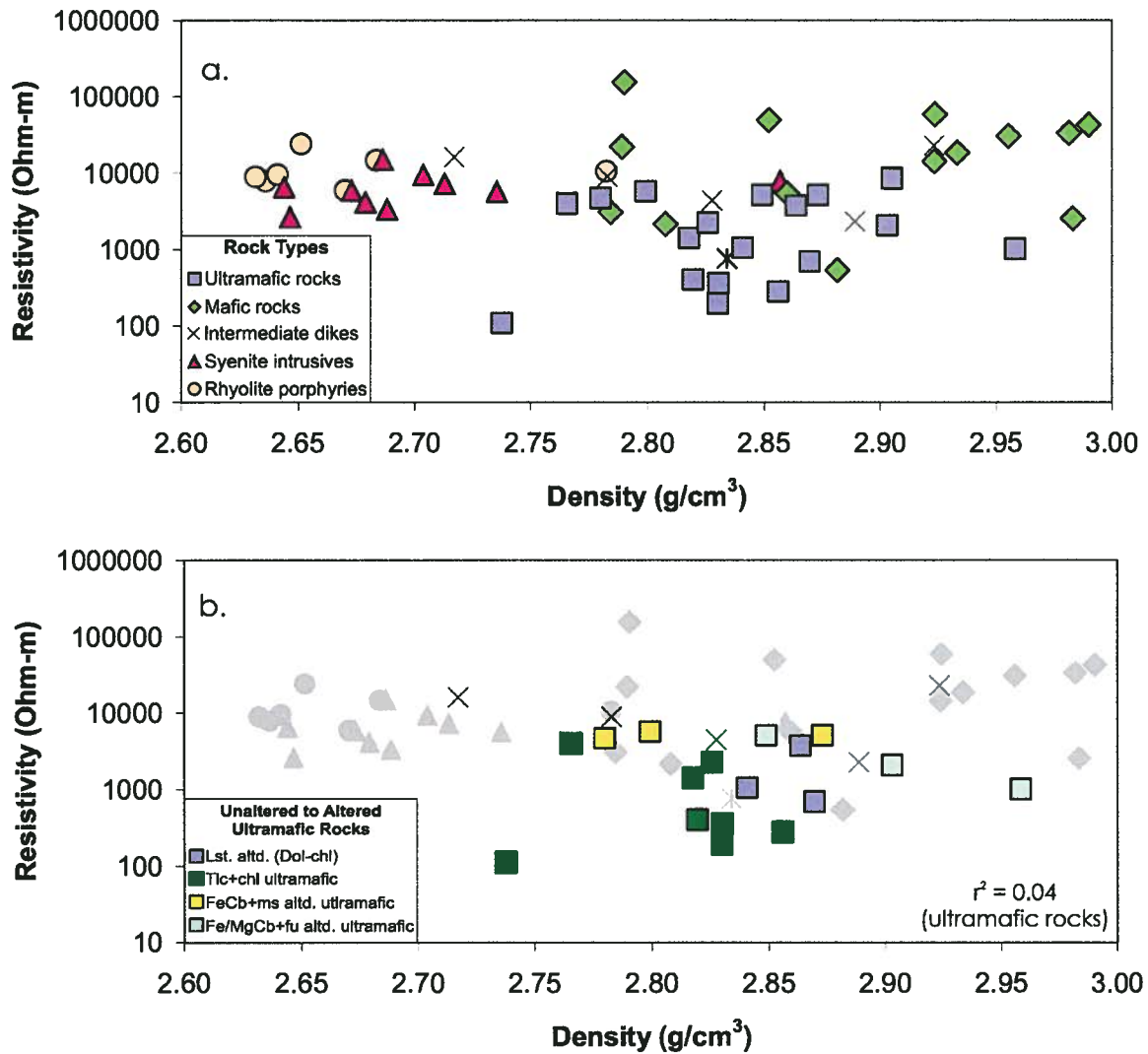


Figure 2.22. Resistivity versus density. a) As with resistivity versus magnetic susceptibility, trends in data when plotted based on rock type are not obvious. b) Subdividing ultramafic rocks based on alteration assemblage reveals that increasing resistivities and densities can be to some extent attributed to carbonate alteration. For abbreviations, see Fig. 2.19. For calculated correlation coefficients see Appendix 2G (ultramafic rocks).

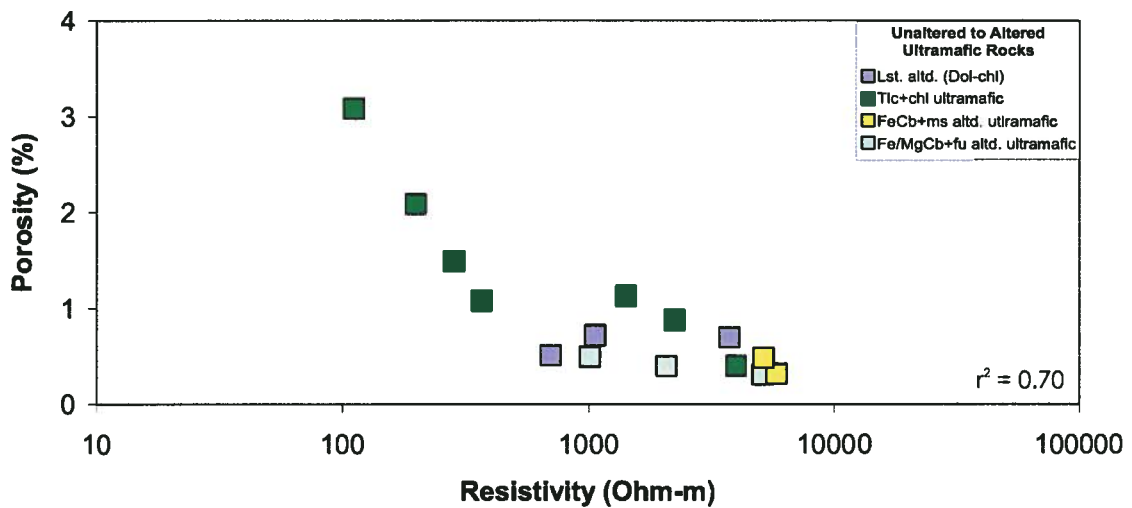


Figure 2.23. A plot of porosity versus resistivity shows that annealing of ultramafic rocks due to precipitation of carbonate minerals during hydrothermal alteration brings about a decrease in porosity and a corresponding increase in resistivity. For abbreviations, see Figure 2.19. For calculated correlation coefficients see Appendix 2G (ultramafic rocks).

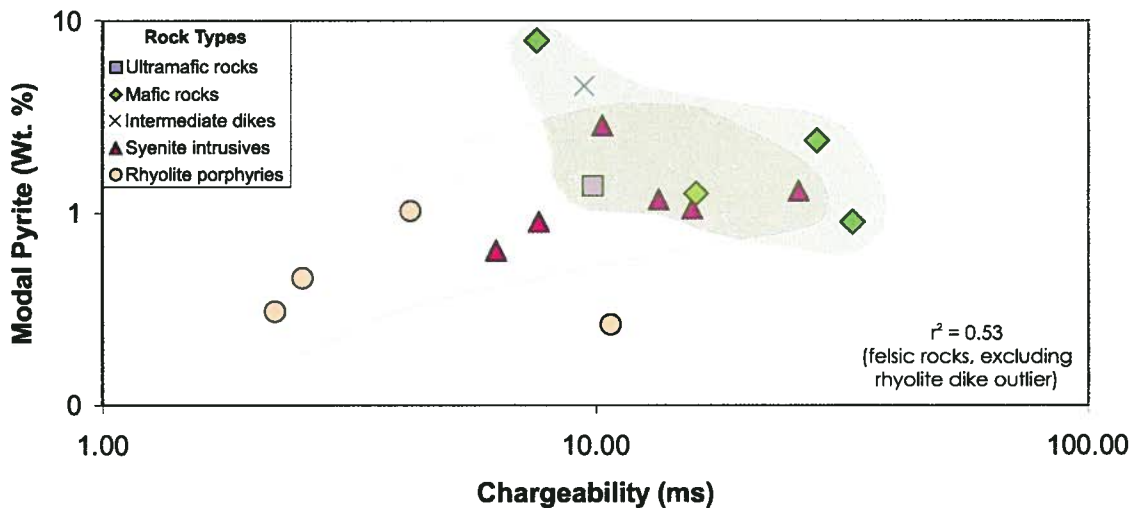


Figure 2.24. A weak positive correlation exists between pyrite abundance and chargeability, however the trend is mainly controlled by porphyritic rhyolite dike and syenite samples. There is no evidence of a consistent relationship between chargeability and pyrite abundance for intermediate to ultramafic volcanic rocks. For calculated correlation coefficients see Appendix 2G (felsic rocks).

This indicates that there may be variables affecting chargeability other than, or in addition to, sulfide abundance. Sulfide grain size and texture, and the relationship between sulfide grains in the rock, are all potential factors that can influence the rock's chargeability (Pelton et al., 1978). As chargeability should increase with increased surface area of sulfide minerals, chargeability values may depend on whether sulfides are disseminated, concentrated in a stockwork system, or controlled by fractures or veins.

Variable porosity may affect the chargeability of mafic volcanic rocks. Chargeability can decrease with porosity; increased fluid pathway volume can be more conducive to electrolytic conduction, prohibiting polarization. For example, chargeabilities may be higher for a crystalline igneous rock containing disseminated sulfides, than for a more porous sedimentary rock containing sulfides, (Telford et al., 1990). Although the dataset is small (few samples have both chargeability data and porosity), there is a weak relationship between porosity and chargeability for mafic rocks at Hislop (Fig. 2.25).

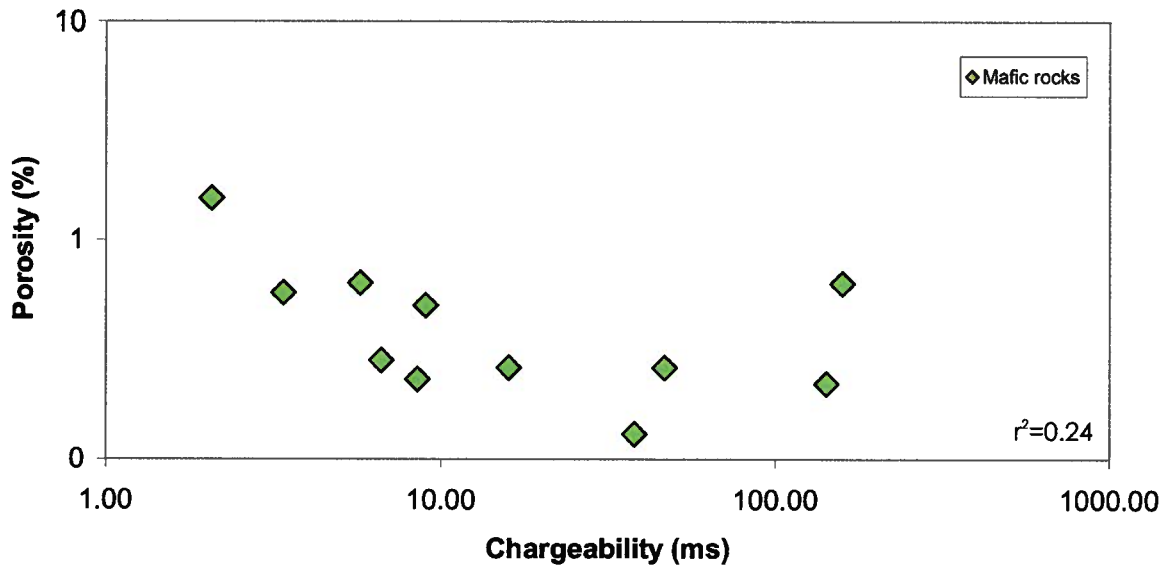


Figure 2.25. A negative correlation between chargeability and porosity in this plot indicates that increases in porosities of mafic volcanic rocks at Hislop may hinder the ability for metallic minerals to become charged. For calculated correlation coefficients see Appendix 2G (mafic rocks).

2.6. DISCUSSION

2.6.1. Exploration using physical properties

Physical properties most useful for isolating prospective rocks at the Hislop deposit

The most useful physical properties for delineating prospective rocks at Hislop from those more likely to be barren are magnetic susceptibility and density. Magnetic susceptibility and density are equally capable of discerning prospective syenite intrusive rocks and porphyritic rhyolite dikes at Hislop from intermediate, mafic, and ultramafic rocks (Fig. 2.26). These physical properties however, do not distinguish between hydrothermally altered and least-altered felsic rocks, as mineralogical changes in these rocks related to alteration processes do not add or remove any significant quantities of dense or magnetic minerals.

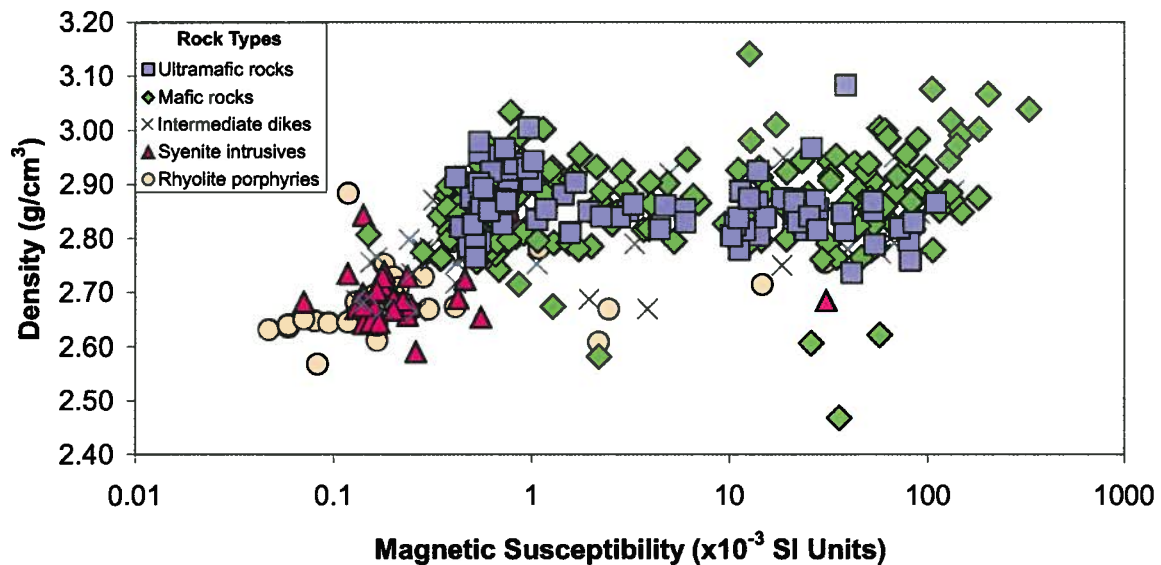


Figure 2.26. Magnetic susceptibility plotted against density for Hislop samples. Syenite intrusives and porphyritic rhyolite dikes have distinctly low density and magnetic susceptibility ranges allowing them to be distinguished from intermediate, mafic, and ultramafic rocks at Hislop.

Magnetic susceptibility and density ranges for intermediate, mafic and ultramafic rocks are large, and generally overlap. These rock types cannot be independently distinguished from one another based on these two physical properties. That being said, potentially prospective carbonate-altered intermediate, mafic, and ultramafic rocks have typically low magnetic susceptibilities; carbonate-altered rocks almost exclusively occur in the lower susceptibility ranges for these rocks (Figs. 2.27a and 2.27b). Thus, when this low range is isolated, the majority of carbonate-altered rocks are targeted. Unfortunately, due to variability in magnetite abundance and distribution in intermediate to ultramafic rocks, and irregular hematization of magnetite, there are relatively unaltered, low-susceptibility rocks at Hislop. Carbonate-altered rocks at Hislop cannot be exclusively delineated from a physical property dataset as a result of this overlap. Nonetheless, targeting low susceptibility rocks would be effective in delineating many prospective carbonate-altered rocks from high susceptibility rocks more likely to be barren of mineralization.

Density provides an additional measure of alteration of ultramafic volcanic rocks only. If ultramafic rocks were isolated, density values could be used to delineate the higher density magnesite + fuchsite rocks from other ultramafic rocks, specifically those with lower density talc + chlorite assemblages.

Resistivity may be useful in distinguishing ultramafic rocks from other rocks in the Hislop physical property dataset, however this is likely of no significance with respect to mineralization, as these rock types are not uniquely mineralized. If dealing solely with ultramafic rocks however, higher resistivity values may be indicative of carbonate-altered, low-porosity ultramafic volcanic rocks. Chargeability values do not distinguish between rock types at Hislop. Although there may be a relationship between pyrite abundance and chargeability for felsic rocks, there are likely other influences on the chargeability of rocks at Hislop, like the texture of sulfides, or that of the host rock itself.

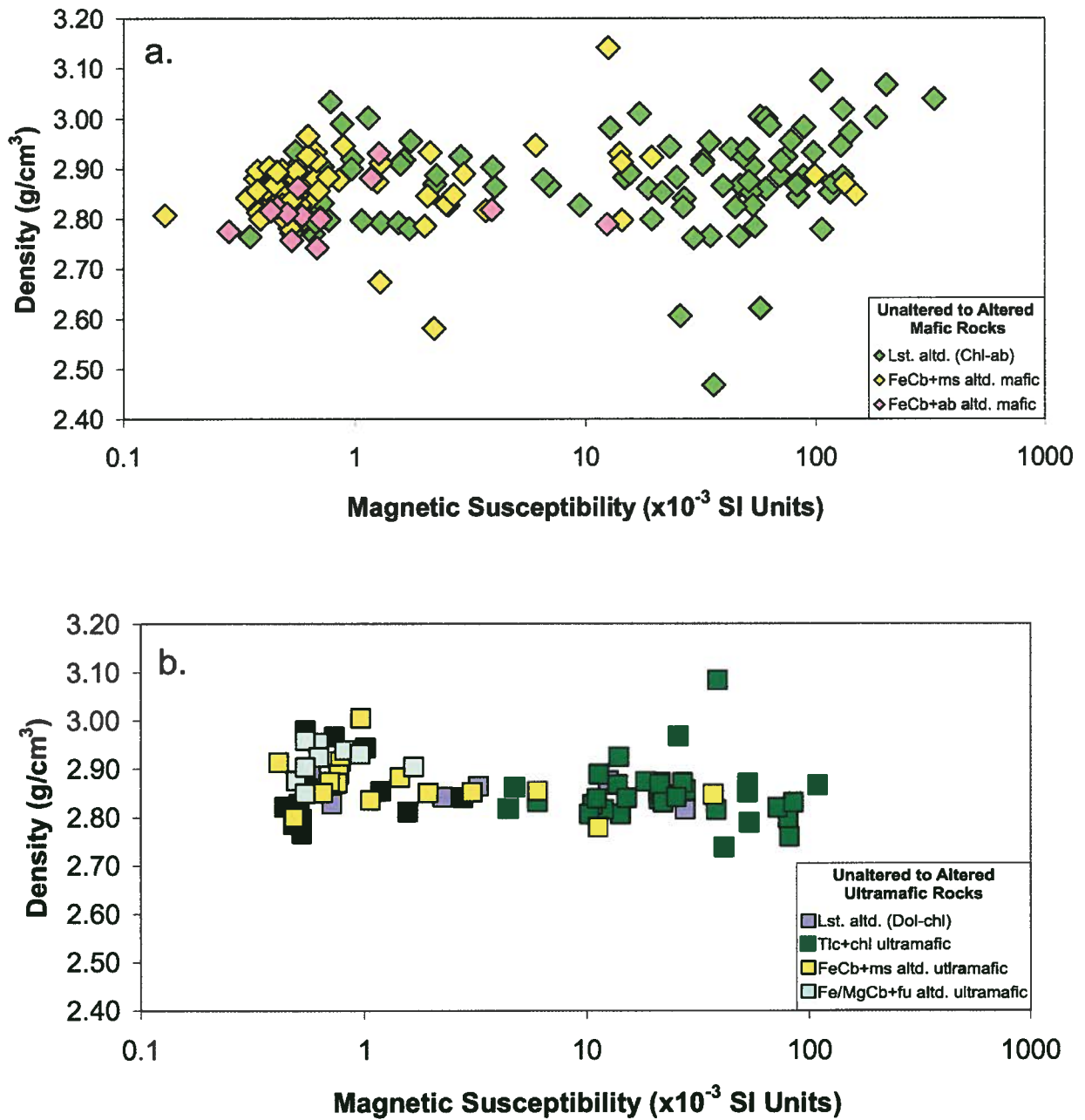


Figure 2.27. Carbonate-alteration destroys magnetite in a) mafic and b) ultramafic volcanic rocks, causing magnetic susceptibility to drop. Density values increase slightly for altered ultramafic rocks. For abbreviations in a) and b) see Figs. 2.20 and 2.19, respectively.

Prospective physical property ranges

Magnetic susceptibility and density constitute the two most well understood physical properties at Hislop. They were determined to be the most useful of the four physical properties studied in delineating some of the prospective rocks at Hislop. Table 2.5 summarizes the prospective ranges for magnetic susceptibility and density for Hislop. These ranges were established using the statistical analysis program SPSS Statistics, and anomalously high and low values (extreme cases occurring beyond 3x the interquartile range of values) were eliminated to yield a tighter, more representative, range of values for each of the rock types.

These prospective cut-off values are used to query the Hislop physical property database for the purposes of determining the effectiveness of these cut-offs to distinguish between possible gold-related rocks and rocks likely to be barren. The dataset was queried first to isolate prospective felsic rocks (susceptibility $<0.42 \times 10^{-3}$ SI Units, density $<2.8 \text{ g/cm}^3$), and then queried to identify altered intermediate to ultramafic rocks (susceptibility $<5.96 \times 10^{-3}$ SI Units, density between 2.67 g/cm^3 and 2.97 g/cm^3) from the remaining data. The results can be assessed in two ways:

(1) No. of targeted rock types recalled / total known to occur in database;

(2) No. of targeted rock types recalled / total recalled in query

where the 'targeted rock types' refer to felsic rocks, or hydrothermally altered rocks. Table 2.6 compiles the results from this query. Out of 70 total felsic samples in the database, 55 were recalled, falling within the statistically significant susceptibility and density ranges for these rocks, yielding a 79% success rate. However, this query yielded 73 samples in total, out of which 18 were not felsic intrusive rocks, thus mislabeling 25% of the results.

Table 2.5. Statistical data for prospective rocks at Hislop, and cut-off values used for querying physical property data.

Rock Type	Magnetic Susceptibility (10^{-3} SI)				Density (g/cm^3)				Cut-off values for querying data		
	No.	Mean	Median	Range	No.	Mean	Median	Range	Rock Type	Mag. Sus.	Density
Unaltered ultramafic (dolomite-chlorite assemblage)	8	6.03	1.49	0.57-12.5	8	2.85	2.86	2.82-2.89	Carbonate-altered ultramafic	0.41-5.96	2.80-2.96
Unaltered ultramafic (talc-chlorite assemblage)	46	24.12	14.61	0.44-84.4	46	2.85	2.84	2.79-2.94			
Fe-carbonate-muscovite altered ultramafic	16	5.73	1.01	0.41-5.96	15	2.87	2.85	2.80-2.91			
Magnesite-fuchsite altered ultramafic	9	0.75	0.62	0.49-0.95	9	2.91	2.92	2.85-2.96			
Unaltered mafic	107	40.09	21.50	0.35-141	101	2.87	2.87	2.70-3.08	Carbonate-altered mafic	0.2-2.19	2.76-2.97
Fe-carbonate-muscovite altered mafic	75	6.86	0.60	0-2.19	71	2.85	2.86	2.78-2.97			
Fe-carbonate-albite altered mafic	14	1.71	0.58	0.28-1.27	13	2.82	2.81	2.76-2.86			
Unaltered intermediate intrusive	11	41.11	18.40	0.24-135.29	11	2.83	2.81	2.72-2.95	Carbonate-altered intermediate intrusive	0.13-3.8	2.67-2.95
Carbonate altered intermediate intrusive	22	10.95	0.58	0.13-3.8	22	2.79	2.78	2.67-2.95			
Carbonate-muscovite altered intermediate intrusive	10	0.75	0.69	0.32-1.55	10	2.85	2.86	2.76-2.94			
Syenite	34	1.19	0.20	0.07-0.42	32	2.70	2.69	2.64-2.74	Felsic intrusives	0.05-0.42	2.57-2.80
Rhyolite porphyry	37	1.59	0.16	0.05-0.41	35	2.69	2.67	2.57-2.80			

Table 2.6. Results from magnetic susceptibility and density queries of the Hislop physical property dataset.

Target rock	Total target rock samples in database	Total recalled samples from query	No. target rock samples recalled using query	% target rock samples out of known amount in database (1)	% target rock samples out of total recalled samples (2)
Felsic intrusive rocks	70	73	55	79	75
Generally-altered intermediate, mafic, and ultramafic rocks	188	221	142	76	64
Carbonate-altered intermediate, mafic and ultramafic rocks	146	221	112	77	51

Of 188 variably altered intermediate, mafic, and ultramafic samples (this includes some obscure alteration types not thoroughly reported on in this work, in addition to carbonate altered rocks), 142 altered samples were recalled by the query, yielding a 76% success rate. Seventy-nine out of the 221 total recalled samples were relatively unaltered samples, thus 36% of the resulting sample set were misclassified. Out of 146 total dominantly carbonate-altered samples in the dataset 112 were recalled by the same query, giving a 77% success rate in detecting these samples from the dataset.

The mafic and ultramafic samples misidentified as being altered, upon examination, are largely unaltered low susceptibility mafic volcanic rocks that overlap the physical property ranges of carbonate-altered mafic volcanic rocks.

Although some unprospective, low susceptibility rocks would inevitably be targeted, many of the barren rocks are eliminated from consideration. Results of such queries would not provide definitive targets for exploration, but could act as important mineral vectoring criteria for consideration in association with any other geological, geophysical, geochemical, or mineralogical data available from the area.

Physical properties and 3D geophysical inversion modeling

It is anticipated that physical property cut-off values similar to those used to target prospective samples from the Hislop physical properties database would be equally successful when applied to 3D physical property models generated from geophysical inversions in the Hislop area. However, the number of rock types at Hislop, and their structurally complicated relationships to one another, would make direct referencing to specific rock types and alteration assemblages based on physical property data difficult. At larger scales of modeling low magnetic susceptibility values may be effective in isolating felsic rocks and strongly carbonate-altered intermediate, mafic and ultramafic rocks. Density information would help further confirm identification of felsic rocks, isolating them from other magnetic susceptibility lows. With perhaps more localized inversion modeling, smaller scale variations in physical properties, like for example, subtle changes in mafic and ultramafic units related to the presence of felsic intrusions or of carbonate-alteration zones, could become apparent in regions that appear to be more homogeneous at a larger scale.

The use of physical property data to highlight mineralization, or prospective geology and alteration, would generally occur at a later stage in exploration when an acceptable inversion model has been established for a property or deposit. Prior to this stage, physical property data can play an important role in guiding geophysical inversions. Knowledge of characteristic physical property values of rock types from the area of exploration, and of any relationships between physical properties and mineralization, can be input into the inversion to constrain it, which can significantly improve the inversion result (e.g. Williams, 2006).

2.6.2. Comparison to analogous areas

Comparison to regional variations in physical property data

An important goal of this work is to compile a dataset of typical physical properties expected to occur within a representative Archean orogenic gold environment, for future use in guiding and interpreting inversions both at Hislop and in similar mineral deposit environments. Before this data is used, however, it is important to determine whether the physical property values and ranges from Hislop represent those typically found in this environment.

A regional physical property study covering Matheson and Kirkland Lake areas to the west and south of the Hislop deposit area, respectively, was completed for a large sample set of over 1000 samples (Ontario Geological Survey, 2001). Magnetic susceptibility, density, and resistivity were measured. Comparing the magnetic susceptibility and density data from the OGS study to the Hislop data helps to define the local extent to which these physical properties vary in this part of the Abitibi greenstone belt. This dataset was assessed and rock types considered to be equivalent to the primary rock types at Hislop were compiled and subdivided. Histograms comparing OGS physical property data to Hislop data are presented in Figure 2.28 and Figure 2.29.

Magnetic susceptibility

Mafic and ultramafic rocks from the two studies have similar magnetic susceptibility distributions. Fe-carbonate-altered mafic volcanic rocks from the Matheson and Kirkland Lake areas have similar data distributions as Fe-carbonate altered rocks from the Hislop area (Fig. 2.30). It was not possible to compare any other altered rock data from the OGS dataset to similar altered rocks from Hislop as no other samples in the OGS dataset were subdivided based on alteration assemblages.

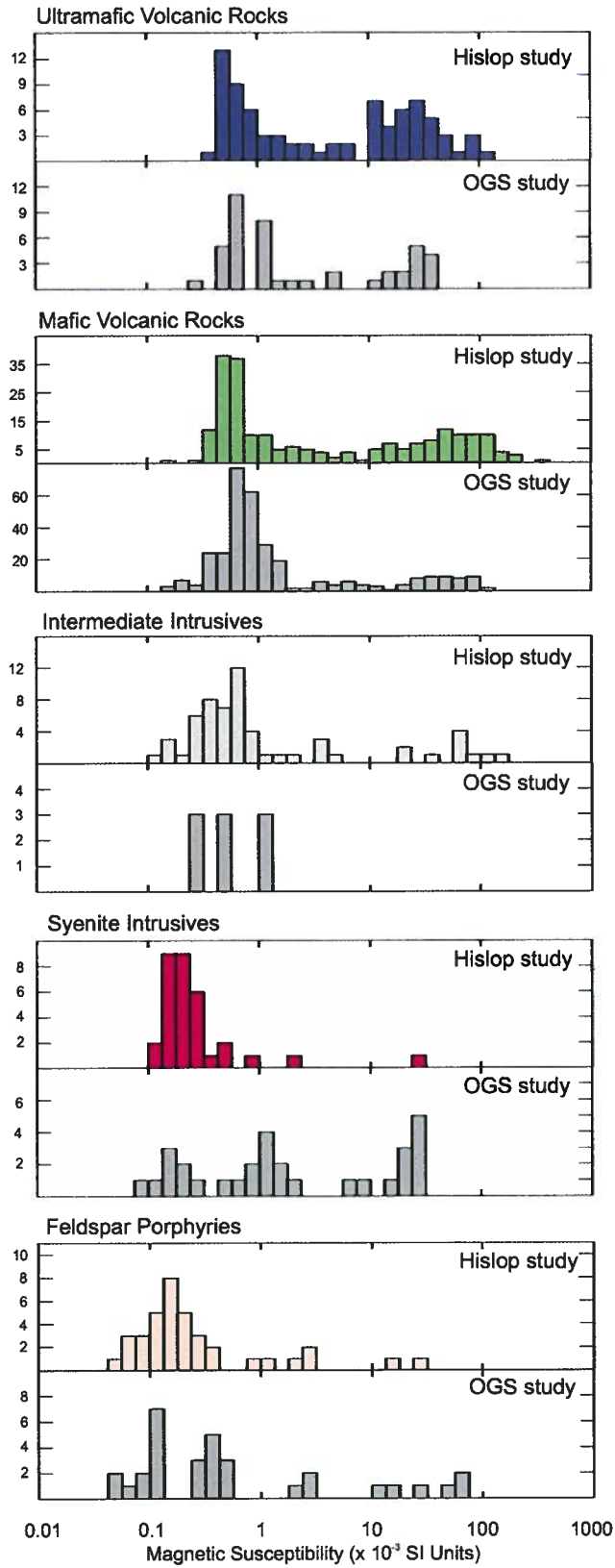


Figure 2.28. Magnetic susceptibility histograms comparing data from Hislop rocks, and equivalent rocks from surrounding regional areas.

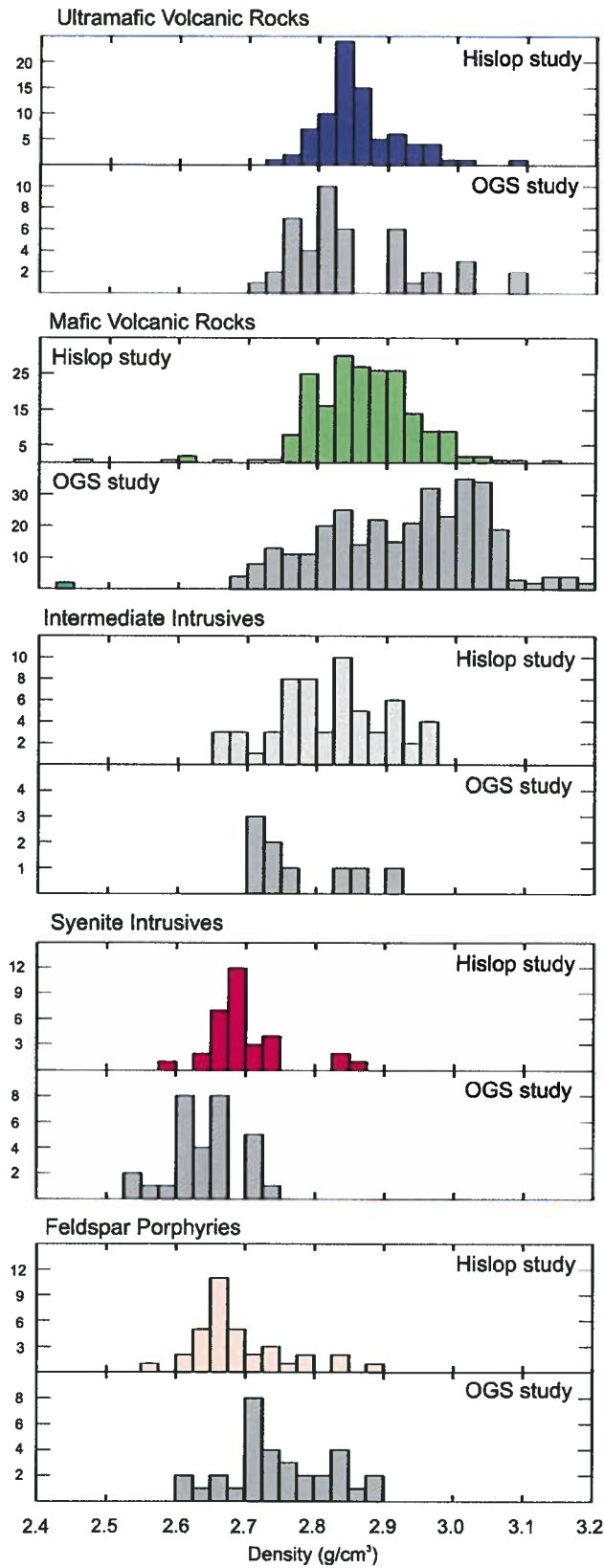


Figure 2.29. Density histograms comparing data from equivalent rock types from Hislop rocks, and equivalent rocks from surrounding regional areas.

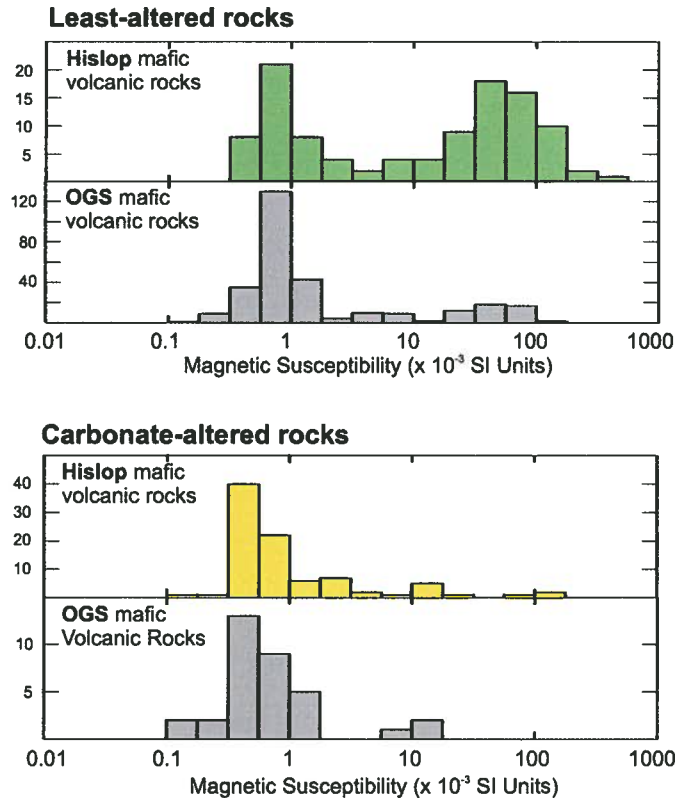


Figure 2.30. A comparison of magnetic susceptibility data associated with least-altered and carbonate-altered mafic rocks from the Hislop deposit, and from the greater surrounding area.

Susceptibilities for local and regional intermediate intrusive samples overlap, however, there are very few regional samples overall. A comparison of syenite and felsic intrusive magnetic susceptibility data from the two datasets illustrates that regionally, there is more variation in magnetic susceptibility of these rock types than what is represented in the Hislop area, with three to four populations distinguishable. A comparison between Hislop and OGS data indicates outliers in Hislop syenite and felsic intrusive data may fall into the higher susceptibility ranges observed for similar rocks in the OGS dataset. The large regional range in susceptibilities may make it difficult to discriminate higher susceptibility, magnetite-rich syenites and felsic intrusives from mafic and ultramafic rocks at the regional scale. If it could be determined that low-susceptibility syenites are more commonly associated with mineralization, then the overlap would not cause a problem for physical property based exploration, and may

actually allow for the identification, based on susceptibility, of prospective syenites from a larger syenite database.

Density

Density distributions for Hislop ultramafic rocks and the regional scale ultramafic rocks are similar, however there is a gap in data in the OGS dataset between 2.85 and 2.90 g/cm³. This may be attributable to the smaller size of the OGS ultramafic rock dataset, which has about half the number of samples of the Hislop dataset. The variety of ultramafic rocks that occur in the region may not be represented in the OGS sample set. Matheson and Kirkland Lake intermediate intrusive rocks have similar ranges of density values compared to Hislop intermediate dikes, however, the Matheson and Kirkland Lake samples, are much fewer in number.

Mafic volcanic rock, syenite intrusive, and felsic intrusive data from these studies are not as comparable to one another. There are a greater number of high density mafic rocks regionally than at Hislop, suggesting there are high density regional scale mafic rocks that are not represented at Hislop.

Regionally, syenites have slightly lower densities, and felsic intrusive rocks have slightly higher densities than the equivalent Hislop rocks. Magnetic susceptibility data for regional syenites and feldspar porphyries indicated that there are multiple populations that exist for these rock types that were not recognized or sampled at Hislop. The different subpopulations of these rocks at the regional scale likely differ in mineral composition, which would explain the inconsistencies between Hislop and OGS sample densities.

Where separated into least-altered and altered rock populations (Fig. 2.31), ranges of density for least-altered mafic rocks are generally equivalent for the local and regional datasets, with the exception of the previously mentioned high density population in the unaltered regional mafic rock dataset. Densities of carbonate-altered mafic rock suites from the individual studies also overlap, however data populations in each sample set do

not match, with an anomalous high density population in the OGS dataset between 3.0 - 3.2 g/cm³. This high density population corresponds with higher density least-altered mafic volcanic samples in the OGS dataset. Perhaps these samples were mislabeled, or incompletely labeled originally and actually represent a population of anomalously high density carbonate-altered mafic rocks not encountered at Hislop. This however would infer that there is an alteration process which yields higher densities in mafic volcanic rocks, which was not observed during Hislop physical property studies

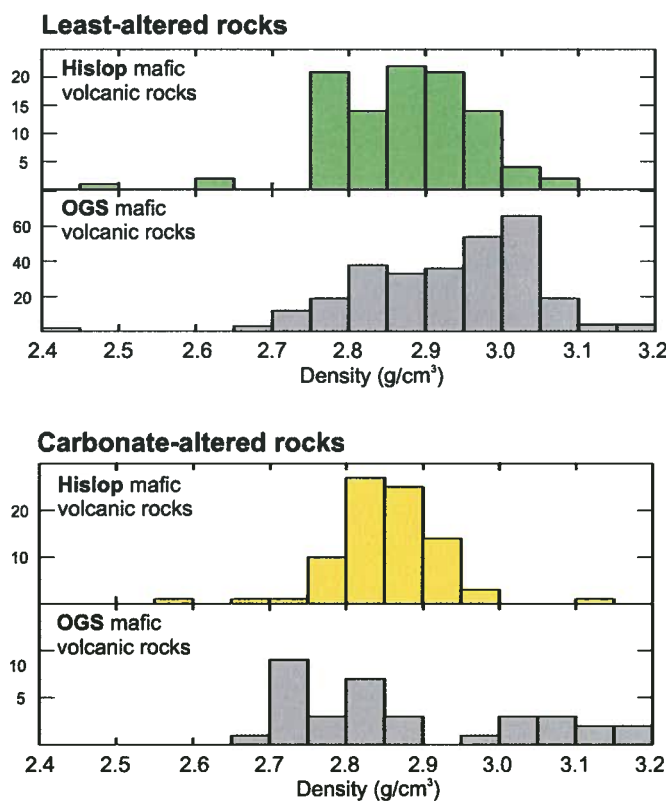


Figure 2.31. A comparison of density data associated with least-altered and carbonate-altered mafic rocks from the Hislop deposit, and from the greater surrounding area.

Due to differences in instruments (the OGS susceptibility data were collected using a Bartington MS-2 susceptibility meter) and techniques used to collect the physical property data, some discrepancies would be expected between the two datasets. Additional differences may arise from misplacement of samples from the OGS dataset into incorrect rock categories for comparison to the Hislop sample suite. As there were no detailed descriptions for the OGS samples, it was not possible to be entirely confident in

assigning the samples to the proper congruent categories. Finally, lack of correspondence between some populations may be the result of rock types not being sampled with equal frequency at the local and regional scales.

In summary, regional magnetic susceptibility data is more representative of local Hislop rocks than density data, especially with respect to intermediate, mafic, and ultramafic rocks. Least-altered mafic and ultramafic rocks from the local and regional datasets have similar means and ranges of magnetic susceptibility, as do altered rocks. This means that physical property queries used in this study should be capable of delineating a significant proportion of carbonate-altered rocks from suites of intermediate to ultramafic volcanic rocks throughout the larger area. Density values are not as consistent between the different scale studies, and are less useful in targeting particular rock types or alteration assemblages at the regional scale. However, since regional syenite densities are always as low as Hislop syenite densities, or lower, these important rock types may be distinguishable at the regional scale using appropriate physical property cut-offs.

Effect of metamorphism on physical property data.

Although greenschist facies rocks are the typical hosts for Archean orogenic gold deposits, these deposits also occur, albeit to a lesser extent, in amphibole or even higher grade rocks (Meuller and Groves 1991; Groves, 1993; Hagemann and Cassidy, 2000). Varying metamorphic grade can have a significant effect on physical property behavior, and must be considered prior to interpretation of sample-based, or geophysical inversion-derived physical property data. A comparison to physical property data from studies of the Weebo/Wildara and Southern Cross greenstone belts in the Yilgarn Craton, Australia, reveals similarities and differences in physical property data from similar geological environments of varying metamorphic grade (Bourne et al, 1993). Metamorphism can invoke changes in mineralogy or texture that can significantly influence the physical property value of a rock. An excellent example is the formation of magnetite during serpentinization. Bourne et al. (1993) have shown that densities and magnetic

susceptibilities are higher overall for amphibolite facies ultramafic and mafic rocks than for greenschist facies ultramafic and mafic rocks. They explain that increases in density of mafic rocks of amphibole facies grade is due to the destruction of low density plagioclase ($2.61\text{-}2.77\text{ g/cm}^3$) to form hornblende ($3.02\text{-}3.45\text{ g/cm}^3$) from actinolite/tremolite. Ultramafic rocks of higher metamorphic grade have increased densities relative to less metamorphosed ultramafic rocks which is related to the replacement of serpentine and talc (2.7 g/cm^3), by olivine (3.3 g/cm^3). Magnetic susceptibility increases with metamorphic grade in both mafic and ultramafic rocks due to increased magnetite content by volume in amphibolite grade rocks, and increased magnetite grain sizes which increases low-field magnetic susceptibility. The increase in susceptibility with metamorphic grade in ultramafic rocks is not consistent with the results of Clark et al. (1992) from the Agnew-Wiluna belt of the Yilgarn Block. A decrease in susceptibilities of ultramafic rocks with metamorphic grade in the Agnew-Wiluna belt may indicate that hydrothermal alteration played a larger role in destroying magnetite that was formed during serpentinization.

Since rock composition influences the products of hydrothermal alteration, for variably metamorphosed rocks there will be different alteration mineral products (Meuller and Groves, 1991; McCuaig and Kerrich, 1998). These variations in alteration mineral assemblages are generally consistent between gold deposits in rocks of the same metamorphic grade. Thus, as long as there are no other significant physical property-altering variables at work competing with mineralogical controls, some predictions can be made regarding the physical property characteristics of hydrothermally altered zones in metamorphosed rocks. An example of a mineralogical change related to increased temperatures and pressures of hydrothermal alteration-related sulfide precipitation that would have a particularly strong effect on physical property behavior, is formation of pyrrhotite instead of pyrite as the main gold-related sulfide (McCuaig and Kerrich, 1998; Hagemann and Cassidy, 2000). This is a high susceptibility mineral in its monoclinic form. The presence of monoclinic pyrrhotite would increase the susceptibility of mineralized areas, and could provide an important vector to gold mineralization.

Effects of alteration of metamorphic mineral assemblages must always be considered. Roberts (1988) explains how amphibolite facies rocks are known to be hydrothermally altered in the Archean orogenic gold setting to mineral assemblages reminiscent of a retrograde metamorphic assemblage (with chlorite, quartz and carbonate), or to an alteration assemblage similar to the amphibolite facies mineral assemblage (with biotite, garnet, anthophyllite, cummingtonite, cordierite, gedrite, and staurolite). These changes to mineralogy will likely affect physical properties, such as magnetic susceptibility and density, which are known to be strongly controlled by mineralogy.

2.7. CONCLUSIONS

Mineralogical and textural modifications within and between the different rock suites explain many of the physical property variations at Hislop. These are related to the range of geological processes, including igneous differentiation/fractionation, metamorphism, and hydrothermal alteration, that have affected the rocks throughout their history. The physical properties most useful for detecting prospective rocks at Hislop are magnetic susceptibility and density. This study illustrates predictable relationships between low susceptibility values and prospective felsic intrusive rocks and carbonate-altered mafic and ultramafic rocks in the immediate Hislop deposit area. Low density values will help confirm the presence of felsic rocks.

The magnetic susceptibility and density cut-off values used to query the Hislop dataset in this study are considered useful for targeting prospective rocks in the Hislop area within physical property datasets generated from drill core measurements. The same cut-offs could be used for locating prospective areas within a 3D physical property model generated from geophysical inversions. Due to overlap between less prospective mafic and ultramafic volcanic rocks with low modal magnetite and prospective, carbonate-altered rocks, any low susceptibility targets would have to be considered alongside other exploration criteria. The cut-off values could be used to filter physical property data as a first pass method of eliminating areas most likely to be barren.

In addition to using physical properties as a means to delineate prospective rocks in the Archean orogenic gold deposit environment, mean values, ranges, and standard deviations of physical property data for the different rock types, and altered subpopulations can be used to constrain geophysical inversions.

Although there is some indication of relationships between hydrothermally altered rocks and resistivity there are not enough electrical property data to confidently use these relationships to identify prospective rocks. Far more magnetic susceptibility and density data were collected and analyzed during the course of this study than resistivity and chargeability data, and as such, there is increased confidence in interpreting magnetic susceptibility and density data, and 3D susceptibility and density inversion models.

By comparison to a more regional scale physical property dataset, the Hislop physical property dataset is generally representative of rocks in this part of the Abitibi greenstone belt, with the exception of there being a greater variability in compositions of felsic intrusives at the regional scale. The Hislop dataset may be less representative of rocks in a similar mineral deposit environment at a different metamorphic grade.

Obtaining prior information about an exploration site, conducting reconnaissance in the area of interest, and collecting representative rock samples would enable a geologist to determine if metamorphic grade, and any overprinting hydrothermal alteration might affect typical physical property ranges characteristic of the Archean orogenic gold deposit environment. Some knowledge of physical properties, be it expected values based on known rock types, or mineral assemblages, will vastly improve the interpretation of physical property models resulting from geophysical inversion.

REFERENCES

Berger, B.R., 1999, Geological investigations along Highway 101, Hislop Township: Ontario Geological Survey, Summary of Field Work and Other Activities 1999, Open File Report, 6000, p. 5-1 – 5-8.

Berger, B.R., 2002, Geological synthesis of the Highway 101 area, east of Matheson, Ontario: Ontario Geological Survey, Open File Report 6091, 124 p.

Bohlke, J.K., 1989, Comparison of metasomatic reactions between a common CO₂-rich vein fluid and diverse wall rocks: intensive variables, mass transfers, and Au mineralization at Alleghany, California: *Economic Geology*, v.84, p. 291-327.

Bourne, B.T., Dentith, M.C., Trench, A., and Ridley, J., 1993, Physical property variations within Archean granite-greenstone terrane of the Yilgarn craton, Western Australia: the influence of metamorphic grade: *Exploration Geophysics*, v. 24, p. 367-374.

Boyd, D., 1984, Aeromagnetic surveys and gold, *in* Doyle, H.A., ed., *Geophysical Exploration for Precambrian Gold Deposits*, Geology Department and University Extension, University of Western Australia, Publication 10, p. 81-96.

Bucher, K., and Frey, M., 2002, *Petrogenesis of metamorphic rocks*, seventh edition, Springer-Verlag Berlin Heidelberg, New York, 431 p.

Card, K.D., 1990, A review of the Superior Province of the Canadian Shield, a product of Archean accretion: *Precambrian Research*, v. 48, p. 99-156.

Card, K. D., and Ciesielski, A., 1986, DNAG Subdivisions of the Superior Province of the Canadian Shield: *Geoscience Canada*, v. 13, p. 5-13.

Cas, R.A.F., and Wright, J.V., 1987, Volcanic successions, modern and ancient: a geological approach to processes, products, and successions: Allen & Unwin, London, United Kingdom, 528 p.

Clark, D.A., 1997, Magnetic petrophysics and magnetic petrology: aids to geological interpretation of magnetic surveys: *Journal of Australian Geology and Geophysics*, v. 17, p. 83-103.

Clark, D.A., French, D.H., Lackie, M.A., and Schmidt, P.W., 1992, Magnetic petrology: application of integrated rock magnetic and petrological techniques to geological interpretation of magnetic surveys: *Exploration Geophysics*, v. 23, p. 65-68.

Coggon, J.H., 1984, Geophysics as an aid to gold exploration in the Yilgarn block, *in* Doyle, H.A., ed., *Geophysical Exploration for Precambrian Gold Deposits*, Geology Department and University Extension, University of Western Australia, Publication 10, p. 113-138.

Colvine, A.C., Fyon, J.A., Heather, K.B., Marmont, S., Smith, P.M., and Troop, D.G., 1988, Archaean lode gold deposits in Ontario: Ontario Geological Survey Miscellaneous Paper 139, 136 p.

Cooper, M.A., 1948, Report on Kelore Mines Ltd., Ramore, Ontario, unpublished, 22 p.

Dockery, B.A., 1984, Geophysical case history of the Lady Susan gold prospect, *in* Doyle, H.A., ed., *Geophysical Exploration for Precambrian Gold Deposits*, Geology Department and University Extension, University of Western Australia, Publication 10, p. 165-182.

Doyle, H.A., 1990, Geophysical exploration for gold – a review: *Geophysics*, v. 55, p. 134-146.

Ellis, R.G., and Oldenburg, D.W., 1994, Applied geophysical inversion: *Geophysical Journal International*, v. 116, p. 5-11.

Fowler, C.M.R., Stead, D., Pandit, B.I., Janser, P.W., Nisbet, E.G., and Nover, G., 2005, A database of physical properties of rocks from the Trans-Hudson Orogen, Canada, *Canadian Journal of Earth Sciences*, v. 42, p. 555-572.

Fyon, J.A., and Crockett, J.H., 1983, Gold exploration in the Timmins District using field and lithogeochemical characteristics of carbonate alteration zones, *in* Hodder, R.W., and Petruk, W., eds, *Geology of Canadian Gold Deposits*, Canadian Institute of Mining and Metallurgy, Special Volume 24, p. 113-129.

Goldfarb, R. J., Baker, T., Dube, B., Groves, D.I., Hart, C.J.R., and Gosselin, P., 2005, Distribution, character, and genesis of gold deposits in metamorphic terranes, *in* Hedenquist, J.W., Thompson, J.F.H., Goldfarb, R.J., and Richards, J.P., eds., 100th Anniversary Volume, *Economic Geology*, v. 100, p. 407-450.

Grant, F.S., 1985, Aeromagnetism, geology, and ore environments, II. Magnetite and ore environments: *Geoexploration*, v. 23, p. 335-362.

Groves, D.I., 1993, The crustal continuum model for late-Archaean lode-gold deposits of the Yilgarn Block, Western Australia: *Mineralium Deposita*, v. 28, p. 366-374.

Groves, D.I., and Foster, R.P., 1991, Archaean lode gold deposits, *in* Foster, R.P., ed., *Gold Metallogeny and Exploration*, Blackie and Son, Glasgow, United Kingdom, p. 63-103.

Groves, D.I., Ho, S.E., and Houstoun, S.M., 1984, The nature of Archean gold deposits in Western Australia with particular emphasis on parameters relevant to geophysical exploration, *in* Doyle, H.A., ed., *Geophysical Exploration for Precambrian Gold Deposits*, Geology Department and University Extension, University of Western Australia, Publication 10, p. 1-63.

Groves, D.I., Goldfarb, R.J., Gebre-Mariam, M., Hagemann, S.G., and Robert, F., 1998, Orogenic gold deposits: a proposed classification in the context of their crustal distribution and relationship to other gold deposit types: *Ore Geology Reviews*, 13, p. 7-27.

Gunn, P.J., and Dentith, M.C., 1997, Magnetic response associated with mineral deposits: Australian Geological Survey, *Journal of Australian Geology and Geophysics Organisation*, v.17, p.145-158.

Hagemann, S.G., & Cassidy, K.F., 2000, Archaean orogenic lode gold deposits, *in* Hagemann, S.G., and Brown, P.E., eds., *Gold in 2000*, Society of Economic Geologists, *Reviews in Economic Geology*, v. 13, p. 9-68.

Hallof, P.G., 1992, Resistivity and induced polarization, the spectral induced polarization method, *in* Van Blaricom, R., compiler, *Practical Geophysics II for the Exploration Geologist*, Northwest Mining Association, USA, p. 39-138.

Hallof, P.G., and Yamashita, M., 1990, The use of the IP method to locate gold-bearing sulfide mineralization, *in* Fink, J.B., Sternberg, B.K., McAlister, E.O., Weiduwilt, W.G., and Ward, S.H., eds., *Induced Polarization: applications and case histories*, Society of Exploration Geophysicists, Tulsa, Ok., p. 227-279.

Harron, G.A., Middleton, R.S., Durham, R.B., and Philipp, A., 1987, Geochemical and geophysical gold exploration in the Timmins area, Ontario: a case history: *Canadian Mining and Metallurgical Bulletin*, v. 82, p. 52-57.

Henkel, H., and Guzman, M., 1977, Magnetic features of fracture zones: *Geoexploration*, v. 13, p. 173-181.

Hodgson, C.J., 1990, An overview of the geological characteristics of gold deposits in the Abitibi subprovince, *in* S.E. Ho, F. Robert, and D.I. Groves, compilers, *Gold and Base Metal Mineralization in the Abitibi Subprovince, Canada, with Emphasis on the Quebec*

Segment, Short Course Notes, Geology Department (key center) and University Extension, the University of Western Australia, publication No. 24, p. 63-100.

Hodgson, C.J., 1993, Mesothermal lode gold deposits, *in* Kirkham, R.V., Sinclair, W.D., Thorpe, R.I., and Duke, J.M., eds., Mineral Deposit Modeling, Geologic Association of Canada, Special Paper 40, p. 635-678.

Hodgson, C.J., and Hamilton, J.V., 1990, Gold mineralization in the Abitibi greenstone belt: end-stage results of Archean collisional tectonics, *in* Keays, R.R., Ramsey, W.R.H., and Groves, D.I., eds., The Geology of Gold Deposits: the Perspective in 1988, Economic Geology Monograph 6, p. 86-100.

Hodgson, C.J., and Troop, D.G., 1988, A new computer-aided methodology for area selection in gold exploration: a case study from the Abitibi greenstone belt: Economic Geology, v. 83, p. 952-977.

Hood, P., Irvine, J., and Hansen, J., 1982, The application of the aeromagnetic gradiometer survey technique to gold exploration in the Val d'Or mining camp, Quebec: Canadian Mining Journal, v.103, p. 21-39.

Holsner, W.T., and Schneer, C.J., 1961, Hydrothermal magnetite: Geological Society of America Bulletin, v. 72, p. 369-385.

Isles, D.J., Harman, P.G., and Cunneen, J.P., 1989, The contribution of high resolution aeromagnetism to Archean gold exploration in the Kalgoorlie Region, Western Australia, *in* Keays, R.R., Ramsey, W.R.H., and Groves, D.I., eds., The Geology of Gold Deposits: the Perspective in 1988, Economic Geology Monograph 6, p. 389-397.

Jackson, S. L., and Fyon, A. J., 1991, The western Abitibi subprovince in Ontario, *in* P.C. Thurston, H.R. Williams, R.H. Sutcliffe and G.M. Stott, eds., Geology of Ontario, Ontario Geological Survey, Special Volume 4, Part 1, p. 405-482.

Johnson, I., Webster, B., Matthews, R., and McMullen, S., 1989, Time-domain spectral IP results from three gold deposits in northern Saskatchewan: CIM Bulletin, v. 82, p. 43-49.

Johnson, G.R., and Olhoeft G.R., 1984, Density of rocks and minerals, *in* Carmichael, R.S., ed., Handbook of physical properties of rocks; Volume III, CRC Press, Florida, p. 1-38.

Kerrich, R., 1989, Geodynamic setting and hydraulic regimes: shear zone hosted mesothermal gold deposits, *in* Bursnall, J.T., ed., Mineralization and Shear Zones, Geological Association of Canada, Short Course Notes 6, p. 89-128.

Kishida, A., and Kerrich, R., 1987, Hydrothermal alteration zoning and gold concentration at the Kerr-Addison Archean lode gold deposit, Kirkland Lake, Ontario: Economic Geology, v. 82, p. 649-690.

Lapointe, P., Morris, W.A., and Harding, K.L., 1986, Interpretation of magnetic susceptibility: a new approach to geophysical evaluation of the degree of rock alteration: Canadian Journal of Earth Sciences, v. 23, p. 393-401.

Li, Y., and Oldenburg, D.W., 1996, 3-D inversion of magnetic data: Geophysics v. 61, p. 394-408.

McCuaig, T.C., and Kerrich, R., 1998, P-T-t-deformation-fluid characteristics of lode gold deposits: evidence from alteration systematics: Ore Geology Reviews, v. 12, p. 381-453.

Meuller, A.G., and Groves, D.I., 1991, The classification of Western Australian greenstone-hosted gold deposits according to wall-rock alteration mineral assemblages: Ore Geology Reviews, v. 6, p. 291-331.

Moore, E.S., 1936, Geology and ore deposits of the Ramore area: Ontario Department of Mines, Annual Report, 1936, v. 45, pt. 6, 37 p.

Ontario Geological Survey, 2001, Physical rock property data from the physical rock property study in the Timmins and Kirkland Lake Areas: Ontario Geological Survey, Miscellaneous Release – Data 91.

Pelton, W.H., Ward, S.H., Hallof, P.G., Sill, W.R., and Nelson, P.H., 1978, Mineral discrimination and removal of inductive coupling with multifrequency IP, *Geophysics*, v.43, p. 588-609.

Phillips, N.D., 2002, Geophysical inversion in an integrated exploration program: examples from the San Nicolas deposit: Unpublished M.Sc. thesis, University of British Columbia, 237 p.

Power, W. L., Byrne, D., Worth, T., Wilson, P., Kirby, L., Gleeson, P., Stapleton, P., House, M., Robertson, S., Panizza, N., Holden, D. J., Cameron, G., Stuart, R., Archibald, N. J., 2004, Geoinformatics evaluation of the eastward extension of the Timmins Gold Camp: Geoinformatics Exploration Inc., Unpublished report for St Andrew Goldfields Ltd.

Prest, V.K., 1956, Geology of the Hislop Township: Ontario Department of Mines, Annual Report, 1956, v. 65, pt. 5, 51p.

Raudsepp, M., and Pani, E., 2003, Application of Rietveld analysis to environmental mineralogy, in Jambor, J.L., Blowes, D.W., and Ritchie, A.I.M., eds., Mineralogical Association of Canada, Short Course Series, Volume 31, Chapter 8, p.165-180.

Ridley, J.R., and Diamond, L.W., Fluid chemistry of orogenic lode gold deposits and implications for genetic models, *in* Hagemann, S.G., and Brown, P.E., eds., *Gold in 2000*, Society of Economic Geologists, Reviews in Economic Geology, 13, p. 141-162.

Robert, F., 1990, Structural setting and control of gold-quartz veins of the Val D'Or area, southeastern Abitibi subprovince, *in* S.E. Ho, F. Robert, D.I. and Groves, compilers, Gold and Base Metal Mineralization in the Abitibi Subprovince, Canada, with Emphasis on the Quebec Segment, Short Course Notes, Geology Department (key center) and University Extension, the University of Western Australia, publication No. 24, p. 167-212.

Robert, F., Poulsen, K.H., Cassidy, K.F., and Hodgson, C.J., 2005, Gold metallogeny of the Superior and Yilgarn Cratons, *in* Hedenquist, J.W., Thompson, J.F.H., Goldfarb, R.J., and Richards, J.P., eds., 100th Anniversary Volume, *Economic Geology*, v. 100, p. 407-450.

Roberts, R.G., 1988, Archean lode gold deposits, *in* Roberts, R.G., and Sheahan, P.A., eds., *Ore Deposit Models*, Geoscience Canada, Reprint Series 3, p. 1-19.

Ropchan, J.R., Luinstra, B., Fowler, A.D., Benn, K., Ayer, J., Dahn, R., Labine, R., and Amelin, Y., 2002, *Economic Geology*, v. 97, p. 291-309.

Roscoe and Postle, 1998, Hislop Mine Property, Roscoe and Postle Associates Inc., St. Andrew Goldfields Ltd. internal report, unpublished, p. 66-89.

Seigel, H.O., Johnson, I., and Hennessey, J., 1984, Geophysics the leading edge: *Geophysics: the Leading Edge of Exploration*, v. 3, p. 32-35.

Telford, W.M., Geldart, L.P., and Sheriff, R.E., 1990, *Applied Geophysics*, Second Edition, Cambridge University Press, 770 p.

Troop, D.G., 1986, Multiple orebody types and vein morphologies, Ross Mine, District of Cochrane: Ontario Geological Survey, *Summary of Field Work and Other Activities*, v. 132, p. 413-420.

Williams, H., Stott, G.M., Thurston, P.C., Sutcliffe, R. H., Bennett, G., Easton, R.M., and Armstrong, D.K., 1991, Tectonic evolution of Ontario: summary and synthesis, *in* P.C.

Thurston, H.R. Williams, R.H. Sutcliffe and G.M. Stott, eds., *Geology of Ontario*, Ontario Geological Survey, Special Volume 4, Part 2, p. 1255–1332.

Williams, N.C., 2006, Applying UBC-GIF potential fields inversions in greenfields or brownfields exploration: Australian Earth Sciences Convention, 2006, Melbourne, Australia, 10 p.

Williams, N. and Dipple, G., 2005, Identifying sulfide mineralization from physical property measurements and its application to mineral exploration inversions, Geological Society of America, 2005 Salt Lake City Annual Meeting, Abstracts with Programs, v. 37, p. 23.

Williams, P.K., 1994, Relationship between magnetic anomalism and epigenetic gold mineralization in the Victory-Defiance area, Western Australia, *in*, Dentith, M.C., Frankcombe, K.F., Ho, S.E., Shephard, J.M., Groves, D.I., and Trench, A., eds., *Geophysical signatures of Western Australian Mineral Deposits*, Geology and Geophysics (Key Center) and UWA Extension, The University of Western Australia, Publication 26, Australian Society of Exploration Geophysicists, Special Publication 7, p. 283-296.

www.mindat.org, Mindat.org mineral and locality database.

www.standrewgoldfields.com, website for St. Andrew Goldfields, Ltd.

www.zonge.com/LabIP.html, website for Zonge Engineering and Research Organization, IP and resistivity measurements.

Chapter 3: Detecting gold-related geology in Archean orogenic gold environments using geophysical inversion: a synthetic modeling study based on the Hislop gold deposit, Ontario²

3.1. INTRODUCTION

3.1.1. Rationale

Three dimensional geophysical inversion modeling, involving the estimation of physical property distributions within the earth's subsurface from observed geophysical data, is used widely as a tool to explore for a range of mineral deposit types. Yet, as different deposit types are characterized by unique combinations of rock types, mineralogy, structure, and morphology, each deposit type may not be equally well imaged by inversion. Expectations regarding the detectability and delineation of orebodies and related rocks in a given mineral deposit setting can be generated through synthetic forward and inverse modeling prior to actual geophysical inversion work.

This study employs synthetic modeling to test the capabilities of geophysical inversion as an exploration tool in the Archean orogenic gold environment. In contrast to its more extensive use in imaging higher tonnage and higher grade deposits like volcanogenic massive sulfide, magmatic sulfide, and porphyry deposits (Oldenburg et al., 1997; Phillips, 2002; Farquharson et al., 2008), geophysical inversion is not as commonly used to explore for, or map, Archean orogenic gold deposits. As a result, there are fewer case histories successfully demonstrating its application, and thus there is less familiarity with the range of outcomes that can accompany inversion of different geophysical datasets over these deposits.

Prior to any geophysical work, it is important to identify the geological and physical property characteristics of typical exploration targets. Gold mineralized rocks

²A version of this chapter will be submitted for publication. Mitchinson, D., and Phillips, N, 2009, Detecting gold-related geology in Archean orogenic gold environments using geophysical inversion: a synthetic modeling study based on the Hislop gold deposit, Ontario

are not easily detectable using geophysics due to low tonnages and grades (Doyle, 1990). Alternate exploration targets must therefore be sought. In the case of many orogenic gold deposits, geological features spatially related to gold include faults, felsic intrusive rocks, and hydrothermal alteration zones. These are commonly narrow, near vertical features that extend to depth, and are hosted within deformed and steeply-dipping stratigraphy.

Physical property studies completed on rocks associated with the Hislop gold deposit, an orogenic gold deposit located east of the world renowned Timmins-Porcupine gold camp in Ontario, indicate that some known gold-related features have distinct physical property ranges that may allow them to be distinguished from likely barren host rocks (see Chapter 2). Synthetic forward and inverse modeling completed on simple 3D models based on the Hislop deposit tests whether these petrophysically distinct gold-related rocks can be detected using inversion methods. Synthetic modeling investigates whether the physical property contrasts are sufficiently strong, and if sizes, shapes, and locations, of gold-related geological features are such that they can be detected within a discretized earth model at a 1 km scale of investigation. Tests are devised to explore the effects of the addition of geological and physical property constraints. Results of the modeling reveal whether realistic physical property values can be recovered, thus lending confidence to the interpretation and querying of the recovered physical property model. Results furthermore highlight possible limitations of inversion at this scale. It indicates maximum depths of investigation, and can identify features not caused by a known source, but rather are artifacts or byproducts of the inversion algorithm.

3.1.2. Objectives

Synthetic modeling work aims to answer a series of questions related to how well inversion is able to image prospective geologic features expected in the Archean orogenic gold setting. Specific questions include:

1. Can a feature of interest be imaged using unconstrained inversion at a <1 km scale of investigation? What range of geometry, and physical property contrasts, can we expect to image within this mineral deposit setting.
2. How well does the inversion reproduce the true model? What are the significant differences between the recovered and true models? What are the causes of discrepancies?
3. Can the model result be improved with addition of basic prior geological knowledge, and what types of constraining information are most effective in improving the model? What differences between the true and recovered models persist?
4. Which geophysical datasets are most beneficial to invert for orogenic gold exploration? What information can each data type provide to help better understand the geology of the subsurface?

3.2. BACKGROUND

3.2.1. Geology of the Hislop gold deposit and relationship to other Archean orogenic gold deposits

The synthetic models presented herein are based on a simplified version of the geology of the Hislop gold deposit, and on average physical property-values determined for the range of significant Hislop rock types (Chapter 2).

The Hislop gold deposit is located approximately 13 km southeast of Matheson, Ontario, in the gold and base metal-rich Abitibi greenstone belt of the Superior Province (Fig. 2.1, Chapter 2). The Hislop deposit area is underlain mainly by mafic and ultramafic

volcanic rocks that have been deformed into near-vertical structural panels (Prest, 1956; Berger, 1999; Power et al., 2004)

Gold at Hislop (Fig. 3.1) is spatially related to an elongate, northwest-trending 30 m to 100 m wide, syenite dike occurring between a mafic, and an ultramafic volcanic unit (Cooper, 1948; Prest, 1956; Roscoe and Postle, 1998; Berger, 1999). The majority of gold occurs with disseminated pyrite within a strongly Fe-carbonate-altered, brecciated equivalent of the ultramafic unit lying adjacent to the southwest margin of the syenite (Cooper, 1948; Prest, 1956; Roscoe and Postle, 1998). Lesser gold occurs within quartz veinlets, stockworks and fractures in mafic volcanic flows north of the syenite, as well as in association with nearby porphyritic rhyolite dikes striking parallel to stratigraphy.

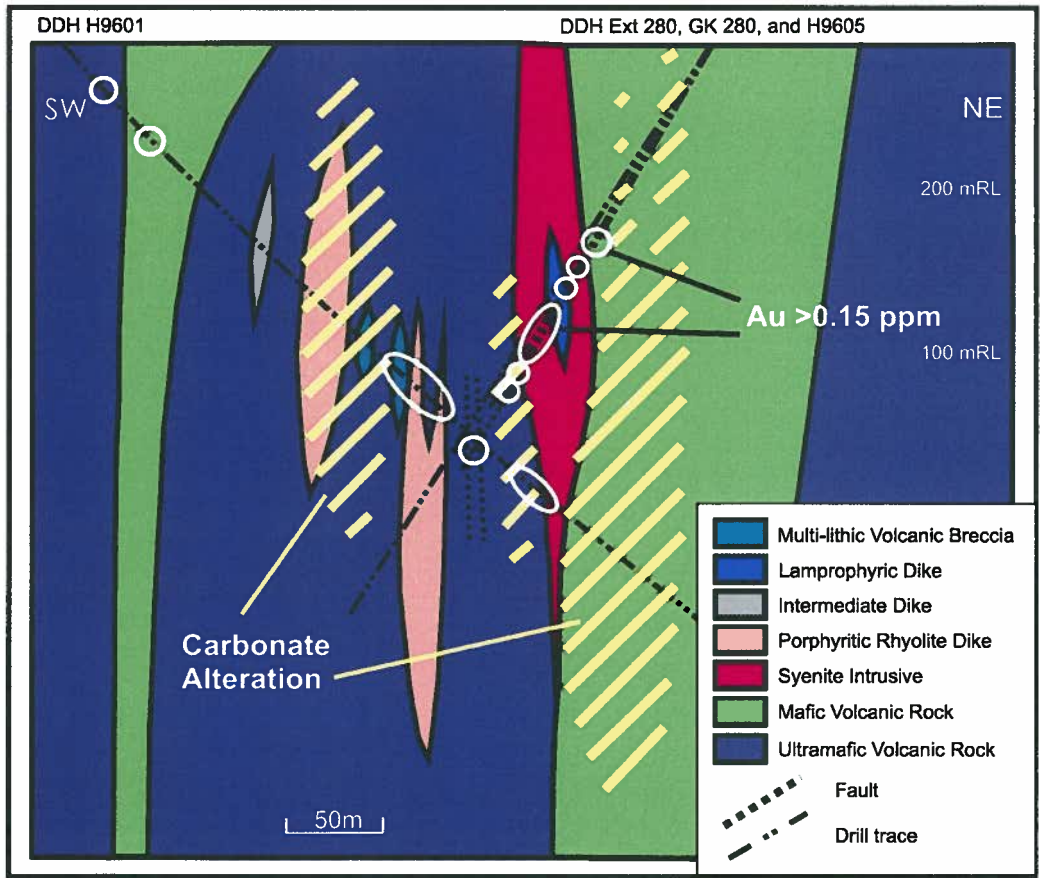


Figure 3.1. Cross-section looking northwest through the Hislop deposit, showing areas of carbonate-dominated alteration and gold mineralization. Cross-section interpreted from drill core logged from the Hislop property.

Geology and alteration mineral assemblages at Hislop are common to many greenschist facies-hosted Archean orogenic gold deposits globally. Orogenic gold deposits are epigenetic, and structurally-controlled. They can be hosted in any rock type, although Fe-rich mafic and felsic intrusive rocks are commonly in spatial proximity. Fe-carbonate + muscovite dominate gold-related hydrothermal alteration mineral assemblages, which usually extend only short distances (centimeter to meter scale) orthogonal to mineralized veins and structures. Gold occurs predominantly adjacent to, or within quartz-carbonate veins, or directly within host rocks associated with disseminated sulfides. A summary of characteristics defining Archean orogenic gold deposits is given in Table 3.1. Because of the shared characteristics between the Hislop deposit and other orogenic gold deposits, results from this study may be useful in guiding inversion work, and interpreting inversion results for other Archean orogenic gold deposits in the Abitibi greenstone belt, and globally.

3.2.2. Physical Properties of rock types and alteration zones at Hislop

Petrophysical contrasts between likely mineralized, and unmineralized rocks are necessary to yield a geophysical target, and as such they must be identified and understood. One difficulty in targeting Archean orogenic gold deposits using geophysics is that, although gold itself is a conductive and dense mineral, it is usually low grade and thus does not contrast significantly enough from the host rocks to be directly detected by geophysical methods (Doyle, 1990). This means that other petrophysically distinct vectors to gold are required. At Hislop, petrophysically distinct target rocks include syenite and rhyolite dikes, carbonate-altered mafic and ultramafic volcanic rocks, and sulfide-rich zones.

Results from a physical property study on the Hislop deposit (see Chapter 2) show that gold-related syenites and porphyritic rhyolite dikes in the Hislop area have low susceptibility and density ranges distinguishing them from higher susceptibility mafic and ultramafic volcanic rocks (Fig. 3.2). Magnetic susceptibility further separates most low

Table 3.1. Characteristics of Archean orogenic gold deposits.

Age	Tectonic setting	Structural association/controls on mineralization	Host rocks/lithological associations	Hydrothermal alteration/geochemical signature	Mineralization
Examples: 2710-2670 Ma (Abitibi); 2630 Ma (Yilgarn Craton); 2670 Ma (Midlands greenstone belt, Zimbabwe Craton)	Form in extensional, compressional, and transtensional environments during deformational processes at convergent plate margins.	Spatially associated with large scale crustal structures; mainly controlled by second and third order faults that occur as splays off of the main fault zone; steeply reverse to oblique, brittle to ductile shears zones	Can form in any rock type, however, Fe-rich mafic and ultramafic volcanic supracrustal rocks, sedimentary rocks (fluvial sequences), and felsic intrusives, are common hosts in the Abitibi; gold-related faults commonly occur at contacts between contrast	Carbonate alteration muscovite/sericite alteration, silicification, and albitization; addition of CaO, CO ₂ , Fe ₂ O ₃ (carbonate alteration), SiO ₂ , K ₂ O, Ba, and Na ₂ O (muscovite alteration, silicification, albitization).	Usually hosted in throughgoing, quartz-carbonate veins, less commonly as disseminated replacement zones, or as stockwork veins.

Darbyshire et al., 1997; Fyon and Crockett, 1983; Groves et al., 1995; Groves et al., 1998; Hagemann and Cassidy, 2000; Hodgson, 1989; Hodgson, 1990; Hodgson, 1993; Hodgson and Hamilton 1990; Hodgson and MacGeehan, 1982; Hodgson and Troop, 1988; Kent et al., 1996; Kerrich, 1989; Kerrich and Cassidy, 1994; Kerrich and Wyman, 1990; Kishida and Kerrich, 1987; McCuaig and Kerrich, 1998; Meuller and Groves, 1991; Robert, 1990; Robert, 2001; Roberts, 1988; Sibson et al., 1988; Weinberg et al., 2004.

susceptibility carbonate-altered mafic and ultramafic rocks from high susceptibility, least altered precursors (Fig. 3.3).

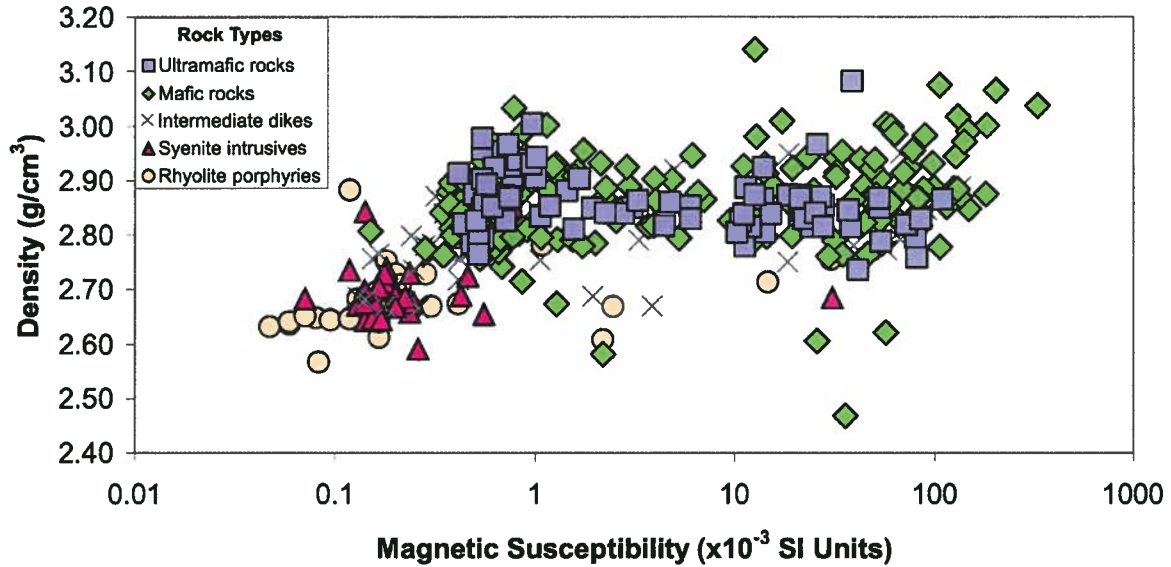


Figure 3.2. Plot of magnetic susceptibility versus density for major rock units at Hislop. Syenite intrusives and porphyritic rhyolite dikes have distinctly low density and magnetic susceptibility ranges, allowing them to be distinguished from intermediate, mafic, and ultramafic rocks at Hislop.

Electric properties, resistivity and chargeability, do not uniquely distinguish prospective rocks at Hislop (Figs. 3.4 and 3.5). There is a large overlap in resistivity values for the rock types studied at Hislop, with the only distinct resistivity range related to sheared talc-chlorite rich ultramafic rocks. These rocks, although not considered prospective, exhibit a fabric which results in lower resistivities (or higher conductivities) than other rocks in the area. Although not explicitly documented in the Hislop physical property study, it is expected that sulfide-rich areas would be conductive. Hence, conductivity ranges for sulfide-rich rocks in the synthetic models are derived from other sources documenting electric properties of rocks (Telford et al., 1990; Connell et al., 2000). As with resistivity, specific chargeability ranges do not characterize the individual

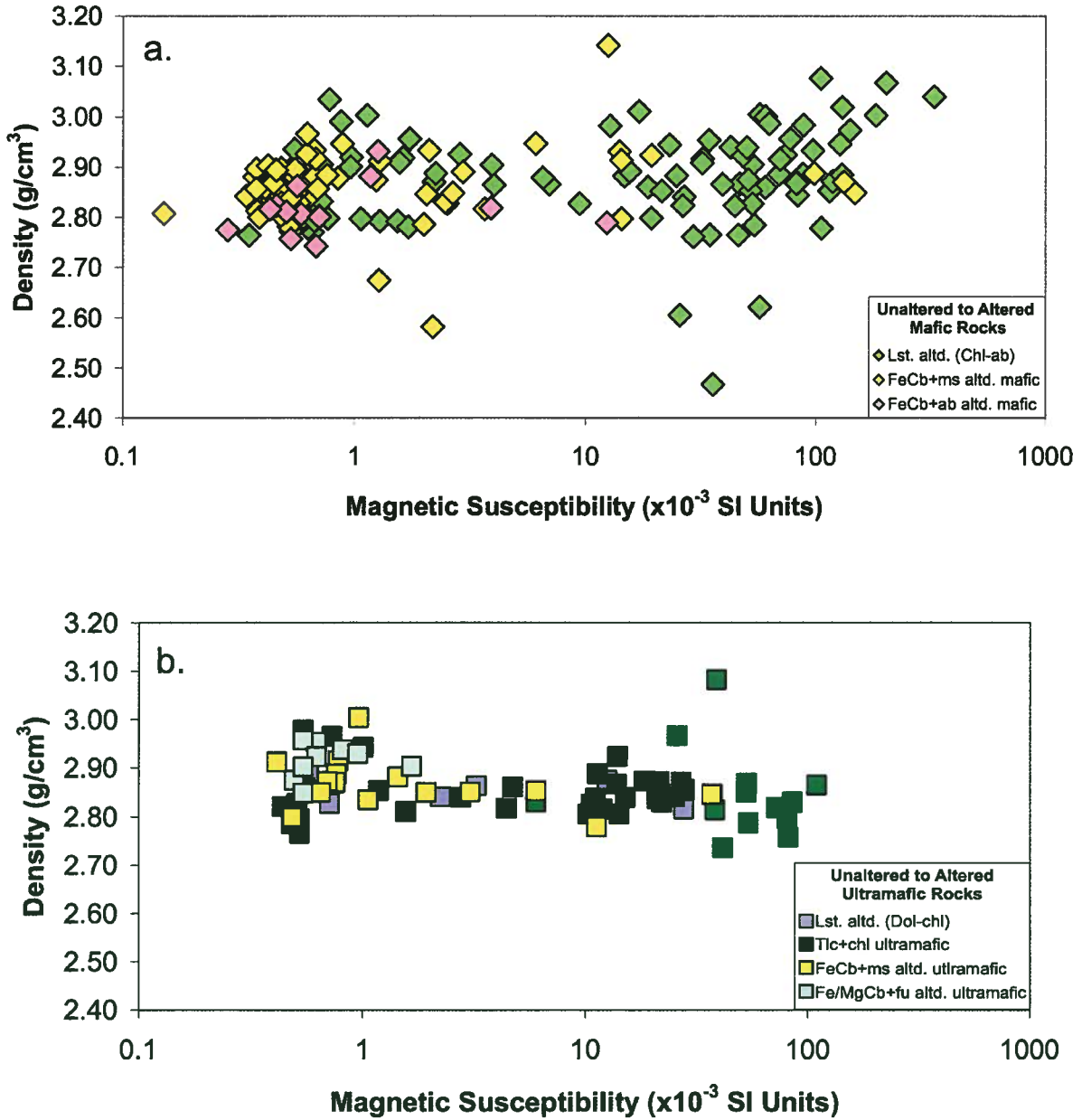


Figure 3.3. Plot of magnetic susceptibility versus density for variably altered mafic volcanic rocks, and variably altered ultramafic volcanic rocks from Hislop. Carbonate-rich alteration (pink and yellow diamonds, and pale green and yellow squares) destroys magnetite in mafic and ultramafic volcanic rocks, causing magnetic susceptibility to drop. Abbreviations in legends: Lst. altd. = least altered assemblage; Chl+ab = chlorite+albite assemblage; FeCb+ms = Fe-carbonate+muscovite; FeCb+ab = Fe-carbonate+albite; Dol+chl = dolomite+chlorite assemblage; Tlc+chl = talc+chlorite; Fe/MgCb+fu = Fe/Mg-carbonate+fuchsite (chrome-muscovite).

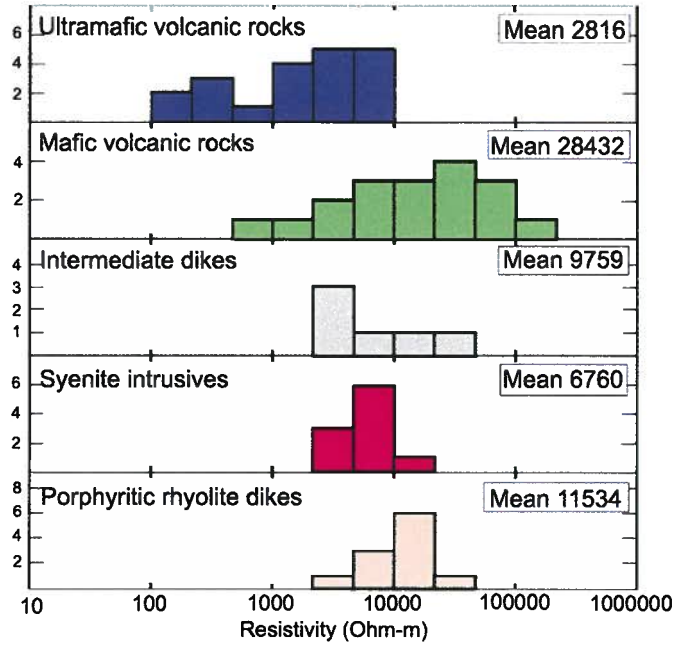


Figure 3.4. Resistivity histograms for Hislop deposit rocks. Data indicates lower overall resistivities for ultramafic volcanic rocks from Hislop.

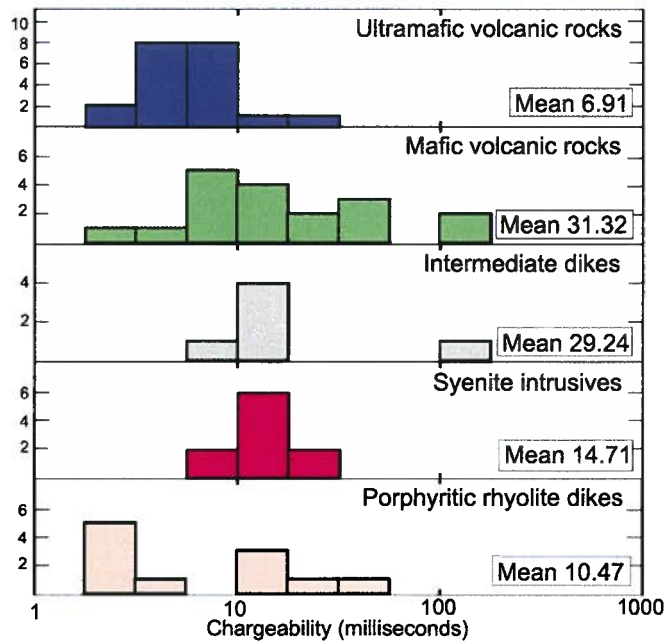


Figure 3.5. Chargeability histograms for Hislop deposit rocks. Chargeability ranges for the individual rock types overlap and are not unique.

prospective rock types at Hislop, and in general, all rocks have low background values of chargeability consistent with published values (Chapter 2). However, values are expected to be high where the rock contains anomalous sulfide abundances (Telford et al., 1990). In the synthetic models, sulfide zones are given values corresponding with the highest chargeabilities found at Hislop, and values published in Telford et al. (1990). Chargeability values referenced from the Hislop physical property study were divided by 1000 to yield values that correspond to the unitless 0-1 chargeability values that are output from induced polarization inversions.

Physical property values used in the synthetic models are given in Table 3.2. It is important to note that gravity inversions produce density contrast models, thus, to build the starting models, density contrasts were used. For this study, the density contrast of each rock type is the difference between the rock's density, and the average density value for all the major rock types (2.81 g/cm^3). Density values are presented as both densities and density contrasts in Table 3.2. Note also that conductivities are used in the starting models for DC resistivity work, and that conductivity models are the product of DC resistivity inversions. Conductivity can be converted to resistivity by taking the reciprocal.

3.2.3. General forward modeling and inversion background

This research employs forward modeling and inversion codes from the University of British Columbia Geophysical Inversion Facility (UBC-GIF). This section provides a brief overview of these applications. Further details are found in Li and Oldenburg (1996, 1998, and 2000).

Forward modeling is essentially a tool for hypothesis testing. Subsurface physical property models are devised, a geophysical survey is simulated over the top of the model, and data are collected. The value of the data collected at each survey point are related to the location of the source in the subsurface, its physical properties, and the strength of the

inducing field in the cases of magnetic, electromagnetic, DC resistivity, and induced polarization methods.

Table 3.2. Physical property values used in synthetic modeling.

Rock Type	Susceptibility (SI Units)	Density (g/cm ³)/ Density contrast (g/cm ³)	Conductivity (S/m)	Chargeability (ms)
Syenite/rhyolite dike	0.00025	2.7/-0.11	1.80E-04	0.016
Mafic volcanic rock	0.032	2.88/+0.07	1.50E-04	0.016
Ultramafic volcanic rock	0.0096	2.85/+0.04	2.27E-03	0.016
Carbonate altered ultramafic/mafic volcanic rock (for comparison)	0.00083	2.82/+0.01	3.20E-04	0.016
Moderately sulfide-rich rock			1.40E-02	0.16
Sulfide-rich rock			3.00E-02	0.3
Source	From Chapter 1 - (Hislop deposit physical property study)	From Chapter 1	Chapter 1; Sulfide rich rock values from Telford et al., 1990, and Connell et al., 2000	Chapter 1 - Anomalous chargeabilities from highest chargeability samples from Hislop study

Anomalous low and high values are highlighted by blue and red borders, respectively

Geophysical inversion involves calculation of the subsurface physical property distribution from collected geophysical data. Subsurface physical properties are calculated based on the known physical relationships between sources and measurement locations at the Earth's surface. Unlike forward modeling, the solution is non-unique. There are far more unknowns than there are data, and thus there are an infinite number of solutions. To reduce the number of possible solutions, a model objective function is defined. For default inversions the model objective function specifies that the model is required to be close to a background value, referred to as the reference model, and has to be smoothly varying in all directions. With increased knowledge of geology or physical

properties, the degree of closeness to the reference model can be manipulated, and the smoothing in the x, y, and z directions can be increased or reduced, by adjusting weightings within the model objective function. In addition to the model objective function, a data misfit is defined. The data calculated by forward modeling the inversion result must be sufficiently close to the observed data. The misfit and model objective function, respectively, are written:

$$\phi_d(m) = \sum_{i=1}^N \left(\frac{d_i^{obs} - d_i^{pred}}{\varepsilon_i} \right)^2$$

$$\begin{aligned} \phi_m = \alpha_s \int (m - m_0)^2 dx + \alpha_x \left(\frac{d}{dx} (m - m_0) \right)^2 dx \\ + \alpha_y \left(\frac{d}{dy} (m - m_0) \right)^2 dy \\ + \alpha_z \left(\frac{d}{dz} (m - m_0) \right)^2 dz \end{aligned}$$

where N is the number of geophysical data, d_i^{obs} is the observed data at location i , d_i^{pred} is the predicted data at location i , and ε_i is the standard deviation. α_s is the alpha weighting determining the degree of closeness to the reference model, α_x , α_y , and α_z determines smoothing in the x, y, and z directions, respectively, m is the model, and m_0 is the reference model.

3.3. METHODS

The 3D ‘Hislop-like’ geologic model shown in Figure 3.6a was converted to the four initial physical property models (Figs. 3.6b-3.6d), based on values in Table 3.2. Physical property models were created using the University of British Columbia

Geophysical Inversion Facility's (UBC-GIF) Meshtools3D program. Relative dimensions and scales of geologic features in these models are similar to those at Hislop. Unconstrained, geophysical inversions were completed using synthetic magnetic, gravity, DC resistivity, and induced polarization (IP) data generated from forward modeling magnetic susceptibility, density, conductivity, and chargeability models, respectively. Table 3.3 summarizes synthetic survey parameters used, and Table 3.4 summarizes inversion parameters. Observed data 'collected' over the starting physical property model, and predicted data generated from forward modeling the inversion result, are compared after each inversion to determine if results are acceptable. Observed and predicted data, and achieved misfit values are found in Appendix 3A.

Magnetic and gravity inversions are investigated first. Based on physical property work, this data is expected to be useful in distinguishing prospective low susceptibility and low density syenite dikes. The synthetic susceptibility model (Fig. 3.6b) depicts a narrow vertical low susceptibility dike located between higher susceptibility mafic and ultramafic rocks. The density model (Fig. 3.6c) consists of a low density dike within higher density mafic and ultramafic rocks. For susceptibility analysis, the dike might also act to represent a low-susceptibility, strongly carbonate altered zone, along a fault between two higher susceptibility units.

DC resistivity and IP methods are investigated for their ability to locate conductive and chargeable sulfides in the subsurface. These synthetic starting models have six sulfide-rich zones extending vertically to depth at the ultramafic rock-syenite dike contact (Figs. 3.6d and 3.6e). Additionally the conductivity models contain a talc+chlorite-rich ultramafic schist, incorporated to determine the effect of its unique range of conductivity values (Fig. 3.6d). DC resistivity and IP data were collected using a Realsection electrode array, the configuration used in the collection of actual DC resistivity and IP data over the Hislop deposit in 1996 for exploration purposes. This type of electrode array employs widely spaced transmitter electrodes placed at a distance outboard of closely spaced receiver electrodes to collect data easily and quickly over

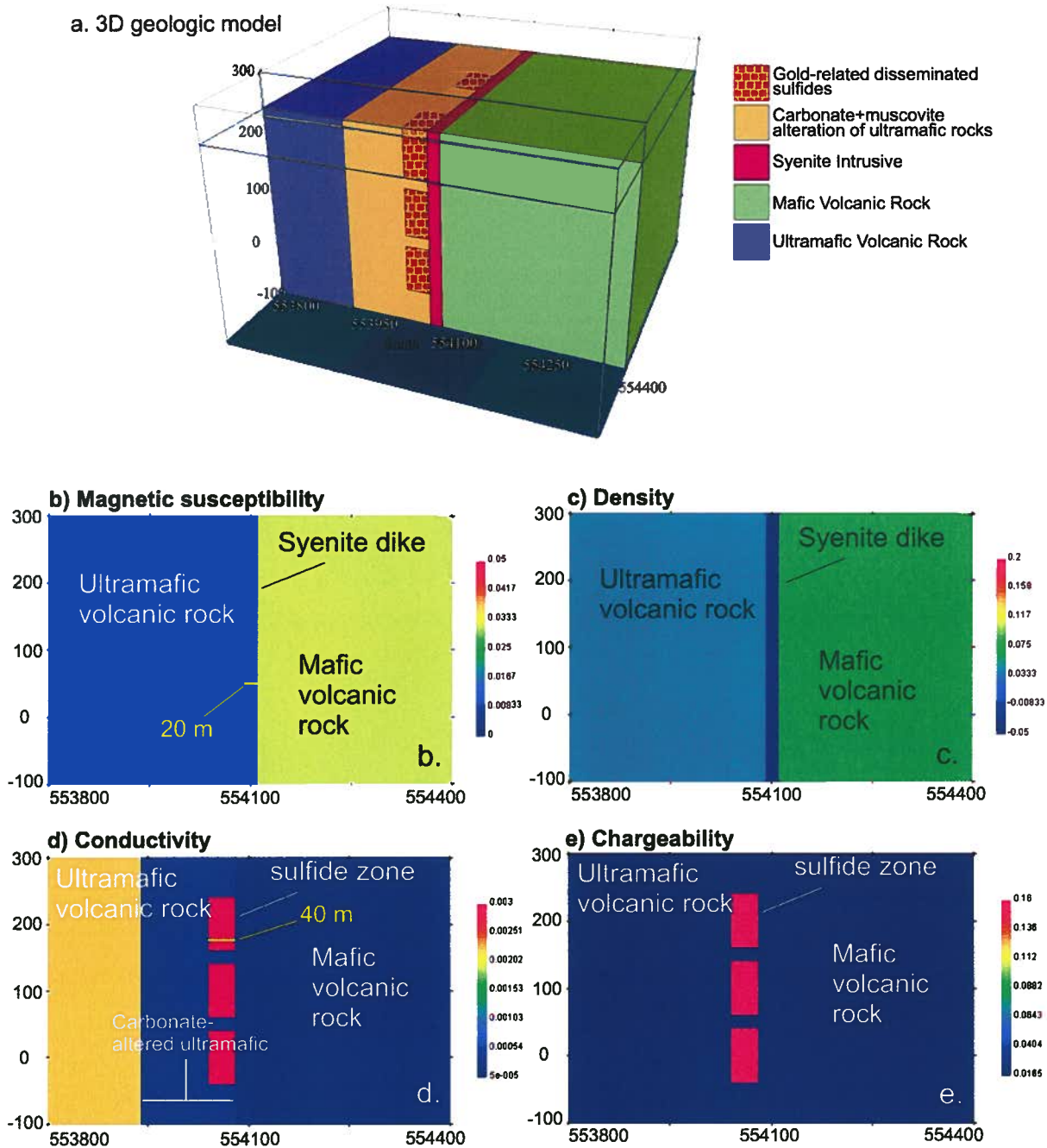


Figure 3.6. a) 3D geological model based on the geologic setting of the Hislop gold deposit. b-e) North-facing cross-sections through 3D physical property models generated from the geologic model: b) magnetic susceptibility model, c) density model, d) conductivity model, e) chargeability model. Susceptibility and density modeling tests detectability of the syenite dike (the alteration zone is not considered here - syenite detection is focused on). Resistivity and chargeability modeling tests detectability of sulfide-rich zones, and low resistivity talc-chlorite dominated ultramafic rocks (carbonate alteration zone is included here).

Table 3.3. Synthetic survey parameters.

Model	Data area (UTM)	Lines	Line spacing	Station Spacing	Height	# Data	Data errors	Other information
Magnetics	x: 553800 - 554400 y: 5373000 - 5373600	E-W	50 m	10 m	320 m	793	5%; 5% floor	Inclination: 75°; Declination: -12°; Strength: 57478 nT
Gravity	x: 553800 - 554400 y: 5373000 - 5373600	E-W	50 m	10 m	320 m	793	0.01 mGal floor	
DC Resistivity	x: 552800 - 555400 y: 5373000 - 5373600	E-W	100 m	20 m	300 m (ground)	2485	5%	Realsection survey - 5 Tx spacings: 1000 m, 1500 m, 2000 m, 2400 m, 3200 m
IP	x: 552800 - 555400 y: 5373000 - 5373600	E-W	100 m	20 m	300 m (ground)	2485	15%	Realsection survey - 5 Tx spacings: 1000 m, 1500 m, 2000 m, 2400 m, 3200 m

Table 3.4. Synthetic inversion parameters.

Inversion	# Data	Inversion core extents (UTM)	# Core cells	Core cell size	# Padding cells	Other
Magnetic	793	x: 553800 - 554400 y: 5373000 - 5373600 z: 300 - (-)100	144000	10 m ³	8000	
Density	793	x: 553800 - 554400 y: 5373000 - 5373600 z: 300 - (-)100	144000	10 m ³	8000	
DC Resistivity	2485	x: 553800 - 554400 y: 5373000 - 5373600 z: 300 - (-)100	18000	20 m ³	30976	Near-surface cell weightings applied to reduce electrode noise
IP	2485	x: 553800 - 554400 y: 5373000 - 5373600 z: 300 - (-)100	18000	20 m ³	30976	Near-surface cell weightings applied to reduce electrode noise

large areas. Surface weighting files were used in the DC resistivity and IP inversion calculations in an attempt to subdue the tendency for high conductivity and chargeability values to accumulate at electrode locations (DCIP3D user manual, Version 2.1).

After testing the four initial ‘Hislop-like’ models from Figure 3.6, the geometry of prospective features, and physical property contrasts between target and host rocks, are manipulated to explore the range of results. Inconsistencies between all true models and recovered models are identified and the cause of these discrepancies is assessed. For select cases, attempts are made to further minimize differences between true and recovered models by applying basic constraints based on prior physical property knowledge. These ‘non-located’ constraints (Phillips et al., 2007) are globally applied by adjusting the model objective function, the inversion function defining the type of model desired (e.g. a smooth model, a model close to a reference model; Li and Oldenburg, 1996).

For this work, the difference between recovered and true models was calculated to compare the closeness of the recovered model to the true model, and to determine if a resulting model has improved with constraints applied. The sum of the differences in physical property values between each pair of equivalent cells from two identically sized models is calculated:

$$\text{Model difference} = \sum_{i=1}^N |m_i - m_i'|,$$

where N = the number of data, m_i = the physical property value of the i^{th} cell in the true model, and m_i' = the physical property value of the equivalent cell in the recovered inversion model. This value gives a global relative measure of difference between the models. Since physical properties related to the different geophysical methods have different characteristic numerical ranges, model difference values might be much smaller for the results of one method versus another. Thus, calculated values can only be

compared between models generated by the same geophysical method. Model differences for all results are given in Table 3.5.

Table 3.5. Model differences calculated between recovered and true models (the lowest model differences for each geophysical method are highlighted with bold text).

Model	Model Difference
Magnetic susceptibility	
20 m syenite between mafic and ultramafic rocks	1781.7
60 m syenite between mafic and ultramafic rocks	1656.9
60 m syenite, buried	1818.8
20 m syenite in mafic volcanic rocks	2396.4
20 m syenite in ultramafic volcanic rocks	721.5
constrained, reference model 0.03 SI Units	1232.4
constrained, upper bounds 0.035 SI Units	906.0
constrained, alpha y and z increased (100)	1644.3
constrained, alpha y and z increased, bounds 0.035	904.5
depth weighting decreased (β and z_0 decreased by 1/4)	705.4
depth weighting decreased, and upper bounds set at 0.035	701.8
Density	
20 m syenite between mafic and ultramafic rocks	4561.7
60 m syenite between mafic and ultramafic rocks	4702.0
60 m syenite, buried	5355.3
20 m syenite in mafic volcanic rocks	5613.3
20 m syenite in ultramafic volcanic rocks	3441.0
Conductivity	
40 m sulfide-rich zones near ultramafic - syenite contact	158.4
40 m sulfide-rich zones - higher conductivity (0.03 S/m)	161.0
40 m sulfide-rich zones - laterally extensive zone	312.1
40 m sulfide-rich zones - one anomalous zone, no sheared ultramafic	160.8
40 m sulfide-rich zones - constrained, reference model 0.001 S/m	173.3
40 m sulfide-rich zones - constrained, alpha y and z increased relative to x	154.4
40 m sulfide-rich zones - constrained, reference model 0.001, alpha y and z increased relative to x	132.6
Dipole-Dipole survey	198.8
Chargeability	
40 m sulfide-rich zones near ultramafic - syenite contact	1632.8
40 m sulfide-rich zones - higher chargeability (0.3 ms)	1742.4
40 m sulfide-rich zones - laterally extensive zone	3362.9

3.4. SYNTHETIC MODELING RESULTS

3.4.1. Potential fields modeling

Magnetic susceptibility models

Hislop-like model: 20 m syenite dike hosted between mafic and ultramafic volcanic units

The contact between the mafic volcanic unit in the east and the central syenite dike is well-resolved to depth by magnetic inversion (Fig. 3.7). In contrast, the contact between the ultramafic volcanic rock in the west and the syenite is essentially unresolved, and as such, the low susceptibility syenite dike is not imaged. Susceptibility values greater than 0.05 SI Units are attained within the area known to be occupied by the high susceptibility mafic volcanic unit. These susceptibilities are over-estimated compared to the known susceptibility of 0.032 SI Units for these rocks. Susceptibilities are underestimated where the ultramafic volcanic unit is present, assuming values close to 0 SI Units compared to true susceptibilities of 0.0096 SI Units. Near the surface, there appears to a low susceptibility 'overburden', where surface cell susceptibility values drop to 0 SI Units.

Varying geometry

Two geometrical variations on the previous model were tested. These new models encompass a syenite dike of greater width, and a buried syenite dike. A 60 m wide syenite dike is resolved near the surface in its correct location, down to about 150 m (Fig. 3.8a). The contact between the syenite and both mafic volcanic and ultramafic volcanic units are detected. With depth however, the geologic contacts are no longer well-constrained. The buried syenite dike inversion result was comparable to the result for the 20 m dike model with the mafic volcanic unit-syenite dike contact being well-imaged to depth (Fig. 3.8b). Again, the ultramafic rock-syenite dike contact is poorly detected and

the syenite is not fully resolved. For the geometrically varied models, problems with over- and underestimation of susceptibility persist.

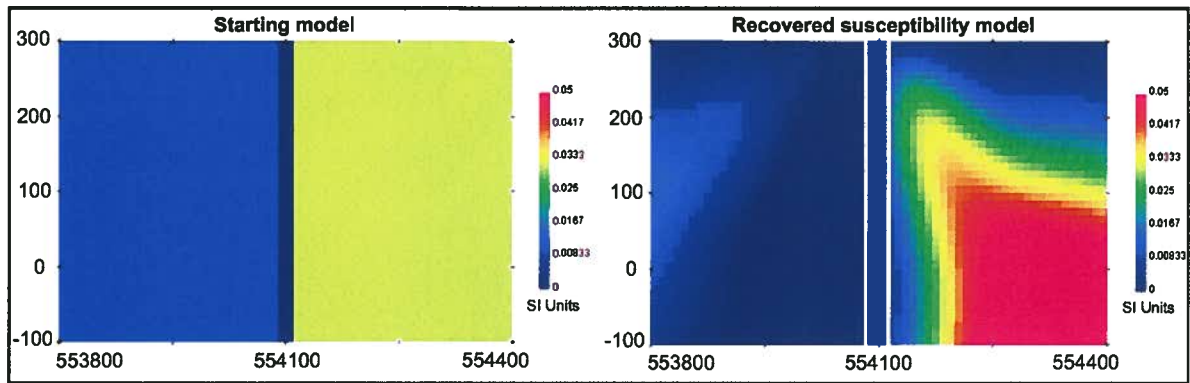


Figure 3.7. Starting model and unconstrained magnetic inversion result for the ‘Hislop-like’ magnetic susceptibility model. Results are shown at the same susceptibility scale as the starting model. The contact between the mafic volcanic unit and the syenite is detected to depth, whereas the contact between the syenite and the ultramafic unit is undetected. Susceptibility values in association with the mafic volcanic rock unit in the recovered susceptibility model are overestimated (>0.05 SI Units, compared to ~ 0.03 SI Units in true model).

Varying physical property contrasts

Two additional models are tested to explore the effect of varying the susceptibility contrast between the target rocks – the syenite dike – and the host rocks. The 20 m syenite dike is first modeled within a mafic volcanic host, and then within an ultramafic volcanic host rock.

Geophysical inversion over a syenite dike hosted in high susceptibility mafic volcanic rocks successfully locates a narrow vertical low susceptibility zone near surface, and down to approximately 350 m depth (Fig. 3.9a). As in previous results, the central low susceptibility zone smooths outward with depth in the model. The low susceptibility values within surface cells persist, and susceptibility values assigned to areas

corresponding with the location of mafic volcanic rocks are overestimated, especially at depth.

The host rock to the syenite dike is next changed from relatively high susceptibility mafic volcanic rock, to a relatively moderate susceptibility ultramafic volcanic rock to investigate resulting inversions. Results indicate the presence of a low susceptibility zone down to 250 m (Fig. 3.9b). In general, although there is a higher contrast between mafic volcanic rocks and syenite, the inversion results for the syenite dike hosted within ultramafic rocks has recovered values more consistent with the true model susceptibility values (see model difference values in Table 3.5).

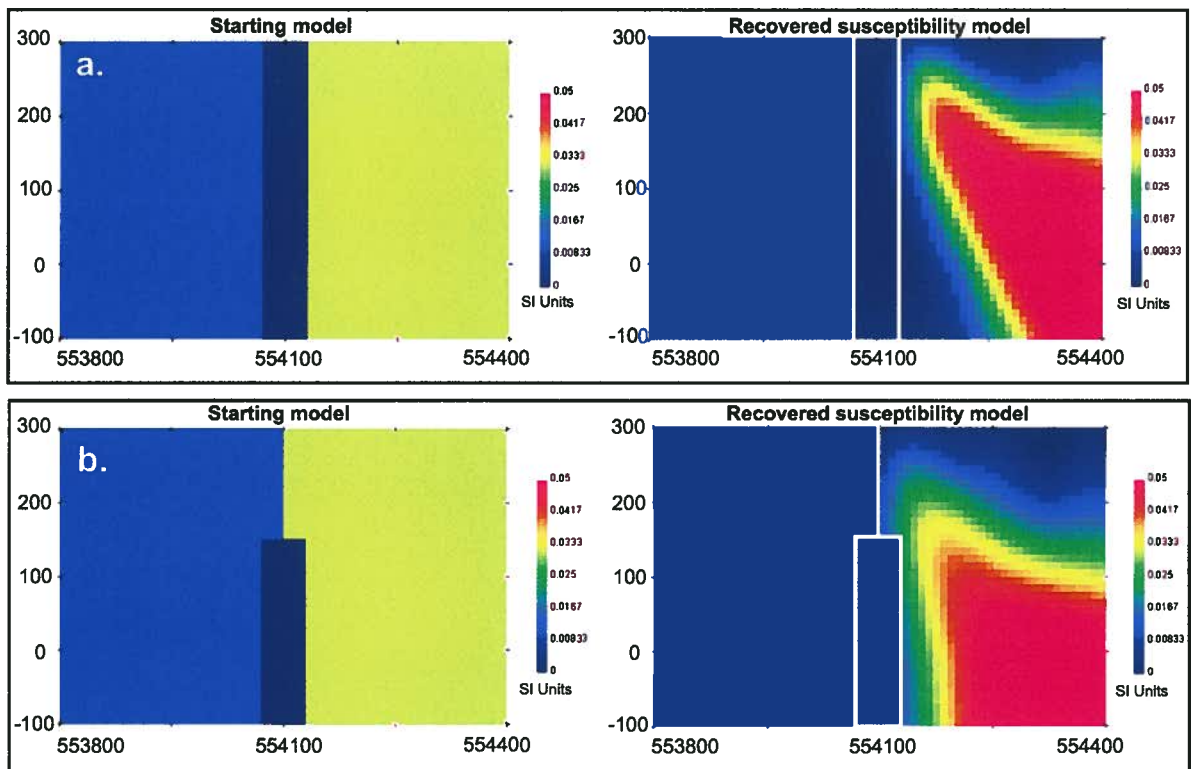


Figure 3.8. Starting models and magnetic inversion results with changes made to geometry of the target body. a) Result for the 60 m syenite hosted by mafic and ultramafic rocks. The location of the syenite is well-imaged near-surface. b) Result for the buried 60 m syenite. The syenite dike is undetected, and the result similar to the initial 'Hislop-like' susceptibility model.

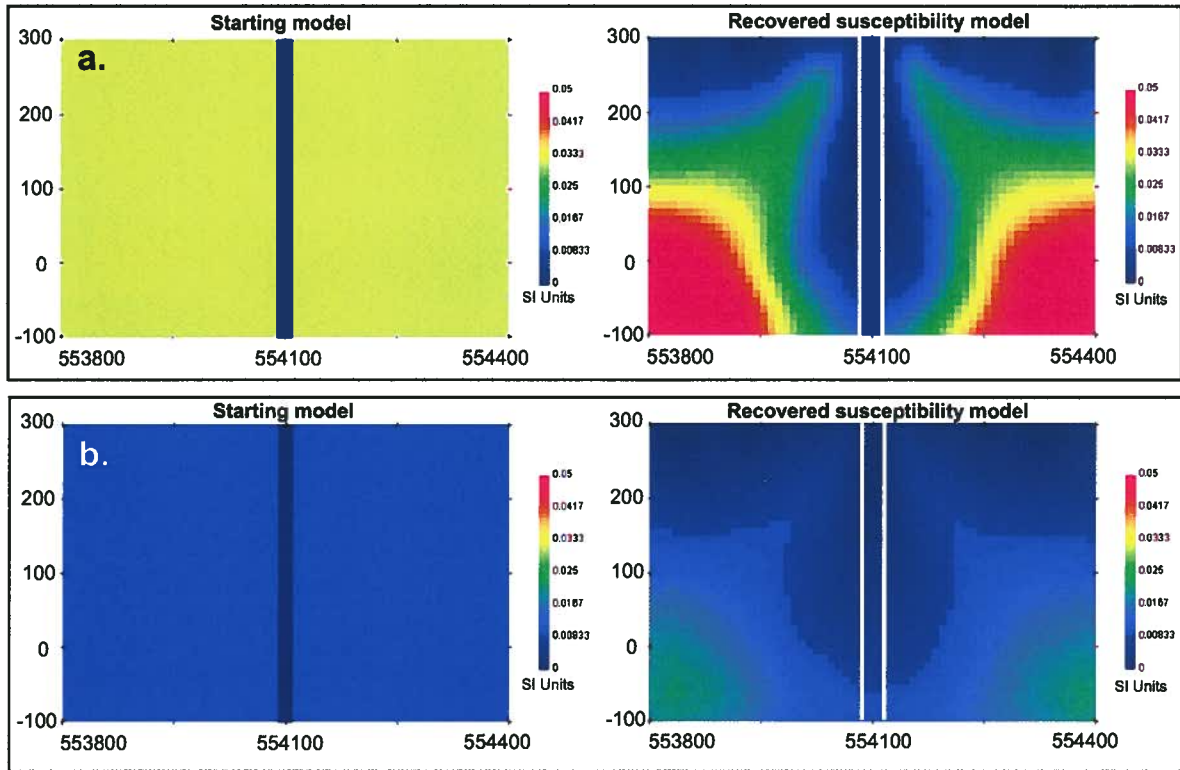


Figure 3.9. Magnetic inversion results for starting models with different physical property contrasts between the target and host rocks. a) Result for the 20 m syenite dike hosted within high susceptibility mafic volcanic rocks. The narrow syenite is detected to depth. Susceptibility values for mafic volcanic rocks are overestimated. b) Result for the 20 m syenite dike hosted in moderately susceptible ultramafic volcanic rocks. Again the syenite is detected to depth. The susceptibility scale is kept the same for all models for comparison – however the features in the recovered model in Figure 3.9b would be better visualized with the scale set to have a lower maximum value.

Density models

Hislop-like model: 20 m syenite dike hosted between mafic and ultramafic volcanic units

The starting Hislop-like density model differs from the susceptibility model in that the ultramafic and mafic volcanic host rocks have similarly high densities, and contrast nearly equally with the low density 20 m syenite, compared to the variable susceptibility contrast between the syenite and rock units on either side in susceptibility models. The gravity inversion result reveals the low density syenite and indicates its extent down to about 200 m depth (Fig. 3.10). The body terminates beyond this as the model becomes smooth. The slightly smaller density contrast between the ultramafic volcanic rock and the syenite, compared to the mafic volcanic rock and the syenite, is apparent in the marginally weaker detection of the western contact of the syenite. In general density values are well-estimated throughout the central region of the model. However, as with magnetic inversion results, there is some overestimation at depth with estimated density contrasts for mafic volcanic rocks of approximately 0.117 g/cm^3 versus known values of 0.07 g/cm^3 .

Varying geometry

The eastern contact between the syenite dike and adjacent mafic volcanic rock is better resolved to depth where the syenite width is increased to 60 m, with the central low density zone now being imaged to approximately 300 m (Fig. 3.11a).

Where the 20 m syenite is buried deeper (Fig 3.11b), the low density body is essentially unresolved by gravity inversion. It is apparent that there is some decrease in density from east to west across the model, but distinct geological units are not obvious. Despite this, density values are still relatively well-estimated throughout the central part of the model.

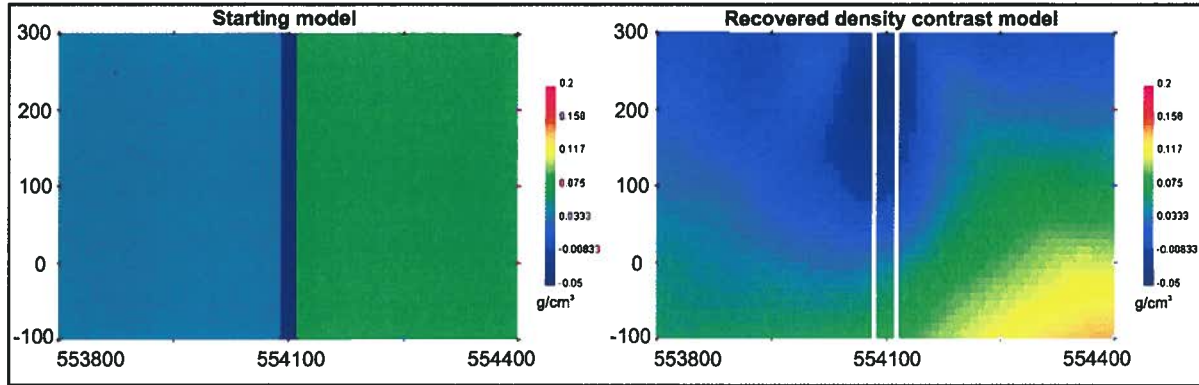


Figure 3.10. Starting model and unconstrained gravity inversion result for the 'Hislop-like' density contrast model. The contact between the mafic volcanic unit and the syenite is better located than the contact between the ultramafic unit and the syenite. Density contrasts are reasonably estimated throughout the central parts of the recovered model.

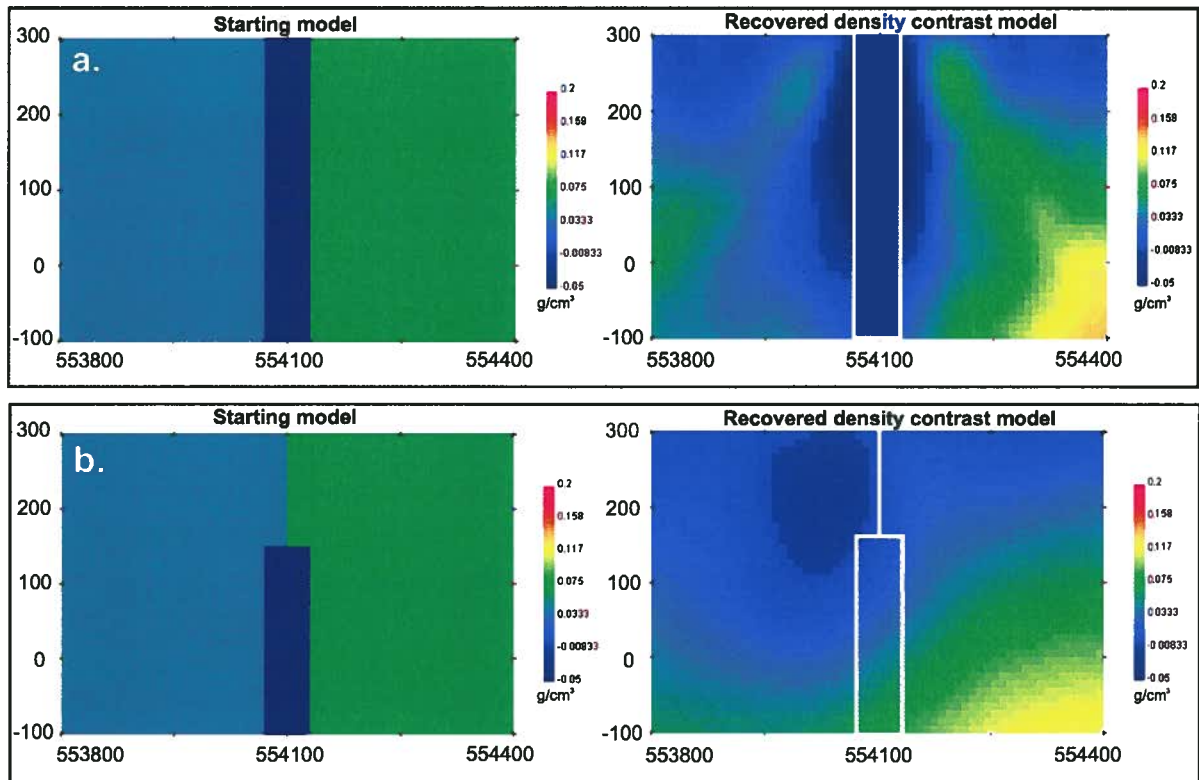


Figure 3.11. Gravity inversion results with changes made to geometry of the target body. a) Result for the 60 m syenite hosted by mafic and ultramafic rocks. The syenite is well-imaged to depth. b) Result for the buried 60 m syenite. The syenite dike is essentially undetected, however an overall change in density from east to west is detected by the inversion, with the contact between mafic and ultramafic rocks being detected near-surface.

Varying physical property contrasts

As the two host rocks in the Hislop-like model are characterized by similar density values, the results of the single-host inversions (Figs. 3.12a and 3.12b) are not dramatically different from the two-host results. Where either mafic volcanic rocks or ultramafic volcanic rocks are the sole host for a syenite dike, the inversion is capable of imaging the low density syenite to depths ranging from 150-200 m. These depths are slightly less than the depths resolved in the susceptibility inversion results for the single-host scenario. The density model becomes smoother with depth.

Discussion of potential fields inversion modeling results

Magnetics

The presence of a 20 m syenite dike hosted between an ultramafic, and a mafic volcanic unit is not obvious in synthetic magnetic inversion results. The inversion only detects an overall gradient here between the lower and higher susceptibility areas. The narrow dike is more successfully imaged between the two different hosts when it has a slightly greater width, or when it is hosted by a single high susceptibility rock type.

The most significant differences between the recovered and true magnetic susceptibility models include 1) smoothing across known contacts, especially across contacts where there is a low susceptibility contrast (such as the contact between the syenite dike and the ultramafic volcanic rock), 2) smoothing with depth, and 3) incorrect estimation of susceptibilities through the model, which generally yields higher maximum susceptibility values than in the true model. The third item encompasses the issue of low susceptibility values being incorrectly assumed near surface.

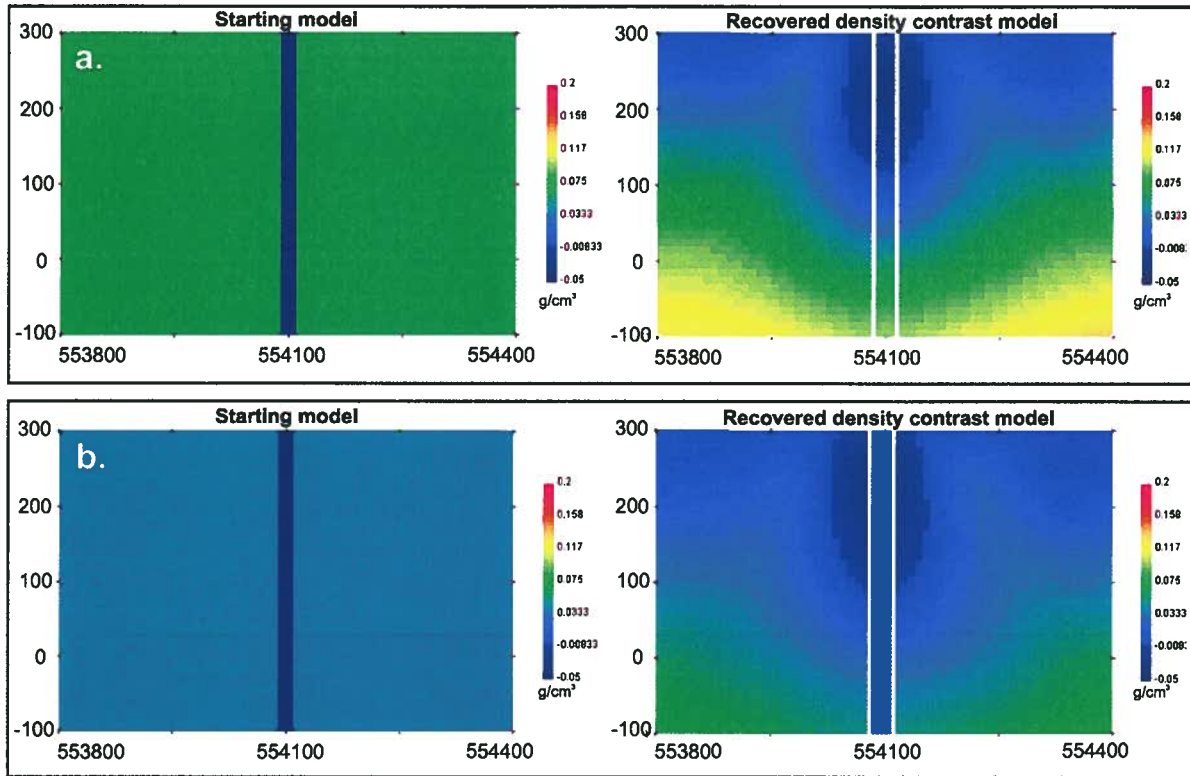


Figure 3.12. Inversion results with different physical property contrasts between the target and host rocks. a) Result for the 20 m syenite dike hosted within higher density mafic volcanic rocks. The narrow syenite is detected down to about 200 m depth. b) Result for the 20 m syenite dike hosted in ultramafic volcanic rocks. There is a marginally deeper detection of the syenite.

Most of the smoothing within the model is a byproduct of the inversion algorithm and choice of model norm. The model objective function for linear potential fields inversions is written such that a smooth, simple model result is calculated. This is facilitated using a L_2 norm calculation which minimizes structure over the volume (Li and Oldenburg, 1996). A smooth model, in the case where there is little prior information about the subsurface, would be desired over a more structured and complicated model. Smoothing at depth is related to the $1/r^3$ decay of the magnetic signature with depth in the subsurface, and the inversion cannot resolve features deeper than the sources that have influenced the magnetic data collected.

Poor susceptibility estimation in near-surface cells may be related to depth weightings. A default depth weighting is written into all potential field inversion calculations (Li and Oldenburg, 1996 and 1998). As there is no inherent depth resolution in potential fields data, when an unweighted inversion is carried out, all susceptibility will occur at the surface as it is the simplest solution explaining the observed data (Li and Oldenburg, 1996 and 1998). Although depth weighting is necessary to offset this, the surface cells appear to be less sensitive, and tend to assume reference model values, which for default inversions is 0 SI Units. The generally overestimated susceptibility values for the model as a whole may also be explained by the depth weighting. To compensate for the lack of susceptibility at the surface, it is necessary for the inversion to place high susceptibility values at depth and increase their overall magnitude, in order to fit the observed magnetic data.

Gravity

The essentially equal contrast between higher density mafic volcanic rocks and ultramafic volcanic rocks, and the lower density syenite, allows for consistent detection of the narrow syenite dike, unless it is buried.

Gravity inversions follow similar calculations as magnetic inversions, with the main difference being only the forward model solution - the physical relationships between subsurface sources and data observations. Thus explanations for discrepancies between true and recovered density models are similar to those for magnetic susceptibility models. As with magnetic inversions, the significant discrepancies are related to smoothing and depth resolution. Smoothing can be related to the choice of model norm used in the inversion algorithm, and decreasing resolution with depth is explained by the known $1/r^2$ decay of the gravity signal with depth. Contacts are not resolved as deep as they are with magnetic inversions. Relative density contrasts versus magnetic susceptibility contrasts might cause the depth detection to be inconsistent between the magnetic and gravity inversion results (i.e. the contrast between low

susceptibility syenite and high susceptibility mafic volcanic rocks is greater than the density contrast between the two rocks). The tendency of the near-surface cells to assume values near 0 g/cm^3 , the reference model value, likely necessitates having overestimated densities at depth.

Combining magnetic and gravity inversion results would better detect the syenite where it is not resolved in the two-host model by magnetic inversions alone. The density result would better locate the ultramafic-syenite contact, and the magnetic inversion result would contribute by providing better depth information.

3.4.2. DC resistivity and induced polarization modeling

Synthetic conductivity and chargeability models are likely less representative of true subsurface geology than susceptibility and density models. Rock type and associated mineralogy strongly influence magnetic susceptibility and density values (Chapter 2) and thus using geology to create starting physical property models is easily justified. Although rock type can play a role in determining conductivity and chargeability values and distribution, these physical properties are more strongly controlled by rock texture, permeability, and the presence of fluids (Telford et al., 1990). Thus it must be kept in mind that in nature, more complicated conductivity and chargeability distributions likely exist than can be represented by the synthetic models.

Resistivity Models

Hislop-like model: 40 m wide sulfide rich zones near ultramafic rock-syenite dike contact

Six high conductivity zones (only three visible on cross-section) within significantly lower conductivity host rocks, but proximal to a moderately high conductivity, sheared ultramafic volcanic unit were not resolved through DC resistivity

inversion (Fig. 3.13). The moderately high conductivity ultramafic rocks, however, were imaged, but only to a depth of approximately 200 m. The recovered conductivity anomaly associated with the ultramafic unit extends faintly toward the general location of the high conductivity sulfide-rich zones. Overall, recovered conductivity values for low conductivity areas are close to true values, however conductivities associated with the sheared ultramafic unit, and obviously those associated with the anomalous conductivity zone, are underestimated.

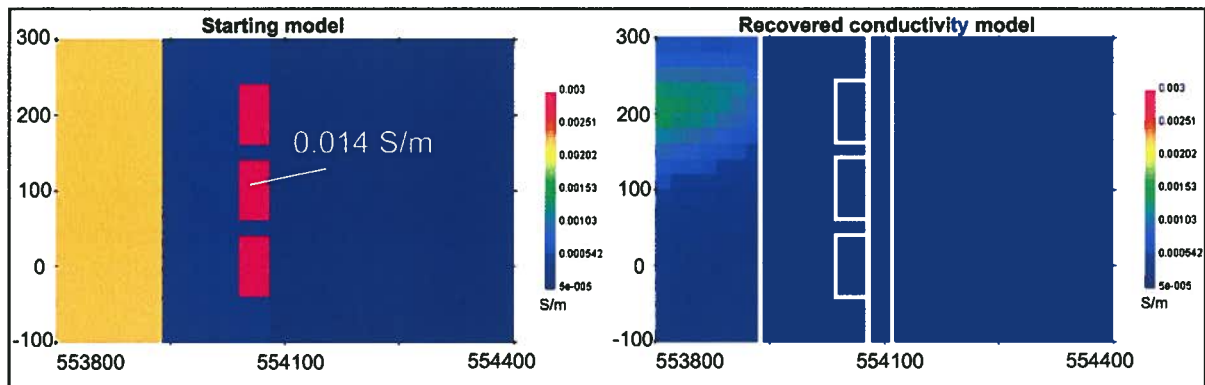


Figure 3.13. Starting model and unconstrained DC resistivity inversion result (conductivity model) for the ‘Hislop-like’ conductivity model. The sulfide-rich high conductivity zones are undetected. The moderately conductive sheared talc-chlorite rich ultramafic rock is detected near-surface, and resolved only to about 200 m depth.

Varying physical property contrasts and geometry

Doubling the conductivity for the discrete sulfide zone model so as to represent a more sulfide-rich rock (Table 3.2), does not improve the recovery of the sulfide rich zones, as they remain undetected (Fig. 3.14a). Since raising the conductivity values of the sulfide zones was ineffective, the high conductivity zone was modified to be a continuous zone extending from north to south and vertically to depth to test whether a more extensive feature might lead to a better recovery (Fig 3.14b). Although the zone is now persistent and reaches the surface, no longer consisting of discrete small zones at depth, it remains undetected by inversion of DC resistivity data. As with the discrete sulfide zone model, a conductivity high is detected in association with the sheared ultramafic unit, and

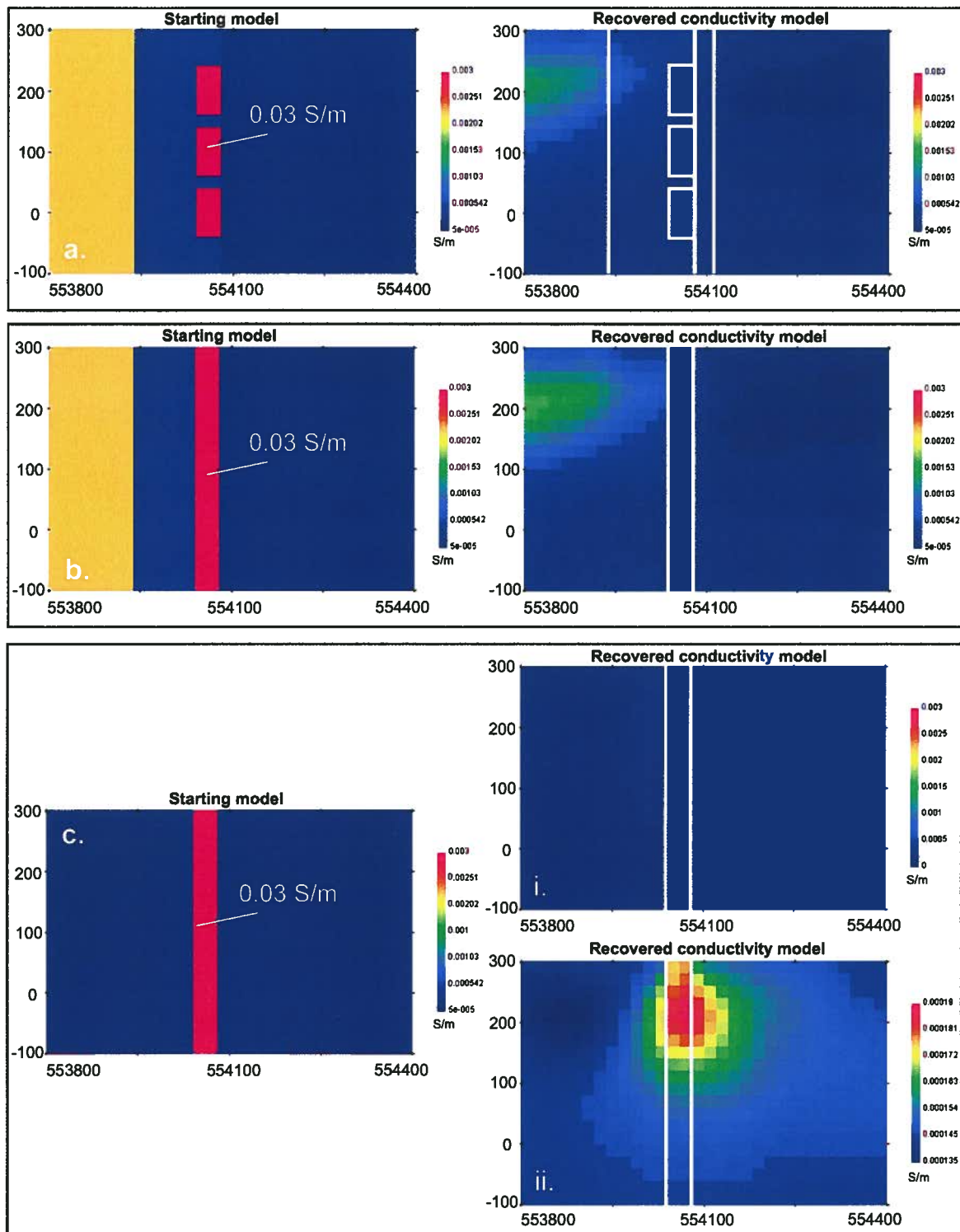


Figure 3.14. DC resistivity inversion results (conductivity models) with changes made to physical property contrasts, and to the geometry of the target body. a) Conductivities are doubled for the sulfide-rich zones, but the targets remain undetected. b) The target is made to be continuous. There is a weak indication of the conductive zone. c) All host rocks are given the same low conductivity background value. Comparing the result at the same scale, (i), the target is essentially undetected. Adjusting the scale (ii) reveals a conductive body, but with highly underestimated associated conductivities.

this zone extends laterally out toward the continuous sulfide zone, marginally more so than in the previous results.

The moderately conductive ultramafic unit was removed, and all other units, aside from the sulfide-rich zone, were assigned a low conductivity value representing mafic volcanic rocks, to test a single continuous high conductivity zone in a low conductivity background (Fig. 3.14c). Comparing the results to the true model at the same conductivity scales, demonstrates there is essentially a complete lack of resolution of the target feature. When the scale is adjusted to encompass the true recovered maximum and minimum values, the feature is revealed. The recovered body is correctly located near the surface, but extends only about 150 m depth. The values coinciding with the high conductivity zone however, are very low and near background values, and would not be considered of an anomalous nature.

Chargeability Models

Hislop-like model: 40 m wide sulfide rich zones near ultramafic-syenite contact

Six sulfide-rich zones (only three visible in the cross-section) are assigned anomalous chargeability values. The anomalous values (Table 3.2) are chosen based on the highest chargeabilities measured from the Hislop deposit chargeability studies (see Chapter 2), and are divided by 1000 to correspond with IP inversion outputs. They are modeled within a low chargeability background. The zones are detected as a single, small anomalous area near the surface, which coincides with the top of the upper sulfide-rich zone (Fig. 3.15). The chargeability values estimated by the inversion are low compared to those of the true model.

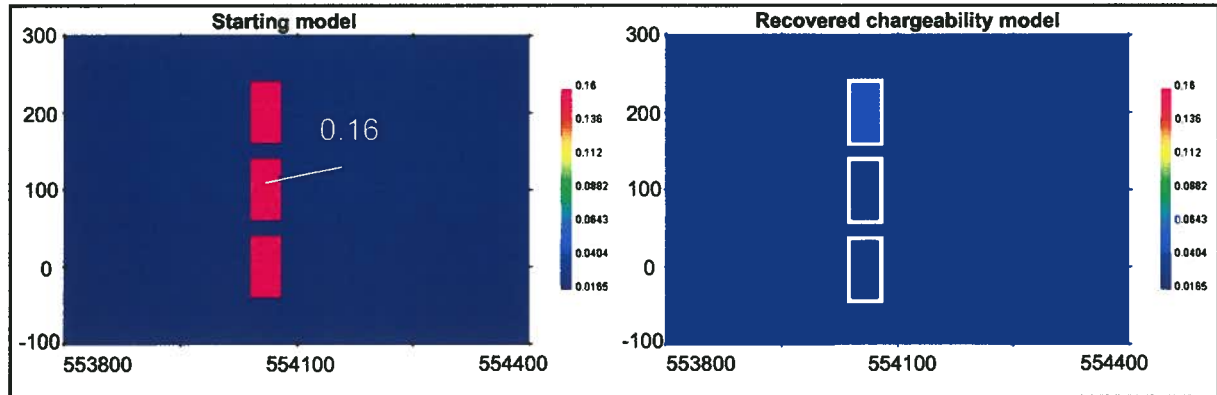


Figure 3.15. Starting model and unconstrained IP inversion result for the ‘Hislop-like’ chargeability model. The sulfide-rich high chargeability zones are only detected near surface down to about 125 m. The chargeability values estimated by the inversion for the chargeable zones are much lower than known values.

Varying geometry and physical properties

The chargeability of the sulfide zones is doubled from the initial model to test their subsequent resolution (Fig. 3.16a). The inversion result is essentially identical to the previous model result, but with marginally higher chargeability values coinciding with known sulfides. The upper chargeability zone is detected, but chargeability values are underestimated.

Where the sulfide zone is made a continuous feature with doubled chargeability values, it is well-located in the subsurface by the inversion, extending down to approximately 300 m depth (Fig. 3.16b). The representative chargeability values are underestimated for the sulfide zone. There is some excess structure occurring near the surface and at depth, which does not occur in the true model.

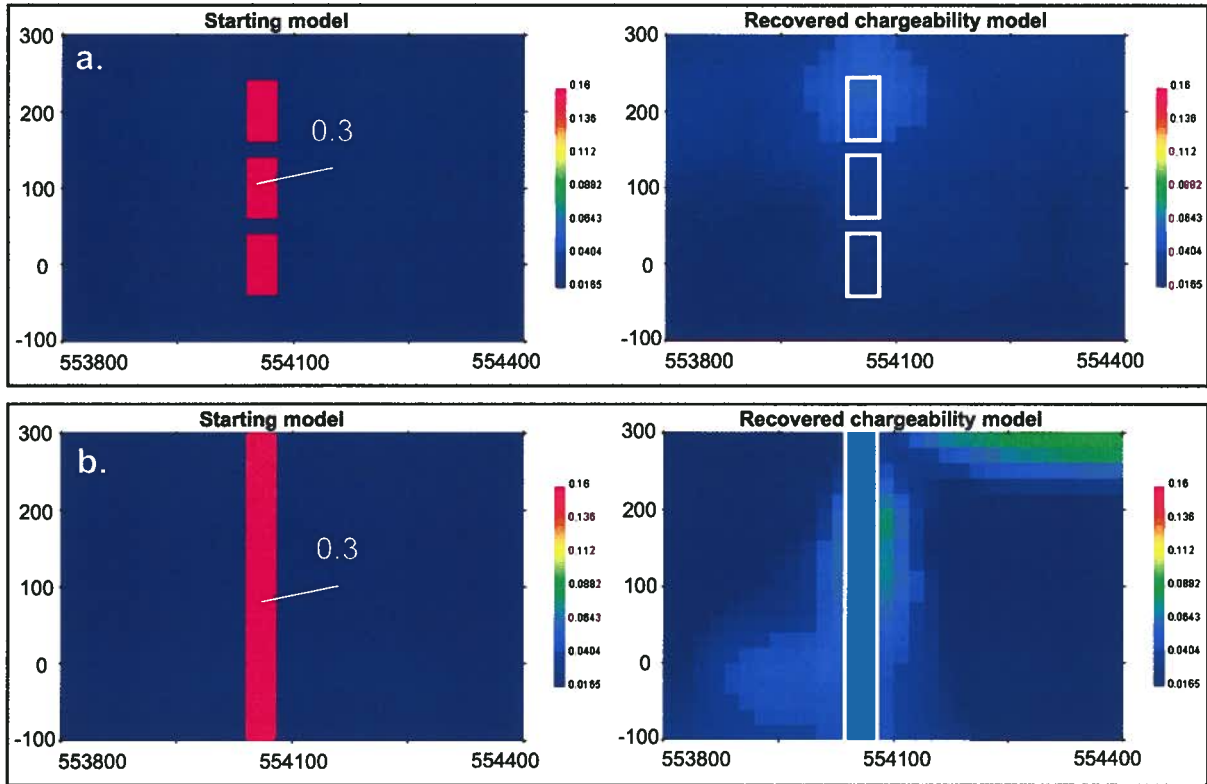


Figure 3.16. IP inversion results with changes made to physical property contrasts and geometry of the target body. a) Chargeabilities are doubled for the sulfide-rich zones. The resolved feature remains restricted to the near surface, but has slightly higher chargeabilities than the previous model result. b) The high chargeability target is made to be continuous. The target is well-located to almost 300 m depth, but has underestimated chargeabilities. Some additional structure in the model is found in near-surface cells and at depth.

Discussion of DC resistivity and IP inversion modeling results

DC Resistivity

The most significant discrepancy between true and recovered conductivity models is the lack of resolution of the central ‘sulfide-rich’, high conductivity zones. Even when the starting model contains only one persistent conductive feature, the recovered values are too low to be considered anomalous. This suggests that the feature may be too narrow, or the contrast between host and target rocks too weak. The fact that the western

ultramafic volcanic unit is resolved, a unit characterized by lower conductivities than the sulfide-rich body suggests that a lack of contrast can not be the explanation. The width of the feature is more likely to hinder its detection. In 3D forward modeling processes, to calculate voltages at a point, conductivities of cells within a 3D mesh must be averaged with those of neighboring cells over the cell volume (Dey and Morrison, 1979). In the case of the Hislop model, there is only one cell boundary that divides the anomalously conductive sulfide zone (the unit is 40 m thick and the cells 20 m wide), and the high value is essentially retained only in the averaging over this one particular boundary. At the dike's contacts, the high conductivities are averaged with the lower conductivities of the host rock, bringing the values down quickly to background conductivities. The aberration in conductivity is thus only weakly represented in the data to be inverted. Making cell sizes smaller, may give the feature a better chance to be accounted for, however, increasing the number of model cells causes the inversion problem to be exceedingly large, especially when employing data from Realsection arrays, where a large mesh is required.

The resolved moderately conductive ultramafic unit is only imaged to about 200 m depth, highlighting the second major discrepancy between true and recovered models - the lack of resolution at depth. This can mainly be attributed to the specific electrode array used. A Realsection array is similar to gradient or Schlumberger arrays in that transmitter electrodes are spaced at large distances outboard of the receiver electrodes (Telford et al., 1990). The poor resolution associated with wide electrode spacings is discussed by Hallof and Yamashita (1990). With increasing distance from the transmitter, the current weakens. Therefore a distant source that is intersected by the current will produce a weak signal, and will likely only be detected when the receiver electrode is sufficiently close, and in this case receiver electrodes are on surface.

The final discrepancy between true and resolved models is the underestimation of conductivity values for known higher conductivity areas. This is interpreted to be primarily associated with smoothing and the subsequent dispersal of conductivity over larger volumes within the mesh. Based on the model objective function defined, the

inversion solution favors the assignment of low conductivities over many cells, rather than high conductivities within more compact volumes.

Induced polarization

The chargeable zones are imaged to various degrees in each of the IP inversion model results, with depth detection improving with increased chargeability contrast between the sulfides and the host rocks. However, the recovered chargeability values corresponding to the sulfide-rich features in each case are underestimated. As with conductivity model results, the small width of the feature likely limits its detection. However, in contrast to the forward modeling of conductivity models, an averaging of chargeabilities between neighboring cells is not used in the IP forward model solution. This means the chargeability values are not as diminished during this step of the synthetic modeling process, which explains the slightly better resolution of the small chargeability anomalies. The poor resolution at depth known for Realsection surveys further reduces the possibility of resolving the sulfide-rich zones.

As with recovered conductivity models, smoothing resulting from the model norm contributes to the dispersion of chargeabilities over a larger volume. The smoothing of the conductivity anomaly over more cells than what are known to contain anomalous values, means that each cell requires less chargeability overall in order to explain the observed data.

The irregularly dispersed high chargeability values at surface thought to be related to the increased sensitivities at electrodes may also partly explain why chargeability values are lower than those from equivalent areas within true models – surface cells might already be taking up some of the required chargeability needed to explain the observed data, resulting in lower values elsewhere.

3.4.3. Improving model results with basic constraints

Inversion model results can be improved by constraining the inversion with additional geologic and physical property information (Phillips, 2002; Williams, 2006). This information can be inferred from the exploration deposit model, from published data, or from direct reconnaissance work. Prior information can be incorporated into the inversion calculation through basic manipulation of the model objective function to produce a model consistent with known geology, physical properties, and geometry (Li and Oldenburg, 1996 and 1998). As with all inversion results, the result must still fit the data within the specified misfit.

In this section, basic constraints are applied to inversions to try and reduce the discrepancies between recovered and true models evident from unconstrained inversions. The constraints are tested only for the Hislop-like resistivity and magnetic susceptibility models. The unconstrained inversions for these models did not fully delineate the target rocks, and as such, these two cases constitute good candidates for testing the possibility of model improvement with constraints. For the globally constrained inversions, physical property values known to be representative of the subsurface geology are used to recover more accurate physical property values, and knowledge of general structural orientations is applied to encourage smoothing of features in the desired directions. With significant amounts of prior physical property knowledge in the form of physical property measurements or geological 3D models, thorough and complex constraints can be applied, however, in this work simple solutions to modifying the models are explored.

The first constraint tested is use of a reference model, which in this case is a single physical property value that is considered representative of expected values. The inversion is required to yield a model close to this reference model, while satisfying the remaining terms of the inversion algorithm. The second constraint tested is setting physical property bounds on the inversion results. The default setting for UBC-GIF inversions usually allows a large range of values to be assumed by the model cells. The bounds can be adjusted to yield results within the range of known or expected values. The

third constraint tested is a geometrical constraint and is chosen based on known geological directionality, or preferred orientations.

The table of model difference values (Table 3.5) can be referred to here to evaluate the quantitative improvements in model estimation in accordance with the various constraints applied. A decrease in the calculated model difference reflects smaller differences between true and recovered physical properties.

Magnetic constraints: 20 m syenite dike between ultramafic and mafic volcanic units

Reference model

A constant reference model value of 0.03 SI Units is used, representing expected high susceptibilities of mafic and ultramafic rocks. As in unconstrained results, only the contact between the contrasting mafic volcanic rock and syenite is detected (Fig. 3.17a). The susceptibility contrast between the ultramafic volcanic unit and the syenite continues to be elusive. Near-surface cells show again the tendency to acquire reference model values, in this case values around 0.03 SI Units (previously 0 SI Units reflecting the default reference model). The calculated model difference is an improvement in overall recovery of the true susceptibility values compared to unconstrained results. This improved susceptibility estimate is explained by the new reference model value (> 0 SI Units) being assumed by the surface cells, resulting in the necessary lowering of susceptibility at depth, where susceptibilities in relation to the mafic volcanic unit were initially highly overestimated to compensate for low surface values. Geological contacts are slightly better located.

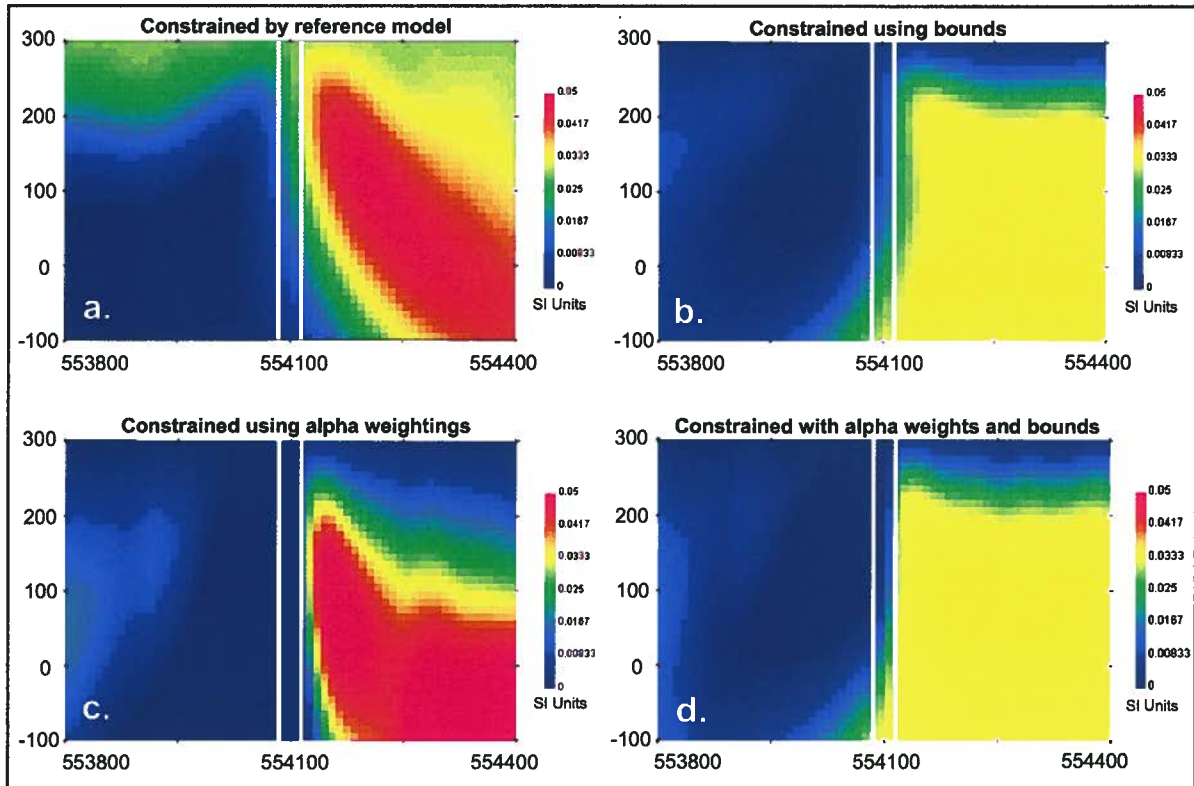


Figure 3.17. Inversion results for the Hislop-like susceptibility model after constraints applied. a) Inversion result with reference model set to 0.03 SI Units; b) Result with bounds set from 0 to 0.035 SI Units; c) Result after α_z and α_y increased relative to α_x ; d) Result with upper bounds set to 0.035 SI Units, and alpha α_z and α_y increased.

Bounds

Bounding the model using a upper susceptibility bound of 0.035 SI Units, a value slightly higher than the known susceptibility of mafic volcanic rocks here, and more suitable than the default upper bound of 1 SI Unit, yields a more qualitatively and quantitatively accurate model (Fig. 3.17b). The cap on the susceptibility values keeps susceptibility from being significantly overestimated. Low susceptibilities near-surface, thought to be caused in previous models by depth weighting, are minimized with appropriate bounds. An overall lowering of the susceptibilities in the vicinity of the mafic volcanic rocks means the high susceptibility zones are not pushed as deep to effectively reproduce the observed data. The mafic volcanic unit/syenite dike contact is well-located,

extending to a depth of about 400 m, however the presence of the syenite dike, is still not obvious.

Alpha weightings

Use of alpha (α) weightings to achieve smoothing along the z and y axes reflecting known structural orientations, results in sharper contacts within the model, but causes unnecessary vertical exaggeration (Fig. 3.17c). Model difference calculations (Tab. 3.5) indicate that susceptibility value estimation has not improved with respect to the unconstrained result. Without putting any restrictions on susceptibility values, susceptibilities are still overestimated.

Combined bounds and directional weighting

By combining alpha weighting in y and z directions with use of more appropriate upper bounds values, a well-estimated model results, with slightly sharper contacts than when bounds alone are constrained (Fig. 3.17d). Model difference values show this result is not necessarily an improvement on setting upper bounds exclusively. Although the gold-related feature, the syenite dike, is not better imaged, the physical property model values are better estimated, and thus geological interpretations of the model will improve.

Resistivity constraints: 40 m wide sulfide rich zones near ultramafic rock-syenite dike contact.

Reference values

The reference value for the conductivity inversion was set to 0.001 S/m, a value lying approximately between the higher conductivity ultramafic and mafic volcanic rocks in order to improve the overall conductivity estimations within the model. The sheared ultramafic rocks are resolved to a slightly greater depth than in the unconstrained DC resistivity result (Fig. 3.18a). Poorly estimated values in this result now appear to be related to the less sensitive, deeper model cells' tendency toward higher reference model values of 0.001, a value higher than those cells at the same depth in the true models. The

effect is shallower cells have more underestimated values than previously, not requiring high conductivities since higher conductivities exist in the deeper cells. Changing the reference model is good practice as seeing where reference values take over at depth within the model allows for determination of maximum depth of investigation, which can be estimated as the depth where a range of models consistently revert to reference model values (Oldenburg and Li, 1999).

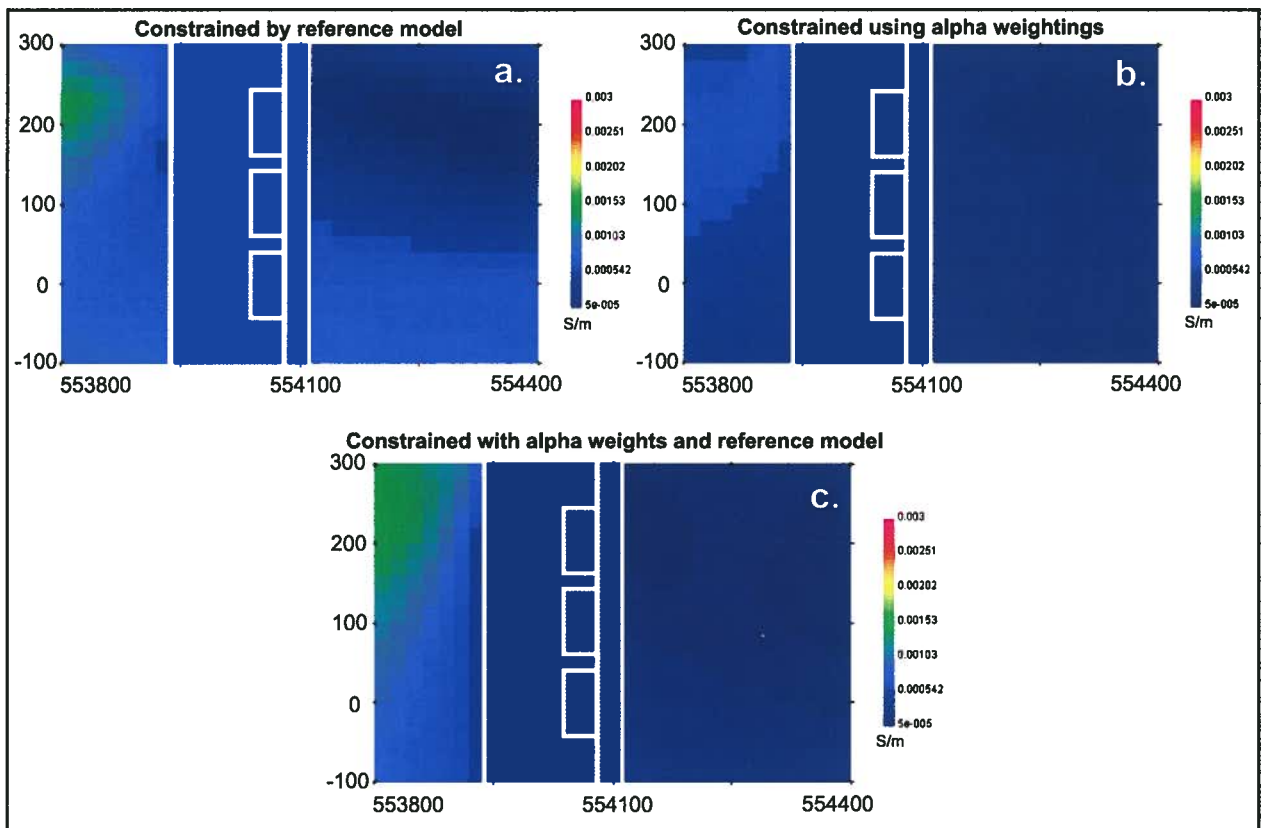


Figure 3.18. Inversion results for the Hislop-like conductivity model after constraints applied. a) Inversion result with reference model set to 0.001 S/m; b) Result with α_z and α_y increased relative to α_x ; c) Result with reference model set to 0.001 S/m, and alpha α_z and α_y increased relative to α_x .

Alpha weightings

Increasing alpha weightings in the z and y directions relative to the x direction to increase smoothing parallel to known structures and contacts causes conductivities

related to sheared ultramafic rocks to extend marginally deeper (Fig. 3.18b). The greater volume encompassed by the conductivity anomaly means the values are lower overall, in comparison to initial inversion results, to explain the observed data.

Combined reference model and directional weighting

Combining alpha weighting with appropriate reference value assignment yields a good, geologically reasonable result with the conductivity anomaly extended to depth as in the true model (Fig. 3.18c). Model difference values for this result are lower than for all previous DC resistivity inversion results. The use of the reference model value of 0.001 S/m keeps conductivity values high, unlike the application of alpha weightings alone. Again, constraining the model using prior physical property and geological knowledge does not improve imaging of the gold target, but yields a more accurate physical property model, which will in turn, lead to improved geological interpretations.

3.4.4. Other solutions for improving model results

Experimentation with additional modifications to inversion and survey parameters were attempted to try to improve the model results where they have not been improved by constraints.

Magnetic susceptibility model improvements – adjusting depth weightings

One of the causes of discrepancy between true and recovered magnetic susceptibility models is the applied depth weightings. Depth weighting written into the potential fields inversion codes (Li and Oldenburg, 1996 and 1998) are necessary to offset the natural decay of the magnetic and gravity signal, and for distributing physical properties to depth. However depth weighting appears to lead to low sensitivities at the surface in susceptibility models, and subsequent overestimation of susceptibility at depth.

To alleviate the problem of surface cells assuming reference model values, the default depth weighting was reduced by decreasing values of β and z_0 (arbitrarily by a

quarter of their default values which were 3 and 20.92, respectively), the variables within the depth weighting function controlling the offset of the natural magnetic decay (Li and Oldenburg, 1996). This should allow more sensitivity within the upper cells in the model. The model results are improved over results with the default weighting used. Model difference values drop with a decrease in the weighting (Fig. 3.19). This change emphasizes that a significant portion of the disagreement between true and recovered models stems from the poor estimation of susceptibility near surface. It is recommended that for magnetic inversions at this scale, the depth weighting be manipulated for comparison to other unconstrained and constrained model results. For larger scale models, there might be problems associated with this manipulation of the default depth weighting, in terms of loss of information at depth.

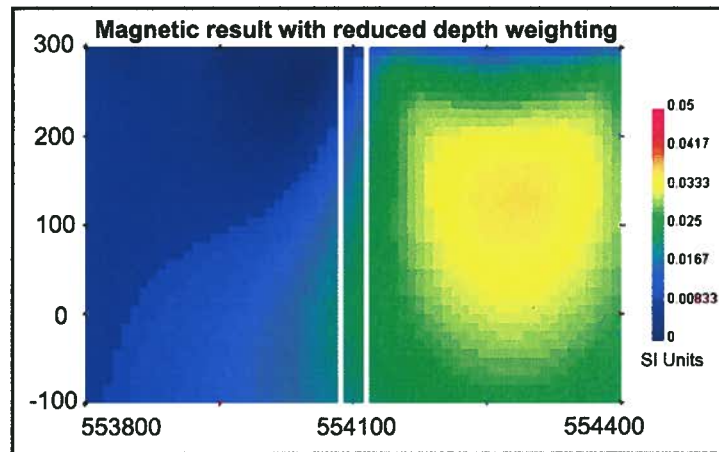


Figure 3.19. Inversion results for the Hislop-like susceptibility model with depth weightings reduced. The susceptibility model is better estimated in the near-surface cells, and susceptibility values are more accurate overall. Smoothing increases with depth.

Resistivity model improvements - survey design

DC resistivity and IP surveys completed using Realsection or Schlumberger arrays tend to have better depth detection than arrays with more closely spaced transmitters, but less spatial resolution overall due to the weakening of the current over

the large distances covered. Hallof and Yamashita (1990) discuss the importance of using closely spaced electrodes for detection of small sulfide-rich zones. The use of a different array configuration where transmitter electrodes are not distant with respect to receiver electrodes might enhance spatial resolution of the conductivity anomalies in the Hislop model. A dipole-dipole array, compared to a Schlumberger array in Figure 3.20, with $a = 40$ m, and $n = 1-10$, was used to test this hypothesis. The result seems to be an improvement on the Realsection inversion result with better estimated conductivity values, and imaging of the upper parts of the conductive sulfide-rich zones (Fig 3.21). Although a full investigation of the effectiveness of different electrode arrays is beyond the scope of this research, this example shows that the chosen survey design can determine whether a feature will be detected in the geophysical data and in inversion results. The possibilities should be well-researched in advance of exploration with consideration of the types of information required and the characteristic sizes and depths of targets.

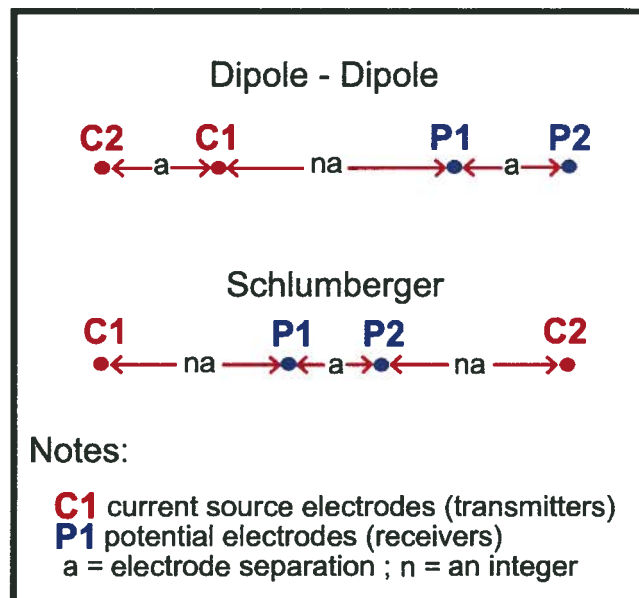


Figure 3.20. Comparison of a dipole-dipole electrode configuration and a Schlumberger configuration which resembles a Realsection array. Dipole-dipole surveys employ closely spaced current and potential electrodes. For the Schlumberger array, current electrodes are distal to potential electrodes (figure modified from Inversion for Applied Geophysics resource package, UBC-GIF).

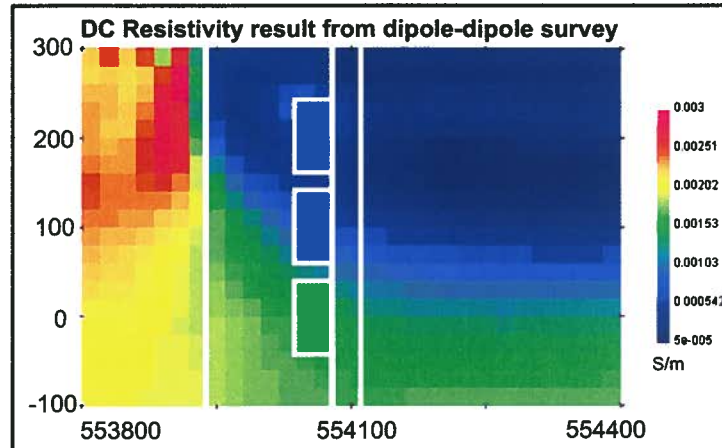


Figure. 3.21. DC resistivity inversion result for resistivity data collected via a dipole-dipole survey. Depth resolution has not increased compared to Realsection results, but there is better spatial resolution and the sulfide-rich zone is detected in addition to the sheared ultramafic unit.

3.5. CONCLUSIONS

Synthetic modeling is important to conduct prior to inversion work. It will reveal whether or not a feature of particular shape, size, and of certain contrast with the host rocks can be resolved using inversion methods. In doing this, limitations of inversion are also revealed, establishing where caution in interpreting results is necessary (e.g. where physical properties recovered may be inaccurate, or if there are artifacts that are byproducts of the inversion), and determining when confidence can be placed in the interpretation or querying of recovered models. Synthetic modeling also tests the effects of constraints, and determines if it is possible to improve the model through their application.

Synthetic modeling was completed in this study to determine whether geological features, specifically rocks related to gold mineralization and characteristic of Archean orogenic gold deposits, are detectable in the subsurface. From previous geological and

physical property studies it was determined that prospective features typical of this mineral deposit setting, which are also petrophysically distinct from host rocks include, near-vertical, or steeply-dipping faults, felsic dikes, carbonate alteration zones, and sulfide rich zones. These features are modeled within ultramafic and mafic volcanic rocks, common hosts to orogenic gold mineralization. The scale of the study is reminiscent of deposit-scale exploration, and inversions are done on a 1 km by 1 km by 600 m mesh. Synthetic magnetic, gravity, DC resistivity, and IP data were modeled.

In general, this work shows there are significant enough contrasts between gold-related targets and host rocks in this environment for geophysics, and geophysical inversion, to be useful exploration tools. Magnetic and gravity inversions were successful in resolving low susceptibility and low density gold-related syenite dikes to depths around 200-350 m. The narrow, 20 m dike is most poorly imaged by magnetic inversion where hosted between a mafic and an ultramafic unit. Where there are two hosts of different susceptibility, yet both of higher susceptibility than the dike, the signature of the dike is lost in the overall gradient from low to high susceptibility areas. A combination of magnetic and gravity inversion results would best detect the syenite dike, with the density resolving the ultramafic-syenite contact, and magnetics resolving features slightly deeper. The main differences between recovered and true magnetic and gravity models result from smoothing due to the choice of inversion model norm, and due to the natural decay of the geophysical signal with depth. Depth weights also cause discrepancies between true and recovered models, which can bring about high estimates of susceptibility or density at depth, leading to poor distributions of physical properties throughout the model.

Resistivity modeling using a Realsection electrode array does not detect narrow anomalous conductive zones related to sulfide-rich rocks, unless the zones are quite anomalous and laterally continuous, and in this case, their associated conductivity values are underestimated. DC Resistivity inversions are, however, effective at modeling larger conductive geological units, but only to shallow depths within the subsurface. Induced polarization inversions detect chargeable zones, especially where they are extensive and

continuous. However, as with conductivity models, the result is only reliable near surface, and anomalous values are underestimated. The lack of resolution at depth accompanying DC resistivity and IP survey methods cause the poor depth resolution in inversion results. The underestimation of anomalous physical property values is due to dispersal of anomalous values over larger areas as a result of smoothing brought on by the inversion model objective function.

Constraining inversion results acts most importantly in limiting physical property ranges and producing a better distribution of physical properties throughout the model. While use of global constraints does not improve the resolution of targets that were not previously detected, they yield qualitatively and quantitatively better results. Applying constraints permits assessment of the range of possible results. Features that persist between various model results are required to exist to fit the observed data and satisfy the requirements of the model objective function, and are likely real.

For all geophysical methods, different results would be expected at larger scales of exploration and modeling. At larger data spacings, there is greater depth of resolution, but inversion models would display less detail since larger model cells are required to keep inversion computation times to a minimum.

Synthetic modeling, and subsequent inversion of true geophysical data, requires knowledge about relationships between physical properties and expected rock types. This is best achieved by having a reconnaissance knowledge of the geology being investigated. Using downhole susceptibility information, or surface sample data, it is recommended that typical physical property ranges be determined for the important rock types and altered equivalents. Sourcing published data is an option where data collection has not been carried out. Physical property studies in various geological settings are becoming more commonplace, and physical property data is being compiled currently on a more regular basis. This information is becoming increasingly valuable with the drive in recent years toward using geophysical methods to explore for deposits in the deeper subsurface.

REFERENCES

Berger, B.R., 1999, Geological investigations along Highway 101, Hislop Township: Ontario Geological Survey, Summary of Field Work and Other Activities 1999, Open File Report, 6000, p. 5-1 – 5-8.

Connell, S., Scromeda, N., Katsube, T.J., and Mwenifumbo, J., 2000, Electrical resistivity characteristics of mineralization and unmineralized rocks from the Giant and Con mine areas: Geological Survey of Canada, Yellowknife, NWT, Current Research 2000-E9.

Cooper, M.A., 1948, Report on Kelore Mines Ltd., Ramore, Ontario, unpublished, 22 p.

Darbyshire, D.P.F., Pitfield, P.E.J., and Campbell, S.D.G., 1996, Late Archean and Early Proterozoic gold-tungsten mineralization in the Zimbabwe Archean craton: Rb-Sr and Sm-Nd isotope constraints: *Geology*, v. 24, p. 19–22.

DCIP3D user manual, Version 2.1, University of British Columbia Geophysical Inversion Facility.

Dey, A., and Morrison, H.F., 1979, Resistivity modeling for arbitrarily shaped three dimensional structures: *Geophysics*, v. 44, p. 753-780

Doyle, H.A., 1990, Geophysical exploration for gold – a review: *Geophysics*, v. 55, p. 134-146.

Farquharson, C.G, Ash, M.R., and Miller, H.G, 2008, Geologically constrained gravity inversion for the Voisey's Bay ovoid deposit: *The Leading Edge*, v. 27, p. 64-69.

Fyon, J.A., and Crockett, J.H., 1983, Gold exploration in the Timmins District using field and lithogeochemical characteristics of carbonate alteration zones, *in* Hodder, R.W., and

Petruk, W., eds, *Geology of Canadian Gold Deposits*, Canadian Institute of Mining and Metallurgy, Special Volume 24, p. 113-129.

Groves, D.I., Ridley, J.R., Bloem, E.M.J., Gebre-Mariam, M., Hagemann, S.G., Hronsky, J.M.A., Knight, J.T., McNaughton, N.J., Ojala, J., Vielreicher, R.M., McCuaig, T.C., and Holyland, P.W., 1995, Lode gold deposits of the Yilgarn block: products of late Archean crustal-scale overpressured hydrothermal systems, *in* Coward, M.P., and Ries, A.C., eds., *Early Precambrian Processes*, Geological Society Special Publication, no. 95, p. 155-172.

Groves, D.I., Goldfarb, R.J., Gebre-Mariam, M., Hagemann, S.G., and Robert, F., 1998, Orogenic gold deposits: a proposed classification in the context of their crustal distribution and relationship to other gold deposit types: *Ore Geology Reviews*, v. 13, p. 7-27.

Hagemann, S.G., and Cassidy, K.F., 2000, Archaean orogenic lode gold deposits, *in* Hagemann, S.G., and Brown, P.E., eds., *Gold in 2000*, Society of Economic Geologists, *Reviews in Economic Geology*, v. 13, p. 9-68.

Hallof, P.G., and Yamashita, M., 1990, The use of the IP method to locate gold-bearing sulfide mineralization, *in* Fink, J.B., Sternberg, B.K., McAlister, E.O., Weiduwilt, W.G., and Ward, S.H., eds., *Induced Polarization: applications and case histories*, Society of Exploration Geophysicists, Tulsa, Ok., p. 227-279.

Hodgson, C.J., 1989, The structure of shear-related, vein-type gold deposits: a review: *Ore Geology Reviews*, v. 4, 231-273

Hodgson, C.J., 1990, An overview of the geological characteristics of gold deposits in the Abitibi subprovince, *in* Ho, S.E., Robert, F., and Groves, D.I., compilers, *Gold and Base Metal Mineralization in the Abitibi Subprovince, Canada, with Emphasis on the Quebec Segment*, Short Course Notes, Geology Department (key center) and University Extension, the University of Western Australia, publication No. 24, p. 63-100.

Hodgson, C.J., 1993, Mesothermal lode gold deposits, in Kirkham, R.V., Sinclair, W.D., Thorpe, R.I., and Duke, J.M., eds., Mineral Deposit Modeling, Geologic Association of Canada, Special Paper 40, p. 635-678.

Hodgson, C.J., and Hamilton, J.V., 1990, Gold mineralization in the Abitibi greenstone belt: end-stage results of Archean collisional tectonics, *in* Keays, R.R., Ramsey, W.R.H., and Groves, D.I., eds., The Geology of Gold Deposits: the Perspective in 1988, Economic Geology Monograph 6, p. 86-100.

Hodgson, C.J., and MacGeehan, P.J., 1982, Geological characteristics of gold deposits of the Superior Province of the Canadian Shield: Canadian Institute of Mining and Metallurgy, Special Volume 24, p. 211-228.

Hodgson, C.J., and Troop, D.G., 1988, A new computer-aided methodology for area selection in gold exploration: a case study from the Abitibi greenstone belt: Economic Geology, v. 83, p. 952-977.

Kent, A.J.R., Cassidy, K.F., and Fanning, C.M., 1996, Archean gold mineralization synchronous with the final stages of cratonization, Yilgarn Craton, Western Australia: Geology, v. 24, p. 879-882.

Kerrick, R., 1989, Geodynamic setting and hydraulic regimes: shear zone hosted mesothermal gold deposits, *in* Bursnall, J.T., ed., Mineralization and Shear Zones, Geological Association of Canada, Short Course Notes 6, p. 89-128.

Kerrick, R., and Cassidy, K.F., 1994, Temporal relationships of lode gold mineralization and accretion, magmatism, metamorphism, and deformation – Archean to present: a review: Ore Geology Reviews, v. 9, p. 263-310.

Kerrick, R., and Wyman, D., 1990, The geodynamic setting of mesothermal gold deposits: an association with accretionary tectonic regimes: Geology, v. 18, p. 882-885.

Kishida, A., and Kerrich, R., 1987, Hydrothermal alteration zoning and gold concentration at the Kerr-Addison Archean lode gold deposit, Kirkland Lake, Ontario: *Economic Geology*, v. 82, p. 649-690.

Li, Y., and Oldenburg, D.W., 1996, 3-D inversion of magnetic data: *Geophysics* v. 61, p. 394-408.

Li, Y., and Oldenburg, D.W., 1998, 3D inversion of gravity data: *Geophysics*, v. 63, p.109-119.

Li, Y., and Oldenburg, D.W., 2000, 3D inversion of induced polarization data: *Geophysics*, v. 65, p.1931-1945.

McCuaig, T.C., Kerrich, R., 1998, P-T-t-deformation-fluid characteristics of lode gold deposits: evidence from alteration systematics: *Ore Geology Reviews*, v. 12, p. 381-453.

Meuller, A.G., and Groves, D.I., 1991, The classification of Western Australian greenstone-hosted gold deposits according to wall-rock alteration mineral assemblages: *Ore Geology Reviews*, v. 6, p. 291-331.

Oldenburg, D.W., and Li, Y., 1999, Estimating depth of investigation in dc resistivity and IP surveys: *Geophysics*, v. 64, p. 403-416.

Oldenburg, D.W., Li, Y., and Ellis, R.G., 1997, Inversion of geophysical data over a copper gold porphyry deposit: A case history for Mt. Milligan: *Geophysics*, v. 62, p. 1419-1431.

Phillips, N.D., 2002, Geophysical inversion in an integrated exploration program: examples from the San Nicolas deposit: Unpublished M.Sc. thesis, University of British Columbia, 237 p.

Phillips, N., Hickey, K., Lelievre, P., Mitchinson, D., Oldenburg, D., Pizarro, N., Shekhtman, R., Sterritt, V., Tosdal, D., and Williams, N., 2007, Applied strategies for the 3D integration of exploration data: KEGS Inversion Symposium, PDAC 2007, extended abstract, 9 p.

Power, W. L., Byrne, D., Worth, T., Wilson, P., Kirby, L., Gleeson, P., Stapleton, P., House, M., Robertson, S., Panizza, N., Holden, D. J., Cameron, G., Stuart, R., and Archibald, N. J., 2004, Geoinformatics evaluation of the eastward extension of the Timmins Gold Camp: Geoinformatics Exploration Inc., Unpublished report for St Andrew Goldfields Ltd.

Prest, V.K., 1956, Geology of the Hislop Township: Ontario Department of Mines, Annual Report, 1956, v. 65, pt. 5, 51 p.

Robert, F., 1990, Structural setting and control of gold-quartz veins of the Val D'Or area, southeastern Abitibi subprovince, *in* Ho, S.E., Robert, F., and Groves, D.I., compilers, Gold and Base Metal Mineralization in the Abitibi Subprovince, Canada, with Emphasis on the Quebec Segment, Short Course Notes, Geology Department (key center) and University Extension, the University of Western Australia, publication No. 24, p. 167-212.

Robert, F., 2001, Syenite-associated disseminated gold deposits of the Abitibi greenstone belt, Canada: *Mineralium Deposita*, v. 36, p. 503-516.

Roberts, R.G., 1988, Archean lode gold deposits, *in* Roberts, R.G., and Sheahan, P.A., eds., *Ore Deposit Models*, Geoscience Canada, Reprint Series 3, p. 1-19.

Roscoe and Postle, 1998, Hislop Mine Property, Roscoe and Postle Associates Inc., St. Andrew Goldfields Ltd. internal report, unpublished, p. 66-89.

Sibson, R.H., Robert, F., and Poulsen, K.H., 1988, High-angle reverse faults, fluid pressure cycling, and mesothermal gold-quartz deposits: *Geology*, v. 16, p. 551-555.

Telford, W.M., Geldart, L.P., and Sheriff, R.E., 1990, *Applied Geophysics*, Second Edition, Cambridge University Press, 770 p.

Weinberg, R.F., Hodkiewicz, P.F., and Groves, D.I., 2004, What controls gold distribution in Archean terranes: *Geology*, v. 32, p. 545-548.

Williams, N.C., 2006, Applying UBC-GIF potential fields inversions in greenfields or brownfields exploration: Australian Earth Sciences Convention, 2006, Melbourne, Australia, 10 p.

Chapter 4: 3D inversion of magnetic, gravity, DC resistivity, and induced polarization data over the Hislop gold deposit, south-central Abitibi greenstone belt³

4.1. INTRODUCTION

4.1.1. Rationale

Magnetic, gravity, DC resistivity, and induced polarization (IP) data were inverted to investigate subsurface geology within a section of the south-central Abitibi greenstone belt hosting the Hislop gold deposit. A large amount of historic drilling has been completed, but much of it is shallow, and concentrated on specific mineral exploration properties. The irregular drilling coverage, and an overall lack of outcrop in the Hislop deposit area suggests that geophysical inversion, the calculation of subsurface distributions of physical properties from geophysical data, could be an extremely useful tool for understanding subsurface geology and establishing mineral exploration targets in this part of the gold-rich Abitibi greenstone belt.

In contrast to its more extensive application for delineation of massive sulfide-style deposits (Oldenburg et al., 1997; Phillips, 2002; Farquharson et al., 2008), geophysical inversion has not been as commonly applied for similar purposes in the orogenic gold environment. The reason for this is that orogenic gold deposits, like the Hislop gold deposit, are characterized by small, discontinuous, and low grade orebodies that do not have a strong petrophysical contrast with typical host rocks. Geological units, hydrothermal alteration zones, and structures that are known to be related to gold, however, can provide larger scale exploration targets. There are only a few examples of case studies employing inversion methods to detect gold-related rocks in Archean orogenic gold settings (UBC-GIF Inversion for Applied Geophysics CD-ROM, 2000-

³ A version of this chapter will be submitted for publication. Mitchinson, D., Phillips, N., and Williams, N., 2009, 3D inversion of magnetic, gravity, DC resistivity, and induced polarization data over the Hislop gold deposit, south-central Abitibi greenstone belt.

2006; Kowalczyk et al., 2002; Mira Geoscience Ltd., 2005a and 2005b; Mueller et al., 2006). The usefulness of these methods as an exploration tool in this mineral deposit environment may therefore not yet be fully appreciated.

The large amount of geophysical data available, and a thorough background understanding of the relationships between geology and physical properties for the Hislop deposit area (Chapter 2), creates an opportunity to conduct a comprehensive study of the types of information that might be acquired by inverting a suite of geophysical data at a range of scales in this mineral deposit setting.

4.1.2. Geological background

The area investigated in this study is located in the south-central Abitibi greenstone belt (Fig. 4.1), east of the Timmins-Porcupine gold camp, which is known for its world-class Archean orogenic gold deposits (Hollinger-McIntyre and Dome deposits), and in general for its large number of gold and base metal deposits and occurrences. The study area (Fig. 4.2) is underlain by northwest-southeast trending ultramafic to mafic volcanic rock sequences, with lesser felsic volcanic units (Prest, 1957; Berger, 1999; Power et al., 2004; Roscoe and Postle, 1998). The volcanic sequences are intruded by variably sized, fine to coarse-grained felsic and intermediate intrusives and dikes. A major crustal-scale fault zone, the Porcupine-Destor Deformation Zone (PDDZ), runs northwest-southeast through the area, parallel to the general regional trend. Gold deposits in this part of the Abitibi greenstone belt have a close spatial relationship with the PDDZ (Jackson and Fyon, 1991; Berger, 2002). It is interpreted to have acted as a conduit through which CO₂-rich and gold-bearing fluids ascended upward through the crust to sites of eventual gold deposition (Kerrich, 1989). Sedimentary rocks from the Porcupine and Timiskaming assemblages, lie north of the PDDZ, likely having originally accumulated in a structurally controlled basin during fault development late in the formation of the greenstone belt (Ayer et al., 2002).

Local and deposit scale geophysical inversions completed for this study focus on the Hislop gold deposit. The Hislop deposit is a structurally controlled Archean orogenic gold deposit. Gold occurs with disseminated pyrite and is distributed within host rocks in proximity to a fault that occurs between a coarse-grained syenite dike, and a metamorphosed ultramafic volcanic unit (Fig. 4.3). Lesser mineralization occurs within small veins and vein stockworks in magnetite-bearing Fe-rich tholeiitic basalts north of the syenite dike. Gold is accompanied by Fe-rich carbonate, and muscovite alteration (Prest, 1956; Roscoe and Postle, 1998; Berger, 2002).

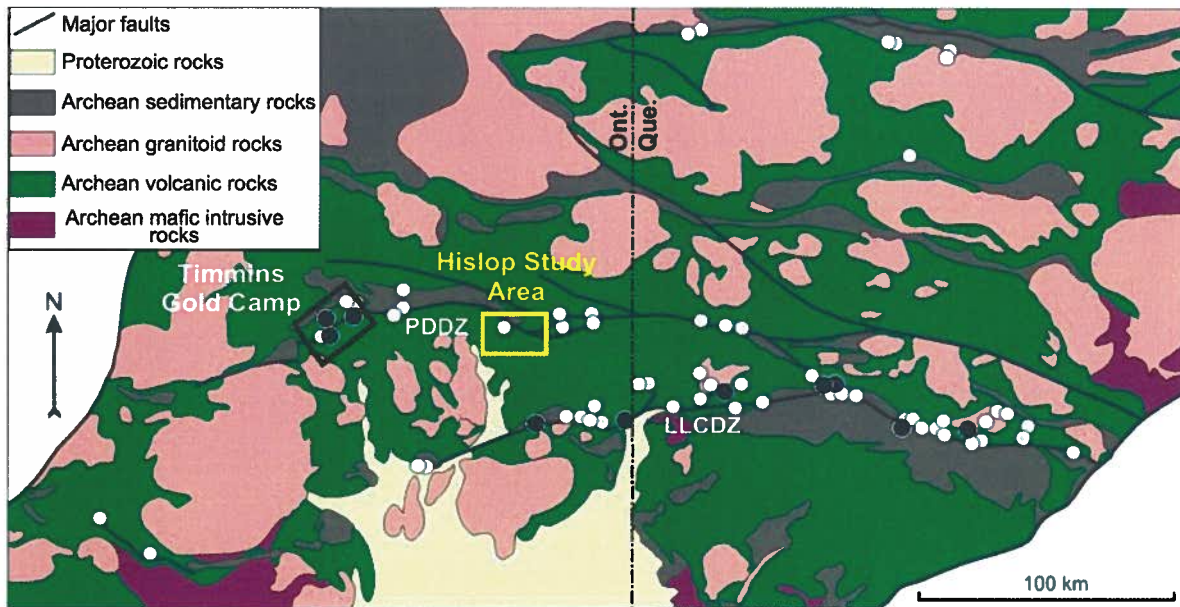


Figure 4.1. Geological map of the southwest Abitibi greenstone belt (modified after Poulsen et al., 2000). The Hislop deposit study area is shown with respect to the Timmins-Porcupine gold camp. White circles represent gold deposits and black circles represent world class gold deposits (>100 t). PDDZ = Porcupine Deformation Zone, LLCZ = Larder Lake-Cadillac Deformation Zone.

The Hislop deposit area was explored by numerous exploration groups from the early 1900's onward, and there are many existing drillholes and associated logs providing geological information for this property. The Hislop deposit was mined during three separate efforts between 1990 to 2006, by St. Andrew Goldfields, Ltd., from underground workings (Shaft Area on map in Fig. 4.2) and a small open pit (West Area). Over 400,000

tonnes of ore was mined over this period, grading between 2.33 g/t and 5.55 g/t (www.standrewgoldfields.com). The mine is currently not in operation.

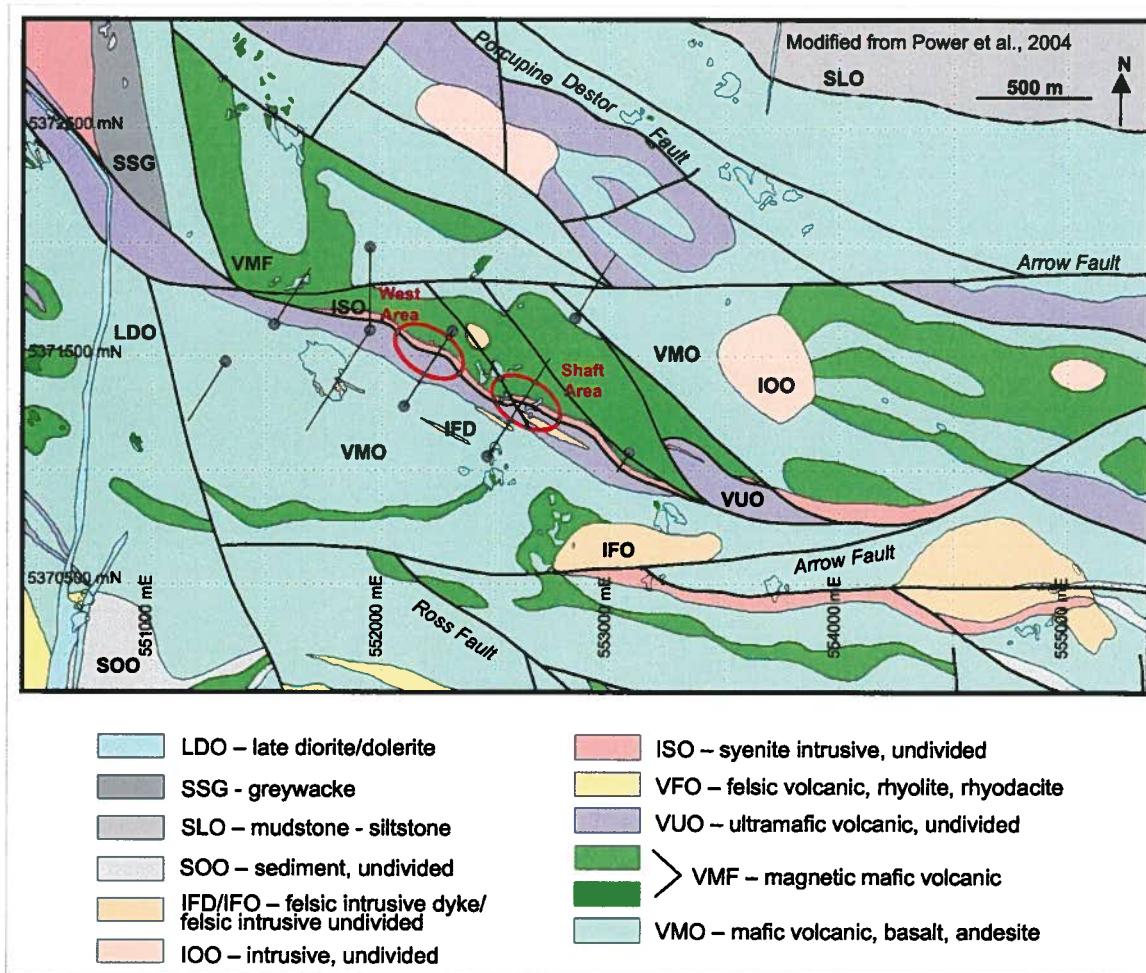


Figure 4.2. Geology of the Hislop deposit area as interpreted by Power et al. (2004) from high resolution aeromagnetics, and previous mapping in the Abitibi greenstone belt. Locations of two mined areas on the Hislop property (West Area open pit; Shaft Area underground) are outlined in red. Also shown are 10 drill holes (one overlapping) logged for this study. The cross-section shown in Figure 4.3 is based on core logging of four drill holes that were drilled in the West Area.

4.1.3. Relationships between geophysics, physical properties, and geology

Although gold itself is a dense and conductive mineral, its characteristic low grades in orogenic gold deposits make its direct detection using geophysical methods

difficult (Seigel et al., 1984; Doyle, 1990). Known vectors to gold such as hosting structures, lithology, or related hydrothermal alteration mineral assemblages, however, may still be targeted remotely. Rock property studies on the Hislop deposit revealed the existence of consistent relationships between certain physical properties, and potentially mineralized rocks (Chapter 2). A summary of the results of these physical property studies are presented in the following sections. Table 4.1 summarizes the physical property ranges for each rock type, and indicates anomalous ranges unique to some of the prospective rocks in the Hislop area.

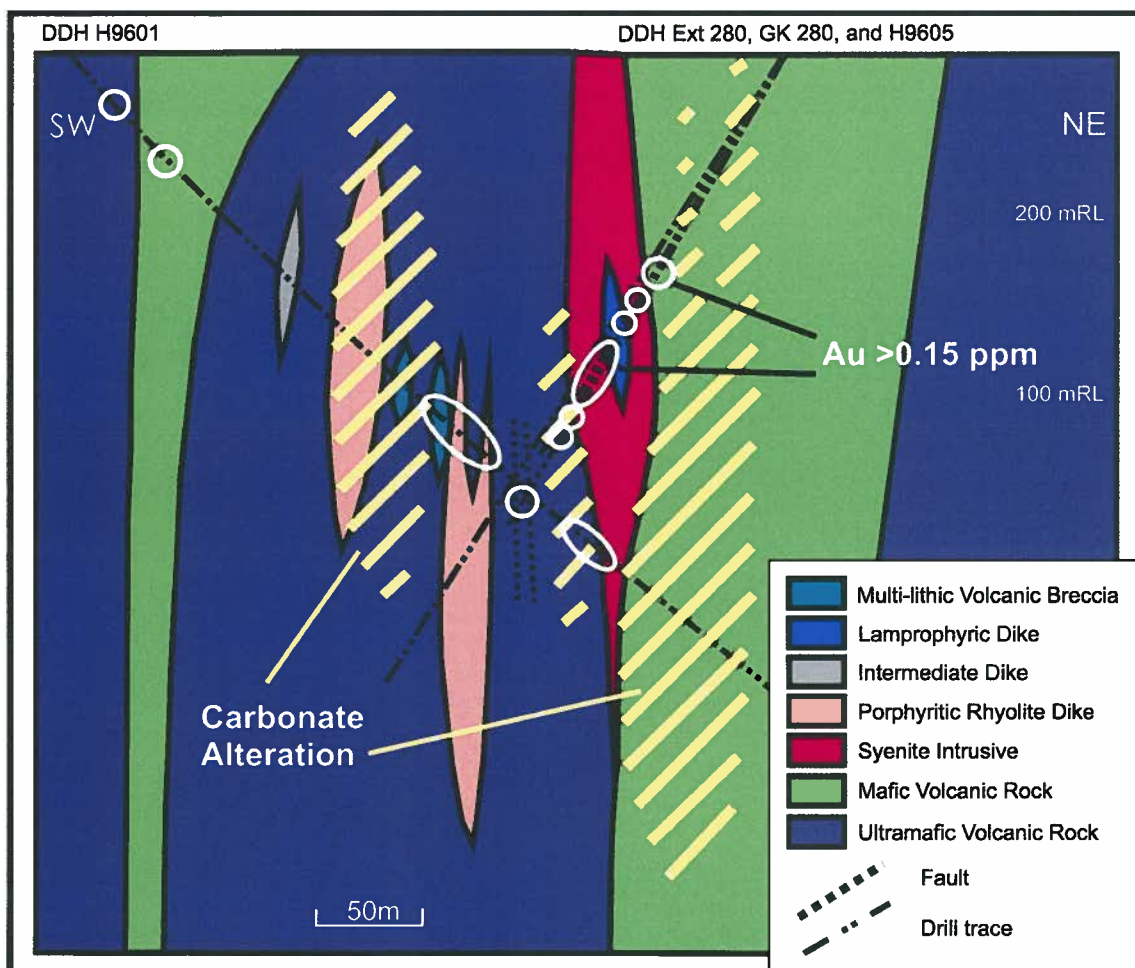


Figure 4.3. Cross section looking Northwest through the Hislop deposit, showing locations of carbonate-dominated alteration and gold mineralization. Cross section interpreted from drill core logged from the West Area of the Hislop property (see Figure 4.2).

Table 4.1. Typical and anomalous physical property ranges for principal rock types occurring in the Hislop deposit area.

Rock Type	Mag. Sus. ($\times 10^{-3}$ SI)	Density (g/cm^3)	Resistivity (Ohm-m)	Chargeability (ms)	Cut-off values for querying data					
	Range	Range	Range	Range	Rock Type	Mag. Sus.	Density	Res.	Chg.	
Unaltered ultramafic (dolomite-chlorite assemblage)	0.57-12.5	2.82-2.89	(all ultramafic rocks) 111-8546	(all ultramafic rocks) 2.90-15.967	Ultramafic rocks			111-8546		
Unaltered ultramafic (talc-chlorite assemblage)	0.44-84.4	2.79-2.94								
Fe-carbonate-muscovite altered ultramafic	0.41-5.96	2.80-2.91				Carbonate-altered ultramafic	0.41-5.96	2.80-2.96		
Magnesite-fuchsite altered ultramafic	0.49-0.95	2.85-2.96								
Unaltered mafic	0.35-141	2.70-3.08	(all mafic rocks) 541-58754	(all mafic rocks) 2.07-46.5	Carbonate-altered mafic					
Fe-carbonate-muscovite altered mafic	0-2.19	2.78-2.97				0.2-2.19	2.76-2.97			
Fe-carbonate-albite altered mafic	0.28-1.27	2.76-2.86								
Unaltered intermediate intrusive	0.24-135.29	2.72-2.95	(all intermediate rocks) 2314-22613	(all intermediate rocks) 9.45-15.4	Carbonate-altered intermediate intrusive					
Carbonate altered intermediate intrusive	0.13-3.8	2.67-2.95				0.13-3.8	2.67-2.95			
Carbonate-muscovite altered intermediate intrusive	0.32-1.55	2.76-2.94								
Syenite	0.07-0.42	2.64-2.74	(all syenites) 2631-9400	(all syenites) 6-15.67	Felsic intrusives	0.05-0.42	2.57-2.80			
Rhyolite porphyry	0.05-0.41	2.57-2.80	(all rhyolite dikes) 8976-11525	(all rhyolite dikes) 2-20.4						
Sulfide-rich rocks	Based on anomalies in inversion results			Anomalous sulfides				<1540	>120	

Magnetic susceptibility

Syenite and porphyritic rhyolite dikes have low susceptibility ranges distinct from most intermediate to ultramafic rocks at Hislop (Fig. 4.4). Their susceptibility values range from $0.05 - 0.42 \times 10^{-3}$ SI Units. Mafic and ultramafic volcanic rocks, and intermediate intrusive rocks have bimodal susceptibility populations (Fig. 4.4). This distribution indicates there are two distinct populations that make up the data. The high susceptibility population ($> \sim 10 \times 10^{-3}$ SI Units) is predominantly composed of least-altered Fe-rich tholeiitic basalts and ultramafic volcanic rocks (mainly talc-chlorite schists). Physical property studies revealed that the lower susceptibility population is partly composed of carbonate-altered intermediate, mafic and ultramafic rocks. These altered rocks (Figs. 4.5a and 4.5b) have susceptibility ranges from $0.13 - 5.96 \times 10^{-3}$ SI Units. Thus, for exploration targeting purposes, any rocks with susceptibilities above $5-10 \times 10^{-3}$ SI Units, where the break in data in Figures 4.4 and 4.5 occurs, can be excluded as less prospective.

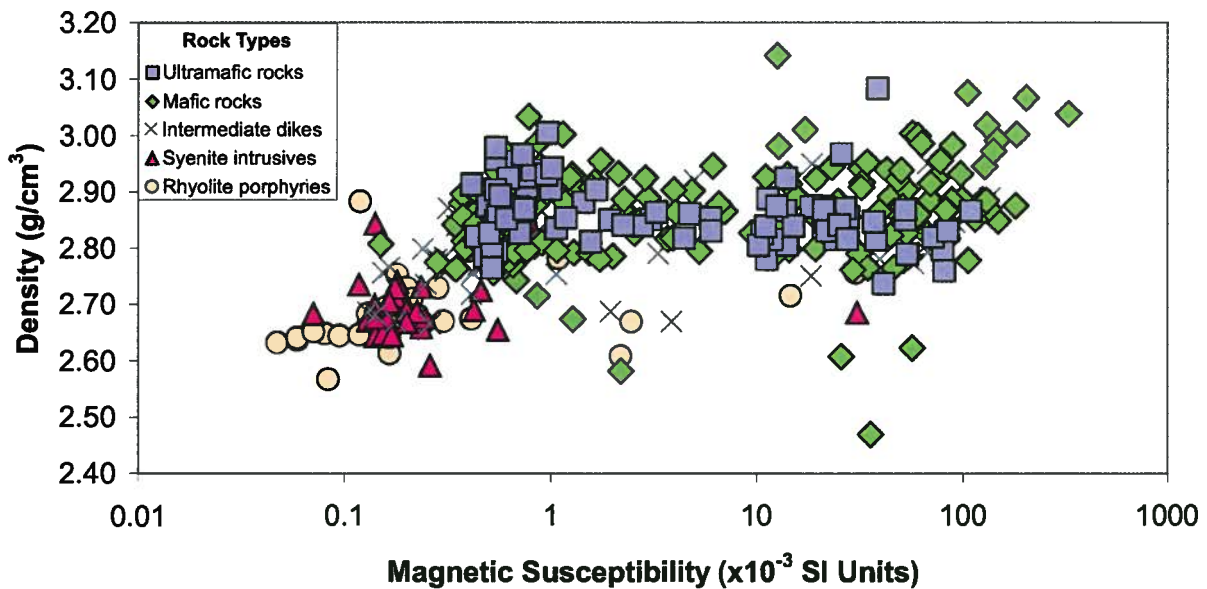


Figure 4.4. Magnetic susceptibility plotted against density for the major rock types at Hislop. Syenite intrusives and porphyritic rhyolite dikes have distinctly low density and magnetic susceptibility ranges allowing them to be distinguished from intermediate, mafic, and ultramafic rocks at Hislop.

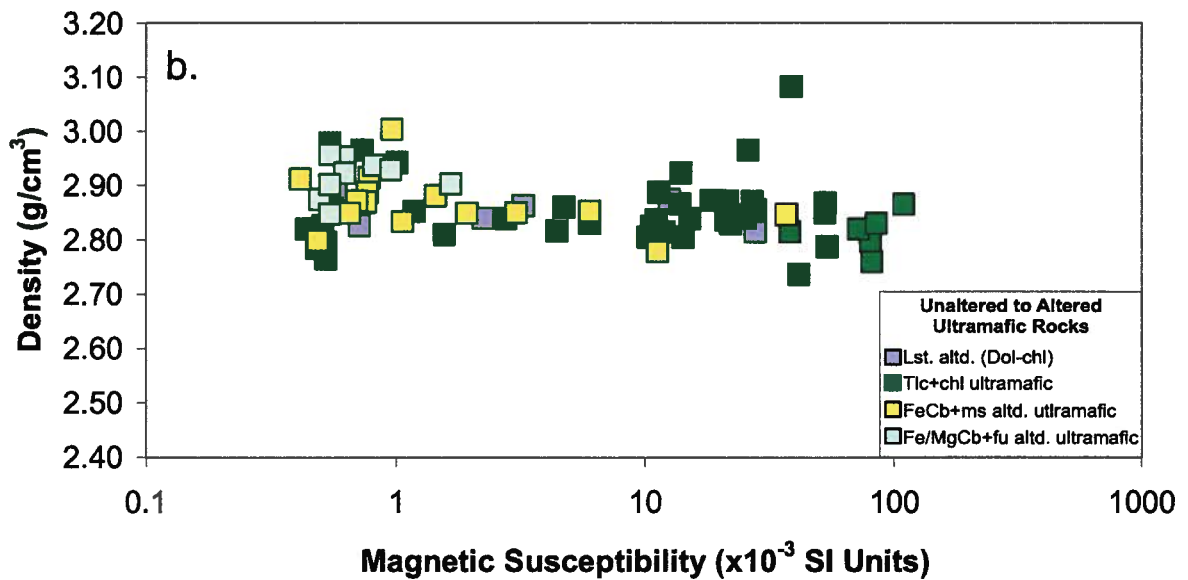
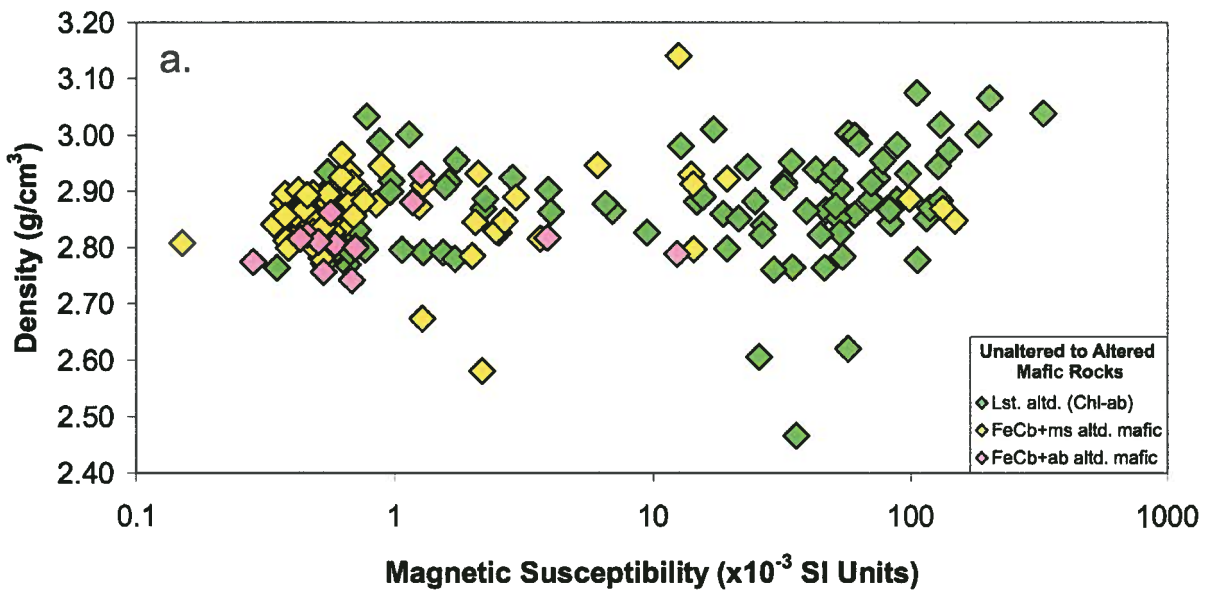


Figure 4.5. Magnetic susceptibility plotted against density for a) mafic and b) ultramafic volcanic rocks from the Hislop deposit area. Carbonate-alteration destroys magnetite in mafic and ultramafic volcanic rocks, causing magnetic susceptibility to drop. Density values increase slightly for altered ultramafic rocks. Abbreviations in legends: Lst. altd. = least altered assemblage; Chl+ab = chlorite+albite assemblage; FeCb+ms = Fe-carbonate+muscovite; FeCb+ab = Fe-carbonate+albite; Dol+chl = dolomite+chlorite assemblage; Tlc+chl = talc+chlorite; Fe/MgCb+fu = Fe/Mg-carbonate+fuchsite (chrome-muscovite).

Low susceptibilities, however, do not uniquely identify felsic intrusive rocks and carbonate-altered samples. Fe-poor tholeiitic basalts (not differentiated from Fe-rich basalts on plots) have low susceptibilities that overlap with the susceptibility range of prospective carbonate altered rocks. This means that targeting low susceptibility areas will not exclusively target prospective rocks, and if possible, other criteria should be used to further discriminate the different rocks types that exist within the low susceptibility range.

Density

Density studies indicate that syenite and porphyritic rhyolite dikes have low densities compared to other rock types in and around the Hislop deposit area with ranges from 2.57-2.80 g/cm³ (Fig. 4.4, and Tab. 4.1). All other rock types and their altered equivalents have higher density ranges generally greater than 2.75 g/cm³. Density data may thus be used to further distinguish between low susceptibility felsic intrusive rocks, and low-susceptibility carbonate-altered rocks or Fe-poor tholeiitic basalts, where felsic rocks would have low susceptibilities and low densities, and carbonate-altered rocks and Fe-poor tholeiites would have low susceptibilities and higher densities.

Although density ranges for least-altered and altered mafic and ultramafic rocks generally overlap, a trend of increasing density in altered ultramafic rocks with carbonate alteration was indicated (Fig. 4.5b, and Chapter 2). This suggests that where ultramafic rocks are known to dominate within an area, it may be possible to identify carbonate-altered rocks using density in addition to susceptibility.

Resistivity and chargeability

Resistivity values measured in the lab are not consistently representative of larger scale measurements since there can be large scale features in the rock controlling resistivity that are not present at the hand sample scale (www.zonge.com/LabIP.html). For interpreting resistivity data and relationships to geology, sample measurements are best compared to one another on a relative scale. From Hislop physical property studies, resistivity was determined to be partly controlled by rock texture, specifically porosity and schistosity. Low resistivity (or high conductivity) values associated with sheared and

porous ultramafic volcanic rocks may distinguish them from other Hislop rock types, which otherwise have higher, overlapping ranges of resistivity (Fig. 4.6). A pattern of increasing resistivity with carbonate-alteration occurs in ultramafic rocks. The increased resistivity ranges related to carbonate-altered ultramafic rocks, however, begin to overlap with the resistivity ranges for other rock types.

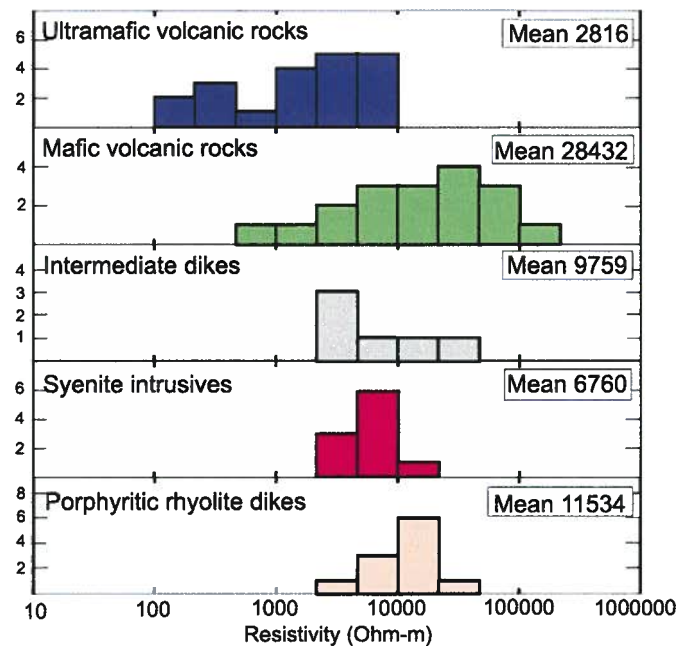


Figure 4.6. Resistivity histograms for Hislop deposit rocks. Data indicates lower overall resistivities for ultramafic volcanic rocks from Hislop.

Although most sulfides are known to be conductive (Telford et al., 1990), there were no significant correlations observed between pyrite abundances derived from XRD (Rietveld) analyses and resistivity during physical property work (Chapter 2, Appendix 2G).

Compared to resistivity measurements, chargeability measurements made in the lab are less inconsistent with larger scale measurements, and can thus be trusted to better represent in-situ chargeability. Chargeability values do not distinguish between different

rock types at Hislop as chargeability ranges essentially overlap for the suite of samples (Fig. 4.7). Although it is widely known that chargeability is strongly controlled by the presence of sulfide minerals (Telford et al., 1990), physical property studies at Hislop indicate only a weak trend between pyrite abundance and chargeability, and only for felsic rocks (Fig. 4.8). Chargeability studies at Hislop also suggest that porosity may decrease chargeabilities, complicating relationships between this physical property and mafic volcanic rocks (Fig. 4.9, Chapter 2). Despite the lack of direct correlation between sulfides and higher chargeabilities for Hislop drillhole and surface samples, induced polarization has been used successfully to target sulfides in previous exploration efforts in similar geological settings (Johnson et al., 1989; Bate et al., 1989; Hallof and Yamashita, 1990).

4.1.4. Inversion background

Geophysical inversion methodology is regularly used throughout industry, government, and academia, to investigate the Earth's subsurface geology and explore for mineral deposits (Oldenburg et al., 1998). Geophysical inversion can be considered the opposite of geophysical forward modeling processes. Whereas forward modeling involves calculation of a geophysical response from a known, or hypothetical subsurface physical property model, geophysical inversion involves a calculation of the subsurface arrangement of physical properties, based on surface measurements, that is capable of causing an observed dataset.

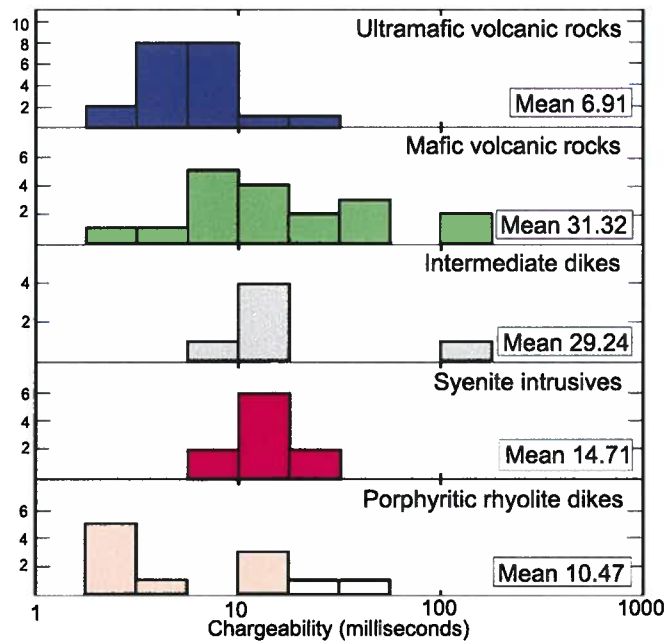


Figure 4.7. Chargeability histograms for Hislop deposit rocks. Chargeability ranges for the individual rock types overlap and are not unique.

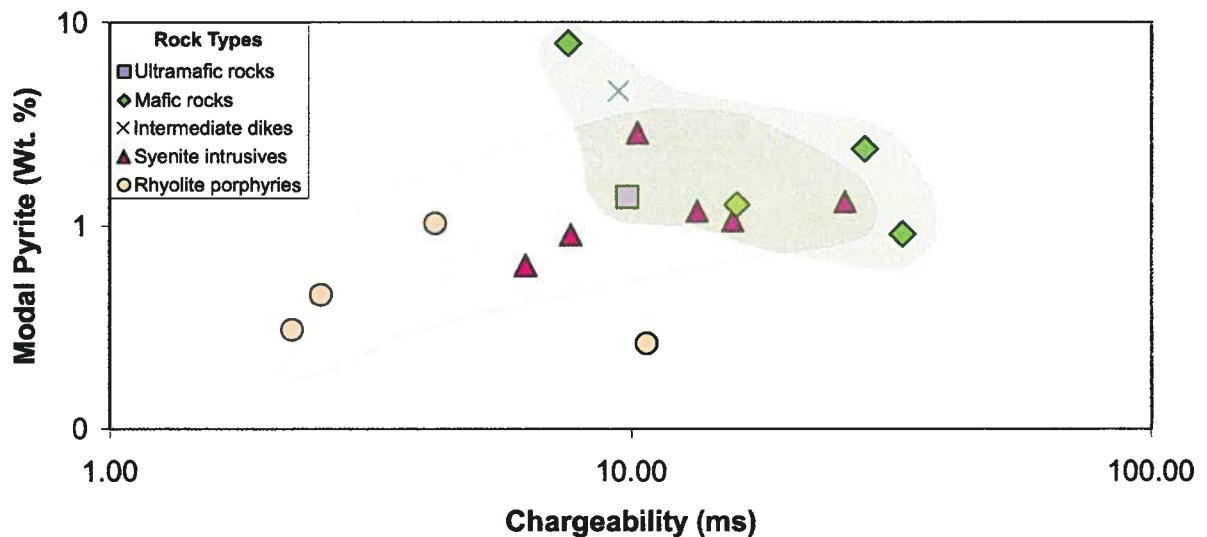


Figure 4.8. Chargeability plotted against pyrite abundance for Hislop samples. A weak positive correlation exists between pyrite abundance and chargeability, however the trend is mainly controlled by porphyritic rhyolite dike and syenite samples. There is no evidence of a consistent relationship between chargeability and pyrite abundance for intermediate to ultramafic volcanic rocks.

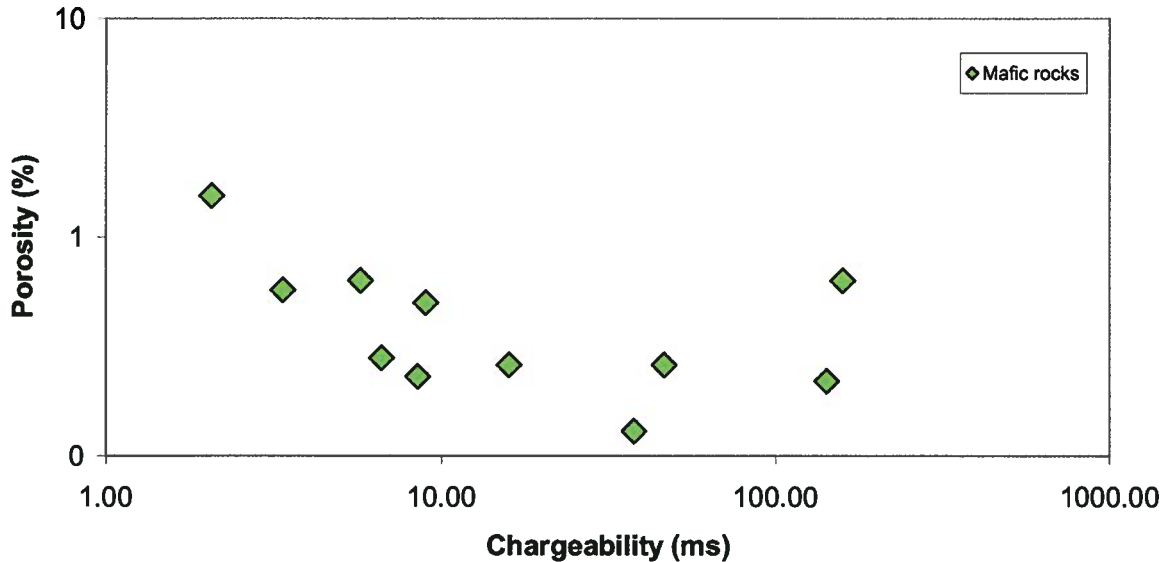


Figure 4.9. Chargeability versus porosity for mafic rock samples from Hislop. A negative correlation between chargeability and porosity in this plot indicates that increases in porosities of mafic volcanic rocks at Hislop may hinder the ability for metallic minerals to become charged.

One of the limitations of inverting geophysical data is that the solution is non-unique. Due to the fact that there are a greater number of unknowns (i.e. cells in the discretized model volume), than there are data, the problem is underdetermined. There are many distributions of physical properties that can cause the same observed data set. To alleviate this non-uniqueness, a model objective function, or model ‘goal’, is defined, so that the model outcome is consistent with expected geology. Additionally, a specific misfit must also be achieved between observed data and predicted data calculated from the recovered model. The inversion process is an iterative process. The model will be re-computed numerous times in an attempt to minimize differences between the predicted and observed data sets, and to satisfy the terms of the model objective function. Detailed inversion calculations can be found in Li and Oldenburg’s (1996, and 1998) papers on 3D gravity and magnetic inversions.

Where geology is better understood, and/or where physical property data is available (published data, downhole data, drill core, or outcrop measurements) inversions can be more thoroughly constrained. Physical property data, or reference models are incorporated into the discretized volume of interest. The model then has to be estimated

such that the incorporated data is honored. Physical property bounds can be specified to limit the range of values that are allowed to be taken up by the model cells. Finally, smoothing of physical properties in the x, y, or z directions using weightings written into the inversion algorithm (alpha weightings, α_x , α_y and α_z) can invoke geological directionality.

Constraining inversions should result in more accurate models, and better estimated physical properties throughout the model (Phillips, 2002; and Williams, 2006; also Chapter 3). It also further reduces non-uniqueness. Generating multiple inversion models with varying constraints will result in improved interpretations of the models - consistently occurring features between model results can be assigned higher confidence.

4.2. INVERSION APPROACH

4.2.1. General strategy

Unconstrained inversions of airborne magnetic data, airborne gravity data, and DC resistivity and IP data, were completed over the Hislop deposit area. As there exists a significant amount of magnetic susceptibility data for Hislop deposit area rocks, and there are well-established relationships between magnetic susceptibility and geology, magnetic inversions are also inverted with constraints incorporated via reference models built using William's (2008) GIFTtools ModelBuilder software. Constraining data include downhole susceptibility measurements, and surface sample susceptibility measurements. Additionally, cells within the model mesh where the physical property values can be estimated based on interpreted geology are also constrained. Further details on ModelBuilder applications are given in section 2.5. Both unconstrained and constrained magnetic inversion results are presented herein. Gravity, DC resistivity, and IP inversions are constrained using only 'non-located' constraints, as described by Phillips et al., (1997), which are applied globally to the model. Non-located constraints, such as global reference models, and bounds on physical property ranges, were used successfully to improve inversion results in synthetic modeling studies (Chapter 3). Only constrained gravity, DC

resistivity, and IP inversion results are presented here, although all results are included in Appendix 4A.

Inversion results are interpreted with respect to mapped and interpreted surface geology, and geology logged from drill core. Recovered models are interrogated through querying based on relationships between geology (lithology, alteration, mineralization), and physical properties (magnetic susceptibility, density, resistivity, and chargeability), identified during physical property studies on the Hislop gold deposit (Chapter 2).

4.2.2. Magnetic inversions

A high resolution airborne magnetic survey completed in 2002 covers an area of roughly 58 km by 20 km in the eastern Abitibi greenstone belt. Lines were flown north-south, at spacings of 50 m, and data was collected along lines at 7-10 m intervals. The magnetic data extents are shown in Figure 4.10, and the magnetic data are given in Figures 4.11 to 4.13. The datasets to be used in the inversion must include estimated standard deviations. For the Hislop magnetic datasets, the assigned standard deviation was 2-5%, and a floor value of 2-5% of the maximum measured field strength (in nT) was added, such that very low values do not have unrealistically low errors. All survey parameter details are compiled in Table 4.2.

Magnetic inversions are completed at three scales, referred to in this study as 'regional scale' (20 km x 18 km), 'local scale' (6 km x 4 km), and 'deposit scale' (2 km x 1.5 km). Cells making up the core volume of interest in the regional, local, and deposit scale models are 200 m², 50 m², and 25 m², respectively. Inversion parameters are detailed in Table 4.3. Local and deposit scale inversions are completed from magnetic data that has had larger scale magnetic signatures removed using regional removal methods described by Li and Oldenburg (1998). There is not sufficient data coverage to remove any larger scale geophysical signatures for the Hislop 20 km x 18 km regional scale inversions.

Surface data extents and inversion volumes (Tabs. 4.2 and 4.3), were chosen based on maximum coverage required to explain any subsurface features that might occur within the core volume of interest. Padding cells were added along the perimeters of the inversion

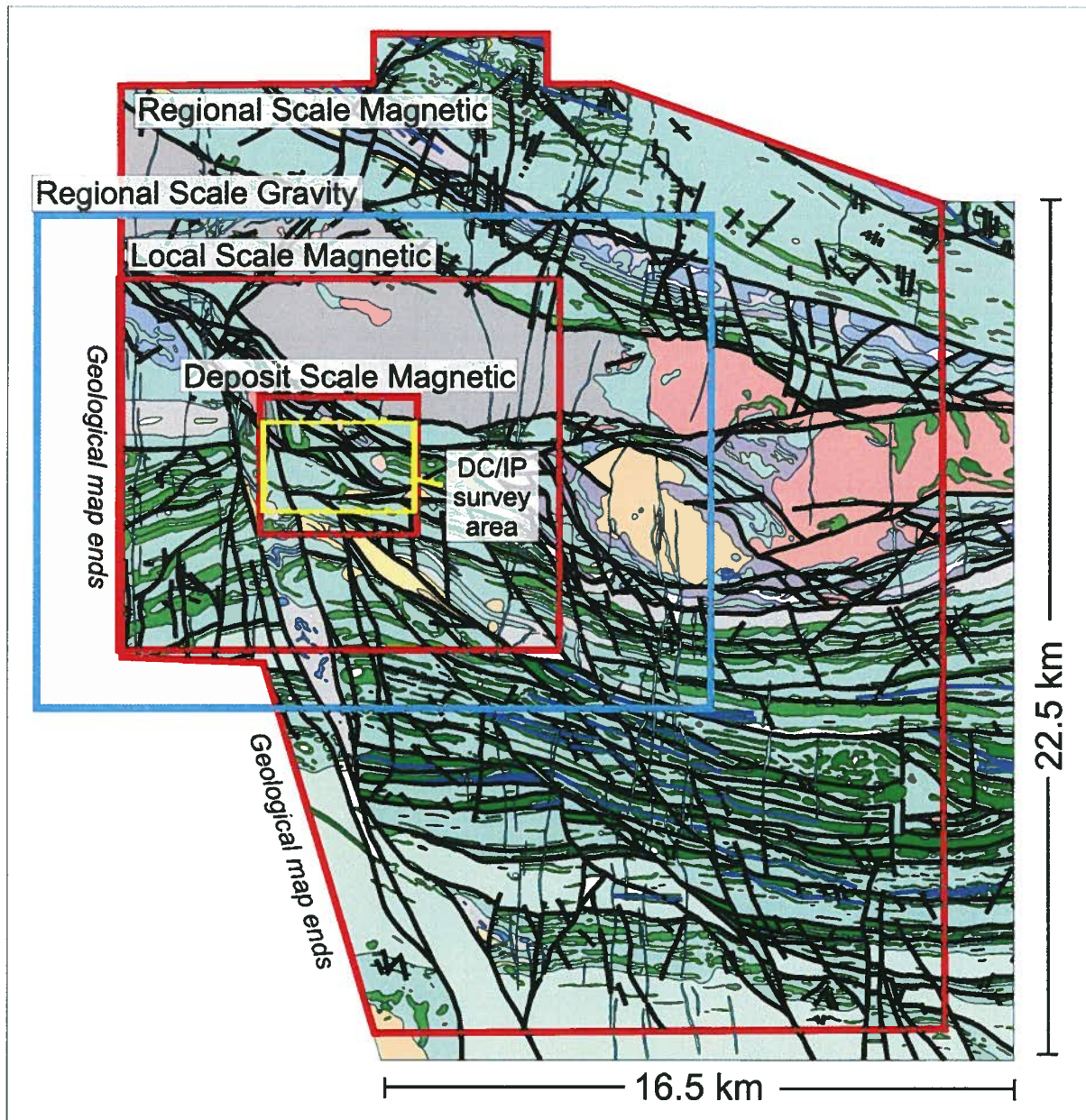


Figure 4.10. Extents of magnetic data used in the deposit-, local-, and regional-scale magnetic inversions (red outlines), of gravity data (blue outline) used in the regional-scale gravity inversion, and of DC Resistivity and IP data used in corresponding deposit and local scale inversions (yellow outline). Geological map from Power et al., 2004. See Figure 4.2 for geology legend.

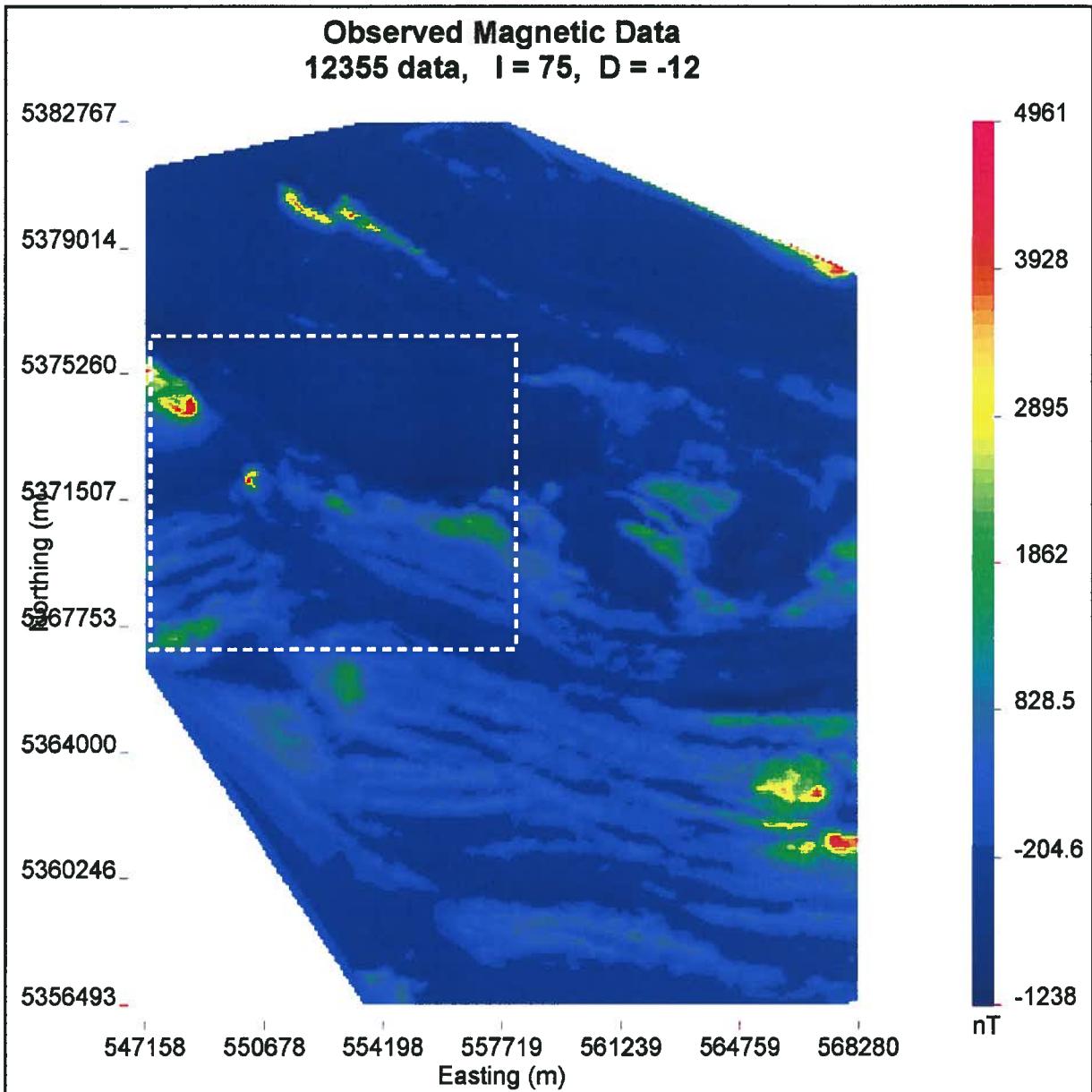


Figure 4.11. Data used in regional-scale magnetic inversion. Local-scale magnetic dataset outlined. Refer to Figure 4.10 for corresponding geology.

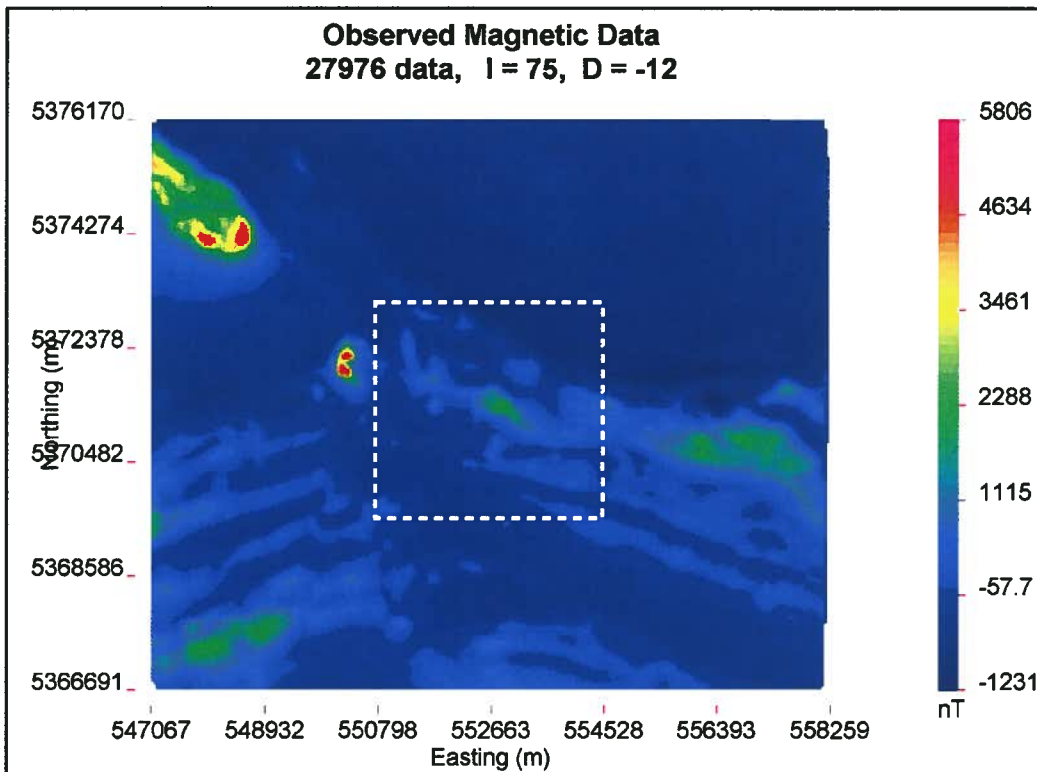


Figure 4.12. Data used in local-scale magnetic inversion. Deposit-scale magnetic dataset outlined. Refer to Figure 4.10 for corresponding geology.

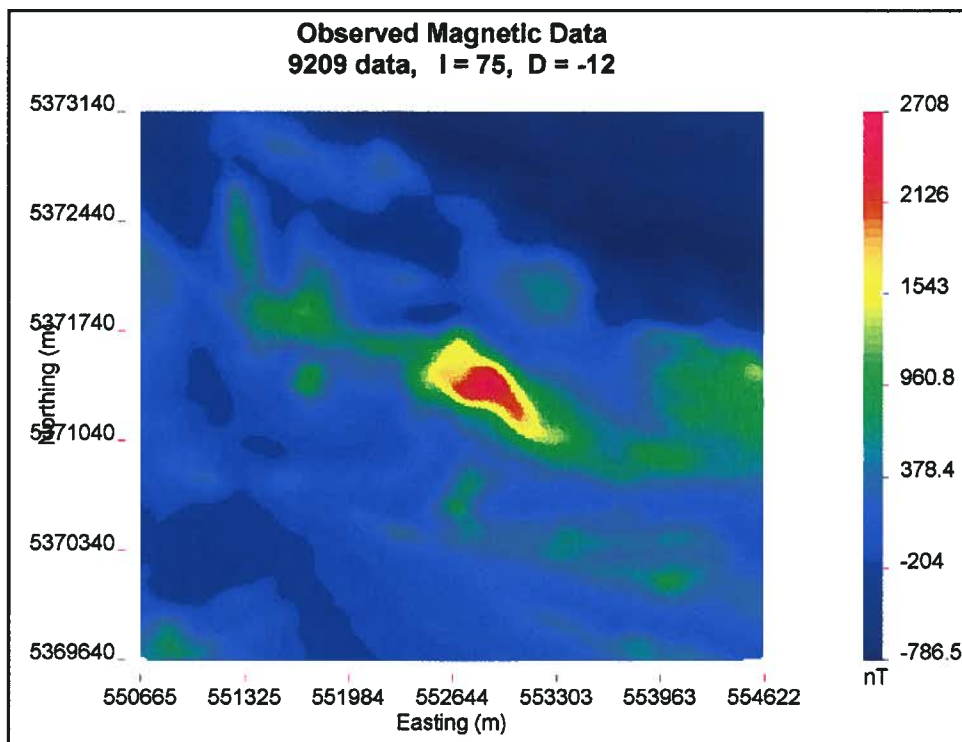


Figure 4.13. Data used in deposit-scale magnetic inversion. Refer to Figure 4.10 for corresponding geology.

Table 4.2. Survey parameters.

Model	Data area (UTM)	Lines	Line spacing	Station Spacing	Height	# Data	Data errors	Year	Other information
Magnetics (regional)	x: 547158 - 568280 y: 5356493 - 5382767	N-S	200 m	200 m	draped 50 m	12361	5%; 300nT floor	2002	Inclination:75°; Declination:-12°; Strength: 57478 nT
Magnetics (local)	x: 547067 - 568259 y: 5366691 - 5376170	N-S	margins (100 m) centre (~50 m)	margins (100) centre (~50)	draped 50 m	27982	2%; floor 140nT	2002	Inclination:75°; Declination:-12°; Strength: 57478 nT
Magnetics (deposit)	x: 550665 - 554622 y: 5369640 - 5373140	N-S	50 m	25 m	draped 50 m	9209	2%; floor 50nT	2002	Inclination:75°; Declination:-12°; Strength: 57478 nT
Gravity	x: 545003 - 561995 y: 5365060 - 5377899	E-W	500 m	250 m	constant 468 m	1850	0.01 mGal floor	2003	
DC Resistivity (local)	x: 550100 - 555300 y: 5370100 - 5372400	SW-NE	100 m	20 m	ground	6545	10% max. Voltage	1996	Realsection survey - 5 Tx spacings: 1000 m, 1500 m, 2000 m, 2400 m, 3200 m (26 lines)
DC Resistivity (deposit)	x: 551100 - 554300 y: 5370400 - 5372400	SW-NE	100 m	20 m	ground	4576	10% max. Voltage	1996	Realsection survey - 5 Tx spacings: 1000 m, 1500 m, 2000 m, 2400 m, 3200 m (20 lines)
IP (local)	x: 550100 - 555300 y: 5370100 - 5372400	SW-NE	100 m	20 m	ground	6545	10% max. Voltage	1996	Realsection survey - 5 Tx spacings: 1000 m, 1500 m, 2000 m, 2400 m, 3200 m (26 lines)
IP (deposit)	x: 551100 - 554300 y: 5370400 - 5372400	SW-NE	100 m	20 m	ground	4576	10% max. Voltage	1996	Realsection survey - 5 Tx spacings: 1000 m, 1500 m, 2000 m, 2400 m, 3200 m (20 lines)

Table 4.3. Inversion parameters.

Inversion	# Data	Inversion core extents (UTM)	# Core cells	Core cell size	# Padding cells	Achieved misfit	Other
Magnetics (regional)	12361	x: 541700 - 563500 y: 5381350 - 5361550 z: 500 - (-)4700	280566	200 m ³	178101	12321	<i>unconstrained</i> : $\alpha_s = 0.0001$, $\alpha_{xyz} = 16$;
Magnetics (local)	27982	x: 550050 - 555150 y: 5369780 - 5373080 z: 450 - (-)2150	165312	centre 50 m ³ margins 100 m ³	116928	29190 (unconstr.) / 28452 (constr.)	<i>unconstrained model</i> : default alphas; <i>constrained model</i> : using reference model built in GIFtools (Tab. 4.4); $L_{xyz} = 200$
Magnetics (deposit)	9209	x: 551630 - 553630 y: 5370640 - 5372140 z: 450 - (-)550	192000	25 m ³	236064	9013/ 9142	<i>unconstrained model</i> : default α values; <i>constrained model</i> : using reference model built in GIFtools (Tab. 4.4); $L_{xyz} = 100$
Gravity	1850	x: 547500 - 559500 y: 5367400 - 5375400 z: 500 - (-)1500	15360	250 m ³ (xy); 200 m ² (z)	56460	1892/ 1856	<i>unconstrained</i> : $L_{xy} = 500$, $L_z = 400$ <i>constrained</i> : $L_{xy} = 750$, $L_z = 600$
DC Resistivity (local)	6545	x: 550700 - 554700 y: 5370100 - 5372400 z: 400 - (-)800	51520	50 m ³	159680	6529/ 6455	Near-surface cell weightings applied; <i>unconstrained</i> : default alphas; <i>constrained</i> : $L_{xz} = 200$; $L_y = 100$; reference value = 0.00015 S/m
DC Resistivity (deposit)	4576	x: 551500 - 553900 y: 5370400 - 5372400 z: 400 - (-)200	184320	25 m ³	249856	4670/ 4486	Near-surface cell weightings applied; <i>unconstrained</i> : default alphas; <i>constrained</i> : $L_{xz} = 100$; $L_y = 50$; reference value = 0.00015 S/m
IP (local)	6545	x: 550700 - 554700 y: 5370100 - 5372400 z: 400 - (-)800	51520	50 m ³	159680	6369/ 6445	Near-surface cell weightings applied; <i>unconstrained</i> : default alphas; <i>constrained</i> : $L_{xz} = 200$; $L_y = 100$; reference value = 0.031 ms
IP (deposit)	4576	x: 551500 - 553900 y: 5370400 - 5372400 z: 400 - (-)200	184320	25 m ³	249856	4412/ 4519	Near-surface cell weightings applied; <i>unconstrained</i> : default alphas; <i>constrained</i> : $L_{xz} = 100$; $L_y = 50$; reference value = 0.031 ms

Topography used in all models

Relationship of α (alpha weight) to L (length scale): $(L_x)^2 = (\sqrt{\alpha_x/\alpha_s})^2$; similar for L_y , L_z

volumes to a distance that is required to explain any features that might occur in the dataset but not directly within the volume of interest.

Topographical information was used in all inversions. Topography data was downloaded from the Shuttle Radar Topography Mission (SRTM) online database. Data was collected at approximately 90 m spacings.

Located constraints applied to magnetic inversions are discussed in Section 2.5.

4.2.3. Gravity inversions

Airborne gravity surveys over the northeastern, northwestern, and southern Timmins areas were completed in 2003 as part of the Discover Abitibi Initiative (Ontario Geological Survey, 2004). For the eastern Timmins survey (Fig. 4.10 and Fig. 4.14), lines are east-west trending, and 500 m apart. Data spacing is 120 m (Tab. 4.2). Two north-south trending tie lines occur 5 km apart. The sparse data spacing meant that only a regional scale inversion could be performed with cell sizes of 250 m to correspond with an intermediate spacing between the 500 m lines and the 120 m data spacing (Tab. 4.3). Regional removal was not performed on the gravity data, as the gravity dataset does not extend far enough beyond the chosen regional scale area to effectively remove a regional signature. A good correlation between gravity data and mapped geology indicates that a larger regional trend does not contribute strongly to the dataset, and the lack of a regional removal should not be detrimental to the inversion result. Gravity data was assigned standard deviations of 0.01 mGal for Hislop gravity inversion work.

Regional gravity inversions were constrained with non-located constraints. Bounds were used to restrict densities in the inversion result to within the range expected for the rocks in the study area, and inversion smoothing weightings were increased.

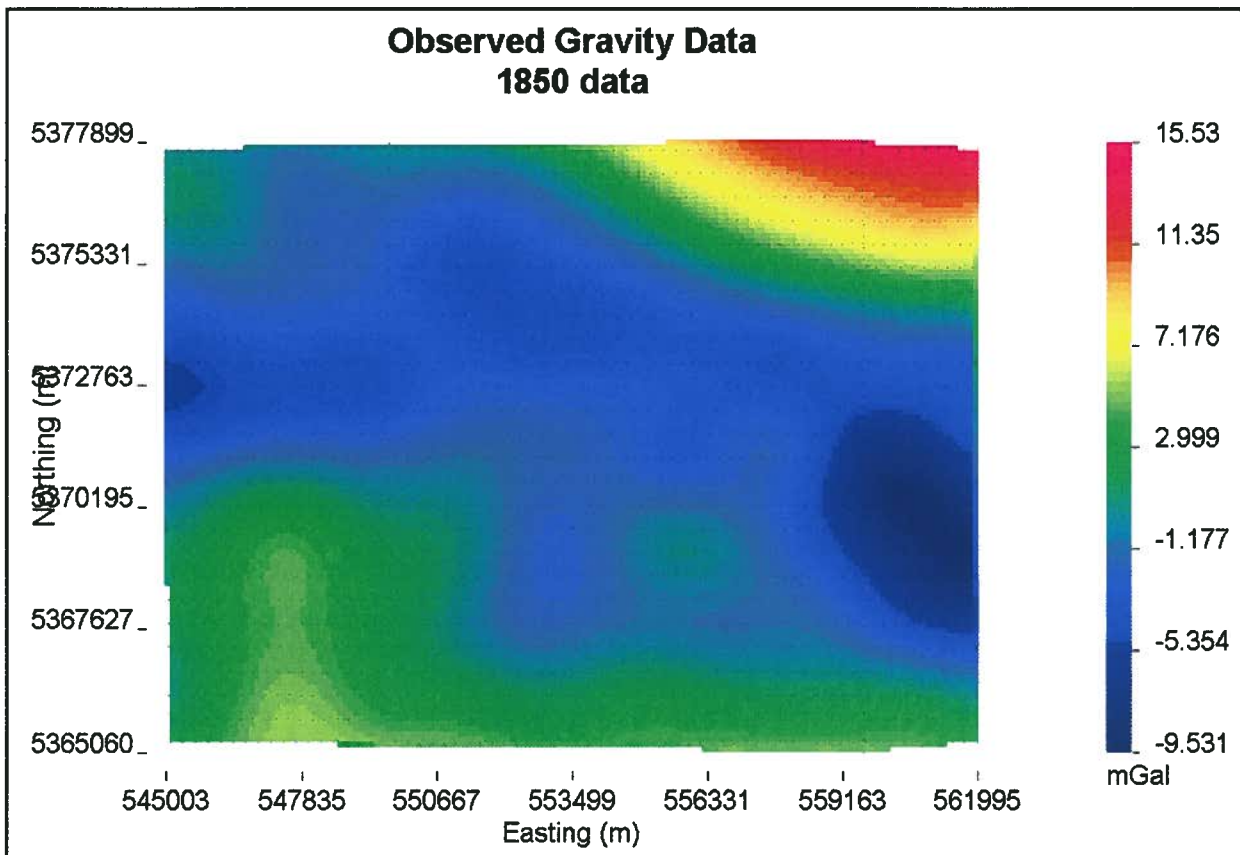


Figure 4.14. Data used in regional-scale gravity inversion. Refer to Figure 4.10 for corresponding geology.

4.2.4. DC resistivity and IP inversions

A combined DC Resistivity and induced polarization (IP) survey was completed in 1996 (Roscoe and Postle, 1998). Thirty-nine lines of Realsection data were collected (Fig. 4.15). Lines were spaced 100 m apart, transmitter electrodes were spaced from 1000 m up to 3200 m along lines, and receiver electrode spacing was 20 m. Measurements were made in time domain for both DC resistivity and IP surveys. The required data format for inversion of DC resistivity data is the potential in Volts normalized by the current (DCIP3D User Manual, version 2.1).

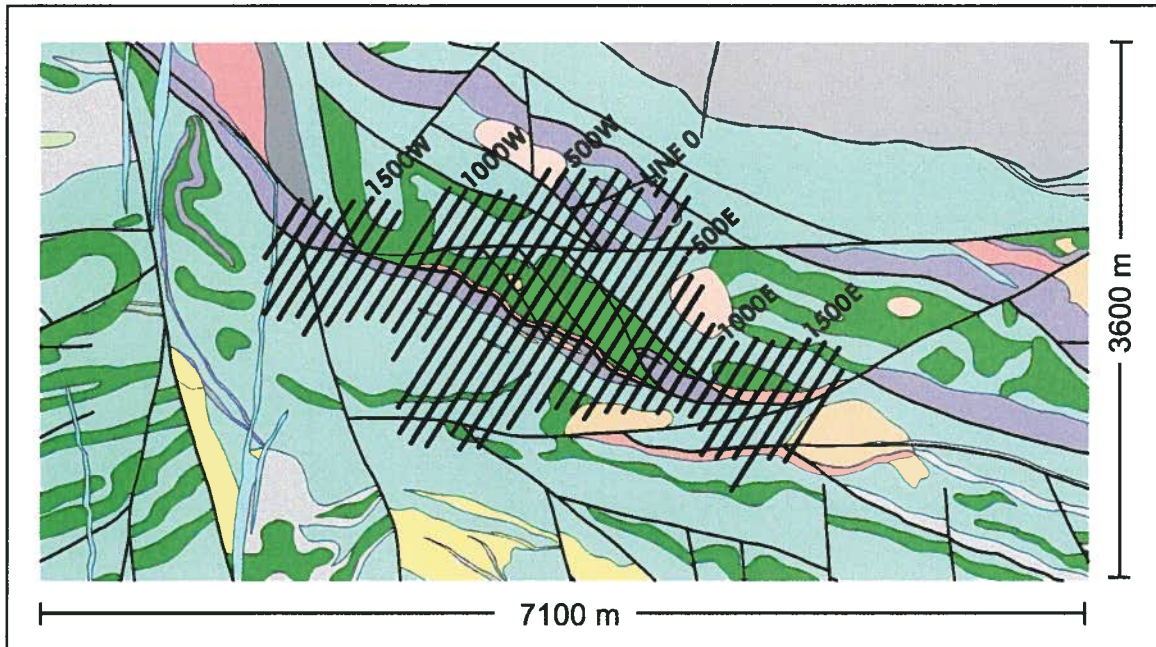


Figure 4.15. Location of DC resistivity and IP lines used for 3D DC resistivity and IP inversions. Local mine grid line numbers shown. See Figure 4.2 for geology legend.

Induced polarization effects are caused by the build up of charge at physical interfaces within a medium. Chargeability is measured by assessing the decay of voltage over time when the electrical current is shut off (Telford et al., 1990). Data over the Hislop deposit was collected over 10 different time windows. Measured data is in mV/V and a total apparent chargeability is calculated for this work as the sum of the voltages recorded for time windows 2 to 8, multiplied by 0.8. The value is divided by 1000 to get data into the form V/V, the correct units for IP inversion calculations. Standard deviations on DC resistivity data and IP data are assigned at 10%, with a floor of 10% of the maximum voltage to avoid small errors on low data values (Tab. 4.2).

When DC resistivity and IP data are displayed as pseudosections, the depth is usually arbitrarily assigned for visualization purposes based on n-spacings, or the distance between the transmitters in this case (Telford et al., 1990). Pseudosections are simply a method of displaying the data, and the z-scale does not represent depth. The positions and shapes of features also do not likely reflect the true geology. Inverting DC

resistivity and IP data is thus very useful as it can indicate the correct location of features, and can resolve the true shape of features within the subsurface.

2D DC resistivity and IP inversion models were initially completed separately for each of the 39 survey lines prior to running 3D inversions. This helped to determine appropriate errors for 3D inversions, and to examine depth of investigation (Oldenburg and Li, 1999). 2D results were also compared to cross-sections through 3D inversion results, and consistencies between the two indicated robust, consistent modeling (Appendix 4B).

A 4 km x 2.3 km area, and a 2.5 km x 2 km area immediately surrounding the Hislop deposit were focused on for the 3D DC resistivity and IP inversions. The core volume for the 'local' scale inversions was discretized into 50 m² cells, and the core volume for the 'deposit' scale models was discretized into 25 m² cells (Tab. 4.3).

Non-located constraints were used to refine local scale and deposit-scale DC resistivity and IP inversions. A global reference model of 0.00015 S/m was applied to DC resistivity inversions, and a reference model of 0.031 ms was applied to IP inversions. This acts to guide results toward reasonable values consistent with prior physical property information. α_x and α_z , were increased relative to α_y , to impart known geological fabrics.

4.2.5. Constraining magnetic inversions with reference models built in Modelbuilder

Magnetic inversions at the local and deposit scales were constrained using geological and physical property data collected during Hislop physical property studies (Chapter 2). A test version of the UBC GIFtools ModelBuilder program (Williams, 2008) was used to compile the geological and physical property data into a reference model.

To build susceptibility reference models, susceptibility data from the Hislop physical property study, as well as from a regional physical property study focused on

geology west and south of the Hislop deposit area (Ontario Geological Survey, 2001), were used. Although the OGS regional study examined geology outside the extents of the Hislop study area, geological units are generally continuous across the greenstone belt, and relationships between physical properties and geology are expected to be consistent (Chapter 2).

Physical properties measurements made down hole, and on surface samples or outcrop, can be input into the reference model with the appropriate associated drillhole collar and survey information, and with XYZ locations. These measurements, along with their linked geological and alteration information, form the basis of a physical properties database for the reference model being created. Any other empirical geological information, including geological maps, outcrop maps, downhole geology logs, and 3D geological volumes, can be painted onto the model cells and subsequently translated into physical properties by way of the program looking up the average physical property value calculated from previous property measurements for the rock type identified in the model cell. Thus, it is possible to populate an entire layer of cells with physical properties based on a geological map that covers the area, or to populate all cells intersected by a drillhole without actual measurements made on the core. Since potential fields geophysics is sensitive to near-surface sources it is important to be sure that constraints used near-surface are reliable. Synthetic modeling testing inversion results for a Hislop-like geological setting (Chapter 3) showed that poor susceptibility estimation for near-surface cells can affect the distribution of susceptibility throughout the whole model. Thus, while geological maps are available covering the area surrounding the Hislop deposit, only outcrop observations were used to populate near-surface cells. Geological contacts and rocks types from outcrop maps were considered more reliable than larger scale regionally interpreted geology maps.

It is not uncommon to have more than one physical property data existing within one cell. For the Hislop deposit inversions, cells are 25 to 50 m. Susceptibility measurements were collected every 5 m on Hislop drillcore, adding 5 to 10 measurements to a single cell as a result. Where cells have more than one type of data

(e.g. downhole physical property measurements, plus data assigned based on geological mapping or logging) a single representative value must be chosen. The ModelBuilder program presents a number of options for choosing the representative value, depending on the types and amount of data available. For the Hislop susceptibility reference models, this value is the average of: a) the mean of actual physical property measurements, and b) the mean of measurements assigned based on geological observations, with both information sources considered equally reliable.

Smallness weights are assigned to the constrained cells. These weights relay to the inversion the degree of reliability of its assigned physical properties. If a high smallness weight is specified, the inversion will attempt to achieve values close to the cell's reference value. If properties within a cell are expected to be consistent over a surrounding volume, a 'buffer' can be designed around the cell. The information within the central cell is extrapolated to the cells of the buffer. Buffer cells might be assigned a low smallness weight, having a lower reliability than cells containing measured data.

Refer to Table 4.4 for all constrained model parameters chosen for magnetic inversions. The resulting susceptibility reference models constrain 10% of the local scale susceptibility model, and 8.4% of the deposit scale susceptibility models.

4.2.6. Inversion model display

Figure 4.16 outlines the surface extents of each of the model results to be discussed herein. Inversion results are displayed as cross-sections through the recovered 3D model for comparison to overlying mapped and interpreted geology. The location of the cross-section, indicated in Figure 4.16, is consistent between the displayed results, and represents a north-south slice through the model directly beneath the Hislop deposit. Isosurface models from each inversion result highlight the 3D distributions of anomalous material in the subsurface, and are interpreted based on previously noted correlations with geology. It is difficult to show the full 3D distribution of physical properties in a single 3D representation. To appreciate the shapes and depths of anomalous areas throughout

Table 4.4. GIFtools ModelBuilder options chosen for building Hislop reference models.

GIFtools parameters	Local scale magnetic inversion	Deposit scale magnetic inversion
Default parameters		
Lowest possible measurement (lower values rejected)	0	0
Highest possible measurement (higher values rejected)	3000x10 ⁻³ SI	3000x10 ⁻³ SI
Reference property value (where no constraining data exists in a cell)	0	0
Smallness weight (reliability weight - defines desired degree of closeness to reference model values)	1 (low)	1 (low)
Property lower bound (default upper bound where no data)	0	0
Property upper bound (default upper bound where no data)	1000x10 ⁻³ SI	1000x10 ⁻³ SI
Source data		
Downhole property measurements	1034	1034
Surface sample measurements	113	58
Drillholes with geological observations and property measurements	10	10
Drillholes with geological observations	1934	903
Weights and bounds		
Bounds assigned to a cell are controlled by the contained property data, and are defined by data within the confidence interval of:	99.7%	99.7%
Representative block size	25 m	25 m
% of block required to be filled before bounds allowed to be applied	75%	75%
Relative smallness weight (reliability weight) for surface measurements	100	100
Relative smallness weight for drilling measurements	100	100
Relative smallness weight for drilling geology logs	50	50
Relative smallness weight for outcrop geology map	50	50
Buffers		
Smooth interpolation across cells		
Maximum buffer distance for surface measurements	200 m	100 m
Maximum buffer distance for drilling measurements	200 m	100 m
Maximum buffer distance for drilling geology	200 m	100 m
Maximum buffer distance for outcrop map	200 m	100 m
Strike	115	115
Dip	90	90
Pitch	0	0
% model constrained	10%	8.4%
Models built		
Reference model & smallness weights		
Lower & upper bounds model		
Smoothness weights		

the model volume, the models should be viewed with a 3D viewer such as UBC-GIF's MeshTools3D, or with a Gocad viewer. The models and their associated meshes are included, along with a MeshTools3D model viewer, as an appendix on a CD accompanying the thesis (Appendix 4A). Instructions on how to use the viewer can be found on the UBC-GIF website, <http://www.eos.ubc.ca/ubcgif/>, under "Software manuals". Observed versus predicted data for all inversion results are plotted in Appendix 4C (on CD).

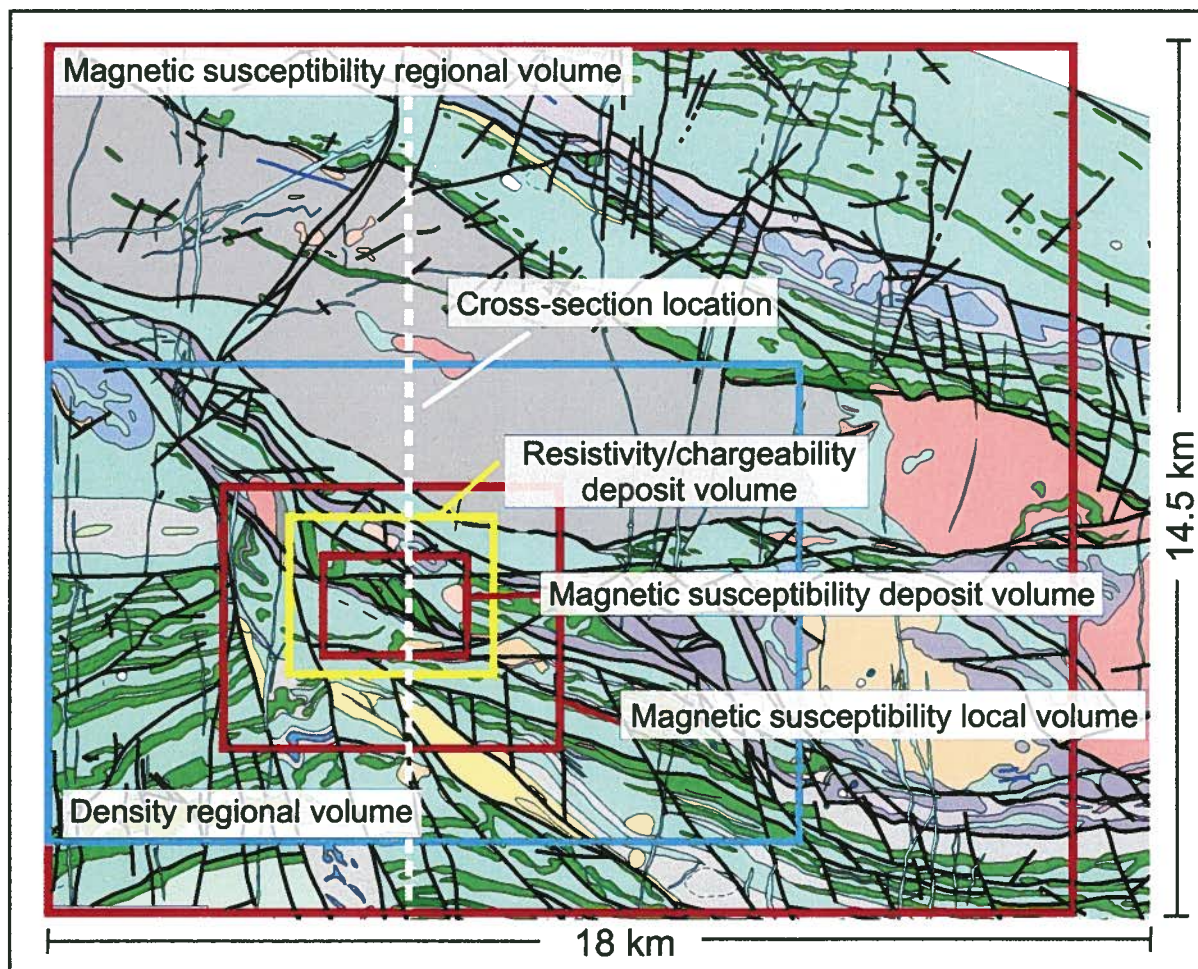


Figure 4.16. Extents of inversion model volumes, with cross-section location indicated.

4.3. INVERSION RESULTS AND ANALYSIS

4.3.1. Magnetic susceptibility models

Regional scale 18 km x 20 km model from unconstrained magnetic inversion

High susceptibilities ($>10 \times 10^{-3}$ SI Units) in the regional magnetic model are associated with the dark green units on the Hislop area geologic map, which correspond to Fe-rich tholeiitic basalts (Fig. 4.17). The faulting and folding of a series of Fe-rich mafic rocks near the center of the map area, seems to thicken this rock package causing the significant central high susceptibility anomaly. The central faulted package of Fe-rich basalt units that dominate the northern part of the Hislop deposit stratigraphy appear to bottom-out at a depth of ~3000 m. The anomaly conveys a steep dip to the southwest. A low susceptibility zone south of the central Fe-rich basalt package represents volcanic stratigraphy dominated by Fe-poor tholeiitic basalts and felsic volcanic rocks. It is not possible to distinguish between these two low susceptibility rock types in the susceptibility model result. High susceptibilities correlating with a series of Fe-rich volcanic flows persist through the southern region of the model, extending to depths of around 7000 m.

A strong contrast occurs between the central high susceptibility zone, and low susceptibility rocks in the north, which is interpreted to be the manifestation of the location of the Porcupine Deformation Zone. The belt scale PDDZ, mapped at the surface to occur along the southern margin of an Fe-poor basalt unit south of the Porcupine and Timiskaming assemblage sedimentary rocks, is indicated to dip about 45° - 60° southward beneath the interlayered mafic and ultramafic volcanic strata. This structure may be truncating mafic and ultramafic rock packages at depth. The very low susceptibility volume north of the interpreted fault likely represents the sedimentary rock sequences of the Porcupine and Timiskaming assemblages, or a combination of sedimentary rocks and Fe-poor mafic volcanic sequences.

The isosurface model in Figure 4.18 shows the regional subsurface distribution of Fe-rich mafic and ultramafic rocks recovered by the magnetic inversion.

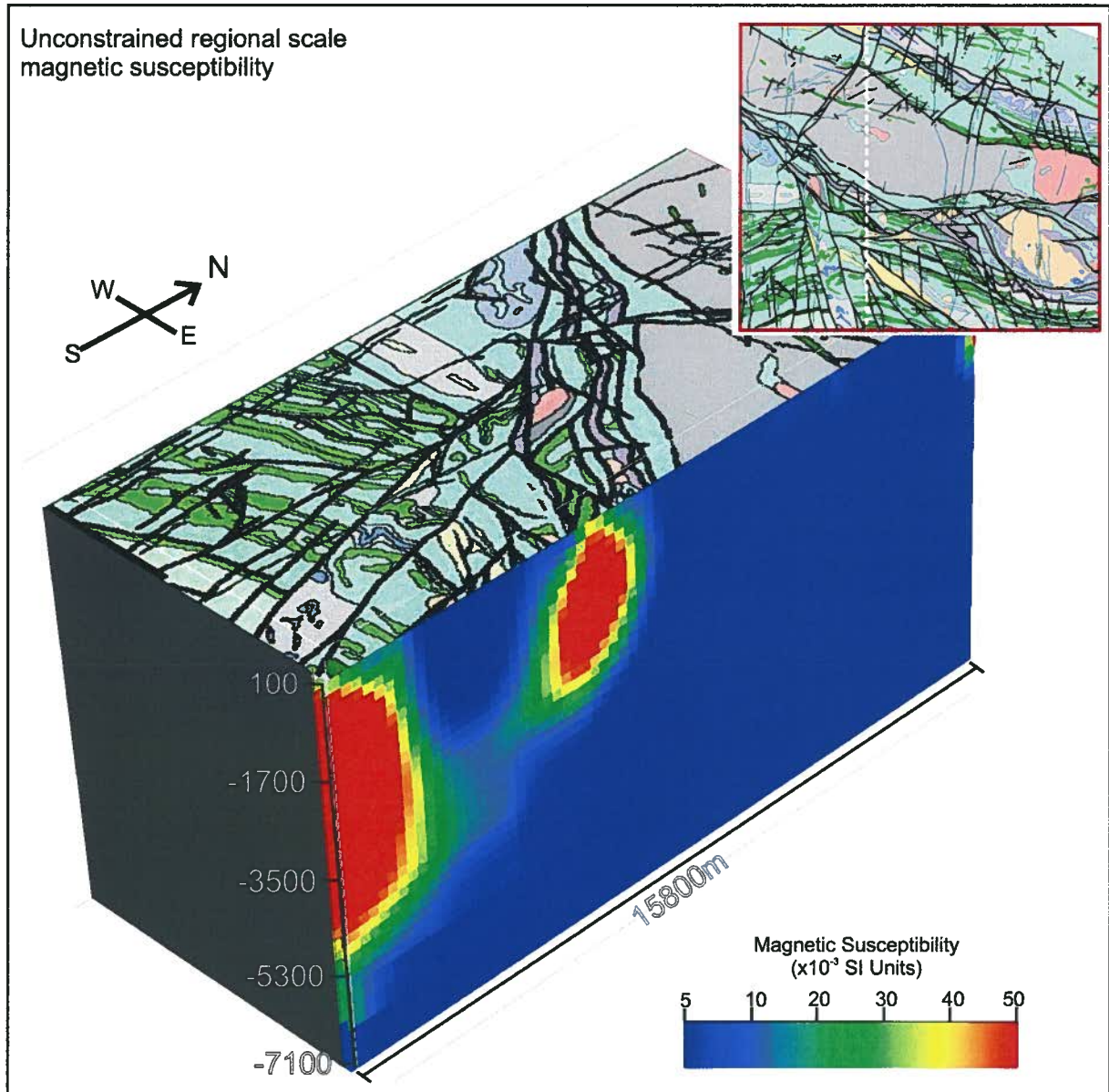


Figure 4.17. North-south cross-section through the regional-scale unconstrained magnetic inversion result, with overlying geologic map of the greater Hislop deposit area. For geological legend see Figure 4.2. Inset shows extent of model volume and cross-section location. Figure 4.16 can also be referred to.

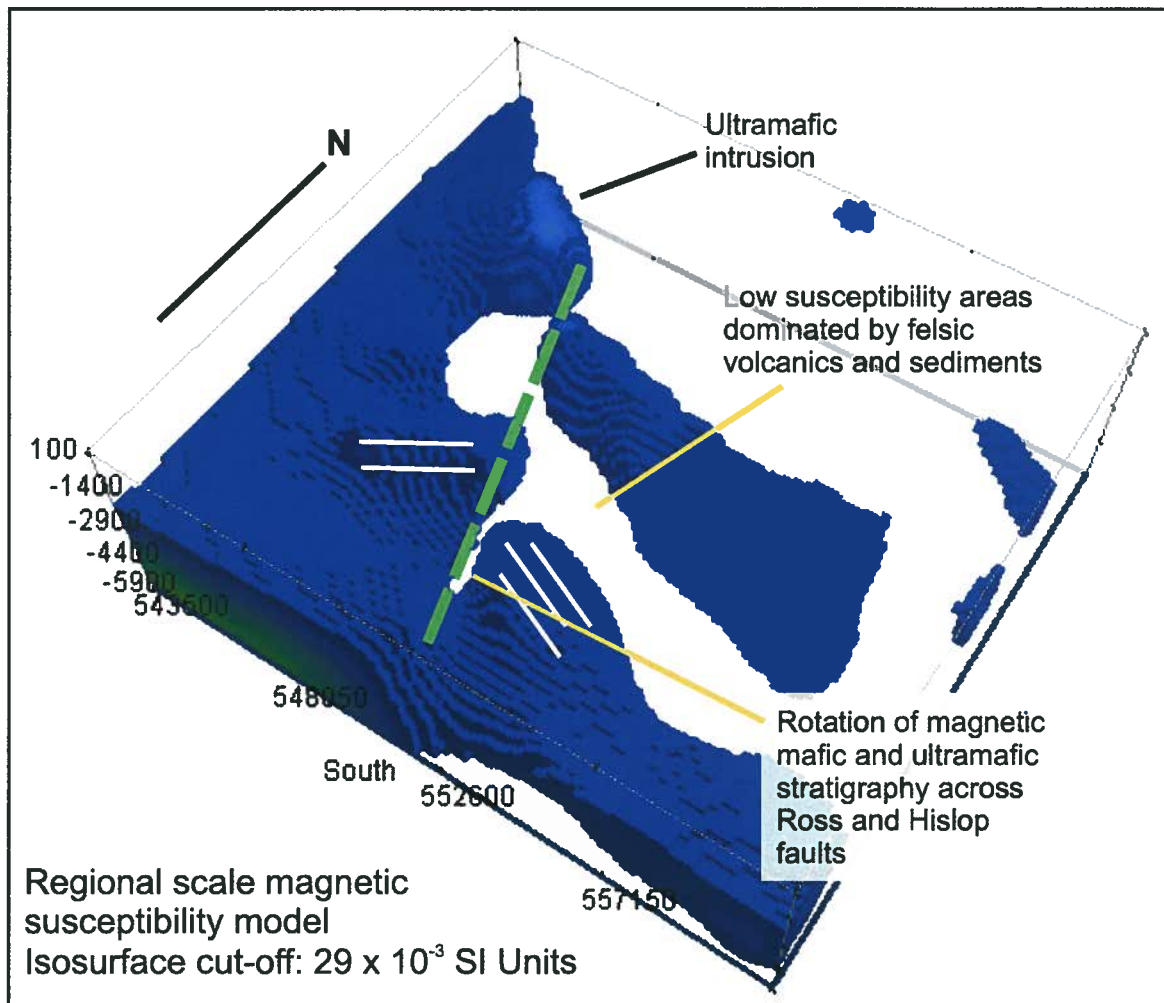


Figure 4.18. Isosurface model from regional scale magnetic inversion results.

Local scale 4 km x 6 km model

This inversion essentially zooms in on the structure of the central high susceptibility body seen in the regional magnetic inversion result.

Unconstrained inversion

The highest susceptibilities are related to the central Fe-rich tholeiitic basalts (Fig. 4.19a). The local scale inversion result suggests a ~2500 m depth for this basalt package, slightly shallower than the depth indicated in the regional result. This may be related to inversion-related smoothing over smaller distances in accordance with smaller cell sizes. The local scale model indicates the main susceptibility body is more structured than suggested in the regional model. The central susceptibility bodies extending in segments to depth gives the appearance of having once been one coherent unit, that was later dissected by near-vertical faults. A vertical low susceptibility zone in the south projects upward to correlate with a fault interpreted at the surface (the Ross Fault, Fig. 4.2). Magnetite in the rocks adjacent to these faults may have been destroyed as a result of structurally controlled CO₂-rich hydrothermal fluid circulation. As in the regional results, the Fe-rich basalts appear to dip generally southward.

Other, more narrow Fe-rich mafic and ultramafic units are associated with shallow high susceptibility bodies. A high susceptibility body to the north is likely related to a mapped ultramafic unit. The associated susceptibilities of this northern body are consistent with those of talc-chlorite rich ultramafic rocks from the Hislop physical property studies, being somewhat lower than susceptibilities characteristic of Fe-rich basalts (Chapter 2).

Low susceptibilities are associated with Fe-poor basalts, rhyolite units, felsic intrusives, and faulted areas. The extremely low susceptibility area north of the PDDZ and at depth is presumably reflecting thick packages of sedimentary rocks, which

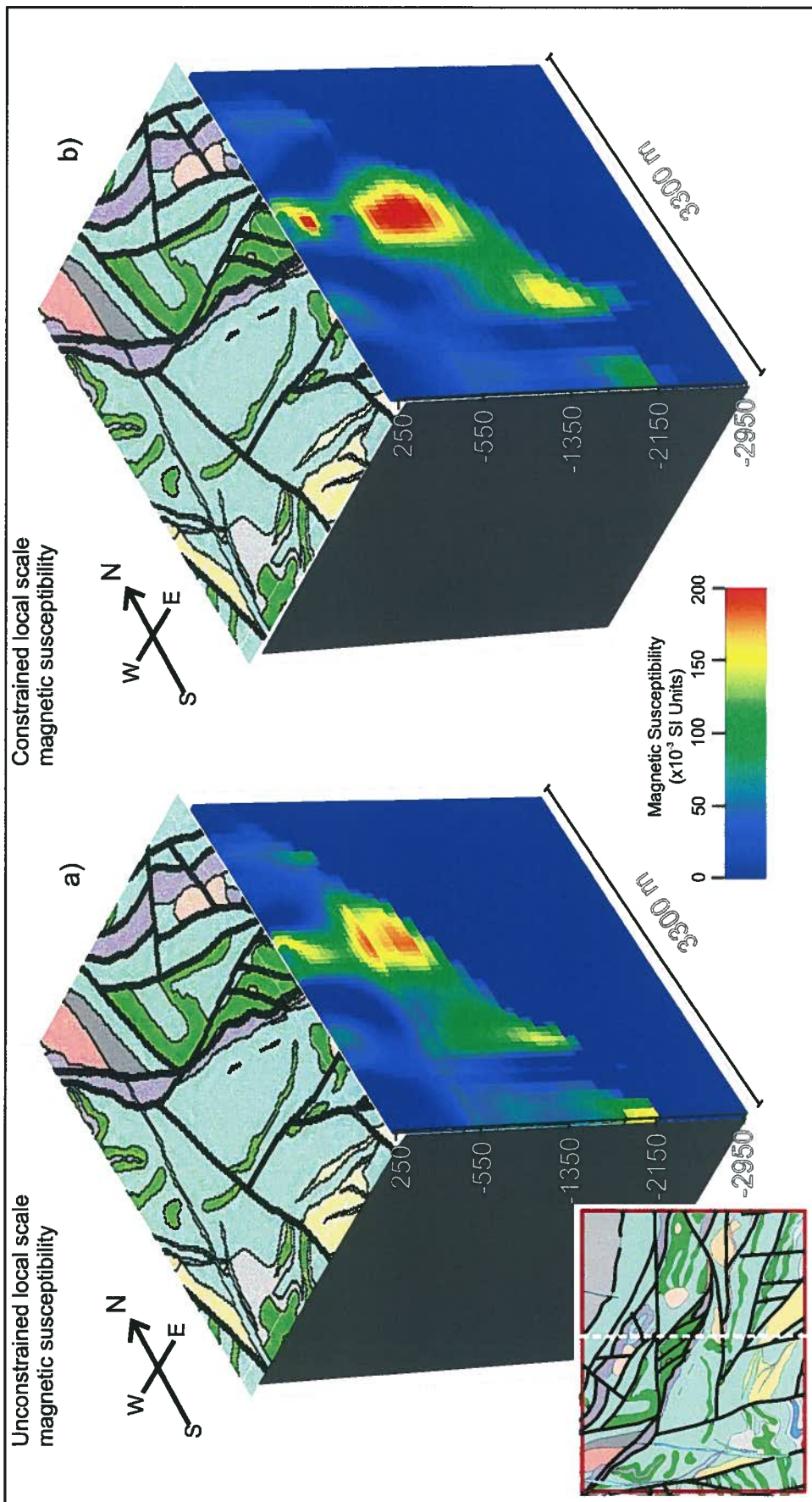


Figure 4.19. North-south cross-sections through the local-scale a) unconstrained, and b) constrained magnetic inversion results, with overlying geologic maps. The cross section spans the main ore zone at Hislop. For geological map legend see Figure 4.2. Inset shows extent of model volume and cross-section location. Figure 4.16 can also be referred to.

were mapped north of the PDDZ on the geological map (Fig. 4.2), or Fe-poor mafic volcanic rocks, also mapped in the northern areas.

The inferred Porcupine Deformation Zone, mapped just north of the northern ultramafic units, separates high and low susceptibility regions. Its dip is slightly shallower in this result than in the regional model result.

Constrained inversion

The constrained local scale results exhibit some noticeable differences from unconstrained results (Fig. 4.19b). The core high susceptibility body is clearly separated from a smaller susceptibility anomaly closer to the surface. The ultramafic body north of the high susceptibility Fe-rich basalt units is more clearly disconnected from the basalts, and now has a more wedge-like appearance. Constraining the result also pushes high susceptibility bodies to a greater depth, steepening the dip angle of the inferred PDDZ, making it more consistent with the $\sim 45^\circ - 60^\circ$ angle suggested in the regional model results. The steep dip angle of the central mafic volcanic rock package, and additional features not seen in the cross-section are illustrated in the isosurface model in Figure 4.20.

Deposit scale 1.5 km x 2 km model

This inversion focuses on the core portion of the central high susceptibility basalts interpreted from the local scale magnetic inversions. The goal is to attempt to uncover more fine scale structure, and to locate narrow low susceptibility syenite and rhyolite dikes, and alteration zones known to be spatially related to gold mineralization.

Unconstrained inversion

From the recovered model (Fig. 4.21a), a sharp gradient is obvious between the mapped Fe-rich basalt units, and the gold-related syenite. From synthetic modeling work (Chapter 3), an ultramafic rock-syenite dike contact was not detectable at these scales of inversion, and the equivalent contact is not obvious here. The ultramafic rocks south of the central syenite dike are

apparently low susceptibility, which, from physical property studies, could indicate their alteration to a carbonate-rich assemblage. Rhyolite dikes mapped to intrude the ultramafic unit could also be lowering the susceptibility here. Low susceptibilities are spatially related, in Figure 4.21, to Fe-poor mafic units, ultramafic units, and faulted rocks.

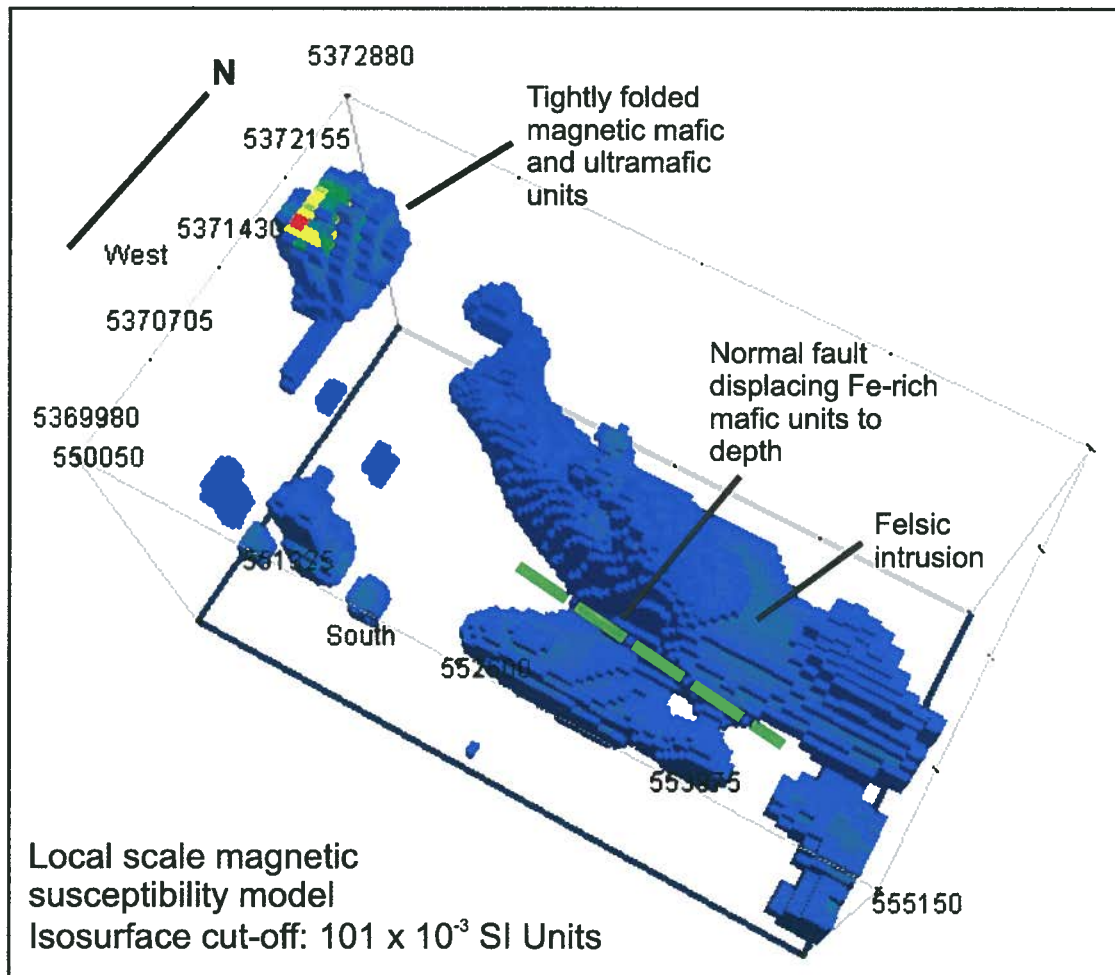


Figure 4.20. Isosurface model from local magnetic inversion results.

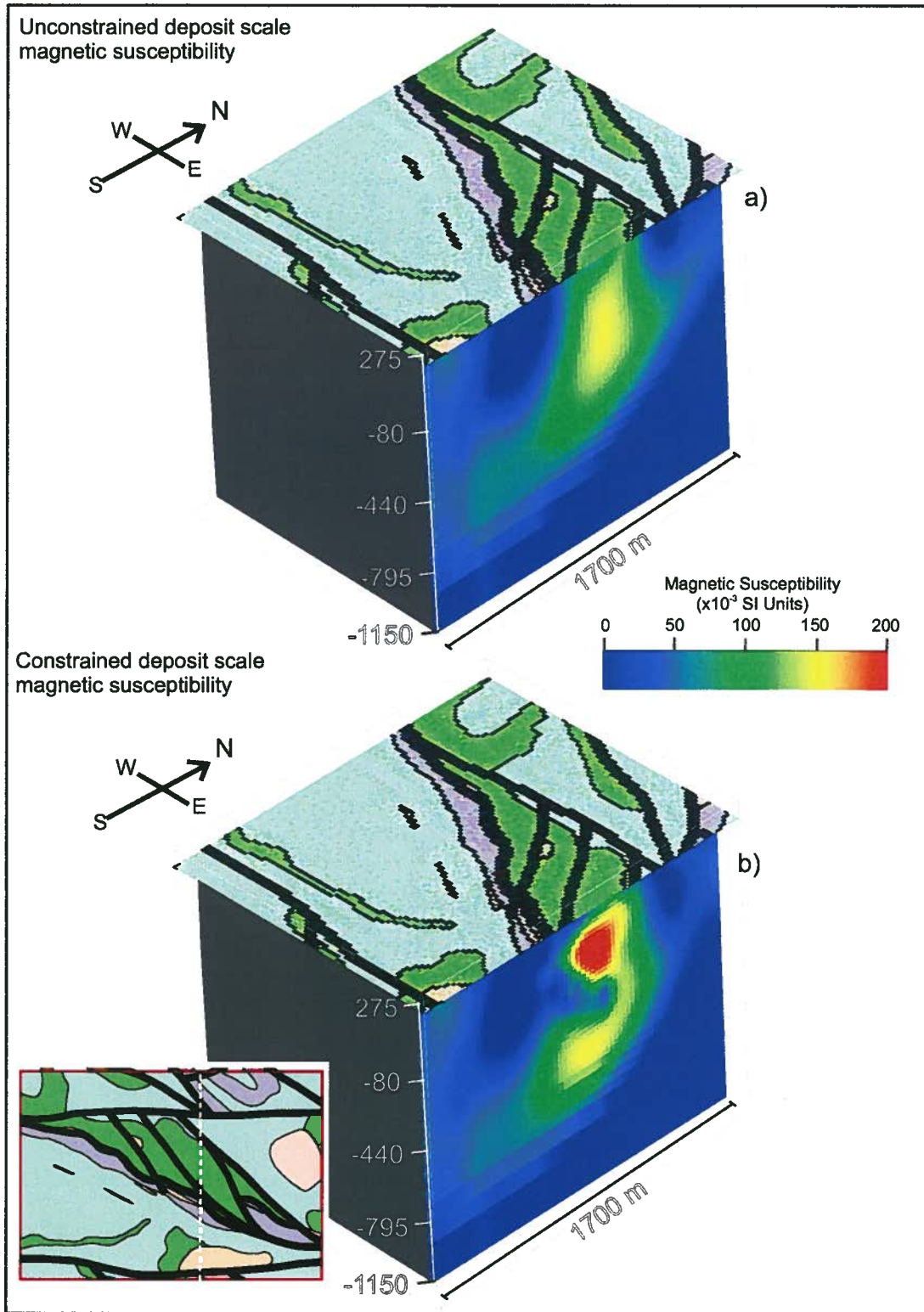


Figure 4.21. North-south cross-sections through the deposit-scale a) unconstrained, and b) constrained magnetic inversion results, with overlying geologic maps. The cross section spans the main ore zone at Hislop. For geological legend see Figure 4.2. Inset shows extent of model volume and cross-section location.

The depth of the anomaly (~1000 m), and dip angle of the bottom of the high susceptibility body is similar to the local inversion outcome. But, despite cell sizes being smaller in the deposit-scale model (25 m³), there is little more resolution gained. In fact, a separation in the anomaly apparent in the local result does not occur in the unconstrained deposit model. The apparent lower resolution at the deposit scale might be explained by the default α weightings or length scales (Mag3D User Manual, version 3.0, 2005). Length scales are applied in inversion work to manipulate smoothing in given directions according to cell size and prior geologic information. The default length scales used in magnetic inversions corresponds to cells sizes of 50 m (as was used in the local-scale inversions). Since the length scales were not reduced to correspond to smaller sizes in the unconstrained deposit-scale model, smoothing in the x, y, and z directions may be excessive.

No obvious narrow low susceptibility zones characteristic of felsic dikes or altered rocks are distinguished within the susceptibility anomaly. The 50 m x 25 m spacing of the magnetic data used for this inversion limits the resolution of features smaller than this. In addition, as discussed in Chapter 3, smoothing inherent in the inversion result brought about by the choice of a model norm that gives priority to smooth results, would further obscure small-scale low susceptibility zones.

Constrained inversion

Constrained deposit-scale results indicate there is more complex structure within the high susceptibility zones related to the Fe-rich basalts (Fig. 4.21b). Although the irregular shape of the low susceptibility area within the central high susceptibility area is obviously an artifact of the location of the drillhole, and buffer zones, used to constrain the inversion, rendering the result not particularly geologically realistic, it indicates the existence of more fine scale structure within the central susceptibility anomaly. The internal low susceptibility zones were determined from drill core assessment to be related to the presence of syenites, Fe-poor basalts, and carbonate-altered rocks. Hislop drill core logs presented in Chapter 2 indicate that significant changes in rock type and alteration mineral assemblages, and thus susceptibility, can occur at the centimeter scale. The cell sizes in the inversion limits the ability to resolve these fine scale fluctuations. Nonetheless, constraints can offset some of the smoothing that occurs in the

inversion result and highlight some of these small scale features. The presence of the low susceptibility zones forces susceptibility to be redistributed within the model, and its magnitude to increase in the upper portion of the anomaly.

As with the local-scale constrained inversion results in the previous section, a high susceptibility zone to the north interpreted to be related to ultramafic rocks, now appears to be more detached from the central high susceptibility Fe-rich basalts. An isosurface model for the deposit-scale constrained magnetic inversion is shown in Figure 4.22.

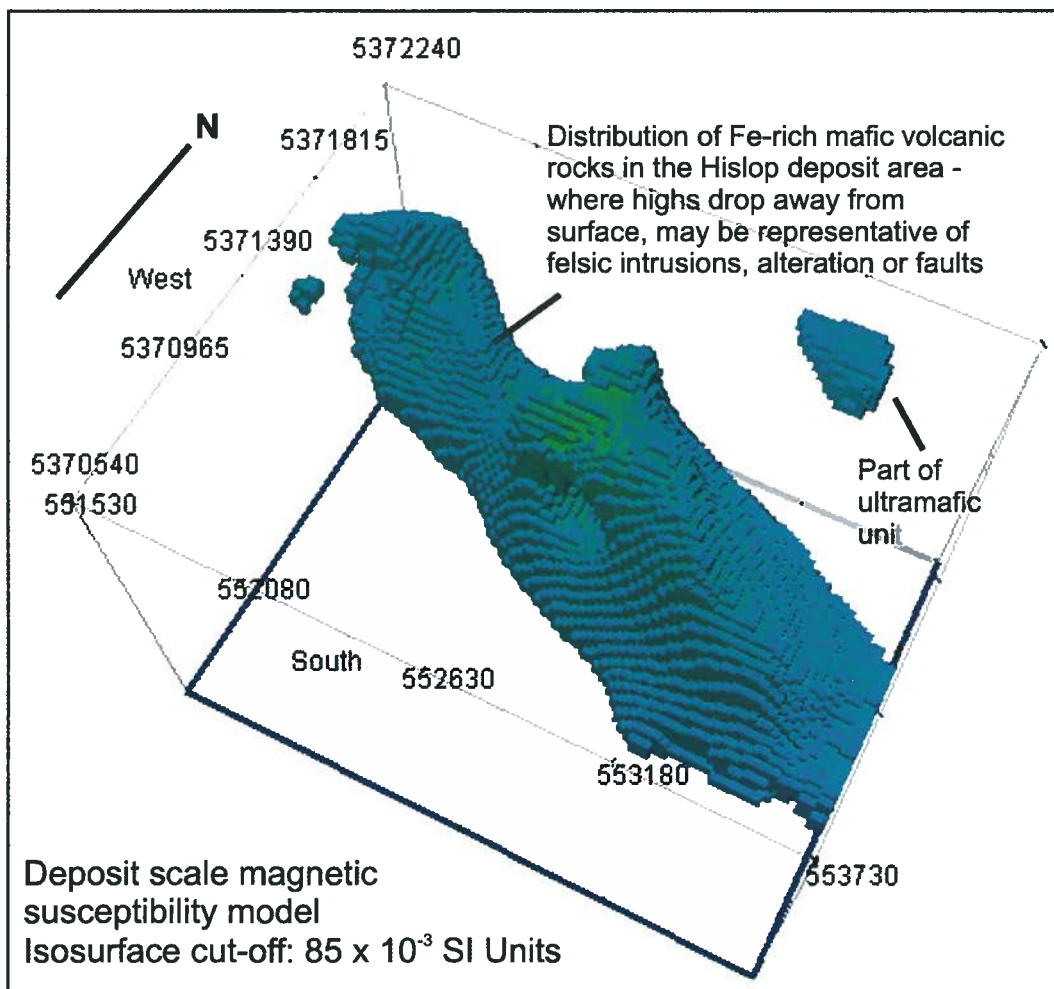


Figure 4.22. Isosurface model from deposit-scale magnetic inversion results.

4.3.2. Density model

Gravity data spacing over the greater Hislop deposit area is large (500 m x 120 m), as such only a regional scale inversion was carried out. The corresponding large cell sizes (250 m) means only large scale features representing larger volumes dominated by low density felsic or sedimentary rocks versus high density mafic and ultramafic rocks are resolved.

Fe-rich and Fe-poor mafic, and ultramafic volcanic rocks that underlie the central portion of the mapped area, cause a high density zone to dominate the core of the inversion volume (Fig. 4.23). To the north, there exists low density material likely related to sedimentary rocks of the Porcupine and Timiskaming assemblages. Low magnetic susceptibilities in the same location confirm the dominance of sedimentary rocks at depth. The boundary between the central high density area and the northern low density area here is not the same boundary that separates high and low susceptibility rocks in the regional magnetic results (see Fig. 4.17). This represents the contact between dense Fe-poor tholeiitic basalts north of the PDDZ, and the adjacent sedimentary assemblages. This may explain the difference in the apparent dip of the geologic units composing the central Hislop area between the magnetic and gravity inversion results.

Low density areas in the southern regions of the model correlate with a package of rhyolitic volcanic rocks (pale yellow unit in inset of Fig. 4.23) and sedimentary rocks that extend southeastward out of the section. The 3D distribution of mafic and ultramafic rocks versus felsic and sedimentary rocks can be observed from the isosurface model Figure 4.24.

4.3.3. Resistivity models

DC resistivity and IP inversion modeling was completed at two scales (Tabs. 4.2 and 4.3), however, since results are similar, only figures corresponding to the deposit-scale results are shown.

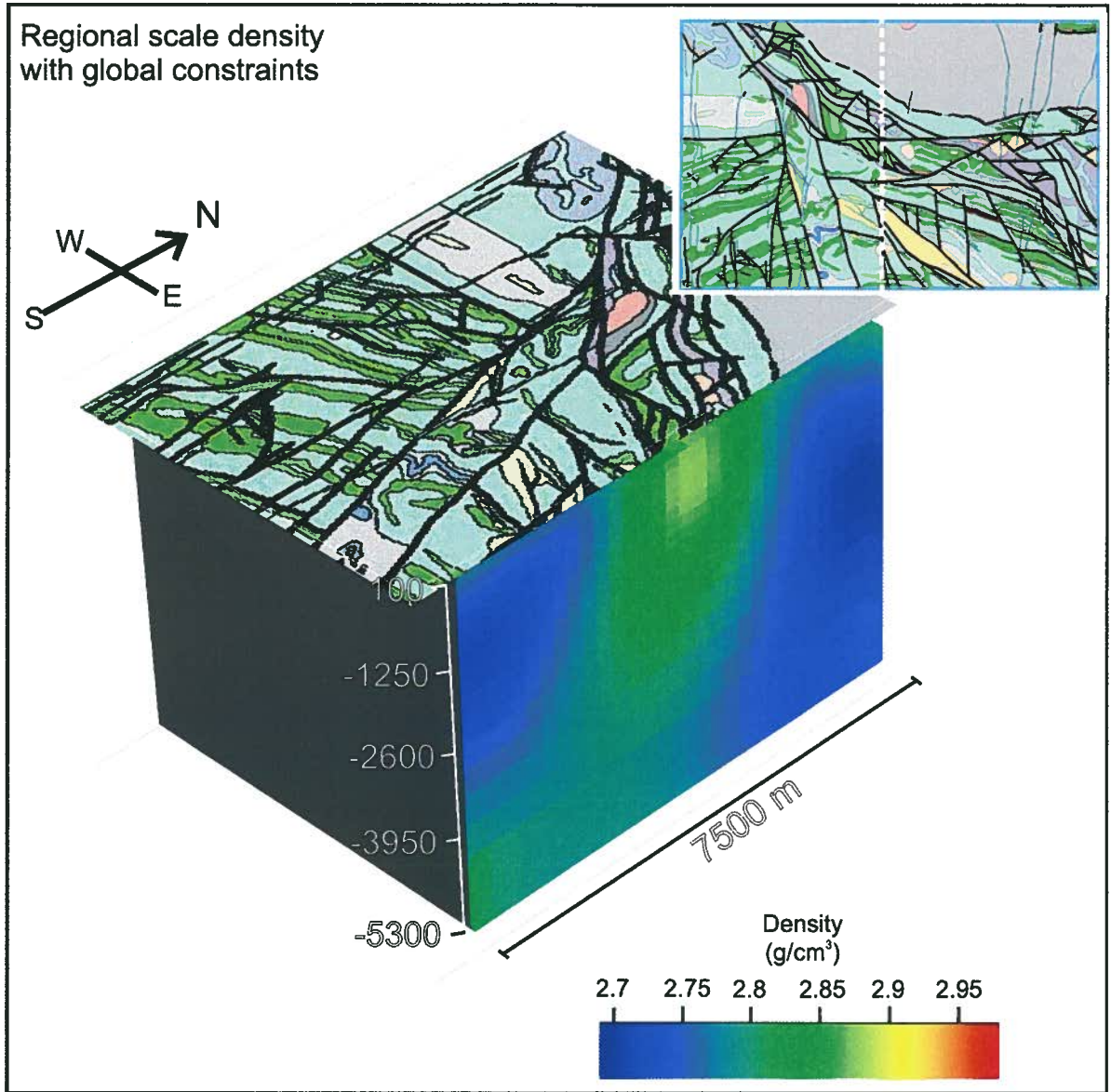


Figure 4.23. North-south cross-section through the regional-scale gravity inversion result, inverted with non-located constraints. The geologic map of the greater Hislop deposit area overlies the model. For geological legend see Figure 4.2. Inset shows extent of the model volume and cross-section location.

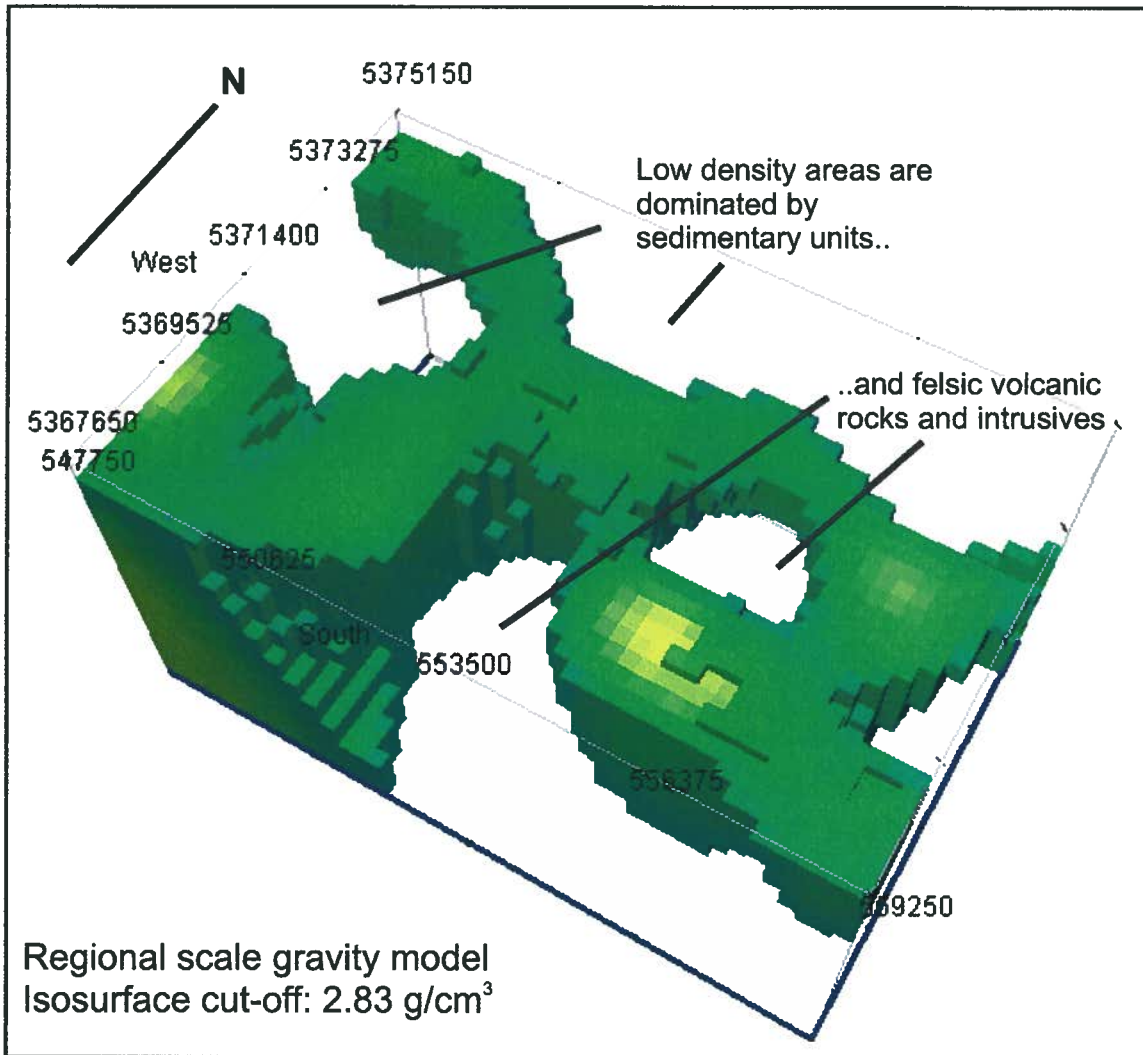


Figure 4.24. Isosurface density model from regional-scale gravity inversion results.

From physical property studies, high conductivities (low resistivities) were found to be associated with metamorphosed ultramafic rocks (talc-chlorite schists), whereas other rock types were less conductive. Higher conductivities in the DC resistivity inversion result, as expected, are associated with ultramafic rocks in the northern and central parts of the model (Fig. 4.25a). High conductivities however, may be instead, or additionally, correlated with Hislop deposit sulfides near the center of the map, or with interpreted faults. Two significant anomalies not represented in the cross-section, but seen in the isosurface model (Fig. 4.26a), correlate spatially with felsic intrusive rocks. Since felsic rocks are normally

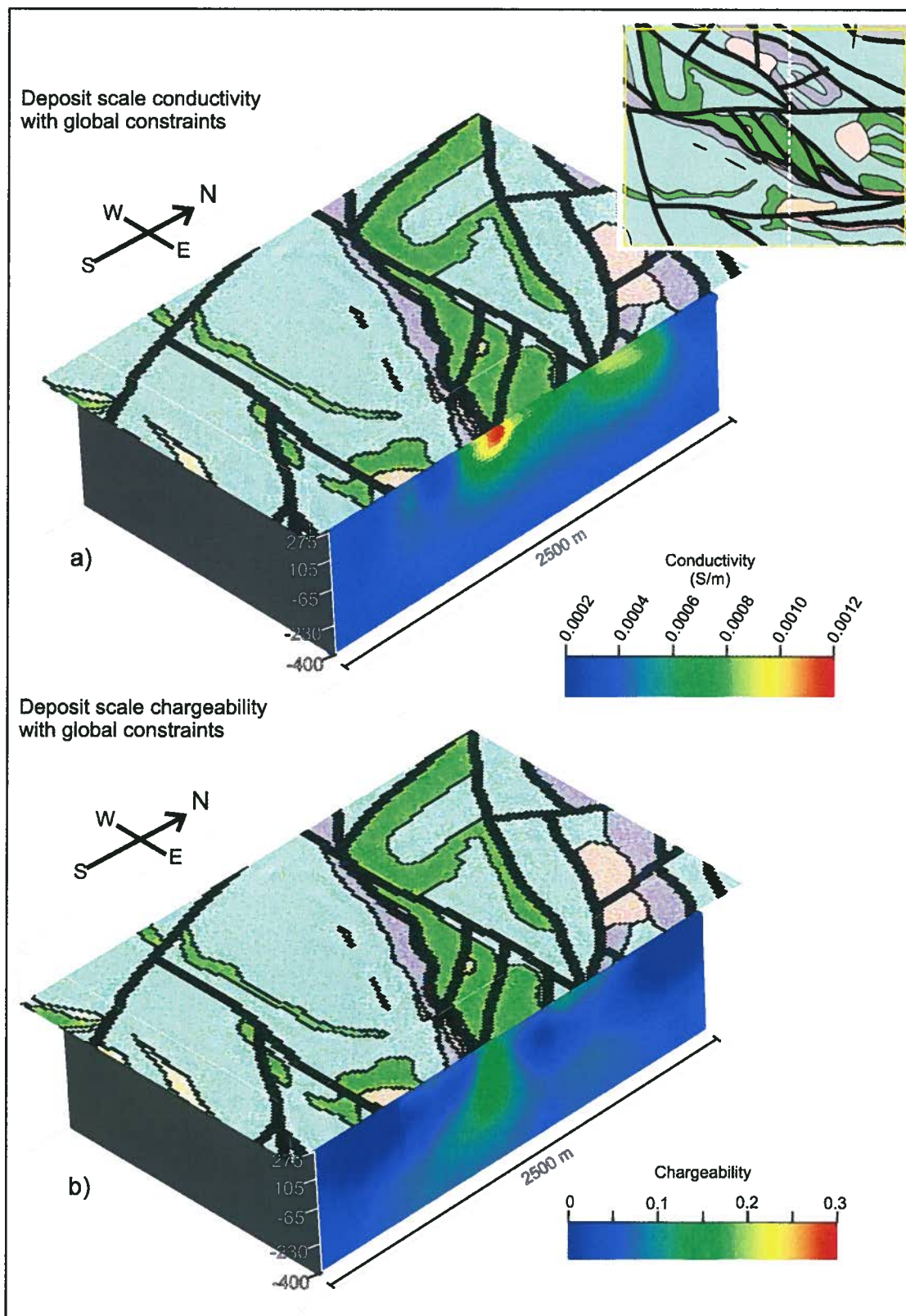


Figure 4.25. North-south cross-section through the deposit-scale a) DC resistivity and b) IP inversion results, both inverted with non-located constraints. Hislop area geologic map overlies models. For geological legend see Figure 4.2. Inset shows extent of the model volume and cross-section location.

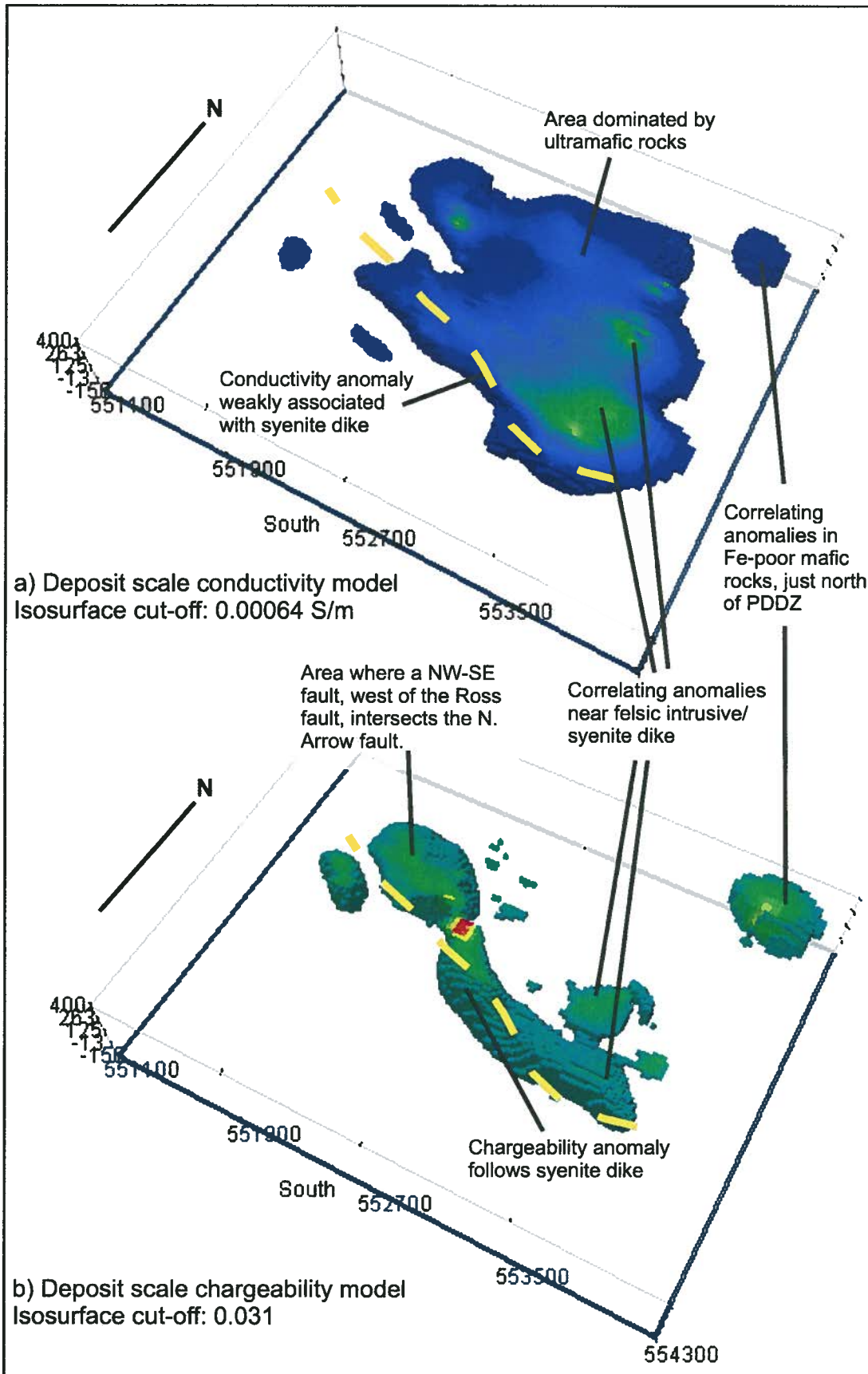


Figure 4.26. Isosurface models for deposit-scale a) conductivity, and b) chargeability results.

resistive, these anomalies may reflect the presence of sulfides. Alternatively, high conductivities may be associated with a conductive overburden, a feature indicated in inversion models generated for this area by Mueller et al. (2006). Outside of ultramafic rock-dominated areas and faulted areas, where geology is dominated by mafic and felsic rocks, lower conductivities (higher resistivities) occur.

Depth of investigation tests (Oldenburg and Li, 1999) were conducted for selected lines during 2D inversion work on the Hislop DC resistivity and IP datasets (Appendix 4B), and indicate that subsurface features are generally not resolvable below about 400-600 m depth.

4.3.4. Chargeability models

A distinct high chargeability zone, likely to represent the presence of sulfides, occurs in the subsurface beneath the mapped syenite dike (slightly obscured in figure) at Hislop, and extends to depth, dipping slightly to the southwest (Fig. 4.25b). This anomaly disperses horizontally at depth. The horizontal displacement does not correspond to any known features and is similar to artifacts in synthetic inversion models for IP data in Chapter 3. Additionally, from depth of investigation tests, it is suspected that the model is essentially unreliable at these depths. An additional small anomaly occurs just north of the central chargeability anomaly in proximity to some interpreted faults, and overlapping with a conductivity high.

When the 3D model is viewed, the central chargeability anomaly extends a few hundred meters to the northwest and to the southeast following the syenite dike, before it detaches from the surface and moves to depth (Fig. 4.26b). Northwest of the West Area open pit, a significant anomaly correlates with the northern Arrow Fault (refer to Fig. 4.2). In the isosurface model, three chargeability highs correlate with conductivity highs. Two of the anomalies are in proximity to felsic rocks, and the third occurs in the

northeast in mafic rocks north of the PDDZ. The correlation between the two physical properties could indicate sulfide-rich rocks.

4.4. QUERYING COMBINED INVERSION RESULTS

Data from Hislop 3D inversion models were combined using Gocad 3D GIS software with Mira Links add-ons, and the resulting ‘common earth models’ queried in an attempt to define spatial extents of rock units, and potentially prospective areas for exploration targeting. It is important to note that the local and deposit-scale magnetic susceptibility models used are from constrained inversions, whereas all other inversion results making up the common earth models are unconstrained.

This process involved projecting properties from the different inversion results onto one discretized mesh. For Hislop, three common earth models were created, a regional scale model where susceptibility and density were projected onto a mesh with 200 m cells, a local scale model, where susceptibility and chargeability from local scale inversions were projected onto a mesh with 50 m cells, and a deposit scale model, with susceptibility and chargeability data held in 25 m cells. During data projection, each ‘client’ cell in the common earth model grid takes on the value of the closest ‘server’ (inversion) cell center.

Physical property cut-offs used to query the common earth model were determined using descriptive statistics calculated during Hislop physical property studies. In essence, susceptibility and density are queried at the regional scale with expectations of modeling lithological units, or significant packages of rocks, and susceptibility and chargeability are used at the local and deposit scales to find sulfide-bearing felsic intrusives, and carbonate-altered rocks. Conductivity values do not uniquely define prospective rock types, or hydrothermal alteration (Tab. 4.2), and is thus not used in the queries. High conductivities can indicate the presence of faults that act as important

structural traps for gold mineralization, or sulfide-rich rocks, but high conductivities can also be related to least-altered and likely unmineralized ultramafic volcanic rocks.

The cut-off values used for common earth model queries are based on physical property ranges characterizing rock types and alteration at Hislop (Tab. 4.2). The query results are presented in plan-view in the corresponding figures, with a transparent geological map overtop.

4.4.1. Regional scale query (susceptibility and density)

Three different queries were applied to the regional combined susceptibility-density model in an attempt to target the three populations of rocks indicated in the Hislop susceptibility versus density plot (Fig. 4.4): 1. low susceptibility-low density felsic rocks (Fig. 4.27), 2. high susceptibility-high density least-altered mafic and ultramafic rocks (Fig. 4.28), and 3. low susceptibility-high density carbonate-altered or Fe-poor mafic rocks (Fig. 4.29).

By targeting low susceptibility ($<3 \times 10^{-3}$ SI Units) and low density ($<2.75 \text{ g/cm}^3$) areas of the model at the regional scale, two felsic intrusives in the south, and sedimentary rocks mainly associated with the Porcupine and Timiskaming assemblages in the northeast map area are isolated (Fig. 4.27). Felsic intrusive bodies near the center of the mapped area overlying this model are not detected by this query. This might relate to the large cell sizes used and the overwhelming of smaller lower susceptibility and density zones by the more abundant susceptible and dense mafic and volcanic units, an effect noticed in synthetic modeling results (Chapter 3).

A query targeting high susceptibility ($>5 \times 10^{-3}$ SI Units), and high density ($>2.8 \text{ g/cm}^3$) cells in the regional scale common earth model targets areas dominated by Fe-rich basalts and ultramafic volcanic rocks in the central and southern parts of the map area

(Fig. 4.28). High susceptibilities and densities stop abruptly at the mapped location of the PDDZ.

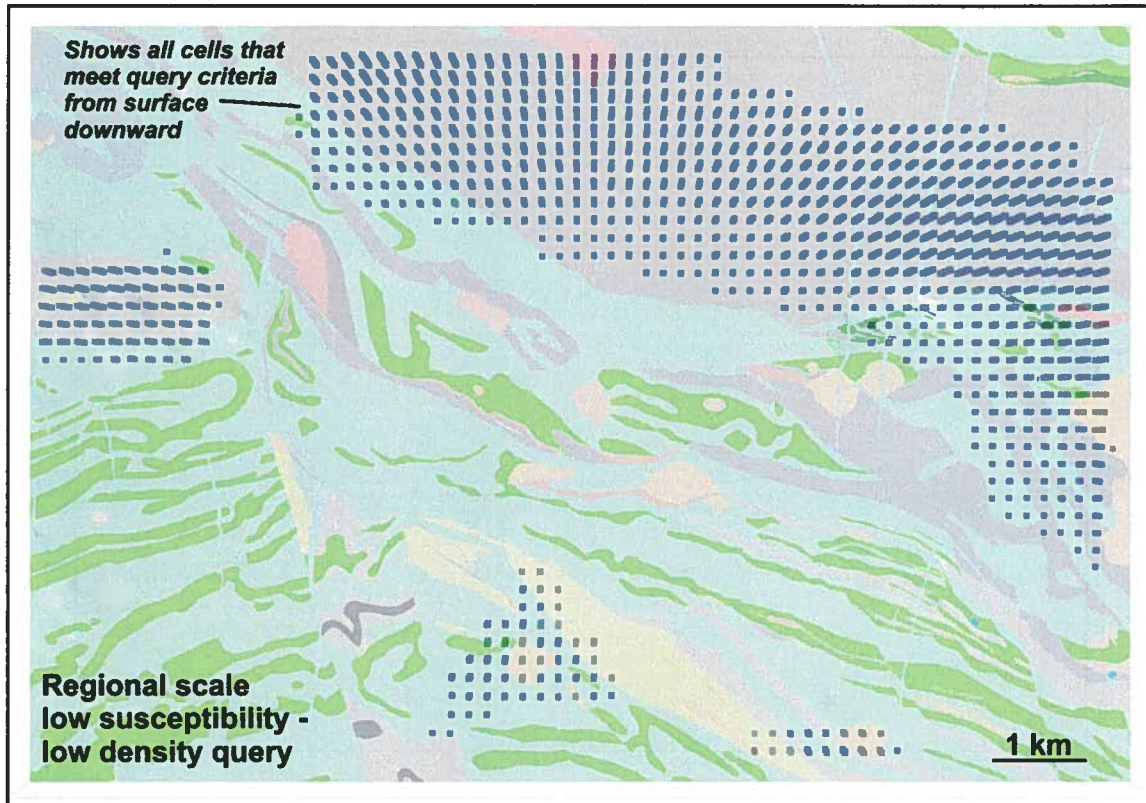


Figure 4.27. Result for a physical property query targeting low magnetic susceptibility-low density cells within the regional-scale common earth model. Anomalous zones extend to greater than 2000 m depth. Plan view with transparent geology. Geological legend in Figure 4.2.

A low susceptibility ($<3 \times 10^{-3}$ SI Units) and high density ($>2.8 \text{ g/cm}^3$) query identifies areas dominated by Fe-poor basalts, or possibly areas of carbonate-altered Fe-rich basalts or ultramafic rocks (Fig. 4.29). Cells highlighted by this query, underlying mapped Fe-rich basalts and ultramafic rocks, may warrant further inspection as the low susceptibilities here could indicate carbonate alteration of these normally high susceptibility rocks. A northern zone of low susceptibility-high density cells extends from a sequence of mafic rocks just north of the PDDZ, into the mapped Porcupine assemblage sedimentary rocks. Sedimentary rocks elsewhere have typically low densities, and this anomaly might indicate that the contact is interpreted incorrectly.

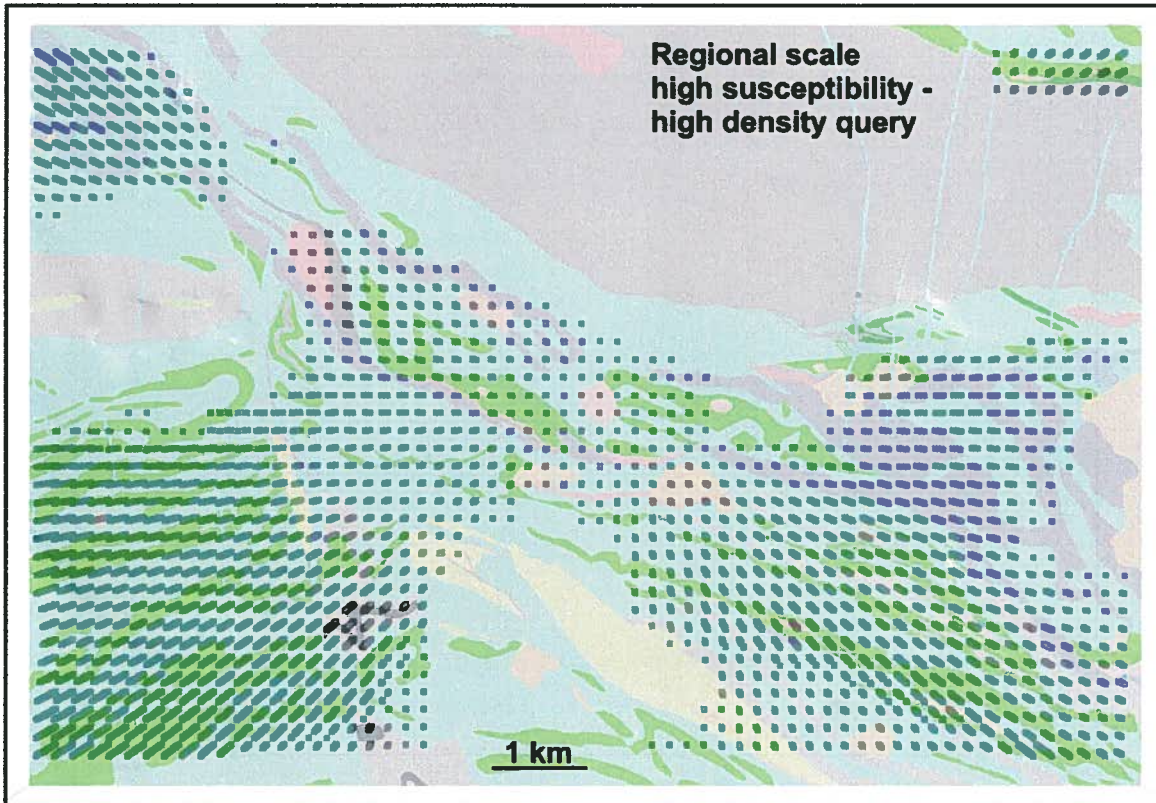


Figure 4.28. Result for a physical property query targeting high magnetic susceptibility - high density cells within the regional-scale common earth model. Anomalous zones extend to greater than 2000 m depth. Plan view with transparent geology. Geological legend in Figure 4.2.

4.4.2. Local scale query (susceptibility, chargeability)

Cells in the local scale common earth model containing low susceptibilities ($<3 \times 10^{-3}$ SI Units) combined with high chargeabilities (>0.12) were targeted to identify potentially prospective felsic intrusive rocks, carbonate altered zones, and sulfide-rich areas.

This query result highlighted a number of areas focused near the Hislop deposit. These zones are concentrated along geological contacts (marginal to the faulted Fe-rich basalt unit), and especially where the contacts are faulted, or where two or more faults intersect. Along the southern central syenite dike contact the highlighted zones are

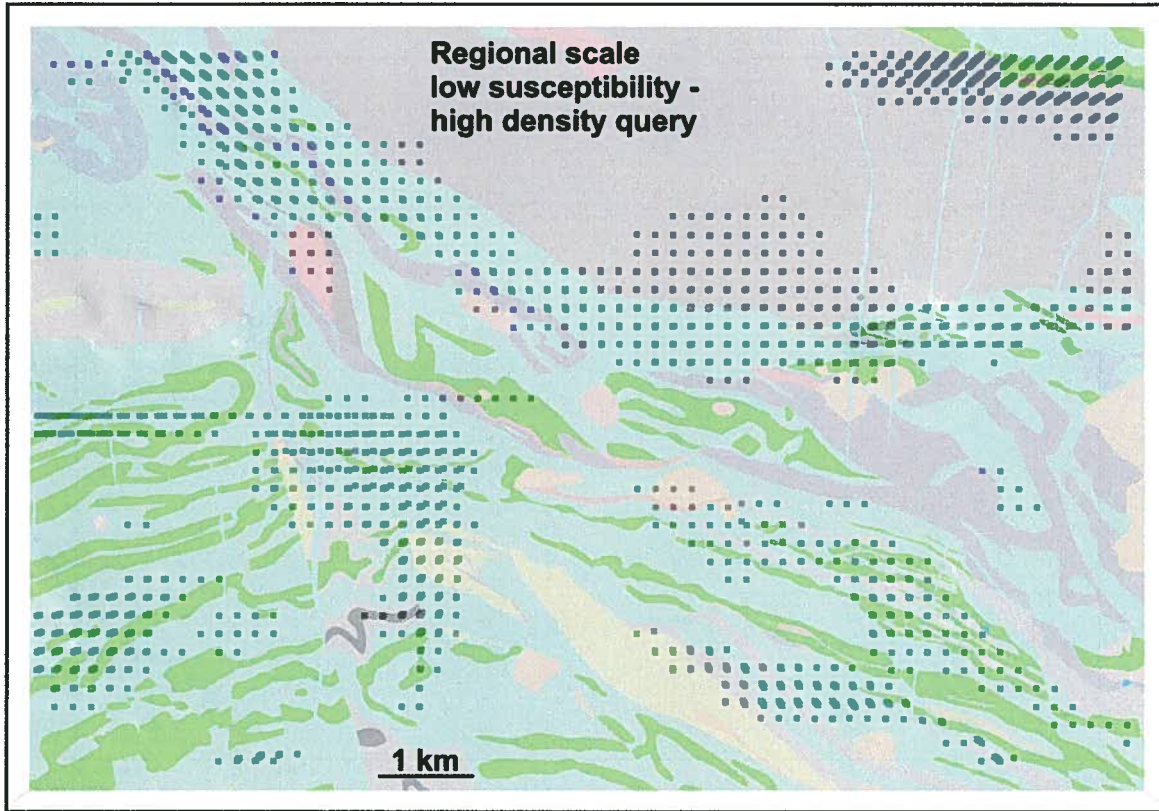


Figure 4.29. Result for a physical property query targeting low magnetic susceptibility - high density cells within the regional-scale common earth model. Anomalous zones extend up to 1500-2500 m depth. Plan view with transparent geology. Geological legend in Figure 4.2.

coincident with some high gold abundances (Fig. 4.30). Returned anomalies also coincide with higher gold concentrations near the northern Arrow Fault, and where the northern Arrow Fault intersects the north-south trending fault west of the Ross Fault. An anomaly northwest of the mapped PDDZ is also marginal to drillholes with anomalous gold. One, low susceptibility, high chargeability zone occurring just east of the Hislop deposit, near a felsic intrusion, is in an area of minimal to no drilling.

Some high gold values occur in association with a drilled area southwest of the Hislop deposit, near the Hislop Fault. Only about half of this drilled area is contained within the common earth model. The query did not identify prospective rocks here. Referring back to the regional susceptibility-density queries however, this area correlates with low susceptibilities. It is possible that the gold here is not associated with sulfides

and thus chargeability values are not anomalous at this location. This area is currently being explored by Stroud Resources (www.stroudresourcesltd.com), and the endeavor is confusingly called the Hislop Project.

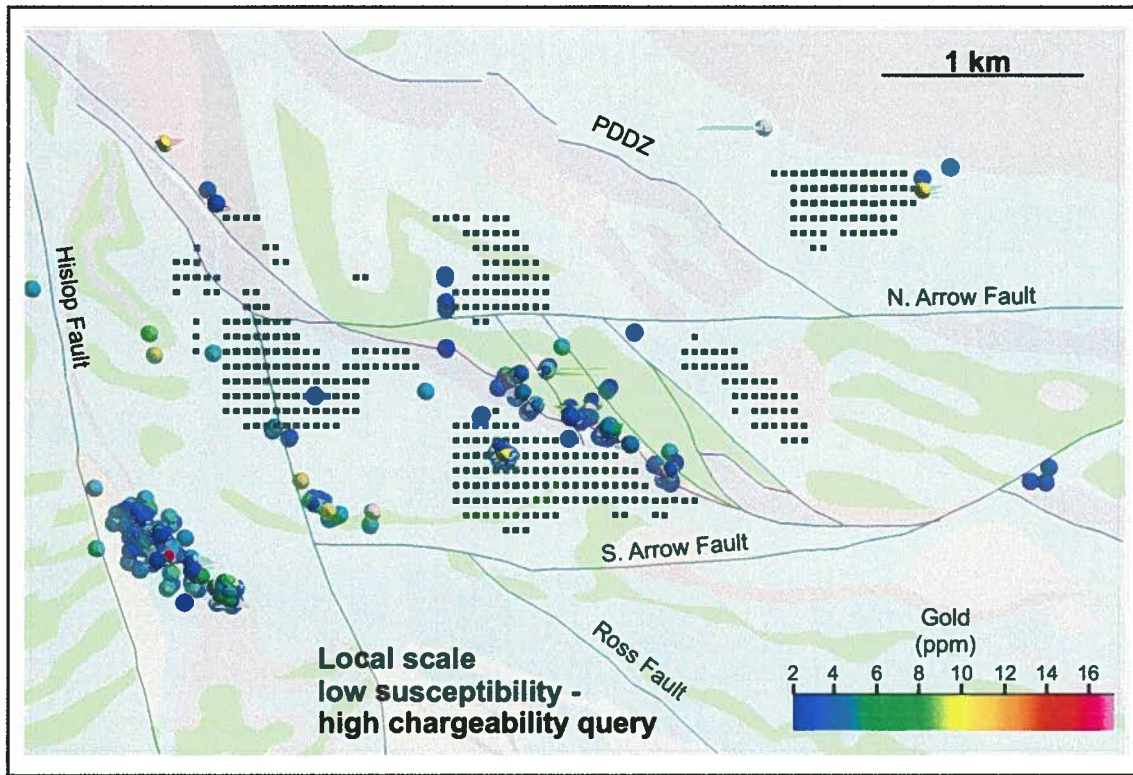


Figure 4.30. Result for a physical property query targeting low magnetic susceptibility - high chargeability cells within the local-scale common earth model. Anomalous zones extend up to 300-600 m depth. Anomalous downhole gold assays are indicated. Plan view with transparent geology. Geological legend in Figure 4.2.

4.4.3. Deposit scale query (susceptibility, chargeability)

Querying the deposit scale common earth model using the low susceptibility and high chargeability criteria, returns several zones with the desired characteristics, whose locations are generally consistent with local scale query results (Fig. 4.31). There is slightly more detail compared with the local scale results, with some additional small regions highlighted, and others eliminated. Again, most prospective areas are spatially

associated with areas of complex faulting, and are also proximal to felsic intrusives and dikes (some narrower dikes south of the main syenite dike are obscured by the anomalies and plotted gold assays, but can be see more clearly in Fig. 4.2). As with the local-scale results, there are areas of high gold concentrations not detected by the query that may represent mineralization not accompanied by disseminated sulfides.

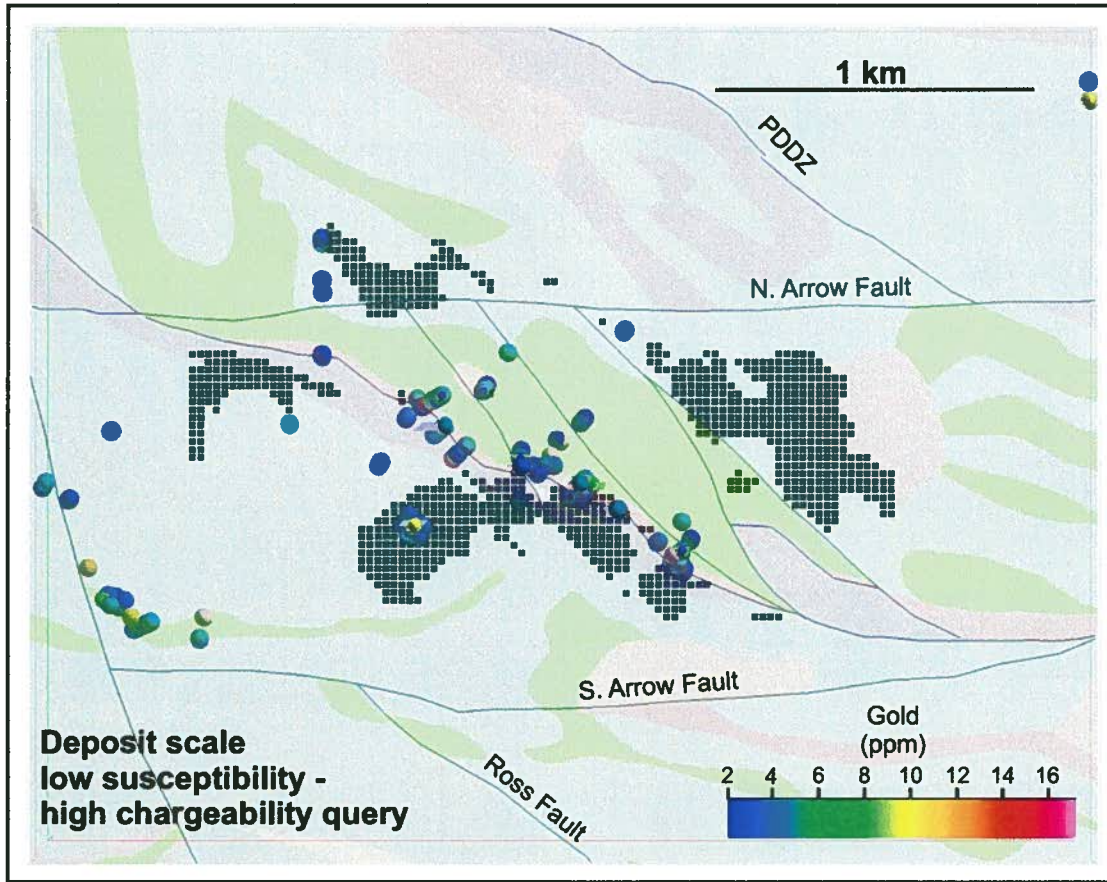


Figure 4.31. Result for a physical property query targeting low magnetic susceptibility - high chargeability cells within the deposit-scale common earth model. Anomalous zones extend up to 60-500 m depth. Anomalous downhole gold assays are indicated. Plan view with transparent geology. Geological legend in Figure 4.2.

The query results are not expected to detect all subsurface areas meeting the criteria. Constrained deposit scale magnetic inversion results indicate that there are small scale low susceptibility zones that can be masked by smoothing of high susceptibility

values in the inversion result. There is likely more detail in high susceptibility rocks that cannot be resolved using inversion, or querying techniques at this scale.

4.5. SUMMARY AND DISCUSSION

Geophysical inversion of a series of geophysical datasets over the Hislop gold deposit in the south-central Abitibi greenstone belt, was carried out at a range of scales of investigation. Results show that inversion is a useful tool for detecting specific lithologic packages, and altered and mineralized rock, and for interrogating their 3D subsurface distribution.

Regional scale inversion results highlight large scale structures, and lithological boundaries. Magnetic results show packages of susceptible rocks, dominated by Fe-rich tholeiitic basalts, extending to depth in the crust up to about 7 km. This depth is consistent with published depths for crustal rocks above granitic basement rocks in the Abitibi greenstone belt (Reed et al., 2005). Magnetic inversion traces the crustal scale Porcupine Deformation Zone, a regionally important gold-related structure, into the subsurface from its interpreted location at the surface, and indicates a southward dip (about 45° - 60°) as it undercuts and possibly truncates the overlying packages of volcanic rock. This southward dip is consistent with results for recent seismic work, and magnetic and gravity inversions completed in the Currie Township west of the Hislop deposit (Reed, 2005; Reed et al., 2005). The dip of the PDDZ is interpreted to vary along its trace, however, changing from 45°- 65° in the Hislop area to steeper angles closer to the Ontario-Quebec border (Berger, 2002).

At the regional scale, major lithologic units and domains are mapped using combined magnetic and gravity inversion results. Querying the combined results revealed three petrophysically distinct lithological packages, and importantly, allowed felsic and sedimentary rocks (low susceptibility-low density) to be distinguished from Fe-poor tholeiites and potentially carbonate-altered mafic and ultramafic rocks (low

susceptibility-high density). Exploration at the regional scale might focus generally on the range of low susceptibility regions, which are expected to contain dominantly felsic rocks, and carbonate-altered rocks. Associated lithogeochemical studies testing various alteration indices (Davies et al., 1990; Eilu et al, 1995; Piche and Jebrak, 2003) could be helpful in further distinguishing least-altered Fe-poor mafic rocks from carbonate-altered rocks. Regional scale inversions may be more appropriate for mapping geology in areas of poor outcrop than for generating targets directly. Although high susceptibility and high density rocks are likely to reflect mainly least-altered mafic and ultramafic rocks, it is possible that smaller zones of prospective low susceptibility-low density rocks within these larger rock packages are not being detected.

At the local and deposit scales of magnetic inversion, more detail is resolved within the subsurface. Distributions of Fe-rich basalt, versus Fe-poor basalt and felsic rocks are better defined, and locations and orientations of near-vertical faults dissecting a central package of high susceptibility Fe-rich basaltic rocks are discernible. There is not a significant increase in detail visible in 25 m³ cell deposit scale inversion over the 50 m³ cell local scale inversion. Features smaller than 25 m, which might constitute narrow, mineralization-related felsic dikes and alteration zones, are simply not detectable at these scales, with magnetic data spacing limited to 50 m x 25 m, and typical inversion-related smoothing occurring. More detail was indicated however, when constrained magnetic inversions are completed at the deposit scale, and it becomes apparent that there are small scale heterogeneities in the physical property distributions that are not being detected by unconstrained inversions. Synthetic modeling studies showed that narrow low susceptibility and low density zones can be imaged down to at least a few hundred meters at deposit-scales of exploration, when data spacing is 50 m x 10 m and cells are 10 m³ (Chapter 3). It should be noted however, that with smaller cell sizes and smaller data spacing, the computation times for inversion are increased significantly.

From physical property studies (Chapter 2), and synthetic modeling work (Chapter 3), it is clear that density is a useful physical property for targeting felsic dikes, and helpful in distinguishing low susceptibility mafic rocks from felsic rocks.

Unfortunately gravity data available for this work was extremely sparse and could not be used to model the subsurface at the local or deposit scales. Having both high resolution magnetic and gravity data available for deposit-scale exploration would be very useful for geological mapping, and detecting gold-related rock types at smaller scales of investigation.

DC resistivity inversions image some ultramafic volcanic units in the Hislop area, as was predicted by the consistently low resistivities (high conductivities) of these commonly sheared rocks indicated from physical property studies on hand samples (Chapter 2). Through inversion work, it was shown that high conductivities are also correlated spatially with faults. Whether this is related to fluid content and porosity which increases conductivity (Telford et al., 1990) or to the presence of sulfides was not determined. Conductivity was not used in common earth model queries. Conductivity does not consistently detect prospective rocks in the Hislop area. High conductivities may indicate faults which do not necessarily host mineralization, or conductive talc-chlorite schists which are not typically mineralized. Induced polarization inversions locate chargeability anomalies that are interpreted to be due to the presence of sulfides. These anomalies align with the immediate location of the Hislop deposit proximal to the central northwest-southeast trending syenite dike.

Again, by combining the results of different inversions, the most information is gained. At the local and deposit scales, queries of combined susceptibility and chargeability data were used to try and locate sulfide-rich felsic dikes and carbonate-altered rocks. Query results highlighted zones focused along the mainly faulted contacts between Fe-rich basalts and other rocks, and near cross-cutting faults. These areas highlighted by the queries in the area of the Hislop deposit are geologically ideal gold targets, with faults providing conduits and structural traps for hydrothermal fluids, and nearby Fe-rich rocks that promote sulfidation processes leading to gold precipitation (Mikucki, 1998). Some areas where high gold grades were intersected during drilling were targeted by the queries, confirming prospectivity.

Although gold mineralization hosted in greenstone facies rocks does not usually have a strong geophysical signature due to its typically low grades, it is still possible to remotely target Archean orogenic gold deposits using alternative exploration vectors such as hosting lithology, and alteration mineral assemblages. Geophysical inversion not only allows detection of prospective gold-related rocks but can indicate the spatial extent of these rocks in the subsurface. Geophysical based mapping of geology, and exploration target generation is so valuable in Archean greenstone terranes since they are often characterized by low percentages of outcrop.

The key to getting the most from inversions is by understanding relationships between physical properties in the geological environment or mineral deposit setting of interest. With this prior knowledge inversions can be constrained to yield results consistent with geological observations, inversions will be more confidently interpreted overall, and queries can be developed to target model cells with the desired combination of physical property characteristics representative of mineralized rocks.

REFERENCES

Ayer, J., Amelin, Y., Corfu, F., Kamo, S., Ketchum, J., Kwok, K., and Trowell, N., 2002, Evolution of the southern Abitibi greenstone belt based on U-Pb geochronology: autochthonous volcanic construction followed by plutonism, regional deformation and sedimentation: *Precambrian Research*, v. 115, p. 63-95.

Bate, S.J., Thorsen, K.R., and Jones, D., 1989, The Casa Berardi area; an exploration case history: *Proceedings of Exploration '87*, Ontario Geological Survey, Special Volume 3, p. 855-870.

Berger, B.R., 1999, Geological investigations along Highway 101, Hislop Township: Ontario Geological Survey, Summary of Field Work and Other Activities 1999, Open File Report, 6000, p. 5-1 – 5-8.

Berger, B.R., 2002, Geological synthesis of the Highway 101 area, east of Matheson, Ontario: Ontario Geological Survey, Open File Report 6091, 124 p.

Davies, J.F., Whitehead, R.E.S., Huang, J., and Nawaratne, S., 1990, A comparison of progressive hydrothermal carbonate alteration in Archean metabasalts and metaperidotites: *Mineralium Deposita*, v.25, p. 65–72.

DCIP3D User Manual, version 2.1, A program library for forward modelling and inversion of DC resistivity and induced polarization data over 3D structures: UBC-Geophysical Inversion Facility, University of British Columbia.

Doyle, H.A., 1990, Geophysical exploration for gold – a review: *Geophysics*, v. 55, p. 134-146.

Eilu, P., Groves, D.I., Mikucki, E.J., McNaughton, N.J., and Ridley, J.R., 1998, Alteration indices and pathfinder elements in wallrock alteration zones around Archaean

lode-gold deposits, *in* Pasava, J., Kribek, B., and Zak, K., eds., *Mineral Deposits; from their Origin to their Environmental Impacts*, Third Biennial SGA Meeting, Prague, Czech Republic, p. 113-116.

Farquharson, C.G, Ash, M.R., and Miller, H.G, 2008, Geologically constrained gravity inversion for the Voisey's Bay ovoid deposit: *The Leading Edge*, v. 27, p. 64-69.

Hallof, P.G., and Yamashita, M., 1990, The use of the IP method to locate gold-bearing sulfide mineralization, *in* Fink, J.B., Sternberg, B.K., McAlistar, E.O., Weiduwilt, W.G., and Ward, S.H., eds., *Induced Polarization: applications and case histories*, Society of Exploration Geophysicists, Tulsa, Ok., p. 227-279.

Jackson, S. L., and Fyon, A. J., 1991, The western Abitibi subprovince in Ontario, *in* P.C. Thurston, H.R. Williams, R.H. Sutcliffe and G.M. Stott, eds., *Geology of Ontario*, Ontario Geological Survey, Special Volume 4, Part 1, p. 405-482.

Johnson, I., Webster, B., Matthews, R., and McMullen, S., 1989, Time-domain spectral IP results from three gold deposits in northern Saskatchewan: *CIM Bulletin*, v. 82, p. 43-49.

Kerrich, R., 1989, Geodynamic setting and hydraulic regimes: shear zone hosted mesothermal gold deposits, *in* Bursnall, J.T., ed., *Mineralization and Shear Zones*, Geological Association of Canada, Short Course Notes 6, p. 89-128.

Kowalczyk, P., Thomas, S., and Visser, S., 2002, 3D inversion of resistivity and IP data, two case studies from mineral exploration: *SEG extended abstracts*, SEG International Exposition and 72nd Annual Meeting, 4 p.

Li, Y., and Oldenburg, D.W., 1996, 3-D inversion of magnetic data: *Geophysics* v. 61, p. 394-408.

Li, Y., and Oldenburg, D.W., 1998, 3D inversion of gravity data: *Geophysics*, v. 63, p.109-119.

Mag3D User Manual, version 4.0, 2005, A program library for forward modelling and inversion of magnetic data over 3D structures: UBC-Geophysical Inversion Facility, University of British Columbia.

Mueller, E.L., Reford, S.W., Dawson, D.J.W., Morrison, D.F., Pawluk, C., Grant, J., Spector, A., Rogers, D.S., and Savage, T., 2006, Acquisition, inversion and presentation of geophysical data for geoscientific profiles in the Timmins–Kirkland Lake area: Discover Abitibi Initiative, Ontario Geological Survey, Open File Report 6189 , 28 p., 15 sheets.

Mikucki, E.J., 1998, Hydrothermal transport and depositional processes in Archean lode-gold systems: A review: *Ore Geology Reviews*, v. 13, p. 307–321.

Mira Geoscience Limited, 2005a, Detectability of mineral deposits with electrical resistivity and induced polarization methods: Ontario Geological Survey, Miscellaneous Release – Data 181.

Mira Geoscience Limited, 2005b, Detectability of mineral deposits with potential field methods: Ontario Geological Survey, Miscellaneous Release – Data 177.

Oldenburg, D.W., and Li, Y., 1999, Estimating depth of investigation in dc resistivity and IP surveys: *Geophysics*, v. 64, p. 403-416.

Oldenburg, D.W., Li, Y., Farquharson, C.G., Kowalczyk, P., Aravanis, T., King, A., Zhang, P., and Watts, A., 1998, Applications of geophysical inversions in mineral exploration problems: *The Leading Edge*, v. 17, p. 461 - 465.

Oldenburg, D.W., Li, Y., and Ellis, R.G., 1997, Inversion of geophysical data over a copper gold porphyry deposit: A case history for Mt. Milligan: *Geophysics*, v. 62, p. 1419-1431.

Ontario Geological Survey 2001, Physical rock property data from the Physical Rock Property Study in the Timmins and Kirkland Lake Areas: Ontario Geological Survey, Miscellaneous Release – Data 91.

Ontario Geological Survey, 2004, Ontario airborne geophysical surveys, gravity data, northeast, northwest, and south Timmins areas: Ontario Geological Survey, Geophysical Data Set 1051.

Phillips, N.D., 2002, Geophysical inversion in an integrated exploration program: examples from the San Nicolas deposit: Unpublished M.Sc. Thesis, University of British Columbia, 237 p.

Piche, M., and Jebrak, M., 2003, Normative minerals and alteration indices developed for mineral exploration: *Journal of Geochemical Exploration*, v. 82, p. 59-77.

Poulsen, K.H., Robert, F., and Dube, B., 2000, Geological classification of Canadian gold deposits: *Bulletin - Geological Survey of Canada*, Report 540, 106 p.

Power, W. L., Byrne, D., Worth, T., Wilson, P., Kirby, L., Gleeson, P., Stapleton, P., House, M., Robertson, S., Panizza, N., Holden, D. J., Cameron, G., Stuart, R., and Archibald, N. J., 2004, Geoinformatics evaluation of the eastward extension of the Timmins Gold Camp: Geoinformatics Exploration Inc., Unpublished report for St Andrew Goldfields Ltd.

Prest, V.K., 1956, Geology of the Hislop Township: Ontario Department of Mines, Annual Report, 1956, v. 65, 51 p.

Reed, L. E., Snyder, D. B., and Salisbury, M. H., 2005, Two-dimensional (2D) reflection seismic surveying in the Timmins-Kirkland Lake area, northern Ontario; acquisition, processing, interpretation: Discover Abitibi Initiative, Ontario Geological Survey, Open File Report 6169, 68 p., 10 plates.

Reed, L. E., 2005, Gravity and magnetic three-dimensional (3D) modeling: Discover Abitibi Initiative, Ontario Geological Survey, Open File Report 6163, 40 p., 4 sheets.

Roscoe and Postle, 1998, Hislop Mine Property, Roscoe and Postle Associates Inc., St. Andrew Goldfields Ltd. internal report, unpublished, p. 66-89.

Seigel, H.O., Johnson, I., and Hennessey, J., 1984, Geophysics the leading edge: Geophysics: the Leading Edge of Exploration, v. 3, p. 32-35.

Telford, W.M., Geldart, L.P., and Sheriff, R.E., 1990, Applied Geophysics, Second Edition: Cambridge University Press, 770 p.

UBC-GIF Inversion for Applied Geophysics CD-ROM, 2000-2006, a teaching and learning CD-ROM, by Oldenburg, D.W., and Jones, F.M.: University of British Columbia, Geophysical Inversion Facility.

Williams, N.C., 2006, Applying UBC-GIF potential fields inversions in greenfields or brownfields exploration: Australian Earth Sciences Convention, 2006, Melbourne, Australia, extended abstract, 10 p.

Williams, N.C., 2008, Geologically-constrained UBC-GIF gravity and magnetic inversions with examples from the Agnew-Wiluna greenstone belt, Western Australia: Unpublished Ph.D. Thesis, The University of British Columbia, 479 p.

www.standrewgoldfields.com, website for St. Andrew Goldfields, Ltd.

www.stroudresourcesltd.com, website for Stroud Resources Ltd.

www.zonge.com/LabIP.html, website for Zonge Engineering and Research Organization,
IP and resistivity measurements.

Chapter 5: Summary and future work

5.1. SYNTHESIS OF RESEARCH PRESENTED

The goal of this research was to apply an understanding of the characteristic geology and physical properties of a typical Archean orogenic gold deposit to geophysical inversion for improved mapping of geology and delineation of gold-related rocks in the subsurface. The Hislop deposit of eastern Ontario was used as an example of this deposit type in the case study.

Key relationships between geology and alteration, and physical properties were established for Hislop, and ranges of physical properties representing more prospective geology were identified. Physical property information was eventually used to improve inversion results through their incorporation as inversion constraints. Synthetic modeling revealed the sizes and depths, and necessary physical property contrasts required to image petrophysically distinct gold-related features in the subsurface. It allowed depths of investigation to be roughly determined, and allowed certain inversion artifacts to be identified. Preliminary physical property, and synthetic forward and inverse modeling work contributed strongly to how eventual inversion models for the Hislop deposit were interpreted.

At larger scales of investigation, magnetic and density data can be used for mapping geology, and for determining regional-scale exploration targets based on the distribution of the geologic units and structures modeled. Results are especially useful in the parts of the Abitibi greenstone belt that were modeled during this study, as outcrop percentages are low. At deposit-scales of investigation, induced polarization (IP) inversion methods were effective in detecting sulfide-rich rocks, with chargeability anomalies correlating well with known mineralization. DC resistivity inversion results were not easily interpretable due to the variable behavior of conductivity. Some correlations between chargeability and conductivity anomalies in select areas surrounding

the Hislop deposit, however, may suggest the presence of potentially gold-bearing, sulfide-rich rocks. Magnetic inversions at the local and deposit scales identified a complex distribution of faults characterized by low susceptibilities possibly brought on by magnetite-destructive carbonate alteration. Smaller scale features, such as the gold-related syenite dike at Hislop, were obscured by smoothing of higher susceptibilities within the inversion volume. Synthetic modeling work has indicated that more detail can be derived from inversion, permitting better resolution of the narrow features that characterize typical Archean orogenic gold deposits. But to attain this detail, it is necessary to focus on a small area, collect closely-spaced data, and to use small inversion cell sizes. The density data available for the Hislop area was very widely spaced. From physical property studies and inversion investigations, it is expected that smaller scale density data in combination with closely spaced magnetic data would be effective in establishing geological contacts and rejecting least-prospective rocks at the deposit scale.

5.2. SIGNIFICANCE AND CONTRIBUTIONS TO THE FIELD

There is limited published information detailing geophysical inversion modeling efforts in Archean orogenic gold environments. The work presented in this thesis provides a comprehensive case study focused on the application of inversion methods for orogenic gold exploration, and may act as a reference point for others embarking on using inversion to explore in this deposit setting.

As previously discussed, an understanding of physical properties lays the groundwork for applying geophysics or geophysical inversion as exploration tools. The extensive physical property work completed constituted a major component of this thesis and is an important contribution to geophysics-based exploration. A significant amount of physical property data was generated for Hislop deposit rocks, and physical property ranges for typical host rock types and for prospective rocks were delineated. This data may eventually be contributed to a regional or national physical property databases,

enhancing the sources on which to draw for geophysics-based exploration in similar areas where little sampling or physical property reconnaissance has been done.

Synthetic modeling of a typical gold deposit provided insight into the features that will, and will not be imaged for a given survey design and mesh discretization. It also allowed application of various basic constraints to be tested to assess their influence on recovered models. This compilation might provide some guidance for geophysical survey, or inversion design, in a similar setting.

Inversion of the range of geophysical data available over Hislop, at a range of scales made for a unique case study with significant breadth. Querying combined physical property models was shown to be a valuable application of inversion results. It was demonstrated that the combination of magnetic susceptibility and density models were useful for distinguishing sedimentary and felsic rocks from Fe-rich mafic and ultramafic rocks, and Fe-poor mafic and ultramafic rocks, and for outlining their 3D subsurface distributions at the regional scale. The queries used constitute important mapping tools in areas of poor outcrop in this part of the Abitibi greenstone belt. At smaller scales, prospective areas can be distinguished by combining chargeability and susceptibility results, as was indicated by correlation between known mineralization, and high chargeability-low susceptibility anomalies. Physical property studies (Chapter 2) indicated similarities in local and regional scale physical property ranges and distributions. As such, these queries could be applied to other inversion results regionally.

5.3. LIMITATIONS OF THE THESIS RESEARCH

Due to their ease of collection, it was possible to amass a large number of magnetic susceptibility and density measurements for Hislop samples. An equivalent number of measurements for resistivity and chargeability were not generated, as equipment was not available to make the measurements in-house. Measurements had to be completed at the physical properties laboratory at Zonge Engineering and Research

Organization, Inc., resulting in a limited dataset. This meant the rock types in their least-altered and variably altered states are not well-represented. It was not possible to make a thorough assessment of the effects on alteration on these two electrical properties, and in addition, to have confidence in relationships that were indicated between these properties, and sulfide abundance or porosity.

All modeling possibilities were not considered, and synthetic modeling and inversion work could both be expanded on. For example, synthetic modeling was only carried out at one representative scale of exploration, the deposit-scale, with data collected only on a 50 m x 10 m grid. With anticipation of completing regional inversions it would be beneficial to model the deposit at a more regional scale. Only select variations on the geological setting of the modeled gold deposit were considered during synthetic modeling studies, and constraints only demonstrated for a subset of these scenarios. There are obviously many different scenarios that can be tested, but it would take considerable time to assess them all. Similar expansions on work could be applied to inversion of actual data over Hislop. Different combinations of constraining information could be applied to each of the models to explore the full range of possible outcomes. Throughout the course of inversion studies, it was indicated that inversion results can also vary dramatically when geophysical data are scaled differently, and when errors are changed. These parameters might also be investigated more extensively through additional inversions. With the array of possible modifications, it is feasible that there is a better model to be generated in each case.

An additional limitation of the research relates to the previous comments. One of the interesting challenges encountered in completing this project was dealing with the rapid rate at which inversion concepts and methods are developing. At times, a series of models would be completed only to discover that there was a newer version of the inversion code available! This is a relatively new field, and the Geophysical Inversion Facility at UBC are at the forefront of it. The UBC-GIF has developed robust inversion codes that are used worldwide, and the codes are constantly being updated to adapt to the modeling needs of exploration and environmental communities. This means that more

effective codes, or programs with increased functionality, are becoming available on a regular basis, and that the models presented herein might be improved on with application of newer software.

5.4. RECOMMENDATIONS FOR CONTINUED WORK

There were several ideas proposed during the course of this research that were not followed up on. Some of the ideas worthy of further investigation are listed here, along with additional suggestions.

More resistivity and chargeability data is needed to better define relationships between geology and physical properties. Since IP methods are so effective in delineating sulfides at Hislop, and have been shown to be effective in detecting mineralization for other gold deposits, more chargeability data would be useful. It would be beneficial to do a more in depth analysis of relationships between chargeability to sulfides types, sulfide textures and abundances, as well as attempt to define a relationship between gold and chargeability.

As chargeability data was collected at multiple time windows during IP work both in the field, and in the laboratory, there is potentially more information to be gained. To calculate chargeability for this thesis, the value representing the voltage decay over these time windows was chosen to be 80% of the sum of voltages over eight of the time windows. This choice of representative value is somewhat arbitrary, and there exist other standard measurements in the industry. The consistency of measurement methods for a suite of data is of more importance than choice of calculation. By assessing the entire decay curve, or looking at voltages from individual time windows, instead of calculating a representative value, relationships between chargeability and mineralization not previously identified may be revealed.

It may be constructive to automate the synthetic modeling process. Constructing the range of synthetic models and testing them was time-consuming, and only select scenarios were represented. Such a program could automatically vary geometry and physical property contrasts of a target feature for given survey parameters and inversion cell sizes, and assesses model difference values (Chapter 4) to determine conditions where the difference between true and recovered models are low. This may be an effective way to know more accurately and efficiently when a feature is too small or too deep, or has too low of a contrast from host rocks, to be imaged.

From a data management standpoint, another program might be devised to help manipulate the typically large datasets to be used in inversions. Some basic unofficial programs exist, but a formal one could be made. The program should be able to cut a specific range of data from a dataset that covers a larger area, and decimate data to get spacing to correlate with inversion cell sizes, perhaps allowing more dense data at the core and sparse data in outer regions. A formal program that reorganizes DC resistivity and chargeability into an inversion-friendly format would also save time.

Regarding the inversion models, some may be rerun to test application of various combinations of constraints to get a more thorough idea of the range of results possible. There was limited testing of constraints for density, DC resistivity, and IP inversions, although prior information exists to expand on this. Additional constraints can be added to magnetic inversions. An example would be the use of the entire regional geology map, rather than just outcrop geology, to populate all surface cells with reference physical properties, or the construction of 3D domains based on large packages of similar rock, that can be assigned appropriate background reference values.

Initially it was proposed that a 3D geologic model of the Hislop deposit would be created for use as a reference model for inversions, and for general comparison to inversion results and incorporation into common-earth models. The model was initiated, based on cross-sections drawn from select drillholes, however it was not completed. The process of building a 3D geological model requires significant time, reasonable

experience in GIS modeling, and a thorough understanding of geology. There was simply not enough information collected during this study to build anything but a very simple model that is extensively interpreted. There is, however, potential for a 3D model to be built for the Hislop deposit in the future, as there is a wealth of information from the many drillholes that were logged in this area, and now there are geophysical models which can help with geological interpretations at depth. The geological model must be completed with contribution from geologists that are well-familiarized with the geology and structure of the deposit

The Hislop common-earth model can be further developed with the addition of a 3D geological model, and with the contribution of other existing data. Data from a large scale 3D model of the area created in the Fracsis GIS program by Geoinformatics Exploration Inc., including fault and geological contact surfaces, can be converted to forms usable in Gocad. A large quantity of drilling information, along with gold assays, and geochemical information collected by numerous workers throughout Hislop's exploration history can be incorporated into the model for the purposes of mapping and target generation. At the start of this project lithogeochemical data was obtained with the anticipation that there may be relationships existing between this data and physical property data which would allow chemistry to be used to predict physical properties. Unfortunately, no statistically relevant trends emerged. Although geochemical data do not appear to be useful as a direct proxy for mineralogy or physical properties at Hislop, the collected lithogeochemical data might be beneficial to include in common earth models of Hislop. Anomalous abundances of elements reflecting carbonate, muscovite (or sericite), and albite-dominated alteration, such as CO₂, K, and Na, would act as an additional exploration criteria for querying along with geophysical inversion results.

5.5. FUTURE DIRECTIONS OF THE FIELD OF STUDY

The field of geophysical inversion-based exploration is young. The inversion codes developed at UBC are constantly being updated and refined in order to allow more

flexibility with respect to incorporating geological information. They will continue to develop as they are being used to a greater extent in practice.

The GIFtools ModelBuilder program of Williams (2008) is still in development. This program, or at least this type of program, will become a standard in the field that allows all prior geological and physical property knowledge to be input into inversions as constraints. The influence of the input data on the model is determined by the user based on the confidence the user has in the data.

Additional programs to help input geological information into inversions, or make the results consistent with expected geology, are in progress. Diagonal dips and structural trends outside of north, south, east, and west directions can now be input using codes being developed by Lelievre et al. (2008). This is would be of use for inversions in any geologic setting, however could be especially useful in Archean greenstone terranes where there is commonly a strong structural fabric that should be relayed in the inversion. Smoothing inherent in inversions causes physical property values to grade between low and high anomalies. This may not be considered representative of the true geological or physical property situation. Phillips et al., (2007) initially introduced a method that restricts ranges of physical properties allowed to be taken up by model cells. This would be a useful tool where geology is simple, with only a few rock types present, and specific physical property ranges are expected. Lelievre et al. (2008) demonstrate how this application can be used. This technique might be constructively applied to inversions in greenstone belts where smoothing in inversion results can obscure important contacts between petrophysically distinct mafic and felsic units.

The importance of physical property data collection is being increasingly recognized, especially in light of the need to use geophysics to explore for deeper mineral deposits. Large scale, publicly accessible physical property databases will become more common in the future, allowing geoscientists to cull physical property information from specific geographic areas, geologic regimes, and deposit types, to fortify geophysical work. A large data collection effort initiated by the Ontario Geological Survey (2001) in

the central Abitibi greenstone belt was mentioned in Chapter 2. A national physical property database is currently being compiled by the Geological Survey of Canada and Mira Geoscience Ltd. (Parsons and McGaughey, 2007).

The best inversion results are generated when geologists and geophysicists collaborate on the problem. Geologists and geophysicists need to combine efforts to research or investigate physical properties in a given environment prior to inversion. Geologists can play a larger role in geophysical investigations, and will benefit the exploration effort by doing so. Geologists can provide insight when surveys are being designed, and can aid the inversion process by contributing prior geologic information including dominant structural fabrics, typical stratigraphic thicknesses, proportions and volumes of rock types or alteration present, and shapes and sizes of typical orebodies. Significant geologic information can be incorporated into inversions, by directly manipulating basic input parameters or with a complex reference model building program like that of Williams (2008).

Recent collaborations between geologists and geophysicists for the greater understanding of a geological region took place during the Discover Abitibi Project. Greenstone architecture and mineral deposit settings were investigated indepth using a combination of geology and geophysics (Ayer et al., 2005, Reed, 2005, Reed et al., 2005, Mueller et al., 2006). Similar types of collaborations are likely in the future.

In order to have the greater community of geoscientists appreciate the benefits of collaboration between the two disciplines, case studies need to be presented in more general forums or as short courses that will attract members from both fields.

REFERENCES

Ayer, J.A., Thurston, P.C., Bateman, R., Dube., B., Gibson., H.L., Hamilton, M.A., Hathway, B., Hocker., S.M., Houle, M.G., Hudak, G., Ispolatov, V.O., Lafrance, B., Leshner, C.M., MacDonald, P.J., Peloquin, A.S., Piercey, S.J., Reed., L.E., and Thompson, P.H., 2005, Overview of results from the Greenstone Architecture Project: Discover Abitibi Initiative, Ontario Geological Survey, Open File Report 6154, 146 p., 3 sheets.

Lelievre, P., Oldenburg, D., and Williams, N., 2008, Constraining geophysical inversions with geologic information: Society of Exploration Geophysicists, 2008 Annual Meeting, Las Vegas, extended abstract, p. 1223-1227.

Mueller, E.L., Reford, S.W., Dawson, D.J.W., Morrison, D.F., Pawluk, C., Grant, J., Spector, A., Rogers, D.S., and Savage, T., 2006, Acquisition, inversion and presentation of geophysical data for geoscientific profiles in the Timmins–Kirkland Lake area: Discover Abitibi Initiative, Ontario Geological Survey, Open File Report 6189 , 28 p., 15 sheets.

Ontario Geological Survey 2001, Physical rock property data from the Physical Rock Property Study in the Timmins and Kirkland Lake Areas: Ontario Geological Survey, Miscellaneous Release – Data 91.

Parsons, S., and McGaughey, J., 2007, Rock property database system: Proceedings of Exploration '07, Toronto, Ontario, p. 933-938.

Phillips, N., Hickey, K., Lelievre, P., Mitchinson, D., Oldenburg, D., Pizarro, N., Shekhtman, R., Sterritt, V., Tosdal, D., and Williams, N., 2007, Applied strategies for the 3D integration of exploration data: KEGS Inversion Symposium, PDAC 2007, extended abstract, 9 p.

Reed, L. E., 2005, Gravity and magnetic three-dimensional (3D) modeling: Discover Abitibi Initiative, Ontario Geological Survey, Open File Report 6163, 40 p., 4 sheets.

Reed, L. E., Snyder, D. B., and Salisbury, M. H., 2005, Two-dimensional (2D) reflection seismic surveying in the Timmins-Kirkland Lake area, northern Ontario; acquisition, processing, interpretation: Discover Abitibi Initiative, Ontario Geological Survey, Open File Report 6169, 68 p., 10 plates.

Williams, N.C., 2008, Geologically-constrained UBC-GIF gravity and magnetic inversions with examples from the Agnew-Wiluna greenstone belt, Western Australia: Unpublished Ph.D. Thesis, The University of British Columbia, 479 p.

APPENDIX 2A – LIST OF ABBREVIATIONS

Rock Type

IF	felsic intrusive
IFP	feldspar-phyric rhyolite dike
IQFP	quartz-feldspar-phyric rhyolite dike
II	intermediate dike
IIX	brecciated intermediate dike
IM	mafic dike
KMXmag	brecciated K-fsp vein in magnetic mafic volcanic rock
L	lamprophyric dike
MLX	multi-lithic breccia
QMX	brecciated quartz vein in mafic volcanic rock
QUX	brecciated quartz vein in ultramafic volcanic rock
S	syenite dike
Seds	sedimentary rocks
T	volcanic tuff
VM	mafic volcanic rock
VMX	brecciated mafic volcanic rock
VMmag	magnetic mafic volcanic rock
VMXmag	brecciated magnetic mafic volcanic rock
VMP	pillowed mafic volcanic rock
VMPX	brecciated pillowed mafic volcanic rock
VU	ultramafic volcanic rock
VUX	brecciated ultramafic volcanic rock

Alteration

B	carbonate+muscovite alteration (bleached)
B+P	carbonate+muscovite+albite alteration
C	chlorite
CB	chlorite+carbonate+sericite
CH	chlorite+hematite
CS	chlorite+sericite
F	carbonate+fuchsite alteration
FC	Fe-carbonate alteration
FC+H	Fe-carbonate+hematite alteration
FC+H+S	Fe-carbonate+hematite+sericite alteration
FC+Q	Fe(Mg?)-carbonate+quartz alteration
FC+S	Fe(Mg?)-carbonate+muscovite/sericite alteration
H	hematite alteration
S	muscovite/sericite alteration
S+Q	sericite+quartz alteration
T	talc-chlorite metamorphic assemblage
U	generally unaltered

Minerals

ab	albite
act	actinolite
al	alunite
an	anatase
ank	ankerite
ap(hy)	hydroxyl apatite
au	augite
bt	biotite
cal	calcite
clz	clinozoisite
clc	clinocllore
chl	chlorite
dol	dolomite
ep	epidote
Fe-cb	Fe-carbonate
Mg-cb	Mg-carbonate
Fecb	ankerite+dolomite+siderite
hem	hematite
hbl	hornblende
ksp	potassium feldspar
mag	magnetite
mns	magnesite
mc(int)	microcline (intermediate)
mc(or)	microcline(ordered)
ms	muscovite
ms(Mg)	muscovite (magnesium)
mus(tot)	total muscovite
or	orthoclase
par	pargasite
pnt	paragonite
per	periclase
ph	phlogopite
pl	plagioclase
py	pyrite
qtz	quartz
rut	rutile
ser	sericite
sid	siderite
sm	smithsonite
sp	sphalerite
tc/tlc	talc
wt	witherite

APPENDIX 2B - HISLOP DRILLCORE LOGS, CROSS-SECTIONS, AND OUTCROP MAPS

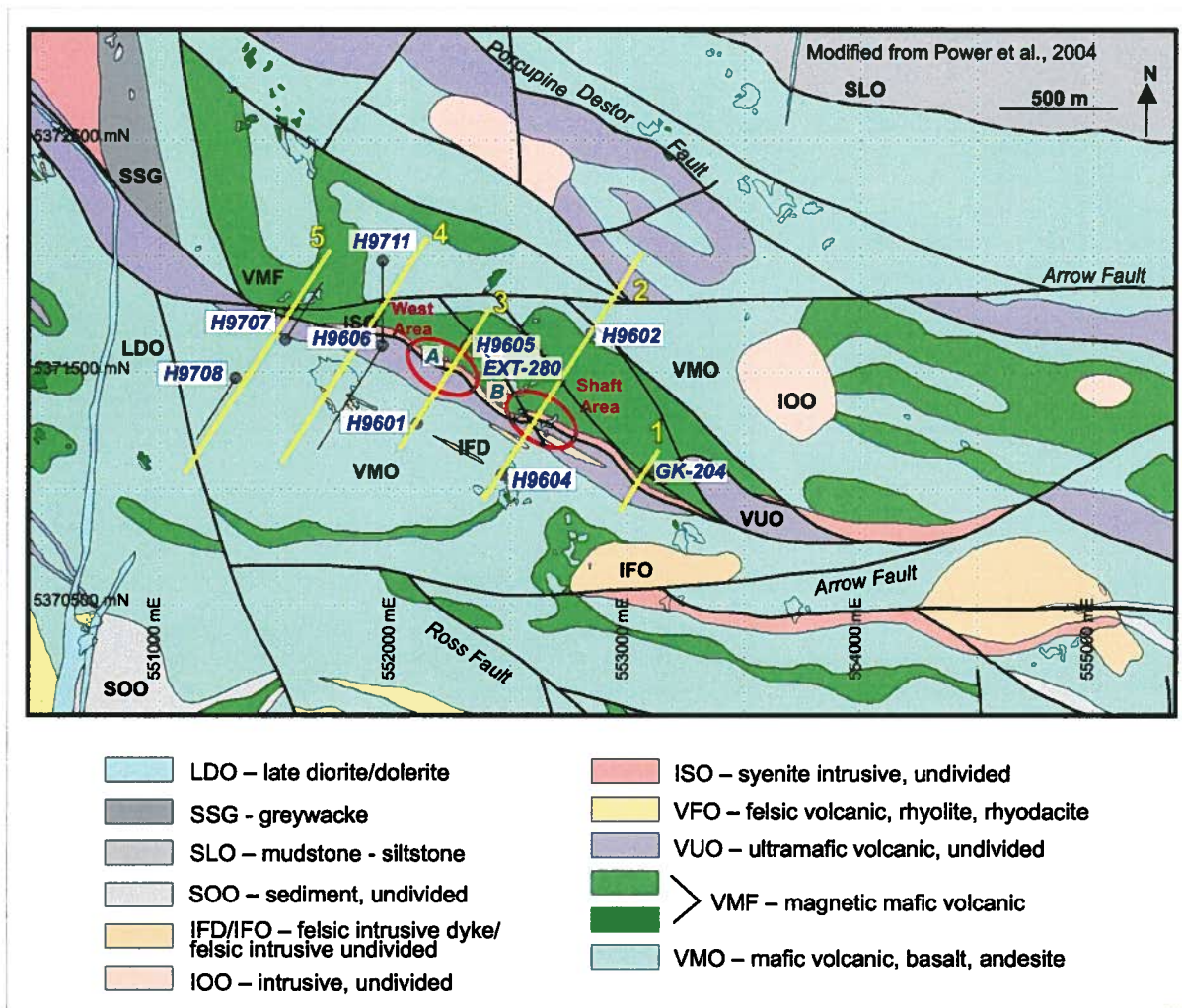
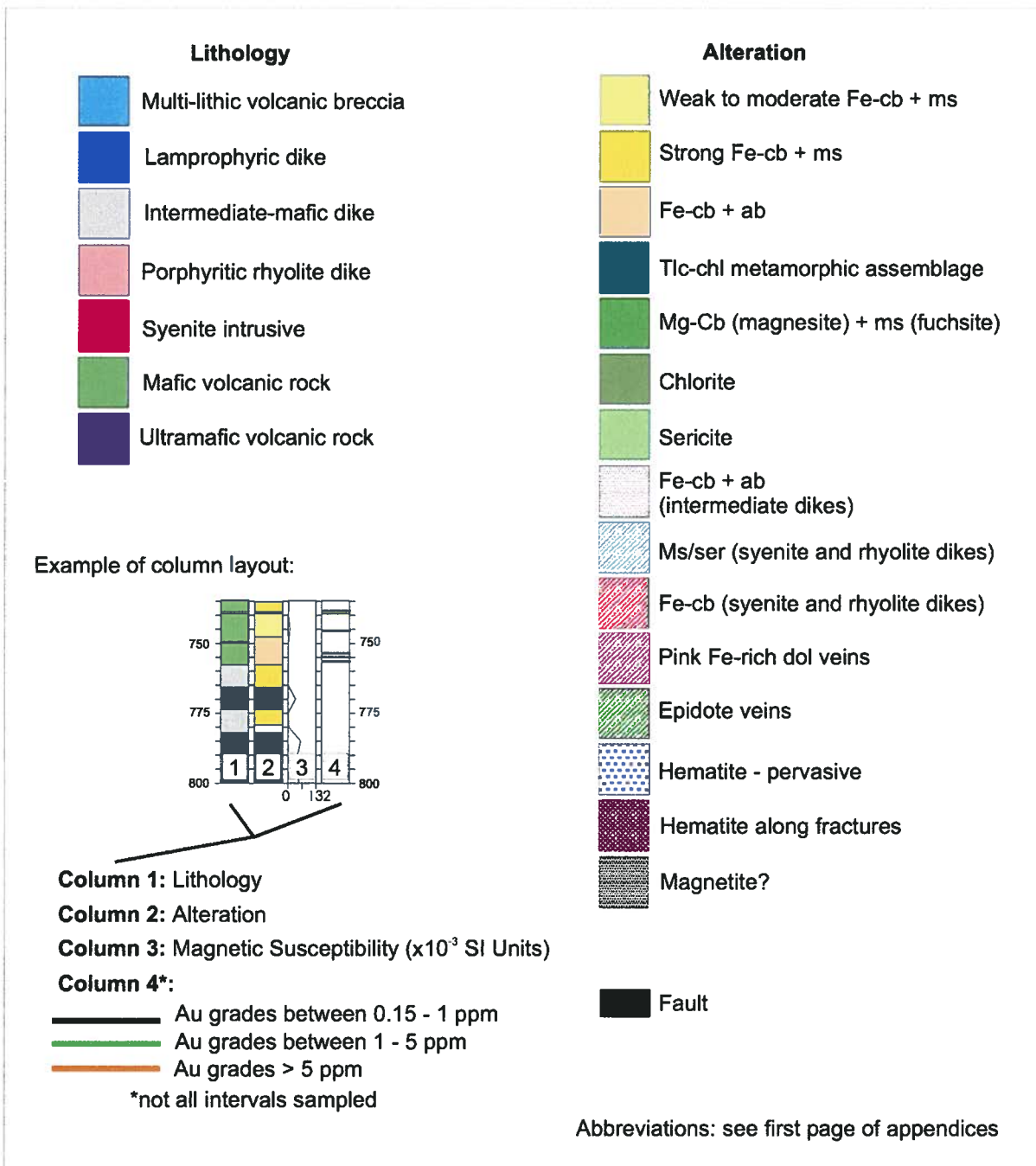
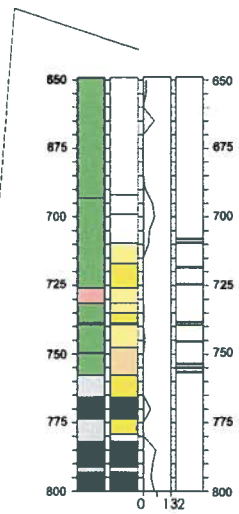
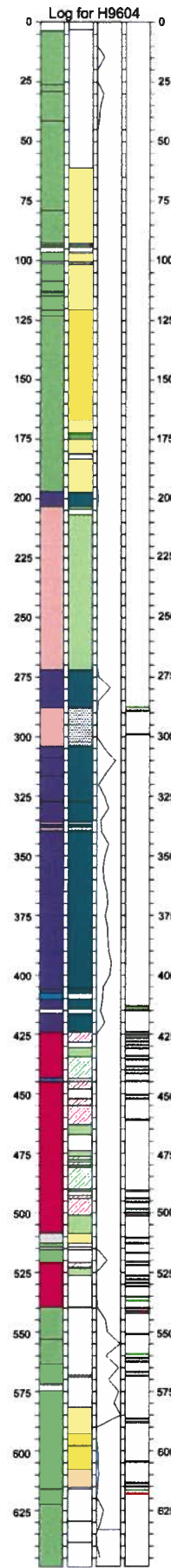
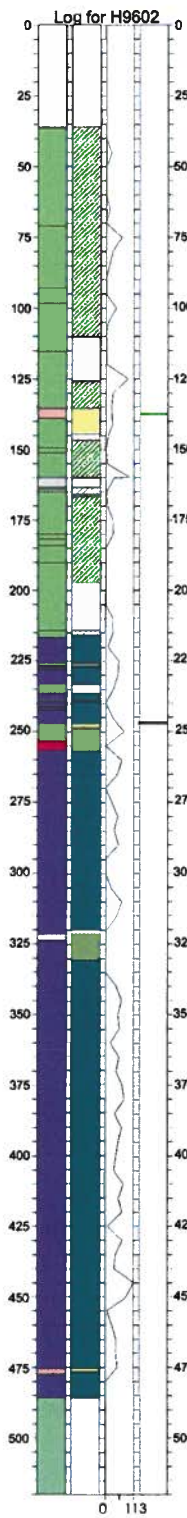
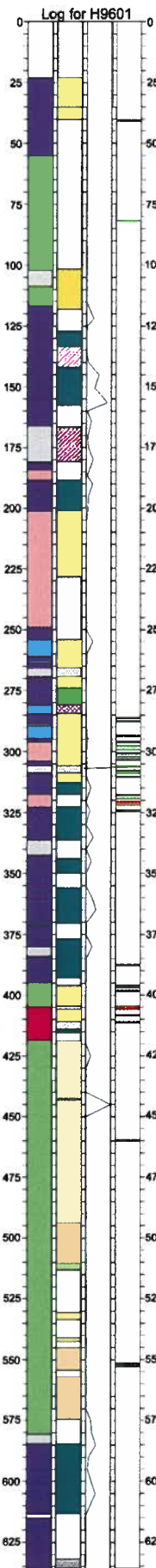
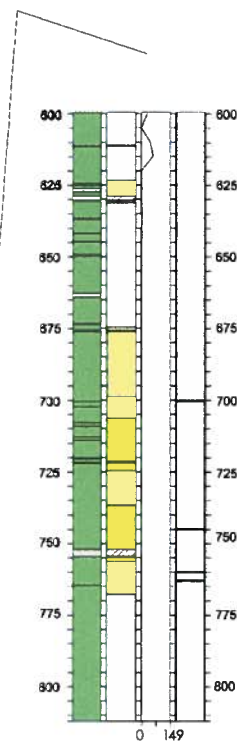
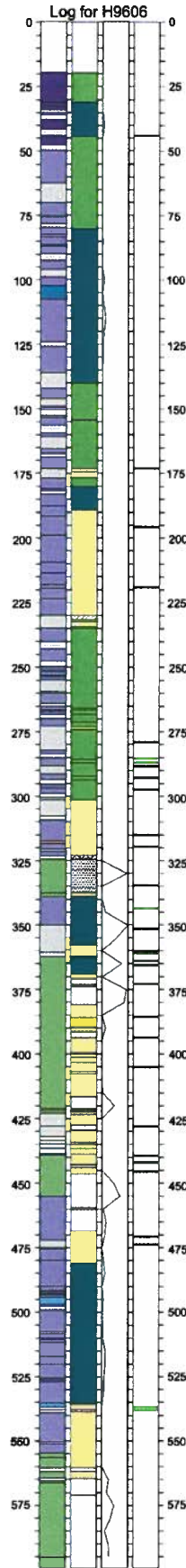
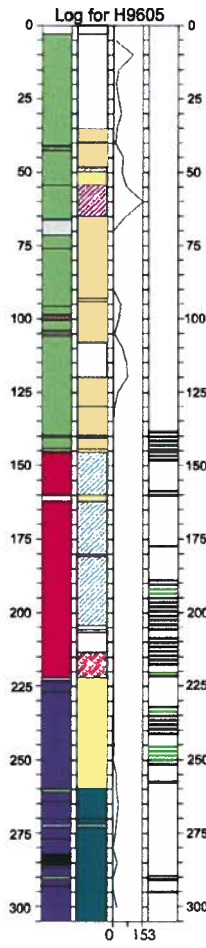


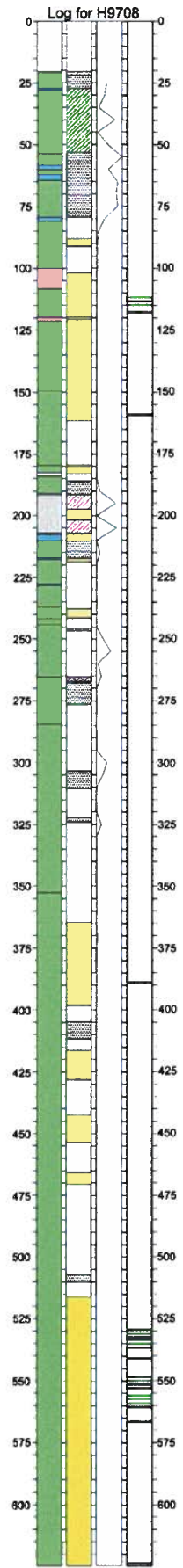
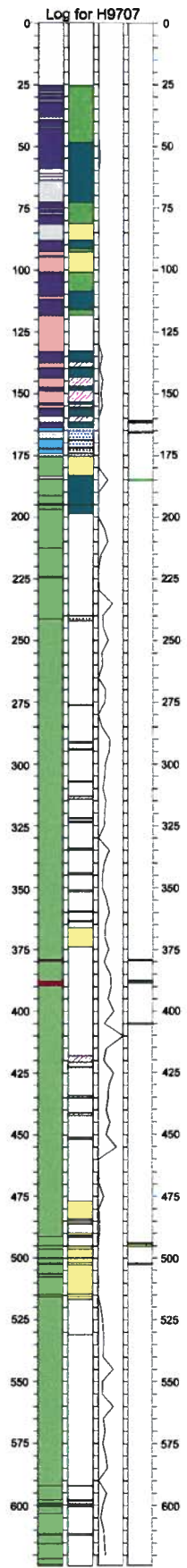
Figure 2B.1. Hislop deposit area geology map (modified from Power et al., 2004) showing locations of mined areas (West Area, and Shaft Area), ten drillholes logged for this study, five geologic cross-sections compiled from drill logs (1-5), and 2 outcrops (A and B).

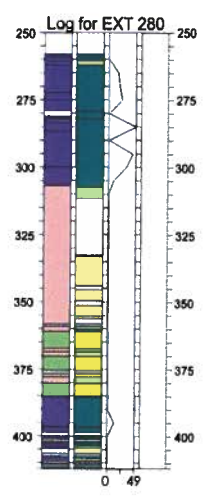
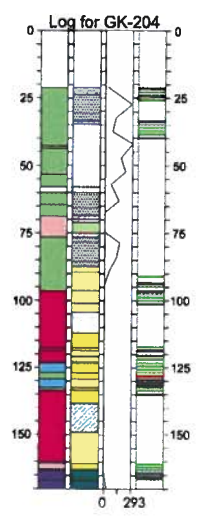
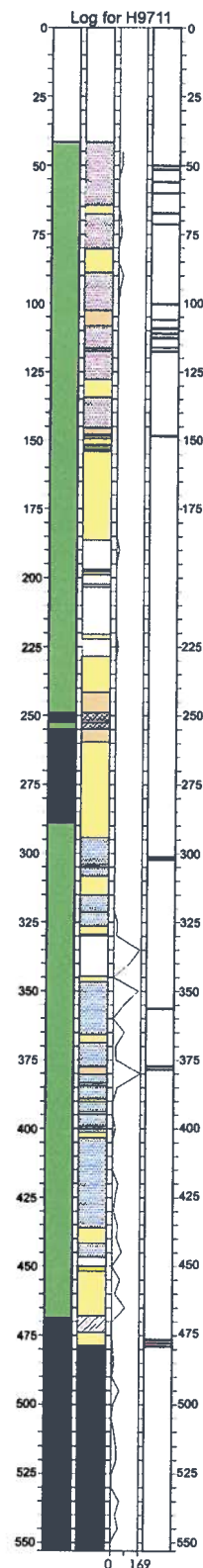


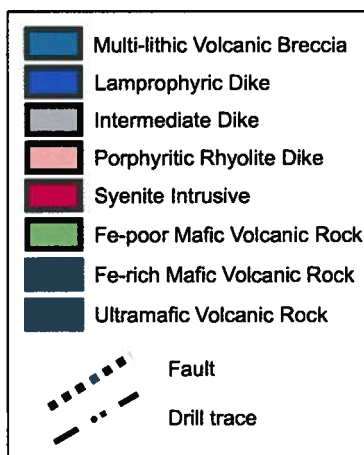
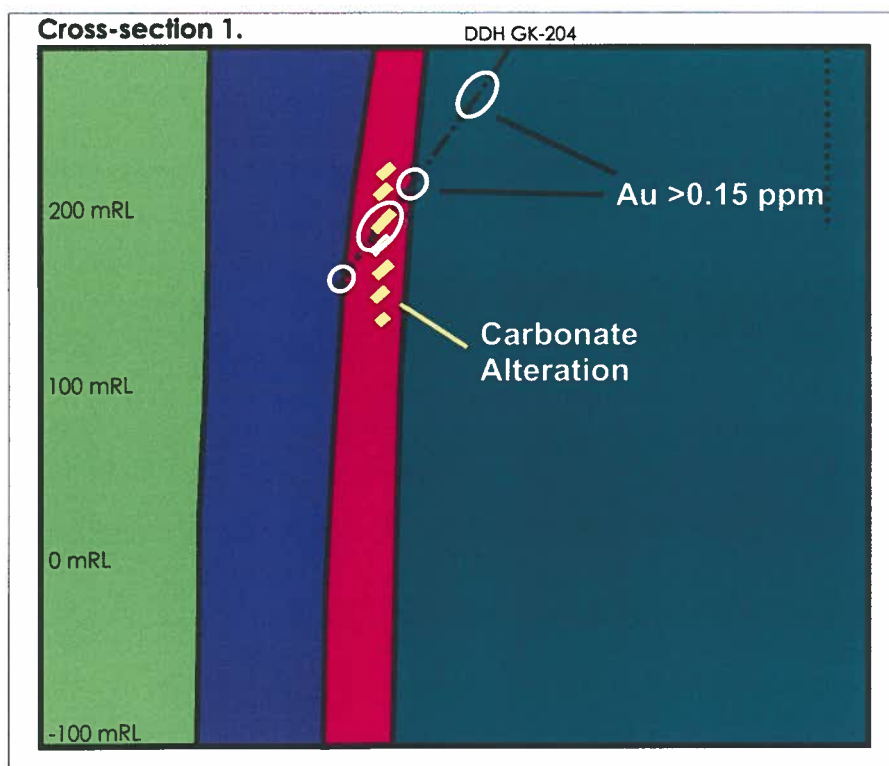
Hislop drill log legend.



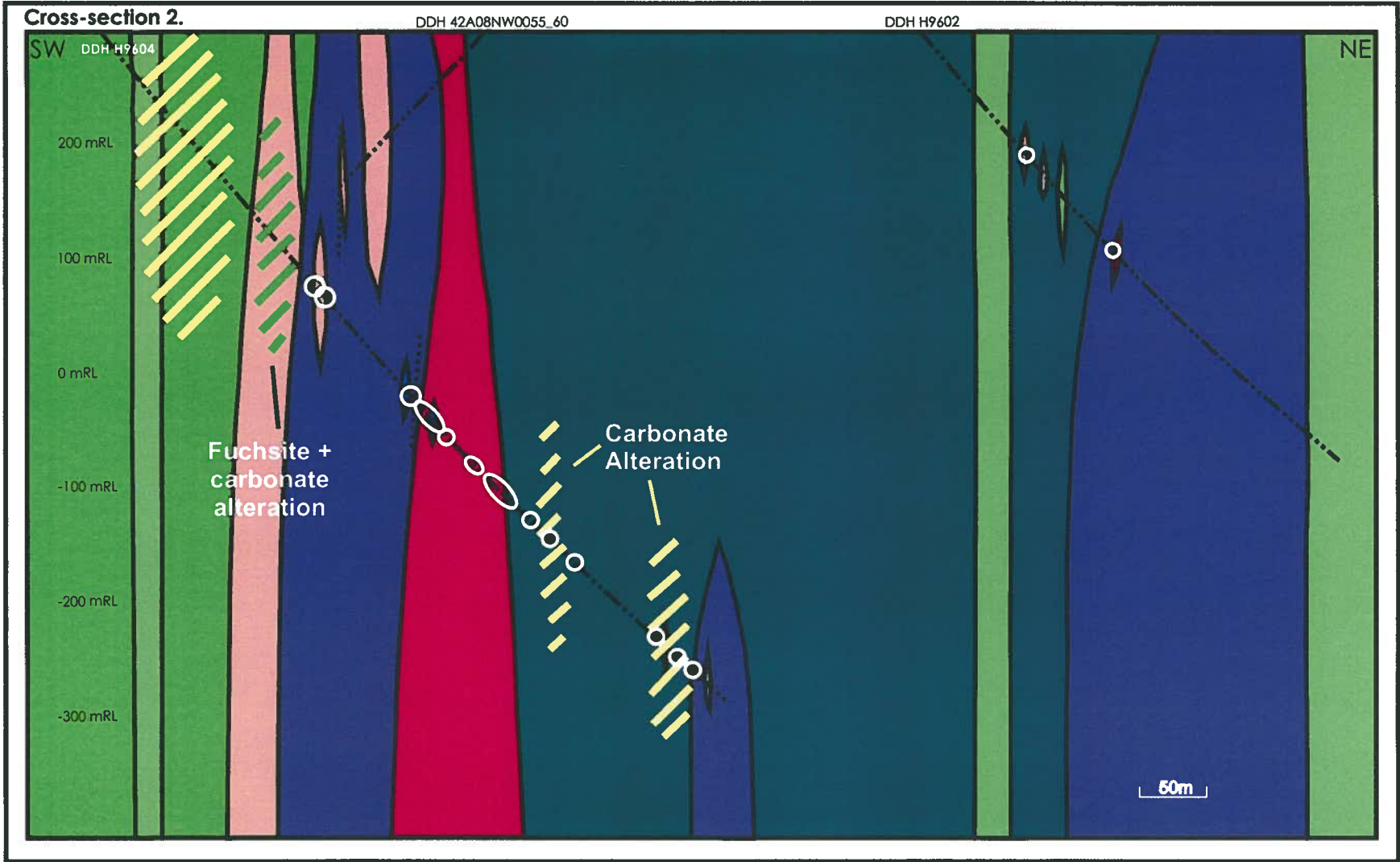


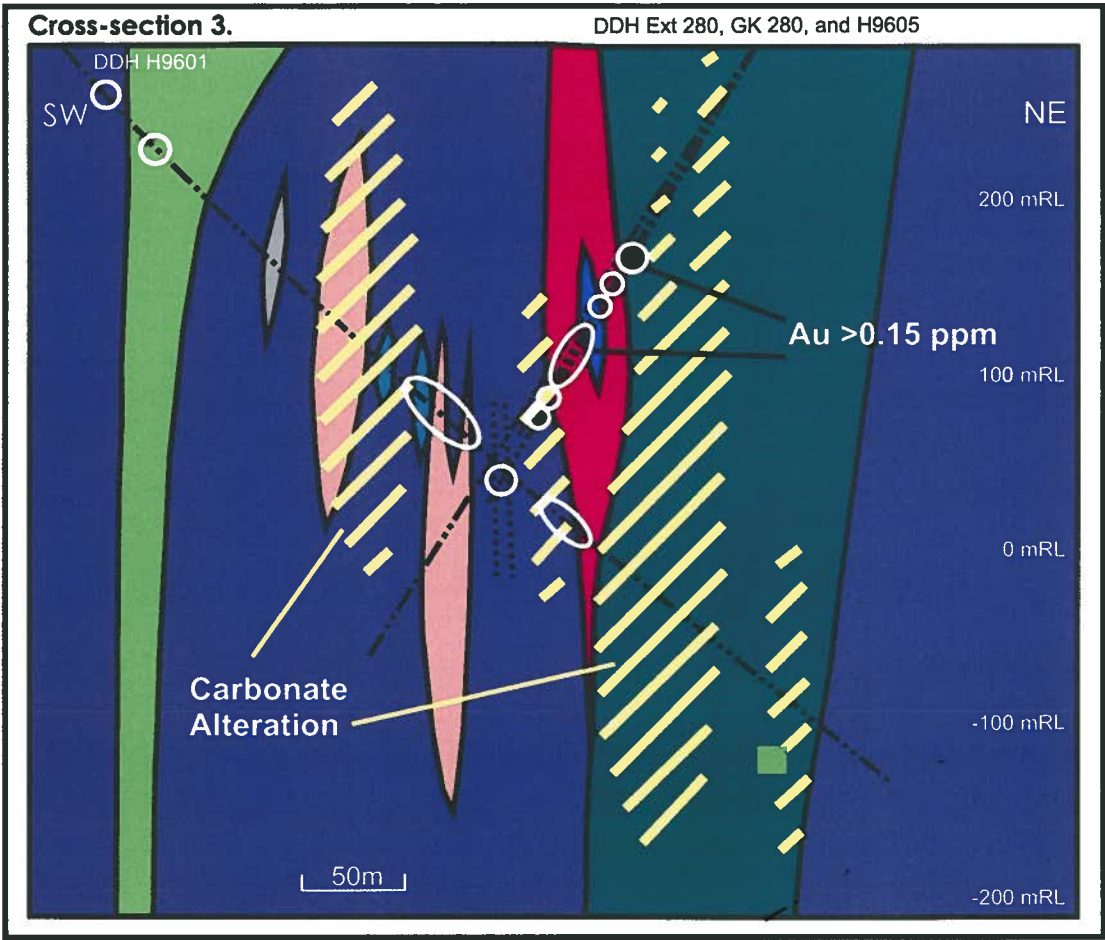


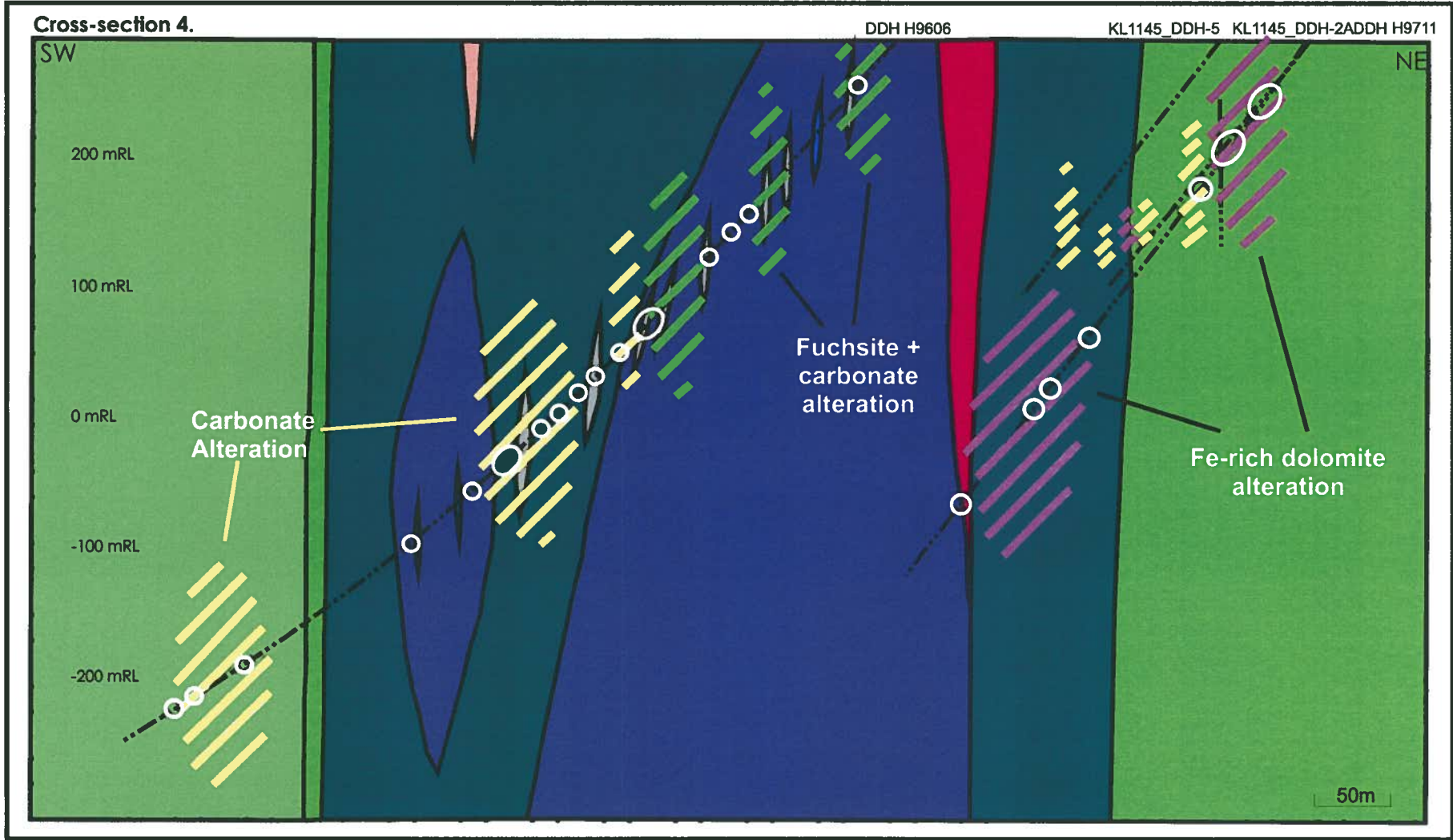




Legend applies to all following cross-sections



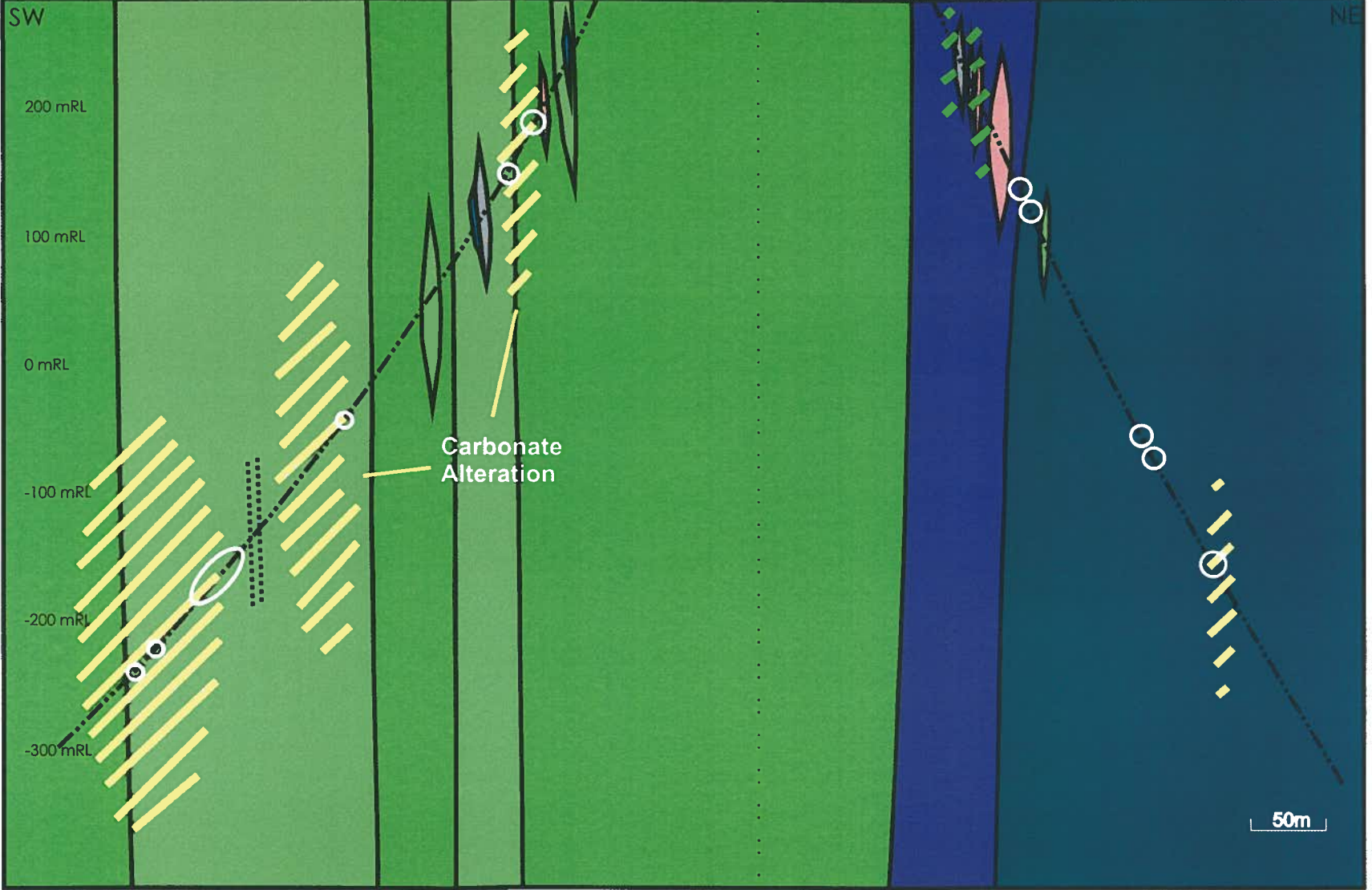


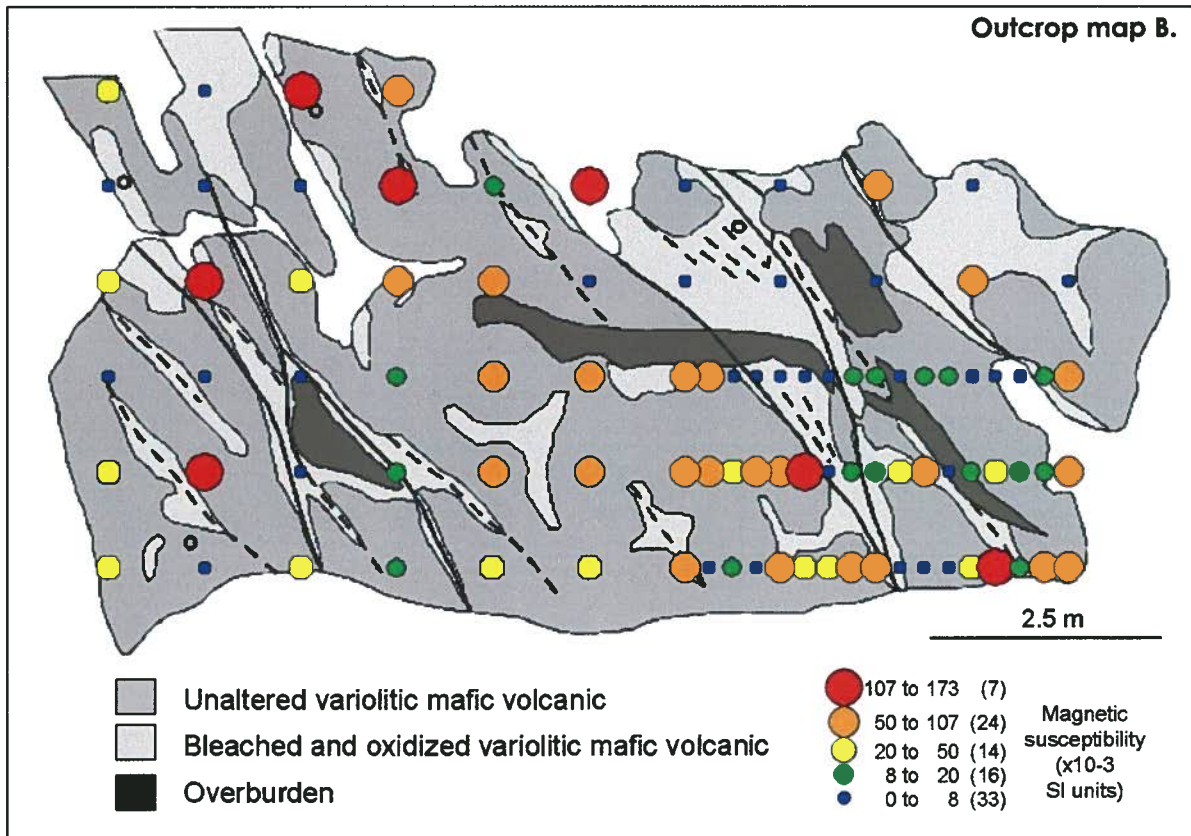
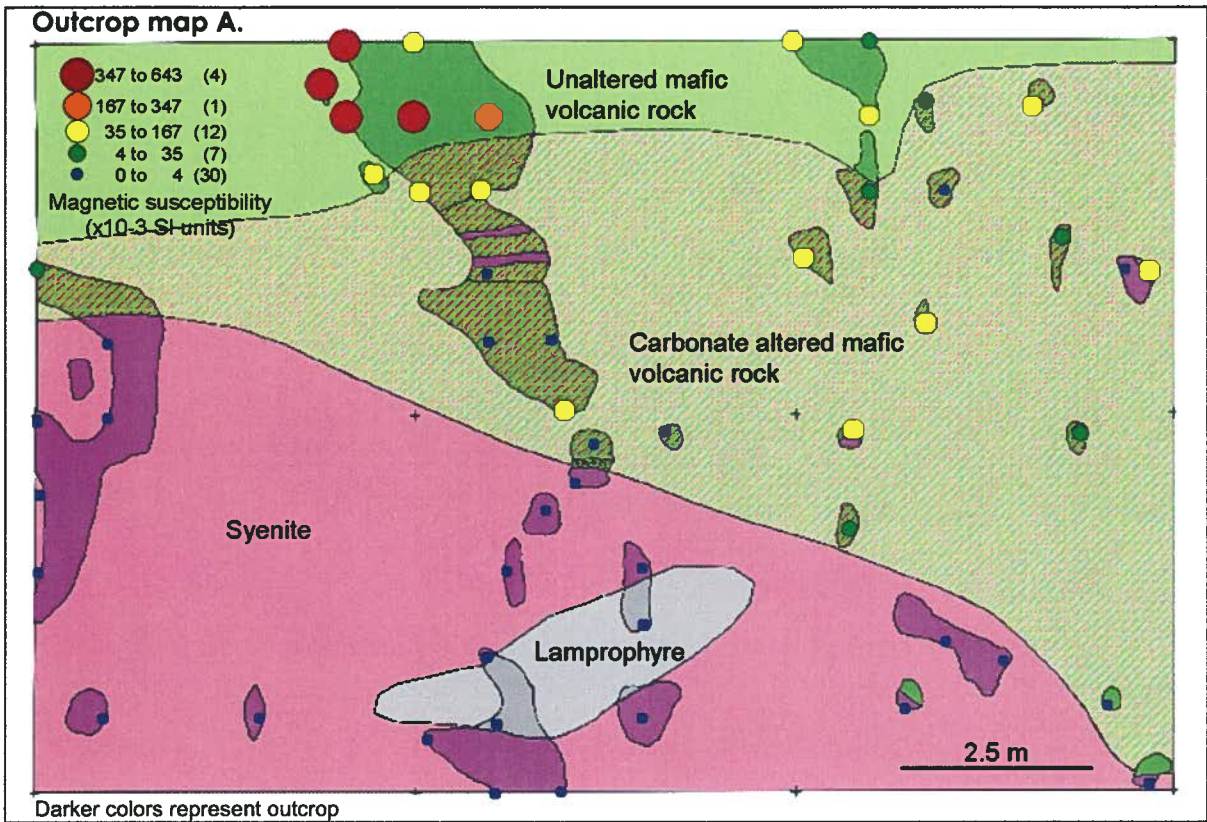


Cross-section 5.

DDH H9708

DDH H9707





APPENDIX 2C - DETAILED AND EXPANDED METHODS

XRD Analysis - Reitveld analysis

The standardless Rietveld refinement method was used to determine mineral abundances for Hislop samples. Samples were prepared and run, and data was analyzed, by Elizabetta Pani at the University of British Columbia. X-ray diffraction (XRD) analyses are first run on powdered bulk rock samples. The sample must first be ground such that particle sizes are $<10\mu\text{m}$ to avoid inaccurate diffraction peak intensities and preferred orientation of grains. Samples are ground in ethanol using a McCrone Micronising Mill with corundum elements. The sample is placed into a back-loading mount. The top of the mount is fit with a textured glass to minimize preferred orientation on the surface of the sample, and is removed before analysis. A modified razor blade may be used additionally to create texture in the top of the sample. Standard X-ray diffraction patterns are collected for samples using a Siemens D5000 diffractometer. X-ray diffraction data are collected in increments of 0.04° , from 3° to $70^\circ 2\theta$. The counting time is 2 seconds/step, and $\text{CuK}\alpha$ radiation is used. The diffractometer used includes a diffracted-beam monochromator, 1° divergence and anti-scatter slits, a 0.6 mm receiving slit, and an incident-beam Soller slit which was removed. A long-fine-focus Cu X-ray tube is used and operated at 40kV and 40mA, with a take-off angle of 6° . The mineral phases are determined using conventional search-match procedures.

The XRD data are analyzed by Rietveld refinement using the program Topas 2.0 (Bruker AXS 2000). For this method, information regarding the crystal structure of all detected phases is used to calculate a diffraction pattern for each phase present. These patterns are summed and then fitted to the collected diffraction pattern using a least-squares refinement. Numerous parameters are considered in the refinement including a series of global parameters (e.g. background, radiation wavelength, correction for the monochromator crystal), and mineral phase-dependant parameters (e.g. atomic coordinates, size and shape of the unit cell, site-occupancy). Using Rietveld methods, the relative masses for each phase can be calculated by considering the scaling factor

determined when observed and calculated data were being fit, the number of formula units per unit cell, the mass of the formula unit, and the volume of the unit cell. Detailed methods are found in Raudsepp and Pani (2003).

Magnetic susceptibility corrections

Core diameter corrections

An Exploranium KT-9 Kappameter was used to collect magnetic susceptibility data from 3.6 cm diameter drill core. Since the meter can only be set to take measurements from drill core with a diameter that is a whole number, the KT-9 was set to take readings for 4 cm drill core, the closest whole number to the diameter of the drill core being used. Through some experimentation, it was determined how to correct the magnetic susceptibility values for 3.6 cm from the 4 cm diameter field data. Susceptibility readings were taken along a few samples of whole core at particular data points (16 different points, Fig. 2C.1) with the meter set to various diameter settings. After this, the data was plotted to try and find a relationship between the magnetic susceptibility values and changes in diameter. First, diameter was plotted against magnetic susceptibility for select sample points to determine a relationship (for an example of this see Fig. 2C.2; for the full experimental dataset, see the spreadsheet labeled Appendix 2C on accompanying CD). It was noted that this relationship changes with variations in magnetic susceptibility between the different point locations measured; the relationship takes the form $y = mx^{-a}$, but a and m are different depending on the susceptibility at a given point. Coefficients a and m calculated from select sample points on four different samples were plotted against susceptibility measured on the 4 cm diameter setting (Figs. 2C.3 and 2C.4). From this it was determined that there were linear relationships between m and magnetic susceptibility and a and magnetic susceptibility. It was concluded that readings at 4 cm can be plugged into the equations $m = 3.2295x^{-33.133}$ and $a = -0.0004x - 0.6506$ (where x = magnetic susceptibility at 4 cm) to get m and a , and then m , a and the diameter we want to correct to (3.6 cm) can be input back into the

equation $y = mx^{-a}$, where x is the new magnetic susceptibility (at 3.6 cm). This correction was applied to all of the whole core data collected in the field.

Split core corrections

Some of the drill core was split lengthwise for sampling purposes, and only one half of these particular intervals was available to test. The KT-9 meter setting was kept on 4 cm diameter for these intervals. It was noticed that there existed discrepancies between the magnetic susceptibilities of whole and split core of similar rock types and it was necessary to correct for this. Similar experiments to the core diameter tests were completed, and susceptibility readings taken along whole core at particular data points (at various diameters), after which the core was split lengthwise using a rock saw and readings taken along the split pieces at the same designated data points. The data collected at each point was compared between the different diameters (this can be seen in spreadsheet 4 in Appendix 2C on the accompanying CD) with the anticipation that the change in values between whole and split core was simply proportional. For each sample the average ratio between whole core and split core values is consistent between various diameter settings. However, from one sample to the next (samples range from felsic rocks which have the lowest magnetic susceptibilities, to ultramafic rocks with higher magnetic susceptibilities) the ratio changes slightly (ranging from about 0.83 to 0.89). Low magnetic susceptibility samples do not consistently change by a different ratio than do high magnetic susceptibility samples when split. From spreadsheet 4, an attempt was made to determine if there was a relationship between susceptibility and this ratio. There appears to be a weak trend that indicates that a higher ratio can be used to correct for low magnetic susceptibility samples while a lower ratio can be used to correct for higher magnetic susceptibility samples (Fig. 2C.5). But the trend is not good, and appears to break down at low magnetic susceptibilities where there appears to be a broad range in “correction factors”. The average ratio was considered to be 0.85, and thus a correction factor of 1.15 was applied to split core samples to get approximate whole core susceptibilities.

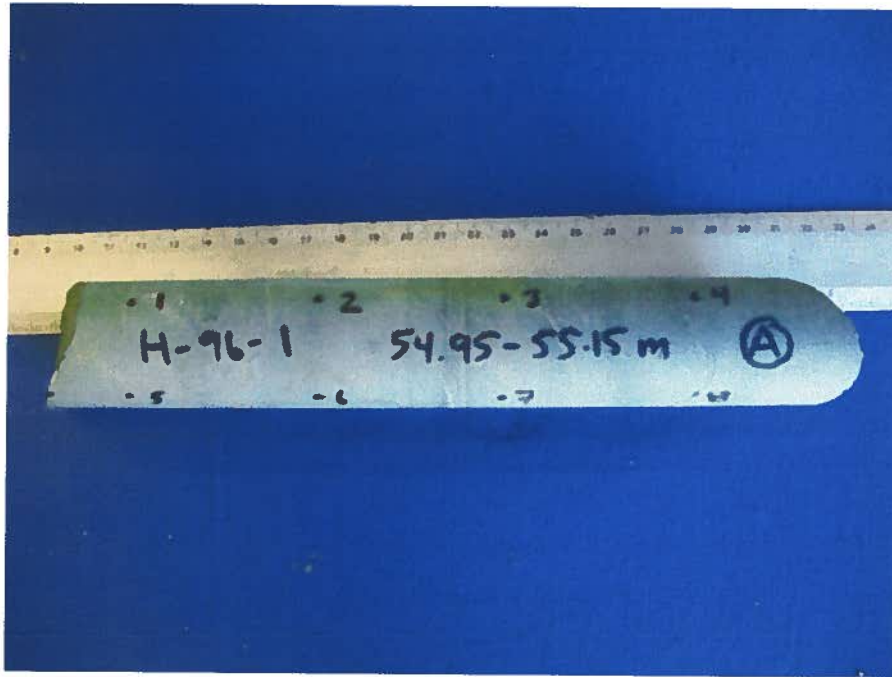


Figure 2C.1. Data points along a whole piece of drill core. Magnetic susceptibility readings were taken at each of 16 data points at various diameter settings (2.54, 3, 4, and 5 cm).

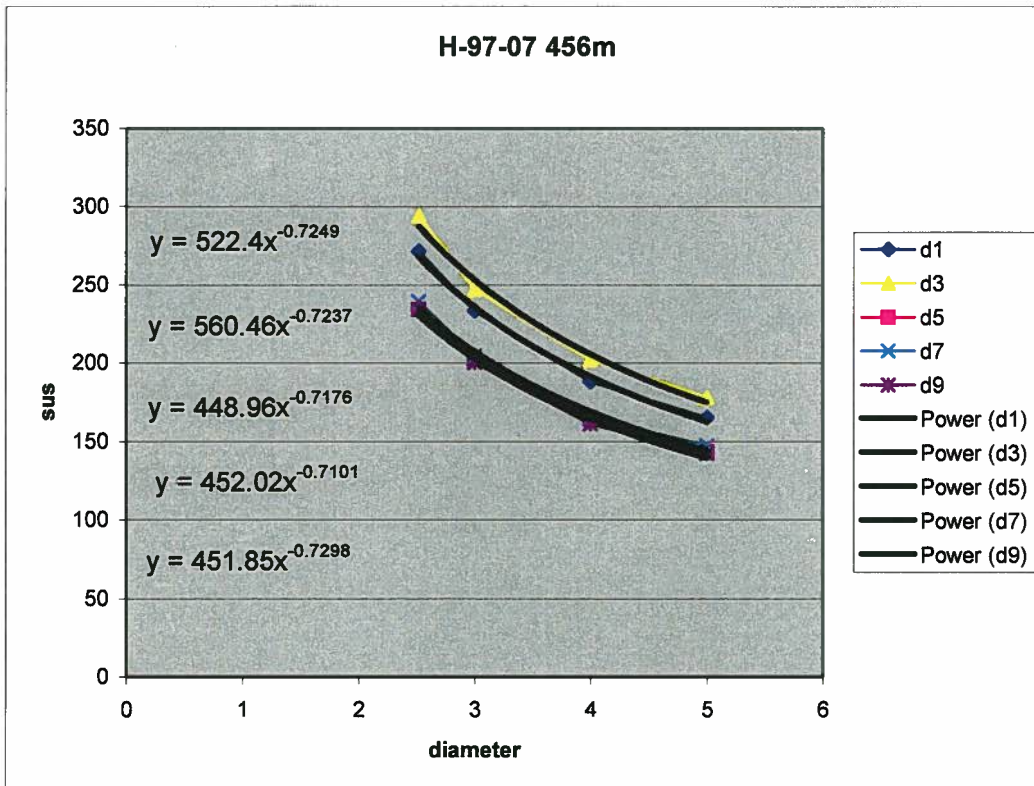


Figure 2C.2. Readings for five sample points (data points d1, d3, d5, d7, d9) for sample H9707-456 with meter set at 2.52, 3, 4, and 5 cm diameters. For a particular sample, there is not a distinct relationship between susceptibility and diameter, i.e., there is not simply one equation. The equation ($y = mx^{-a}$) changes with variations in magnetic susceptibility between the different points tested.

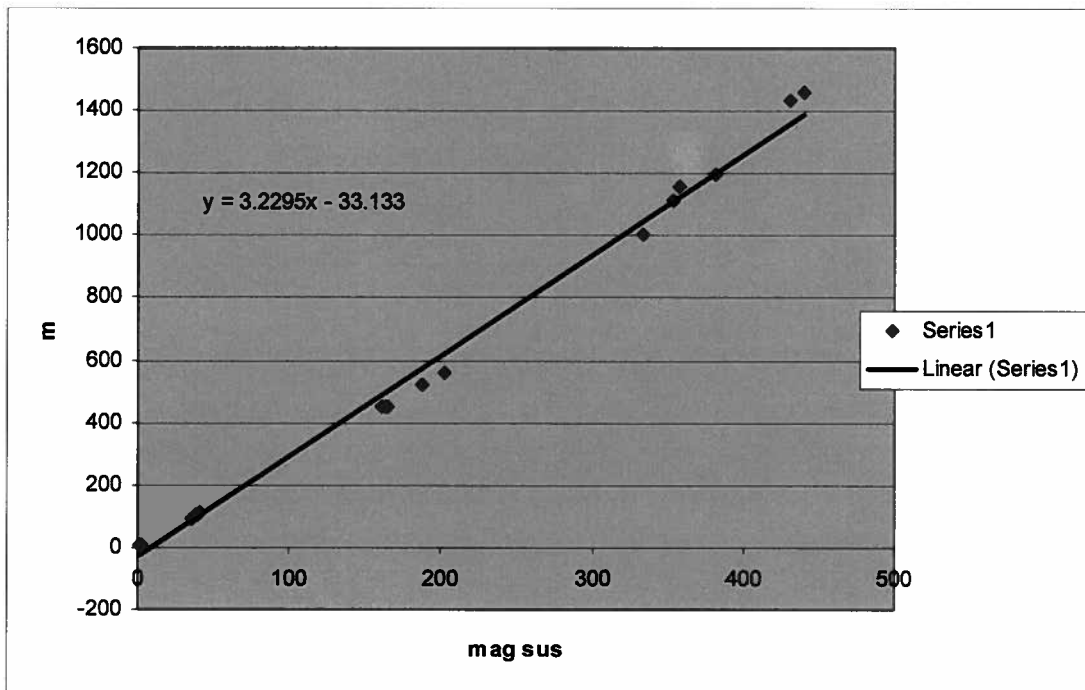


Figure 2C.3. Relationship between susceptibility measured on the 4 cm diameter setting, and m from equation 1, for select points from four different samples. The different samples are obvious as the four clusters of data occurring within narrow susceptibility ranges.

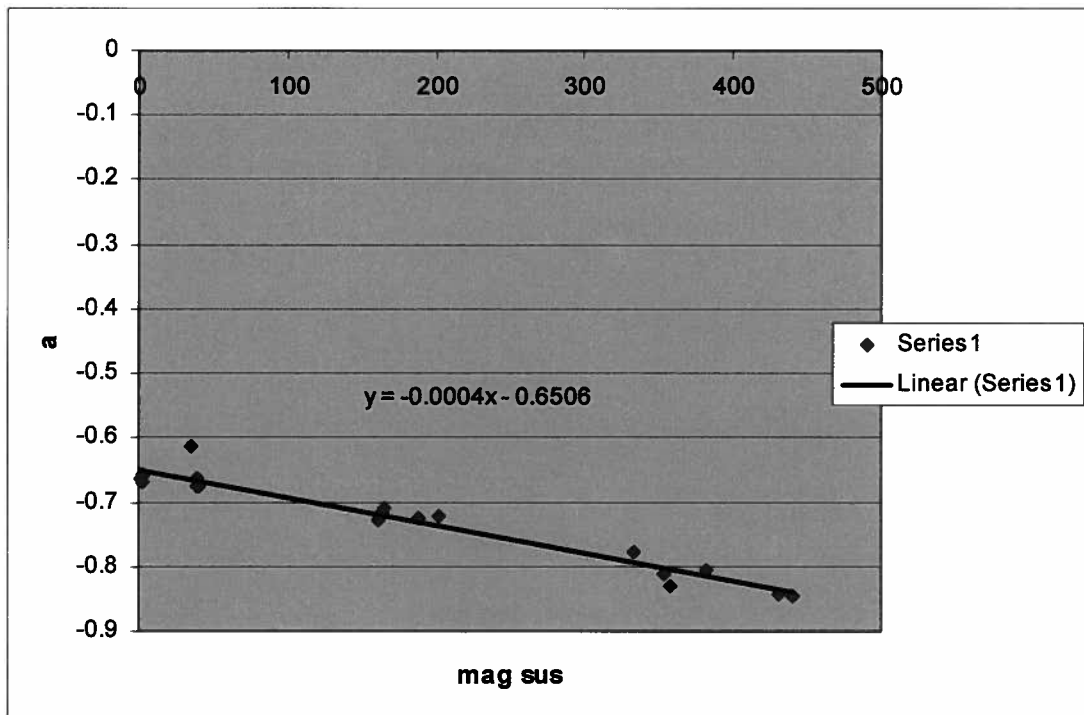


Figure 2C.4. Relationship between susceptibility measured on the 4 cm diameter setting, and a from equation 1, for select points from four different samples. The different samples are obvious as the four clusters of data occurring within narrow susceptibility ranges.

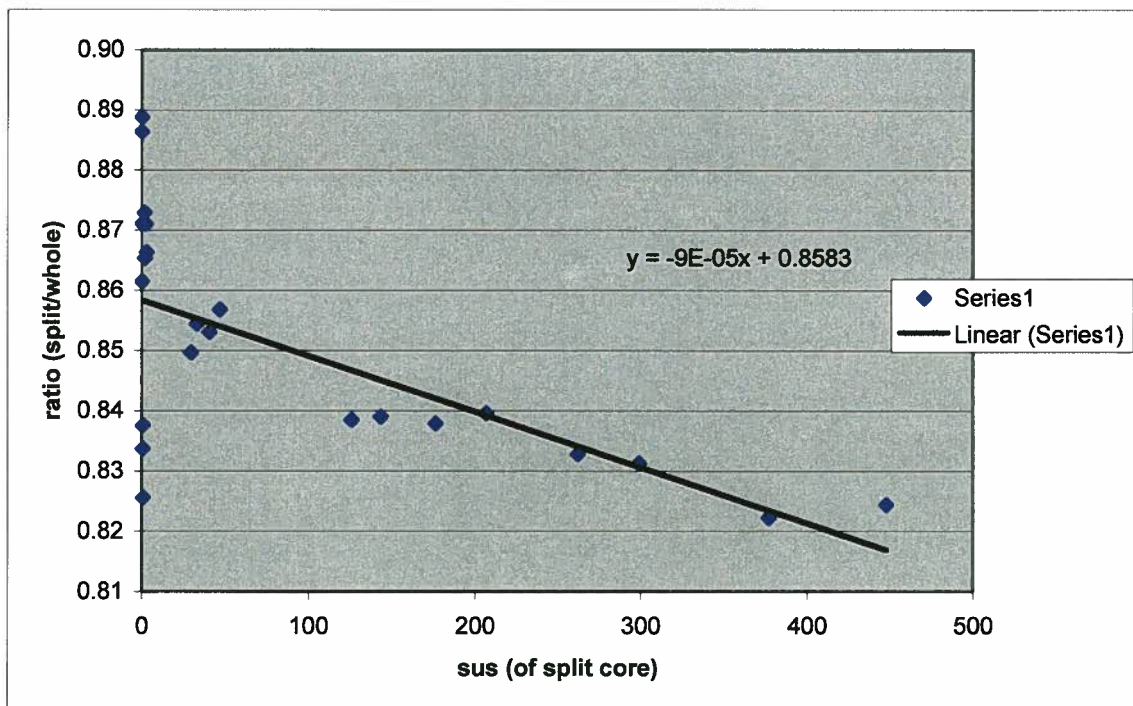


Figure 2C.5. Possible relationship between the susceptibility of split core and the ratio between split core and whole core values. Relationship seems to break down at low susceptibilities.

Comparison of hydrostatic and geometric calculations of density

Density measurements for Hislop samples were made using the hydrostatic method described in Chapter 2, section 4.2.2. To test if this method was generating reliable density measurements, a geometric method was applied to select samples for comparison. Density values are determined by dividing the mass of the sample by its measured volume. The volume of the sample was determined by measuring the length and diameter of a piece of whole drill core using a Mitutoyo caliper (12in/300mm). The drill core was first cut as evenly as possible on each end. Multiple measurements were made of the diameter and length to account for slight irregularities, and the average value was used to calculate the samples volume. Figure 2C.6 shows a plot of density measurements made by the geometric method versus density measurements made using the hydrostatic method. A strong correlation indicates values are accurate.

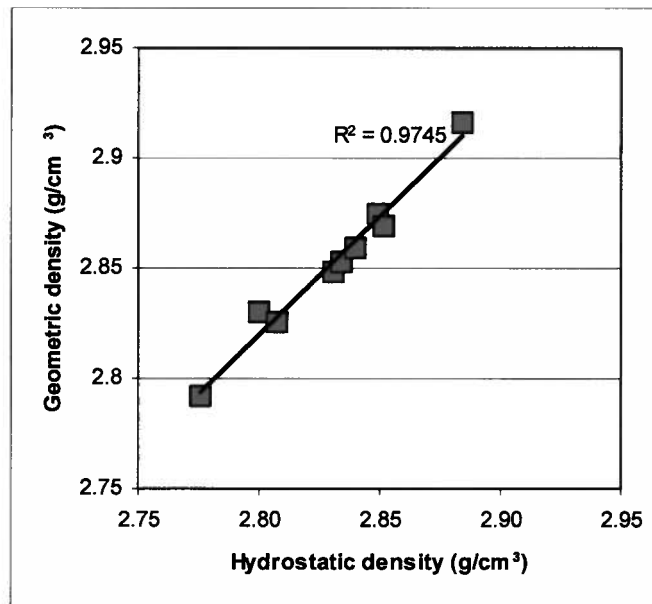


Figure 2C.6. Density data calculated using the hydrostatic method versus the geometric method.

APPENDIX 2D – X-RAY DIFFRACTION ANALYSES

Sample	Rock	Altn	ab(lo)	act	al	an	ank	ap(hy)	au	bt	cal	clz	clc(II)	dol	ep	Fechb	hem	hbl	ksp	mag	mns
H9604-57	VMP	U	37.1		0.8						14.7		17.3								
4THD8	VMP	U	27.1						30.7			10.7	22.0								
4THD104	VMP	U	38.4	4.2					23.4				15.5		12.2						
H9601-439	VM	B	44.0										5.2	20.7		28.0	2.1			1.0	
H9601-122	VM	U	49.6										12.5	18.7		18.7	4.0			0.9	
H9604-28	VM	U	27.6	1.0			0.5		11.1		7.2		30.6	0.5		1.1					
H9604-122	VM	B	3.1			0.5	14.9							14.9		46.8	0.4				
H9605-111	VMmag	U	8.0										2.0	22.4		33.2					
H9707-373	VMmag	U	34.9	29.6					8.3	1.9	0.9		10.8							3.7	
4THD117	VMmag	U	41.7								0.6		2.1	7.1		7.1	2.1			5.1	
4THD100	VMmag	U	36.4						15.6				7.7		13.8						
4THD116	VMmag	B	34.3											16.1		16.1					
4THD114	VMmag	U	16.2							19.1	21.7		15.6				3.2			6.0	
3THD15	VMmag	U	35.6	13.8					21.4	6.8	3.2		7.9							8.2	
H9711-281	VU	B	2.6										16.7	22.9		22.9					
H9606-179	VU	F	2.0										35.0	19.0		19.0					
H9601-200	VU	T	4.0	3.3							11.7		42.1	6.5		6.5	2.5				
H9601-252	VU	U											36.6	23.0		23.0	1.8	4.6			
H9604-379	VU	T									10.4		49.7	5.2		5.2				2.9	
H9601-396.5	VU	B	1.2										5.4	20.6		20.6					44.2
3THD1	VU	B	17.3						4.0				6.1	20.5		20.5				0.6	31.2
H9601-410	S	U	59.3								0.8			2.2		2.2					
H9605-176	S	FC	63.0													0.4					
4THD115	S	FC+S	37.2											0.5		0.5					
H9601-417	S	B																			
H9605-210	S	FC+S	59.4				8.1				0.6			8.1		16.2					
3THD6	S	U	48.5											1.0		1.0					
H9601-406	S	S	58.6											5.2		5.2					
H9601-298	IQFP	U	64.8										0.4	1.2		1.2					
H9604-214	IFP	S	54.0				3.2				2.2			3.2		6.4					
H9601-322	IQFP	U	62.8											5.7		5.7					
H9601-302	IQFP	U	59.8											0.8		0.8					
H9707-137	IM	U	32.2					1.7					32.8	11.6		11.6	3.6			3.1	
H9606-66	II	F	2.5											21.1		44.2				1.5	
H9606-230	II	FC	33.0											20.2		24.3	0.6				
H9606-173	II	B+P	45.8											14.2		14.2					
H9604-444	L	U	14.3										20.7	25.4		25.6					

Sample	Rock	Altn	mc(int)	mc(ord)	ms(2M1)	ms(1M,Mg)	mus(tot)	or	par	pgt	per	ph(1M)	pl	py	qtz	rut	sid	sm	sp	tc(1A)	wt
H9604-57	VMP	U			3.5		3.5							1.3	23.6	1.8					
4THD8	VMP	U			4.7		4.7		0.9						3.8						
4THD104	VMP	U	4.2												2.0						
H9601-439	VM	B			6.7		6.7							0.9	11.1	1.0	7.2				
H9601-122	VM	U			1.8		1.8								11.2	1.3					
H9604-28	VM	U	2.6												19.4						
H9604-122	VM	B					19.1			9.3					34.0	1.7	17.0				
H9605-111	VMmag	U		3.1	33.5		33.5							0.5	19.7	10.8					
H9707-373	VMmag	U	9.9																		
4THD117	VMmag	U	4.9											2.4	34.0						
4THD100	VMmag	U	1.0						24.0						1.6						
4THD116	VMmag	B	14.4											7.9	27.3						
4THD114	VMmag	U	3.3												15.1						
3THD15	VMmag	U	2.7												0.5						
H9711-281	VU	B	3.1		22.8		22.8								30.5				0.3		1.1
H9606-179	VU	F			4.8		4.8				3.1				29.2			6.9			
H9601-200	VU	T													17.3						12.6
H9601-252	VU	U													25.6						8.4
H9604-379	VU	T										6.2									25.6
H9601-396.5	VU	B					1.4								27.1						
3THD1	VU	B												1.4	1.2						17.6
H9601-410	S	U			32.9		32.9								1.3	3.5					
H9605-176	S	FC		18.4	17.3		17.3								0.9		0.4				
4THD115	S	FC+S		23.7	38.0		38.0								0.6						
H9601-417	S	B			35.0	13.1	48.0						43.0	1.1	7.9						
H9605-210	S	FC+S	19.5				8.3								2.9	1.2					
3THD6	S	U	38.3				11.1								1.2						
H9601-406	S	S					23.3								1.7	11.2					
H9601-298	IQFP	U	6.7											0.3	26.2			0.4			
H9604-214	IFP	S					15.4								0.3	25.0					
H9601-322	IQFP	U												1.0	30.4						
H9601-302	IQFP	U	8.4											0.5	30.6						
H9707-137	IM	U			5.8		5.8	1.6						1.1	6.5						
H9606-66	II	F	2.3				28.6								21.0		23.1				
H9606-230	II	FC					17.7	14.2							9.3		4.1				
H9606-173	II	B+P	12.7				15.3							4.6	7.4						
H9604-444	L	U						21.4						2.9	15.1		0.3				

APPENDIX 2E – PHYSICAL PROPERTIES OF HISLOP DEPOSIT ROCKS

Sample No.	HoleID	From	To	Rock type	Gr. size	Altn	notes	MS (x10 ⁻³ SI)	Den (g/cm ³)	Chrg (ms)	Res (Ohm-m)	Por (%)
3THD10	hndsm			IM		FC	equigranular	4.15	2.79			
3THD11	hndsm			VU			sheared	24.80				
3THD12	hndsm			VUX		B	"carbonate breccia"	0.96	3.01			
3THD13	hndsm			Vmmag?		U		17.20	3.01			
3THD14	hndsm			VMmag?		U		50.40	2.94			
3THD15	hndsm			VMmag?		U		88.80	2.98	20.87	2548.9	
3THD16	hndsm			VMmag?		U		82.30	2.87			
3THD17	hndsm			VMmag?		B+P	north of main mine syenite	12.40	2.79	11.17	22052	
3THD18	hndsm			S		FC+S		0.27				
3THD19	hndsm			Vmmag		U		94.70				
3THD1A	hndsm			VU		B	breccia; Fe-carbonate and qtz matrix, disseminated py	11.20	2.78	9.83	4757.6	
3THD2	hndsm			S		FC+S		0.16	2.67	10.57	5852.6	
3THD20	hndsm			Vmmag?		U		41.60				
3THD21	hndsm			VMP		U	pillow tops to NE (060), 10 cm to 0.5 m, some disseminated py	15.60	2.89			
3THD21	hndsm			VMP			disseminated py	15.60				
3THD3	hndsm			IM		FC	equigranular; disseminated py and cpy	0.86	2.77			
3THD4	hndsm			L			massive	12.40				
3THD5	hndsm			IM		FC	syenite "veins", cut by Fe-carbonate veins	6.21	2.73			
3THD6	hndsm			S		U		0.17	2.64	13.40	6507.1	
3THD7	hndsm			VMmag?		U	syenite "veins"; disseminated py and cpy	203.00	3.07	15.17	5034.1	
3THD9	hndsm			IF		FC	carb and disseminated py/cpy fills fractures	0.41	2.67			
4THD10	hndsm			VM	f	U		0.97	2.92			
4THD100	hndsm			VMmag		U		1.14	3.00	6.63	10687	0.28
4THD101	hndsm			VMP	f	U	pillows 20cm to 1m; chlorite selvages; tops to 075	0.55	2.94			
4THD102	hndsm			IM		U		33.00	3.06			
4THD103	hndsm			VM		U		69.50	2.89			
4THD104	hndsm			VMP		U	epidote in selvages	12.80	2.98	8.50	33638	0.23
4THD105	hndsm			VMP	f	U	epidote in selvages		2.97			
4THD106	hndsm			VU		F	Royal Oak pit?	0.62	2.95			
4THD107	hndsm			VM		B	Royal Oak pit?	0.37	2.88			
4THD108	hndsm			VMP		U	Royal Oak pit?	0.52	2.82			

Sample No.	HoleID	From	To	Rock type	Gr. size	Altn	notes	MS (x10 ⁻³ SI)	Den (g/cm ³)	Chrg (ms)	Res (Ohm-m)	Por (%)
4THD109	hndsmp			Seds		U	Porcupine sediments	0.21	2.73	9.73	3478.5	0.54
4THD110	hndsmp			Seds		U	Porcupine sediments	0.28	2.76			
4THD111	hndsmp			IM	c	U	late dike?	35.10	3.06	36.60	16472	
4THD112	hndsmp			IM	c	U	late dike?	26.20	3.04			
4THD113	hndsmp			VMX		U		0.43	2.84			
4THD114	hndsmp			Vmmag		U		74.10	2.92	37.73	58754	0.13
4THD115	hndsmp			S	c	FC+S		0.20	2.69	6.27	3343.8	
4THD116	hndsmp			VMMag		B		0.15	2.81	7.57	2130.9	
4THD117	hndsmp			VMMag		U		54.30	2.78	28.18	3075	
4THD2	hndsmp			VMP	c	U		0.68	2.91			
4THD3	hndsmp			VU		B	similar to rock from Royal Oak pit; Fe-carb alteration along fractures	1.44	2.88			
4THD4	hndsmp			II		U		0.24	2.80			
4THD5	hndsmp			VM		U	disseminated py	0.35	2.76			
4THD6	hndsmp			VM		B	similar to rock from Royal Oak pit; Fe-carb alteration along fractures	0.38	2.81			
4THD7	hndsmp			VMP		U	variolithic, flow-banded pillow basalt; coalescing varioles	0.72	2.90			
4THD8	hndsmp			VMP		U	pillows 30 cm; epidote in selvages	0.88	2.99	3.38	42488	0.57
4THD9	hndsmp			VM		U	epidote in veins	32.40	2.92			
Ext280-258	EXT 280	258.25	258.45	VU	f	T	sheared, fractured; qtz/Fe-carb vein	21.06	2.84			
Ext280-274	EXT 280	274.25	274.5	VU	f	T	rare veins	0.55	2.86			
Ext280-275	EXT 280	275	275.2	VU	f	T	in-situ fragmented and sheared	27.76	2.86	7.80	283.3	1.49
Ext280-287	EXT 280	287.45	287.65	VU	f	T	massive to sheared, abundant qtz amygdules, <1mm	26.90	2.87			
Ext280-306	EXT 280	306.65	306.9	IFP	f	S	20% fsp phenocrysts average <1 to 1mm	0.16	2.66			
Ext280-308	EXT 280	308	308.2	IFP	f	S	phenocrysts diffuse	0.12	2.65			
Ext280-319	EXT 280	319.3	319.55	IFP	f	U	unaltered phenocrysts clearly visible	0.16	2.64			
Ext280-341	EXT 280	341.2	341.45	IFP	f	B		0.16	2.61			
Ext280-353	EXT 280	353.3	353.55	IFP	f	B		0.13	2.66			
Ext280-358	EXT 280	358.2	358.4	II	f	U	sharp contacts	0.39	2.86			
Ext280-365	EXT 280	365.2	365.4	VMmag	m	B		1.28	2.67			
Ext280-365.5	EXT 280	365.45	365.7	IFP	f	S		0.12	2.88			
Ext280-372	EXT 280	372.3	372.55	VMmag	m	B		0.55	2.89			
Ext280-375	EXT 280	375.65	375.85	II	f	H		3.29	2.84			

Sample No.	HoleID	From	To	Rock type	Gr. size	Altn	notes	MS (x10 ⁻³ SI)	Den (g/cm ³)	Chrg (ms)	Res (Ohm-m)	Por (%)
Ext280-388	EXT 280	387.75	388	VU	f	T	sheared; qtz and Fe-carb veins	2.77	2.84			
Ext280-401	EXT 280	401.45	401.7	II	f	H		0.49	2.85			
Ext280-402	EXT 280	402.1	402.3	VUX		T	sheared; qtz and hem(?) altered fragments, 2mm to 4cm	1.18	2.85			
Ext280-406	EXT 280	406	406.25	II	f	FC+S		0.14	2.68			
Ext280-407	EXT 280	407.4	407.6	II	f	H	hornblend phenocrysts, 1-3mm, 5-10%	3.30	2.79			
Ext280-410	EXT 280	410.45	410.7	II	f	S		0.31	2.76			
Ext280-411	EXT 280	411.35	411.55	II	f	FC+S		0.13	2.69			
GK204-101	GK204	101.50	101.8	S	c	C		0.07	2.68			
GK204-109	GK204	108.97	109.27	S	c	FC+S		0.14	2.70			
GK204-116	GK204	116.13	116.43	S	c	FC+S		0.18	2.74			
GK204-128	GK204	127.71	128.02	VMmag	f	B	breccia	0.41	2.86			
GK204-129	GK204	129.08	129.39	MLX		B+P	mylonite?	0.53	2.94			
GK204-168	GK204	168.71	168.86	VU	f	T		14.12	2.81			
GK204-25	GK204	24.99	25.3	VMmag	m	U	equigranular	182.35	3.00			
GK204-60	GK204	59.74	60.05	II	m	U		67.50	2.79			
GK204-74	GK204	73.80	74.1	IF	c	S		0.30	2.67			
GK204-76	GK204	75.90	76.2	IF	c	FC+Q		0.24	2.67			
GK204-84	GK204	84.58	84.89	VMmag	m	C		67.20	2.83			
GK204-93	GK204	92.96	93.27	VMmag	m	B		2.06	2.85			
GK204-97	GK204	97.08	97.38	S	c	FC+S	sulfides	0.14	2.84			
H9601-107	H9601	106.85	107.05	II	m	U		0.70	2.94			
H9601-122	H9601	121.95	122.2	VM	m	U		18.70	2.86	158.17	5400	0.63
H9601-126	H9601	126.5	126.8	VU	m	U	spinifex	0.71	2.83			
H9601-132	H9601	132.4	132.6	VU	m	T		1.56	2.81			
H9601-133	H9601	133.55	133.75	IM	m	U		3.20	2.79			
H9601-135	H9601	135.6	135.8	IM	m	U		53.60	2.75			
H9601-150	H9601	150.4	150.6	VU	m	T	spinifex	21.60	2.85			
H9601-156	H9601	156.4	156.6	VU	m	T		52.60	2.85			
H9601-164	H9601	164	164.2	VU	m	U		12.50	2.87			
H9601-172	H9601	171.8	172	IM	c	FC		11.20	2.77			
H9601-186	H9601	186.55	186.75	IQFP	f	U	crowded porphyry	2.45	2.67	20.40	5969	
H9601-200	H9601	200.65	200.85	VU	m	T	spinifex	4.42	2.82	20.40	1422.4	1.13
H9601-210	H9601	210.45	210.6	IQFP	f	B	crowded porphyry	0.18	2.75			

Sample No.	HoleID	From	To	Rock type	Gr. size	Altn	notes	MS (x10 ⁻³ SI)	Den (g/cm ³)	Chrg (ms)	Res (Ohm-m)	Por (%)
H9601-229	H9601	228.8	229.05	IQFP	f	B	crowded porphyry	0.20	2.73			
H9601-24	H9601	24.7	24.9	VU	m	U	equigranular	0.57	2.89			
H9601-241	H9601	241.25	241.45	IQFP	f	U	crowded porphyry	0.16	2.70			
H9601-252	H9601	252.6	252.8	VU	m	U	equigranular	2.24	2.84	5.25	1062.5	0.72
H9601-258	H9601	258.4	258.6	MLX		B	chaotic, multi-lithic breccia	16.30	2.80			
H9601-266	H9601	266.05	266.25	IQFP	f	FC	weakly qtz and fsp porphyritic	0.28	2.73			
H9601-286	H9601	286.4	286.6	QUX		B	ultramafic breccia, quartz clasts?	0.65	2.85			
H9601-294	H9601	294.6	294.85	VUX	f	T	brecciated, Fe-carb matrix	4.71	2.86			
H9601-298	H9601	298.2	298.4	IQFP	f	U		0.06	2.64	2.23	7856	
H9601-302	H9601	302.1	302.2	IQFP	f	U	1.23 ppm Au from core box	0.05	2.63	2.53	8976	
H9601-308	H9601	308.7	308.9	QUX		B	qtz fragment breccia; 2.69 ppm Au	1.93	2.85			
H9601-314	H9601	314.6	314.8	VU	f	T		13.76	2.87			
H9601-32	H9601	32.75	32.95	VU	m	U		0.61	2.85			
H9601-320	H9601	320.6	320.8	IQFP	f	U	5.16 ppm Au from core box	0.06	2.64	2.90	9580	
H9601-322	H9601	322	322.2	IQFP	f	U	3.15 ppm Au from core box	0.07	2.65	4.20	23970	
H9601-324	H9601	323.9	324.1	VUX		T	sheared, brecciated to massive; Fe-carb and qtz veins	11.07	2.84			
H9601-331	H9601	331.4	331.6	VU	m	T	equigranular	0.48	2.79			
H9601-338	H9601	338.1	338.3	II	f	FC		0.26	2.67			
H9601-361	H9601	361	361.2	VU	m	T		21.41	2.87			
H9601-371	H9601	371.2	371.5	VU	m	U	spinifex	0.74	2.87	4.33	698.39	0.51
H9601-383	H9601	383	383.15	II	f	FC	hbl and fsp phenocrysts	107.00	2.86			
H9601-393	H9601	392.85	393.05	VU	f	T		0.44	2.82			
H9601-396	H9601	395.95	396.15	VM	f	B+P	fractured	0.28	2.77			
H9601-396.5	H9601	396.6	396.8	VU	f	B	fractured	0.78	2.92			
H9601-405	H9601	405	405.2	S		FC-S	2.13 ppm Au from core box	2.31	2.86	27.40	7872.4	
H9601-406	H9601	405.9	406.1	S		FC-S	5.89 ppm Au from core box	0.18	2.73			
H9601-410	H9601	410.4	410.6	S		U		0.16	2.70	25.80	9400.2	
H9601-417	H9601	417.3	417.5	S		B		0.12	2.74	15.67	5703.6	
H9601-419	H9601	419	419.2	VMmag	f	B+P		0.46	2.82			
H9601-422	H9601	422.3	422.5	VMmag	f	B		2.12	2.93			
H9601-43	H9601	43.3	43.55	VUX		B		0.41	2.91			
H9601-436	H9601	435.9	436.1	VMmag	f	U		60.70	2.86			
H9601-439	H9601	439.1	439.4	VM	f	B	strong mag sus contrast between bleached and unbleached areas	??		33.23	49812	

Sample No.	HoleID	From	To	Rock type	Gr. size	Altn	notes	MS (x10 ⁻³ SI)	Den (g/cm ³)	Chrg (ms)	Res (Ohm-m)	Por (%)
H9601-474	H9601	474.35	474.55	VMmag	f	B		0.51	2.82			
H9601-491	H9601	491.45	491.65	VMmag	f	B		0.56	2.85			
H9601-496	H9601	496.3	496.5	VMXmag	m	B+P		0.56	2.86			
H9601-507	H9601	507.4	507.6	VMPX	m	B+P		0.51	2.81			
H9601-516	H9601	516.6	516.8	VMmag	m	B		0.55	2.83			
H9601-529	H9601	529	529.2	VMmag	m	U		1.54	2.79			
H9601-541	H9601	541.6	541.8	VMmag	m	B		0.48	2.80			
H9601-55	H9601	54.95	55.15	VMP	f	U	mafic phenos	0.66	2.77			
H9601-551	H9601	551.55	551.7	VM	m	B+P	pink rhodachrosite or dolomite carbonate veining?					
H9601-571	H9601	571.2	571.4	VMXmag		B		0.76	2.88			
H9601-581	H9601	581.25	581.55	II	f	U		1.06	2.75			
H9601-600	H9601	599.9	600.1	VU	m	T		13.90	2.93			
H9601-614	H9601	614	614.2	II	f	U		0.41	2.72	15.40	16160	
H9601-79	H9601	78.75	79	VMP	f	U		0.57	2.79			
H9601-95	H9601	95.4	95.6	VMP	f	U		0.72	2.83			
H9602-103	9602	103.05	103.25	VMP	f	U		1.74	2.96			
H9602-119	9602	119.7	119.9	VM	m	U		3.95	2.90			
H9602-141	9602	141.15	141.35	VMmag	m	FC	sulfides	27.80	2.86			
H9602-143	9602	143.2	143.4	VMmag	m	U		83.70	2.84			
H9602-162	9602	161.8	162	IM	c	U		37.88	2.97			
H9602-188	9602	188.6	188.9	VMP	f	U		23.20	2.94			
H9602-203	9602	203.25	203.45	VMmag	m	U		0.65	2.93			
H9602-217	9602	217.2	217.45	VU	f	T		25.80	2.97			
H9602-234	9602	234.6	234.8	VMmag	f	U		52.10	2.85			
H9602-242	9602	241.95	242.2	IFP	f	S		14.59	2.71			
H9602-247	9602	247.75	247.95	VMXmag	f	B		132.94	2.87			
H9602-254	9602	254.2	254.4	S	c	C+H	sulfides	0.16	2.71			
H9602-272	9602	271.85	272.05	VU		T		52.70	2.87			
H9602-292	9602	292.15	292.4	VU	m	T	sulfides	1.01	2.94			
H9602-295	9602	295.7	295.9	VU	c	T		0.52	2.80			
H9602-303	9602	303.25	303.45	VU	f	T	spinifex	0.73	2.97			
H9602-320	9602	320.1	320.35	VU		T		0.54	2.98			
H9602-321	9602	321.7	321.9	IM	f	C		0.54	2.81			

Sample No.	HoleID	From	To	Rock type	Gr. size	Altn	notes	MS ($\times 10^{-3}$ SI)	Den (g/cm ³)	Chrg (ms)	Res (Ohm-m)	Por (%)
H9602-326	9602	326.4	326.6	VU	f	C		0.55	2.79			
H9602-343	9602	343.6	343.8	IM		U	hbl phenocrysts	85.90	2.79			
H9602-364	9602	363.8	364	VU	m	T		81.10	2.76			
H9602-450	9602	450.25	450.45	VU		T		80.10	2.80			
H9602-47	9602	47.1	47.35	VM	m	U	epidote	6.99	2.87			
H9602-476	9602	476.35	476.55	IFP	f	B		0.08	2.65			
H9602-479	9602	479.45	479.65	VU	c	T		0.52	2.77	2.97	3994.3	0.40
H9602-498	9602	498.4	498.6	VMP	f	U		0.55	2.87			
H9602-56	9602	56	56.25	VM	m	U		1.63	2.92			
H9602-73	9602	73.75	73.95	VMP	f	U	sulfide-filled amygdules?	69.90	2.92			
H9604-105	H9604	104.95	105.15	VM	f	B		0.44	2.83			
H9604-108	H9604	108.6	108.8	VM	f	B	varioles?	0.51	2.84			
H9604-113	H9604	113.15	113.3	VM	f	B	microfragmental	3.67	2.82			
H9604-117	H9604	117.6	117.8	VM	f	B		6.10	2.95			
H9604-122	H9604	122.7	122.9	VM	f	B	varioles?	0.67	2.93	5.73	18578	0.63
H9604-126	H9604	126.3	126.45	VM	f	B	varioles?	0.89	2.95			
H9604-14	H9604	14.4	14.6	VM	m	U		39.40	2.87			
H9604-150	H9604	150.6	150.85	VM	f	B	fragmental, angular fragments	0.60	2.88	2.07	541.24	1.54
H9604-173	H9604	173.15	173.25	VU	f	F		0.49	2.88			
H9604-182	H9604	181.8	182	VM	f	U		0.57	2.80			
H9604-190	H9604	189.9	190.1	VM	f	B		0.60	2.88			
H9604-201	H9604	201.05	201.25	VU	f	T	strongly sheared	18.35	2.87			
H9604-204	H9604	204.2	204.35	IFP	f	S		0.08	2.57	10.70	11357	
H9604-205	H9604	205.1	205.3	IFP	f	U		0.13				
H9604-214	H9604	214.2	214.4	IFP	f	S		0.13	2.68	10.70	14759	
H9604-229	H9604	229.4	229.65	IFP	f	S		0.09	2.64			
H9604-232	H9604	232.45	232.65	IFP	f	S		0.14				
H9604-260	H9604	260.7	260.9	IFP	f	U		0.18	2.67			
H9604-279	H9604	279.3	279.5	VU	f	T	sheared	71.80	2.82	4.30	405.27	
H9604-28	H9604	28.25	28.45	VM	f	U	dark black mineral (?) fills amygdules	6.54	2.88	N/A	>70000	0.25
H9604-292	H9604	291.85	292.05	IFP	f	U		0.21	2.71			
H9604-303	H9604	303.5	303.7	IFP	f	S+Q		2.18	2.61			
H9604-312	H9604	312.3	312.5	VU	m	T	mottled texture, patches of black minerals	109.00	2.87			
H9604-327	H9604	327	327.2	S	c	U		0.55	2.65			

Sample No.	HoleID	From	To	Rock type	Gr. size	Altn	notes	MS (x10 ⁻³ SI)	Den (g/cm ³)	Chrg (ms)	Res (Ohm-m)	Por (%)
H9604-339	H9604	338.9	339.1	IF	c	U		0.75	2.84			
H9604-357	H9604	357.1	357.3	VU	f	T	some brecciation	84.40	2.83	3.37	197.89	2.09
H9604-379	H9604	379	379.25	VU	f	T	some brecciation	41.20	2.74	4.18	111.16	3.09
H9604-405	H9604	405.7	405.9	II	f	U	hbl and fsp phenocrysts	69.41	2.81			
H9604-407	H9604	407.65	407.85	L		U		49.30	2.87			
H9604-414	H9604	414.45	414.65	II	m	U		67.65	2.95			
H9604-425	H9604	425.5	425.7	S	c	FC		0.25	2.67			
H9604-428	H9604	428.3	428.5	S	c	U		0.20	2.67			
H9604-433	H9604	432.95	433.15	S	c	S		0.20	2.70			
H9604-442	H9604	441.85	442.05	S	c	S		0.15	2.68			
H9604-444	H9604	444.3	444.5	L		U		0.93	2.69	15.58	19664	
H9604-447	H9604	447	447.25	S	c	FC		0.26	2.59			
H9604-475	H9604	475.65	475.85	S	c	S	intensely altered	0.13	2.67			
H9604-504	H9604	504.5	504.7	S	c	S+Q		0.18	2.71	15.67	7245.2	
H9604-512	H9604	512	512.2	II		FC		1.94	2.69			
H9604-517	H9604	517.55	517.75	VMmag	f	B		98.82	2.89			
H9604-532	H9604	531.8	532	S	c	S		0.42	2.69			
H9604-545	H9604	545.5	545.7	VMmag	f	U		106.00	2.78			
H9604-555	H9604	555.05	555.25	VMmag	f	U	mafic phenocrysts	140.00				
H9604-57	H9604	57.7	57.9	VMP	f	U	amygs increase at pillow margin	0.59	2.79	15.98	155090	0.26
H9604-574	H9604	574.2	574.4	II	m	U		135.29	2.89	115.57	2313.6	
H9604-585	H9604	585.45	585.65	VMmag	f	B		148.24	2.85			
H9604-595	H9604	595.6	595.8	VMmag	f	B		0.72	1.94			
H9604-603	H9604	603	603.25	VMmag	f	B		19.41	2.92	12.43	14346	
H9604-609	H9604	609.6	609.8	VMmag	f	B+P		3.91	2.82			
H9604-615	H9604	615.45	615.65	VMmag	f	H		5.24	2.79			
H9604-625	H9604	625.25	625.45	VMmag	m	U		21.50	2.85	141.53	49590	0.22
H9604-635	H9604	635.5	635.75	VMmag	m	U	soft green mineral filling fractures, with pink carbonate core	0.78	3.03			
H9604-673	H9604	672.75	673	VMmag	m	U	pink mineral in vein (dolomite?)	0.61				
H9604-702	H9604	702.7	702.95	VMmag	f	U		46.20	2.77			
H9604-716	H9604	716.7	716.9	VMmag	f	C+B		0.58	2.88			
H9604-719	H9604	719	719.2	VMmag	f	B		0.48	2.83			
H9604-727	H9604	727.6	727.8	IFP	f	FC	sparce phenocrysts	1.08	2.78	46.20	10657	
H9604-738	H9604	738.6	738.8	II	f	FC		0.47	2.77			

Sample No.	HoleID	From	To	Rock type	Gr. size	Altn	notes	MS (x10 ⁻³ SI)	Den (g/cm ³)	Chrg (ms)	Res (Ohm-m)	Por (%)
H9604-745	H9604	745.3	745.5	VMmag	f	U		53.18	2.90			
H9604-757	H9604	757.5	757.75	VMmag	f	B+P		0.59	2.81			
H9604-763	H9604	763.25	763.45	II	c	B		1.55	2.80			
H9604-772	H9604	772.2	772.4	VU	m	T		11.29	2.89			
H9604-776	H9604	776	776.2	II	c	B		0.32	2.87			
H9604-784	H9604	784.1	784.3	VU	m	T		38.00	2.82			
H9604-792	H9604	792.1	792.3	II	m	FC		57.70	2.77			
H9604-90	H9604	90.3	90.5	VM	m	B		0.52	2.78			
H9604-96	H9604	96.2	96.4	II		FC		0.35	2.84			
H9605-111	H9605	111.5	111.7	VMmag	c	U	"syenite" (K-spa-rich) veins	115.00	2.85			
H9605-128	H9605	128.1	128.3	VMmag	c	B	"syenite" (K-spa-rich) veins	2.00	2.79			
H9605-135	H9605	135.7	135.9	II	c	B+P		0.28	2.78			
H9605-139	H9605	139.65	139.9	II	f	FC	f-gr intrusive, purple color, possibly asssd w/nearby syenite	0.18	2.67			
H9605-142	H9605	142.5	142.7	VMmag	c	B+P		0.71	2.80			
H9605-144	H9605	144.7	144.9	VMXmag	f	B	bleached clasts, average 1cm; bleached and chaotic matrix	0.62	2.97			
H9605-145	H9605	145.35	145.55	S	c	FC+S		0.24	2.73			
H9605-150	H9605	150.5	150.75	S	c	FC+S		0.14	2.64			
H9605-157	H9605	157.3	157.5	S	c	FC+S		0.15	2.65	14.43	2630.6	
H9605-162	H9605	161.8	162	II	f	B	mafic phenocrysts, <1 to 2mm, 3%, slightly elongate	0.51	2.83	10.13	4354.6	
H9605-167	H9605	167	167.2	S	c	FC+S		0.14	2.68			
H9605-176	H9605	176.4	176.6	S	c	FC		0.21	2.68	7.65	4150.6	
H9605-180	H9605	180.2	180.4	S	c	FC		0.24	2.66			
H9605-20	H9605	19.8	20	VMmag	f	B		14.40	2.80			
H9605-210	H9605	210.7	210.9	S	c	FC+S		0.22	2.69	10.28	14889	
H9605-217	H9605	217.3	217.5	S	c	FC+S		0.21	2.68			
H9605-224	H9605	224.15	224.35	VU	f	B	sheared, qtz and Fe-carb veining	0.48	2.80	6.97	5820.4	0.32
H9605-238	H9605	237.85	238.05	VU	f	B	sheared, qtz and Fe-carb veining	5.96	2.85			
H9605-264	H9605	263.85	264.05	VU	f	T	massive	21.18	2.87			
H9605-266	H9605	266.5	266.75	VU	f	T	in-situ brecciation, angular clasts, 2cm	22.00	2.83	4.93	366.1	1.08
H9605-27	H9605	27.7	27.95	VMmag	f	U		34.70	2.76			
H9605-272	H9605	272.2	272.4	II	f	U	mafic (hbl?) phenocrysts, average 1mm, 10%, elongate	91.18	2.85			

Sample No.	HoleID	From	To	Rock type	Gr. size	Altn	notes	MS (x10 ⁻³ SI)	Den (g/cm ³)	Chrg (ms)	Res (Ohm-m)	Por (%)
H9605-278	H9605	278	278.2	VM	f	U		0.96	2.90			
H9605-28	H9605	28.4	28.6	VMmag	f	U		51.10	2.87			
H9605-301	H9605	301.3	301.5	VU	f	T	in-situ brecciation, sheared, fragments stretched	11.88	2.82			
H9605-58	H9605	58.4	58.65	VMmag	m	U		327.00	3.04			
H9605-66	H9605	66.65	66.85	IM	c	FC+S		0.82	2.87			
H9605-73	H9605	72.8	73	VMXmag		B+P	in-situ brecciation, altered fragments average 0.5-1cm	0.43	2.82			
H9605-8	H9605	8.25	8.45	VMmag	f	U		29.40	2.76			
H9605-99	H9605	99.45	99.65	IF	c	B		0.14	2.68			
H9606-104	H9606	104.4	104.6	L		U		0.59	2.81			
H9606-119	H9606	118.85	119.05	VU	m	T		37.00	2.85			
H9606-147	H9606	147.1	147.3	II	f	F		0.32	2.76			
H9606-152	H9606	151.75	152	II	f	F		0.68	2.95			
H9606-154	H9606	154.4	154.6	VUX	m	F	mylonite?	0.62	2.92			
H9606-173	H9606	173.2	173.45	II	f	B+P		0.16	2.77	9.45	4243	
H9606-174	H9606	174.5	174.7	II	f	FC		0.59	2.92			
H9606-179	H9606	179	179.25	VU	m	F		0.54	2.85	9.88	5135.4	0.31
H9606-206	H9606	206.15	206.4	VU	m	T		0.51	2.83			
H9606-22	H9606	22.35	22.6	VUX	m	F	fragmental, mylonite?	0.54	2.90	6.45	2077.9	0.40
H9606-230	H9606	230.25	230.45	II	f	FC		0.31	2.78	13.60	8868.9	
H9606-232	H9606	231.85	232.05	II	f	B		0.93	2.80			
H9606-233	H9606	233.5	233.7	II	f	B		0.99	2.85			
H9606-247	H9606	247.7	247.9	II	f	F		0.15	2.76			
H9606-270	H9606	270	270.2	VU		C		1.00	2.91	8.97	8545.9	0.34
H9606-276	H9606	276.4	276.6	II		C		0.61	2.86			
H9606-278	H9606	278	278.2	II		B		0.64	2.90			
H9606-295	H9606	295.5	295.7	VUX		F	multi-lithic mylonite?	0.95	2.93			
H9606-305	H9606	305	305.2	II	m	FC		0.61	2.95			
H9606-323	H9606	323.5	323.7	II		FC		3.85	2.67			
H9606-327	H9606	327.75	327.95	VMmag	f	FC+H		180.00	2.88			
H9606-338	H9606	338.05	338.25	VMmag	f	B+P		1.18	2.88			
H9606-357	H9606	357.3	357.5	II	c	T		0.45	2.84			
H9606-370	H9606	370.05	370.3	VMmag	m	FC+H		1.24	2.93			
H9606-40	H9606	40.4	40.6	VUX	m	T	sheared, fragmental	5.98	2.83			

Sample No.	HoleID	From	To	Rock type	Gr. size	Altn	notes	MS (x10 ⁻³ SI)	Den (g/cm ³)	Chrg (ms)	Res (Ohm-m)	Por (%)
H9606-411	H9606	411.05	411.3	VMmag	m	FC+H		4.85	2.90			
H9606-42	H9606	41.85	42.05	II	m	H		39.53	2.78			
H9606-421	H9606	421.55	421.75	MLX		C+S	multi-lithic breccia; large variation in sus	14.82	2.85			
H9606-424	H9606	424.3	424.5	IIX		B	buff and purple-colored clasts	0.74	2.94			
H9606-430	H9606	429.8	430	II	m	B		0.75	2.88			
H9606-452	H9606	452.3	452.5	VMmag	m	FC+H		124.71	2.89			
H9606-459	H9606	459.75	459.95	VU	m	C	massive	24.00	2.82			
H9606-465	H9606	465.75	465.95	VU	m	U	massive	27.65	2.82			
H9606-471	H9606	471.5	471.7	VU	m	B		36.82	2.85			
H9606-496	H9606	496.35	496.55	MLX		B		7.59	2.84			
H9606-501	H9606	500.9	501.1	VU	m	U		3.24	2.86	15.97	3752.2	0.70
H9606-537	H9606	537.05	537.25	II		B+P		4.95	2.92			
H9606-538	H9606	538	538.2	II	f	FC		0.25	2.73			
H9606-539	H9606	539.5	539.7	VU	m	B	sheared	1.06	2.83			
H9606-569	H9606	569	569.25	VMmag	f	U		25.80	2.61			
H9606-59	H9606	59.5	59.7	VU	m	F	massive	0.54	2.96	3.37	1009.04	0.50
H9606-604	H9606	604.4	604.6	VMmag	f	U		53.20	2.83			
H9606-619	H9606	618.9	619.1	VMP	f	U		0.63	2.78			
H9606-628	H9606	628.25	628.45	II	m	FC	fsp phenocrysts	0.74	2.83			
H9606-629	H9606	629	629.25	II		FC		0.45	2.77			
H9606-630	H9606	630.15	630.35	II		FC		0.68	2.83			
H9606-631	H9606	630.85	631.05	VM	f	B		2.48	2.83			
H9606-649	H9606	649.3	649.55	II	m	U		18.40	2.75			
H9606-66	H9606	65.8	66	II	f	F		0.61	2.92	11.30	22613	
H9606-660	H9606	660.2	660.4	VMP	f	U	qtz amygdules near pillow margins	0.60	2.79			
H9606-675	H9606	675	675.2	VMP	f	B		0.59	2.81			
H9606-675.5	H9606	675.7	675.9	II		B		0.42	2.76			
H9606-706	H9606	706.7	706.95	VMP	f	B		0.67	2.88			
H9606-708	H9606	708.15	708.4	QMX		B		0.35	2.87			
H9606-713	H9606	713.55	713.75	VM	f	B		0.55	2.89			
H9606-718	H9606	718.15	718.4	VMP	f	B		0.54	2.88			0.40
H9606-721	H9606	721.7	721.9	VMP	f	B		0.39	2.80			
H9606-725	H9606	725.25	725.5	VMP	m	B		0.48	2.90			
H9606-745	H9606	745.1	745.35	VMP	m	B	weak fabric	0.55	2.90			0.33

Sample No.	HoleID	From	To	Rock type	Gr. size	Altn	notes	MS (x10 ⁻³ SI)	Den (g/cm ³)	Chrg (ms)	Res (Ohm-m)	Por (%)
H9606-753	H9606	752.8	753.05	II	m	FC		0.55	2.91			
H9606-757	H9606	757.1	757.3	QMX		B	qtz-carbonate breccia; sheared	0.46	2.86			
H9606-784	H9606	784.1	784.35	VMP	f	U		0.60	2.80			
H9606-79	H9606	79.25	79.45	II	m	F		0.40	2.82			
H9606-89	H9606	89.2	89.45	VU	m	T	spinifex	25.18	2.84			
H9606-90	H9606	90.1	90.3	II	f	T		0.80	2.82			
H9608-102	9708	102.55	102.8	IF	c	B		2.47	2.85			
H9608-118	9708	117.85	118.05	VM	f	B	in-situ brecciation	0.71	2.80			
H9608-129	9708	129.45	129.65	VM	f	B		0.51	2.84			
H9608-145	9708	145	145.2	VM	f	B		0.65	2.84			
H9608-176	9708	176	176.2	VMP	f	U		0.67	2.79			
H9608-190	9708	190	190.2	VMP	f	C		31.53	2.79			
H9608-192	9708	192.45	192.65	IM	m	FC		67.53	2.80			
H9608-198	9708	198.2	198.4	IM	m	B		1.00	2.89			
H9608-209	9708	209.4	209.6	T		FC		0.65	2.84			
H9608-217	9708	217	217.3	MLX		B		0.61	2.81			
H9608-217	9708	217.3	217.4	MLX		U		1.52	2.81			
H9608-224	9708	224.65	224.85	VMP	f	U		2.54	2.83			
H9608-24	9708	24.3	24.5	VMP	f	C		70.50	2.91			
H9608-258	9708	258.4	258.6	VM	m	B		0.45	2.85			
H9608-259	9708	258.8	259	VM	m	U		1.57	2.91			
H9608-27	9708	27.55	27.75	T		U		18.50	2.97			
H9608-272	9708	272	272.2	VMPX	f	C		0.72	2.83			
H9608-306	9708	306.4	306.6	VM	m	C		12.50	2.85			
H9608-327	9708	327.35	327.55	VM	m	U		14.80	2.88			
H9608-346	9708	346.15	346.4	VM	m	U		0.62				
H9608-361	9708	361.2	361.4	VMPX	f	U		0.60	2.88			
H9608-37	9708	37.15	37.35	VM	m	U		34.50	2.95			
H9608-378	9708	378.5	378.75	VMP	f	B		0.68	2.92			
H9608-39	9708	38.8	39	VM	m	B	purple mineral (a carbonate?) in vein	14.10	2.93			
H9608-405	9708	405	405.2	VMP	f	C		0.91	2.81			
H9608-419	9708	419.45	419.65	VMP	f	B		0.54	2.84			
H9608-422	9708	422.65	422.85	VMP	f	B		0.58	2.83			
H9608-444	9708	444.6	444.8	VMP	f	B	epidote and cal veins	0.62	2.93			
H9608-463	9708	463.3	463.5	VMP	f	U	unaltd pillow basalt; cal veins	0.53	2.77			

Sample No.	HoleID	From	To	Rock type	Gr. size	Altn	notes	MS (x10 ⁻³ SI)	Den (g/cm ³)	Chrg (ms)	Res (Ohm-m)	Por (%)
H9608-508	9708	508.25	508.45	VMP	f	C		0.56	2.87			
H9608-522	9708	522.2	522.45	VMP	f	B	in-situ brecciation	0.41	2.86			
H9608-537	9708	537.6	537.8	VMP	f	B		0.41	2.86			
H9608-554	9708	554	554.2	VMP	f	B		0.34	2.84			
H9608-562	9708	562.3	562.5	VMP	f	B		0.45	2.87			
H9608-573	9708	573.3	573.55	VMP	f	B		0.42	2.90			
H9608-600	9708	600.1	600.35	VMP	f	B		0.53	2.84			
H9608-639	9708	639	639.2	VMP	f	B		0.38	2.86			
H9608-650	9708	649.9	650.1	VMP	f	B		0.46	2.89			
H9608-657	9708	657.3	657.5	VM	m	B	chlorite amygdules	0.47	2.86			
H9608-674	9708	673.9	674.1	VM	m	B	chlorite amygdules	0.38	2.90			
H9608-68	9708	68.5	68.7	VMP	f	C	chlorite amygdules	44.30	2.89			
H9608-712	9708	712.7	712.9	VM	m	U	chlorite amygdules	0.54	2.90			
H9608-85	9708	85.25	85.45	VM	f	U		4.03	2.86			
H9608-98	9708	97.9	98.1	VM	m	U		1.29	2.79			
H9707-102	H9707	102.5	102.7	VU	f	F	sheared; zoned fragments?	1.66	2.90			
H9707-111	H9707	111.2	111.4	IF	c	U		0.40	2.80			
H9707-122	H9707	121.85	122.1	IF	m	U		0.16	2.66			
H9707-137	H9707	137.3	137.5	IM	c	U		49.53	2.83	8.87	758.82	0.76
H9707-141	H9707	141.6	141.8	VU	m	T	slightly sheared; abund quartz amygdules	10.60	2.83	2.90	2241.6	0.88
H9707-144	H9707	144.35	144.55	IF	m	FC		30.24	2.76			
H9707-160	H9707	160.75	160.95	II	f	FC	abundant py along fracures	18.59	2.95			
H9707-162	H9707	162.65	162.85	VU	f	T	qtz fragments from shearing of veins	10.22	2.81			
H9707-171	H9707	171.2	171.4	MLX		FC+H	felsic and mafic clasts, < 1cm; sub-rounded to sub-angular	14.59	2.75			
H9707-179	H9707	179.7	179.9	VMmag	f	U		2.21	2.87			
H9707-188	H9707	188.15	188.4	VMXmag	f	C	1-2 cm fragments, clast-supported	147.06	2.99			
H9707-194	H9707	194.65	194.85	II	f	B		0.60	2.88			
H9707-204	H9707	204.7	204.9	VMmag	f	U		57.10	2.62			
H9707-219	H9707	219.7	219.9	VMP	f	U	amygdules at margins	0.77	2.80			
H9707-241	H9707	241.1	241.3	VMmag	m	U		35.80	2.47			
H9707-265	H9707	265.1	265.3	VMmag	m	U		2.87	2.92			
H9707-273	H9707	273.2	273.4	VMmag	m	U		42.70	2.94			
H9707-301	H9707	301.05	301.25	VMmag	m	U		57.10	3.00			
H9707-307	H9707	307.05	307.3	VMmag	m	U	"syenite" (Kfsp) veins	119.00	2.87			

Sample No.	HoleID	From	To	Rock type	Gr. size	Altn	notes	MS (x10 ⁻³ SI)	Den (g/cm ³)	Chrg (ms)	Res (Ohm-m)	Por (%)
H9707-317	H9707	317.15	317.4	VMmag	m	U		60.50	3.00			
H9707-351	H9707	351.15	351.4	VMmag	m	U	"syenite" (Kfsp) veins	130.00	2.88			
H9707-36	H9707	36.5	36.7	VU		F	sheared	0.81	2.94			
H9707-373	H9707	373.65	373.9	VMmag	m	U		77.80	2.96	46.50	30556	0.26
H9707-38	H9707	38.25	38.5	ll	f	F		0.51	2.91			
H9707-388	H9707	388.75	388.95	S		U	1% cpy interstitial	30.82	2.69			
H9707-403	H9707	403.7	403.9	VMmag	m	U		128.00	2.95			
H9707-420	H9707	419.8	420	VMmag	m	U		48.30	2.92			
H9707-456	H9707	456.05	456.25	VMmag	m	U		141.00	2.97			
H9707-478	H9707	478.25	478.45	VMmag	m	B		2.19	2.58			
H9707-488	H9707	488.3	488.5	VMmag	m	U		88.24	2.89			
H9707-494	H9707	494.1	494.3	VMmag	m	U		2.26	2.89			
H9707-495	H9707	495.5	495.7	VMXmag		B	strongly bleached fragments <1cm, some qtz clasts	0.69	2.86			
H9707-512	H9707	511.8	512	VMmag	m	B	abundant qtz/Fe-carb veins	2.68	2.85			
H9707-515	H9707	515.2	515.4	VMXmag		FC+S		84.20	2.82			
H9707-522	H9707	522.45	522.65	VMmag	m	U		26.90	2.84			
H9707-540	H9707	540.5	540.7	VMmag	m	U		9.43	2.83			
H9707-554	H9707	553.8	554	VMmag	m	U		19.40	2.80			
H9707-56	H9707	56.7	56.9	VU	f	T	sheared	15.10	2.84			
H9707-575	H9707	575.5	575.7	VMmag	m	U		0.55	2.86			
H9707-599	H9707	599.65	599.85	KMXmag		U	Kspar rich clasts; <2cm frags, may have been a vein	46.82	2.87			
H9707-603	H9707	603	603.2	VMmag		U	in-situ brecciation	97.53	2.93			
H9707-614	H9707	614.35	614.55	VMmag	f	U		32.12	2.91			
H9707-625	H9707	625.25	625.45	VMmag		U	in-situ brecciation <1cm, perlitic; varioles?	105.65	3.08			
H9707-627	H9707	627.1	627.3	VMmag		B		12.59	3.14			
H9707-637	H9707	637.3	637.5	VMmag	f	U		62.90	2.99			
H9707-655	H9707	655.75	655.95	VMmag	m	U		1.72	2.78			
H9707-67	H9707	67.15	67.35	ll	m	T		0.42	2.84			
H9707-677	H9707	677.4	677.6	VMmag	m	U		107.00				
H9707-685	H9707	684.8	685	VMmag	m	U		83.50	2.87			
H9707-690	H9707	690.3	690.5	VMmag	m	U		131.00	3.02			
H9707-84	H9707	84.4	84.6	ll	f	FC+S	minor qtz amygdules (<1mm)	0.69	2.87			
H9707-96	H9707	96.65	96.85	IF	c	U		0.14	2.68			

Sample No.	HoleID	From	To	Rock type	Gr. size	Altn	notes	MS (x10 ⁻³ SI)	Den (g/cm ³)	Chrg (ms)	Res (Ohm-m)	Por (%)
H9711-106	H9711	106.25	106.45	VM	m	B+P		0.49				
H9711-116	H9711	115.95	116.15	VM	m	FC+S		0.56				
H9711-134	H9711	133.9	134.2	VM	f	B		0.53	2.83			
H9711-149	H9711	148.85	149.05	VMX	f	B+P	varioles; bleached clasts	0.68	2.74			
H9711-149.5	H9711	149.4	149.6	VMX	f	B	varioles	0.44				
H9711-162	H9711	162	162.2	VM	m	B		0.61				
H9711-178	H9711	178	178.2	VM	m	B		0.61				
H9711-192	H9711	192.55	192.75	VM	m	U		1.07	2.80			
H9711-211	H9711	211.6	211.8	VM	m	U	mafic phenocrysts	0.67	2.81			
H9711-247	H9711	247.3	247.5	VMX		B+P		0.53	2.76			
H9711-250	H9711	250	250.2	VU		B	sheared	0.76	2.89			
H9711-252	H9711	252.15	252.35	S	f	FH		0.46	2.72			
H9711-265	H9711	265.45	265.65	VU	m	B		0.75	2.87			
H9711-281	H9711	281.5	281.7	VU	m	B	beige "clay-looking" mineral - leucoxene (i.e. was ilmenite)	0.69	2.87	5.34	5164	0.49
H9711-296	H9711	296.65	296.85	VMmag	f	FC+H +S		32.00	2.94			
H9711-313	H9711	313.5	313.7	VM	f	B		1.25	2.87			
H9711-320	H9711	320.6	320.8	VM	f	B	bleached varioles	0.85	2.88			
H9711-344	H9711	344.2	344.4	VMmag	f	U		24.82	2.88			
H9711-368	H9711	368.5	368.8	VM	f	B	varioles	2.95	2.89			
H9711-378	H9711	378.5	378.7	VM	f	B+P		1.27	2.93			
H9711-401	H9711	401.6	401.8	VM	f	B	soft green material in veins	1.29	2.91			
H9711-430	H9711	430.4	430.6	VMmag	f	FC+H +S		11.06	2.93	N/A	>70000	
H9711-439	H9711	439.1	439.35	VMmag	f	B	varioles	14.35	2.91	N/A	>70000	
H9711-446	H9711	445.95	446.15	VMmag	f	U		44.59	2.82			
H9711-466	H9711	465.8	466	VMmag	f	U		26.47	2.82			
H9711-470	H9711	470.05	470.25	S	f	FC		0.80	2.84			
H9711-475	H9711	475.75	475.95	VU	f	B	sheared	3.05	2.85			
H9711-496	H9711	496.4	496.6	VU		T		38.60	3.08			
H9711-521	H9711	521.65	521.85	IFP	f	U	phenocrysts, 1-2 mm, 5-10%	0.22	2.68			
H9711-53	H9711	53.05	53.25	VM	m	U		5.66				
H9711-551	H9711	551.65	551.85	VU		T		53.80	2.79			
H9711-65	H9711	65.5	65.7	VM	m	B		1.19				

Sample No.	HoleID	From	To	Rock type	Gr. size	Altn	notes	MS ($\times 10^{-3}$ SI)	Den (g/cm^3)	Chrg (ms)	Res (Ohm-m)	Por (%)
H9711-99	H9711	99.5	99.7	VM	m	FC+H		0.86	2.72			
HGP-site 1	hndsmp			VM	m					9.00	7453.7	0.50

APPENDIX 2F – PHYSICAL PROPERTIES – DESCRIPTIVE STATISTICS

Magnetic Susceptibility

	No.	SUSCEPTIBILITY (x10 ⁻³ SI Units)				Range
		Mean	Std. Dev.	Log mean	Median	
<i>Ultramafic volcanic rocks - all</i>	82	15.63	22.82	4.29	3.83	0.41-109
Least altered (dol+chl)	8	6.03	9.61	2.15	1.49	0.57-27.65
Talc-chlorite assemblage	46	24.12	26.57	9.6	14.61	0.44-109
Fe-carbonate+muscovite altered	16	2.73	10.41	1.86	1.01	0.41-36.82
Magnesite+fuchsite altered	9	0.75	0.37	0.7	0.62	0.49-1.66
<i>Mafic volcanic rocks - all</i>	218	26.11	45.18	3.86	1.42	0.15-327
Least altered	107	40.09	52.94	9.78	21.5	0.35-327
Fe-carbonate+muscovite altered	75	6.86	25.24	1.03	0.6	0.15-148.24
Fe-carbonate+albite altered	14	1.71	3.21	0.84	0.58	0.28-12.4
<i>Intermediate dikes - all</i>	59	12.07	29.09	1.21	0.61	0.13-135.29
Least altered	11	41.11	47.24	7.02	18.4	0.24-135.29
Fe-carbonate+muscovite altered	10	0.75	0.35	0.68	0.69	0.32-1.55
Fe/Mg carbonate altered	22	10.95	25.91	1.26	0.58	0.13-107
<i>Syenite intrusives - all</i>	34	1.19	5.25	0.25	0.2	0.07-30.82
Least altered	12	2.87	8.8	0.42	0.27	0.16-30.82
Muscovite altered	11	0.36	0.65	0.21	0.15	0.14-2.31
Fe/Mg carbonate altered	4	0.23	0.021	0.23	0.23	0.21-0.25
<i>Porphyritic rhyolite dikes - all</i>	37	1.59	5.41	0.26	0.16	0.05-30.24
Least altered	15	0.35	0.61	0.445	0.16	0.05-2.45
Muscovite altered	13	0.48	0.82	5.71	0.14	0.08-2.47
Fe/Mg carbonate altered	7	2.39	5.39	2.19	0.28	0.12-14.59

Density

	No.	DENSITY (g/cm ³)			
		Mean	Std. Dev.	Median	Range
<i>Ultramafic volcanic rocks - all</i>	81	2.86	0.057	2.85	2.74-3.08
Least altered (dol+chl)	8	2.85	0.023	2.86	2.82-2.89
Talc-chlorite assemblage	46	2.85	0.061	2.84	2.74-3.08
Fe-carbonate+muscovite altered	15	2.87	0.054	2.85	2.78-3.01
Magnesite+fuchsite altered	9	2.91	0.035	2.92	2.85-2.96
<i>Mafic volcanic rocks - all</i>	205	2.86	0.1	2.87	1.94-3.14
Least altered	101	2.87	0.094	2.87	2.47-3.08
Fe-carbonate+muscovite altered	71	2.85	0.13	2.86	1.94-3.14
Fe-carbonate+albite altered	13	2.81	0.051	2.81	2.74-2.93
<i>Intermediate dikes - all</i>	59	2.82	0.078	2.83	2.67-2.95
Least altered	11	2.83	0.077	2.81	2.72-2.95
Fe-carbonate+muscovite altered	10	2.85	0.054	2.86	2.76-2.94
Fe/Mg carbonate altered	22	2.79	0.088	2.78	2.67-2.95
<i>Syenite intrusives - all</i>	32	2.7	0.057	2.69	2.59-2.86
Least altered	10	2.7	0.057	2.69	2.64-2.84
Muscovite altered	11	2.72	0.072	2.69	2.64-2.86
Fe/Mg carbonate altered	4	2.67	0.0096	2.68	2.66-2.68
<i>Porphyritic rhyolite dikes - all</i>	36	2.61	0.45	2.67	2.63-2.88
Least altered	15	2.51	0.7	2.67	2.63-2.84
Muscovite altered	12	2.68	0.074	2.67	2.57-2.85
Fe/Mg carbonate altered	7	2.73	0.082	2.71	2.65-2.88

Resistivity

	RESISTIVITY (Ohm-m)					
	No.	Mean	Std. Dev.	Log mean	Median	Range
<i>Ultramafic volcanic rocks - all</i>	20	2815.99	2451.99	1574.58	2159.75	111.16-8545.9
Talc-chlorite assemblage	8	1127.75	1376.22	573.95	385.69	111.16-3994.3
Carbonate+muscovite altered	7	4451.55	1714.49	3952.65	4757.60	1009.04-3217.4
<i>Mafic volcanic rocks - all</i>	18	28431.94	36820.16	13004.05	16462.00	541.24-155090
Carbonate+muscovite or albite altered	6	17910.02	17881.25	8344.70	16462.00	541.24-49812
<i>Intermediate dikes - all</i>	6	9758.85	8025.69	7193.33	6611.75	2313.6-22613
<i>Syenite intrusives - all</i>	10	6759.51	3528.59	6027.61	6179.85	2630.6-14889
<i>Porphyritic rhyolite dikes - all</i>	11	11534.00	5359.31	10523.10	11136.00	4576-23970

Chargeability

	CHARGEABILITY (ms)				
	No.	Mean	Std. Dev.	Median	Range
<i>Ultramafic volcanic rocks - all</i>	20	6.91	4.46	5.46	2.9-20.4
Talc-chlorite assemblage	8	6.36	5.89	4.24	2.9-20.4
Carbonate+muscovite altered	7	6.63	2.45	5.68	3.37-9.88
<i>Mafic volcanic rocks - all</i>	18	31.32	44.97	13.80	2.07-158.17
Carbonate+muscovite or albite altered	6	12.03	11.04	9.37	2.07-33.23
<i>Intermediate dikes - all</i>	6	29.24	42.35	12.45	9.45-115.57
<i>Syenite intrusives - all</i>	10	14.71	7.04	13.92	6.27-27.4
<i>Porphyritic rhyolite dikes - all</i>	11	10.47	13.19	4.20	2.2-46.2

APPENDIX 2G – CORRELATION COEFFICIENTS FOR PHYSICAL PROPERTIES AND XRD (RIETVELD) - DERIVED MINERAL ABUNDANCES

Calculated using the statistical analysis software SPSS Statistics. Correlation coefficients are calculated for all physical properties. Not all minerals are considered, only ones occurring most commonly.

Spearman's correlation coefficient calculations are used as they are appropriate where data do satisfy normality assumptions.

ALL ROCK TYPES (PAGE 1)

Spearman's rho	MAGSUS	CORRELATION COEFFICIENT	MAGSUS	LOG_MAGSUS	DEN	CHRG	RES	LOG_RES	POR	AB	CAL	CLC
		Sig. (2-tailed)	1.000	1.000	.444*	.278*	-.212	-.214	.175	-.513**	.178	-.188
		N	385	385	369	58	58	58	29	32	11	19
	LOG_MAGSUS	Sig. (2-tailed)	1.000**	1.000	.444**	.279*	-.212	-.214	.175	-.513**	.178	-.188
		N	385	385	369	58	58	58	29	32	11	19
	DEN	Sig. (2-tailed)	.444**	.444**	1.000	.076	-.036	-.038	-.381*	-.846**	.405	-.030
		N	369	369	370	58	58	58	29	32	11	19
	CHRG	Sig. (2-tailed)	.278*	.279*	.076	1.000	.076	-.036	-.381*	-.846**	.405	-.030
		N	58	58	58	60	60	60	27	28	10	17
	RES	Sig. (2-tailed)	-.212	-.212	-.036	.352**	1.000	1.000**	-.813**	.021	.148	-.267
		N	58	58	58	60	60	60	27	28	10	17
	LOG_RES	Sig. (2-tailed)	-.214	-.214	-.038	.354**	1.000	1.000	-.815**	.020	.166	-.264
		N	58	58	58	60	60	60	27	28	10	17
	POR	Sig. (2-tailed)	.175	.175	-.391**	-.516**	-.813**	1.000	1.000**	-.291	-.281	.569*
		N	29	29	29	27	27	27	30	12	6	13
	AB	Sig. (2-tailed)	-.513**	-.513**	-.646**	-.115	.021	.020	-.291	1.000	-.742*	-.395
		N	32	32	32	28	28	28	12	33	10	18
	CAL	Sig. (2-tailed)	.178	.178	.405	-.030	.148	.168	-.281	-.742*	1.000	.571
		N	11	11	11	10	10	10	6	10	11	8
	CLC	Sig. (2-tailed)	-.188	-.188	-.030	-.243	-.267	-.264	.569*	-.395	.571	1.000
		N	19	19	19	17	17	17	13	18	8	20
	DOL	Sig. (2-tailed)	.412*	.412*	.576*	.195	-.007	-.013	-.060	-.622**	-.378	-.099
		N	26	26	26	22	22	22	8	25	7	13
	CB_TOT	Sig. (2-tailed)	.180	.180	.407*	-.168	.083	.085	.087	-.678**	.301	-.037
		N	31	31	31	27	27	27	11	30	11	17
	HEM	Sig. (2-tailed)	.786**	.786**	.072	.850**	.048	.048	-.308	.450	1.000**	.058
		N	7	7	7	8	8	8	5	7	3	6
	MAG	Sig. (2-tailed)	.857**	.857**	.518	.083	-.083	-.083	-.800	-.190	.100	.071
		N	8	8	8	9	9	9	4	8	5	8
	MC_INT	Sig. (2-tailed)	-.456	-.456	.684**	.051	-.191	-.191	-.371	.575*	-.725	-.367
		N	15	15	15	14	14	14	6	15	6	9
	MS	Sig. (2-tailed)	-.515	-.515	-.492	-.297	-.442	-.462	-.300	-.006	-1.000	-.429
		N	10	10	10	10	10	10	5	10	2	7
	MUS_TOT	Sig. (2-tailed)	-.527	-.527	-.592	-.297	-.442	-.462	-.300	-.006	-1.000	-.429
		N	11	11	11	10	10	10	5	10	2	7
	PY	Sig. (2-tailed)	.381	.381	.494*	.383	-.242	-.264		-.347	-.789	.600
		N	17	17	17	15	15	15	1	.173	.112	.208
	QTZ	Sig. (2-tailed)	-.235	-.235	-.163	-.285	-.081	-.077	.308	-.167	.008	.032
		N	30	30	30	26	26	26	12	.386	.983	.900
	FECB_TOT	Sig. (2-tailed)	.431**	.431**	.686**	.259	.251	.248	.000	.672*	-.450	-.242
		N	27	27	27	23	23	23	8	26	7	13

** Correlation is significant at the .01 level (2-tailed).

* Correlation is significant at the .05 level (2-tailed).

Relationships addressed in Chapter 2

ALL ROCK TYPES (PAGE 2)

			DOL	CB_TOT	HEM	MAG	MC_INT	MS	MUS_TOT	PY	QTZ	FECB_TOT
Spearman's rho	MAGSUS	Correlation Coefficient	.417*	.180	.786*	.857**	-.456	-.515	-.527	.381	-.235	.431*
		Sig. (2-tailed)	.034	.332	.036	.007	.088	.128	.096	.132	.211	.025
		N	26	31	7	6	15	10	11	17	30	27
	LOG_MAGSUS	Correlation Coefficient	.417*	.180	.786*	.857**	-.456	-.515	-.527	.381	-.235	.431*
		Sig. (2-tailed)	.034	.332	.036	.007	.088	.128	.096	.132	.211	.025
		N	26	31	7	8	15	10	11	17	30	27
	DEN	Correlation Coefficient	.578**	.407*	.072	.518	-.684**	-.492	-.592	.494*	-.163	.886**
		Sig. (2-tailed)	.002	.023	.878	.188	.005	.148	.055	.044	.389	.000
		N	28	31	7	8	15	10	11	17	30	27
	CHRG	Correlation Coefficient	.195	-.168	.850**	.083	.051	-.297	-.287	.383	-.265	.259
		Sig. (2-tailed)	.385	.403	.007	.831	.884	.405	.405	.159	.158	.233
		N	22	27	8	9	14	10	10	15	26	23
	RES	Correlation Coefficient	-.007	.063	.048	-.083	-.191	-.442	-.442	-.242	.081	.251
		Sig. (2-tailed)	.974	.753	.910	.831	.513	.200	.200	.385	.893	.248
		N	22	27	8	9	14	10	10	15	26	23
	LOG_RES	Correlation Coefficient	-.013	.065	.048	-.083	-.191	-.462	-.462	-.264	-.077	.248
		Sig. (2-tailed)	.954	.748	.910	.831	.513	.179	.179	.341	.708	.255
		N	22	27	8	9	14	10	10	15	26	23
	POR	Correlation Coefficient	-.060	.087	-.308	-.600	-.371	-.300	-.300		.308	.000
		Sig. (2-tailed)	.888	.600	.814	.200	.468	.624	.624		.330	1.000
		N	6	11	5	4	6	5	5	1	12	8
	AB	Correlation Coefficient	-.622**	-.676**	.450	-.190	.575*	-.006	-.006	-.347	-.167	-.672**
		Sig. (2-tailed)	.001	.000	.310	.651	.025	.987	.987	.173	.388	.000
		N	25	30	7	6	15	10	10	17	29	26
	CAL	Correlation Coefficient	-.378	.301	1.000**	.100	-.725	-1.000	-1.000	-.788	.008	-.450
		Sig. (2-tailed)	.403	.369		.873	.103	1.000	1.000	.112	.983	.310
		N	7	11	3	5	6	2	2	5	9	7
	CLC	Correlation Coefficient	-.099	-.037	.058	.071	-.387	-.429	-.429	.600	.032	-.242
		Sig. (2-tailed)	.748	.889	.913	.867	.332	.337	.337	.208	.900	.426
		N	13	17	6	8	9	7	7	6	18	13
	DOL	Correlation Coefficient	1.000	.701**	-.288	-.429	-.152	-.179	-.179	.453	-.055	.917**
		Sig. (2-tailed)	.	.000	.531	.397	.678	.702	.702	.090	.789	.000
		N	27	27	7	6	10	7	7	15	24	27
	CB_TOT	Correlation Coefficient	.701**	1.000	-.371	-.417	-.412	-.183	-.183	.291	.597**	.726**
		Sig. (2-tailed)	.000		.365	.285	.162	.837	.837	.257	.001	.000
		N	27	32	6	9	13	9	9	17	27	28
	HEM	Correlation Coefficient	-.268	-.371	1.000	-.316	-1.000	-1.000	-1.000		-.235	-.721
		Sig. (2-tailed)	.531	.385		.684	1.000	1.000	1.000		.575	.068
		N	7	8	6	4	2	2	2	2	8	7
	MAG	Correlation Coefficient	-.429	-.417	-.316	1.000	.000	1.000	1.000	.500	.107	-.429
		Sig. (2-tailed)	.397	.265	.884		1.000	1.000	1.000	.687	.819	.397
		N	6	9	4	9	5	2	2	3	7	8
	MC_INT	Correlation Coefficient	-.152	-.412	-1.000	.000	1.000			.314	.176	-.285
		Sig. (2-tailed)	.678	.162	1.000	1.000				.544	.566	.425
		N	10	13	2	5	15	1	1	6	13	10
	MS	Correlation Coefficient	-.179	-.163	-1.000	1.000**		1.000	1.000**	-.473	-.200	-.071
		Sig. (2-tailed)	.702	.637	1.000					.284	.806	.887
		N	7	9	2	2	1	11	11	7	9	8
	MUS_TOT	Correlation Coefficient	-.179	-.183	-1.000	1.000**		1.000**	1.000	-.473	-.200	-.071
		Sig. (2-tailed)	.702	.637	1.000					.284	.806	.867
		N	7	9	2	2	1	11	12	7	9	8
	PY	Correlation Coefficient	.453	.291		.500	.314	-.473	-.473	1.000	-.225	.341
		Sig. (2-tailed)	.090	.257		.667	.544	.284	.284		.420	.197
		N	15	17	2	3	8	7	7	18	15	16
	QTZ	Correlation Coefficient	-.055	.597**	-.235	.107	.176	-.200	-.200	-.225	1.000	-.026
		Sig. (2-tailed)	.799	.001	.575	.619	.566	.606	.606	.606	.420	
		N	24	27	6	7	13	9	9	15	31	24
	FECB_TOT	Correlation Coefficient	.917**	.726**	-.721	-.429	-.285	-.071	-.071	.341	-.026	1.000
		Sig. (2-tailed)	.000	.000	.068	.397	.425	.867	.867	.197	.904	
		N	27	28	7	6	10	8	8	16	24	28

** Correlation is significant at the .01 level (2-tailed). Relationships addressed in Chapter 2
 * Correlation is significant at the .05 level (2-tailed).

ULTRAMAFIC VOLCANIC ROCKS

Spearman's rho	MAGSUS	LOG_MA GSUS	DEN	CHRG	LOG CHG	RES	LOG RES	POR	AB	CLC	DOL	CB TOT	MAG	MS	MUS TOT	QTZ	TC	FECB TOT	
Correlation Coefficient	1.000	1.000**	-.204	-.119	-.110	-.679**	-.631**	-.909**	.700	.429	-.464	-.464	1.000	1.000	-.500	-.943**	1.000**	-.040	
Sig. (2-tailed)	.000	.000	.067	.638	.685	.002	.005	.000	.188	.337	.294	.294	.000	.000	.500	.005	.000	.872	
N	82	82	81	18	18	18	18	16	5	7	7	7	2	2	3	6	4	19	
LOG_MAGSUS	Correlation Coefficient	1.000**	1.000	-.206	-.119	-.110	-.679**	-.631**	.700	.429	-.464	-.464	1.000	1.000	-.500	-.943**	1.000**	-.040	
Sig. (2-tailed)	.000	.000	.065	.638	.685	.002	.005	.000	.188	.337	.294	.294	.000	.000	.500	.005	.000	.872	
N	82	82	81	18	18	18	18	16	5	7	7	7	2	2	3	6	4	19	
DEN	Correlation Coefficient	-.204	-.206	1.000	.153	-.145	-.143	-.044	-.353	-.800**	-.643	.607	.750	-1.000	1.000	-.500	.829*	-1.000**	-.029
Sig. (2-tailed)	.067	.065	.000	.543	.565	.572	.881	.179	.037	.119	.148	.052	1.000	1.000	.667	.042	.000	.906	
N	81	81	81	18	18	18	18	16	5	7	7	7	2	2	3	6	4	19	
CHRG	Correlation Coefficient	-.119	-.119	.153	1.000	.999**	.425	.413	-.242	.000	-.257	-.143	.029	-1.000	-1.000	-1.000	-.300	-.400	.348
Sig. (2-tailed)	.638	.638	.543	.000	.999**	.078	.088	.367	1.000	.623	.787	.957	1.000	1.000	1.000	.624	.600	.157	
N	18	18	18	18	18	18	18	16	4	6	6	6	2	2	2	5	4	18	
LOG_CHG	Correlation Coefficient	-.110	-.110	.145	.999**	1.000	.425	.414	-.242	.318	-.319	-.116	.087	-1.000	-1.000	-1.000	-.462	-.400	.349
Sig. (2-tailed)	.665	.665	.566	.000	.999**	.079	.079	.088	.367	.684	.538	.870	1.000	1.000	1.000	.434	.600	.155	
N	18	18	18	18	18	18	18	16	4	6	6	6	2	2	2	5	4	18	
RES	Correlation Coefficient	-.679**	-.679**	.143	.425	.425	1.000	.923**	-.840**	-.800**	-.771	.371	.714	-1.000	1.000	1.000	.600	-.200	.200
Sig. (2-tailed)	.002	.002	.572	.078	.079	.000	.000	.000	.400	.072	.468	.111	1.000	1.000	1.000	.285	.800	.425	
N	18	18	18	18	18	18	18	16	4	6	6	6	2	2	2	5	4	18	
LOG_RES	Correlation Coefficient	-.631**	-.631**	.044	.413	.414	.923**	1.000	-.835**	-.258	-.926**	.463	.772	-1.000			.289	-.318	.187
Sig. (2-tailed)	.005	.005	.861	.088	.088	.000	.000	.000	.742	.008	.355	.072	1.000			.638	.684	.459	
N	18	18	18	18	18	18	18	16	4	6	6	6	2	2	2	5	4	18	
POR	Correlation Coefficient	.909**	.909**	-.353	-.242	-.242	-.840**	1.000	1.000**	.900*	-.800	-.700		1.000	1.000	-.800	1.000**	.032	
Sig. (2-tailed)	.000	.000	.179	.367	.367	.367	.000	.000	.037	.285	.188	.188		1.000	1.000	.200	1.000	.906	
N	16	16	16	16	16	16	16	16	3	5	5	5	1	2	2	4	3	16	
AB	Correlation Coefficient	.700	.700	.000	.316	-.600	-.258	1.000**	1.000	.300	-.300	-.500		1.000	1.000	-.600	1.000	-.300	
Sig. (2-tailed)	.188	.188	.037	1.000	.684	.400	.742	.000	.624	.624	.391	.391		1.000	1.000	.285	1.000	.624	
N	5	5	5	4	4	4	4	3	5	5	5	5	1	2	3	5	2	5	
CLC	Correlation Coefficient	.429	.429	-.643	-.257	-.319	-.771	.900*	.300	1.000	-.536	-.929**	1.000	-1.000	.500	-.143	.400	-.536	
Sig. (2-tailed)	.337	.337	.119	.623	.538	.072	.008	.037	.624	.215	.003	.003	1.000	1.000	.667	.787	.600	.215	
N	7	7	7	6	6	6	6	5	5	5	7	7	2	2	3	6	4	7	
DOL	Correlation Coefficient	-.464	-.464	.607	-.143	-.116	.371	.463	-.300	-.536	1.000	.750	-1.000	1.000	.500	.314	-.800	1.000**	
Sig. (2-tailed)	.294	.294	.148	.787	.827	.468	.355	.285	.624	.215	.052	.052	1.000	1.000	.667	.544	.200	.906	
N	7	7	7	6	6	6	6	5	5	5	7	7	2	2	3	6	4	7	
CB_TOT	Correlation Coefficient	-.464	-.464	.750	.029	.087	.714	.772	-.700	-.500	.929**	.750	1.000	-1.000	1.000	-.500	.314	-.400	.750
Sig. (2-tailed)	.294	.294	.052	.957	.870	.111	.072	.188	.391	.391	.005	.052	1.000	1.000	.667	.544	.600	.052	
N	7	7	7	6	6	6	6	5	5	5	7	7	2	2	3	6	4	7	
MAG	Correlation Coefficient	1.000**	1.000**	-1.000	-1.000	-1.000	-1.000	-1.000		1.000**	-1.000	-1.000	1.000				1.000	-1.000	
Sig. (2-tailed)	.000	.000	1.000	1.000	1.000	1.000	1.000	1.000		1.000	1.000	1.000	1.000				1.000	1.000	
N	2	2	2	2	2	2	2	2	1	1	2	2	2	2	2	0	1	2	
MS	Correlation Coefficient	1.000**	1.000**	1.000**	-1.000	-1.000	-1.000	1.000**	1.000**	-1.000	1.000**	1.000**	1.000**		1.000	1.000	1.000	1.000	
Sig. (2-tailed)	.000	.000	.000	1.000	1.000	1.000	1.000	1.000	1.000	1.000	1.000	1.000	1.000		1.000	1.000	1.000	1.000	
N	2	2	2	2	2	2	2	2	2	2	2	2	2	0	2	2	2	2	
MUS_TOT	Correlation Coefficient	-.500	-.500	-.500	-1.000	-1.000	1.000**	1.000**	1.000**	.500	.500	-.500	-1.000		1.000	1.000	1.000**	.500	
Sig. (2-tailed)	.667	.667	.667	1.000	1.000	1.000	1.000	1.000	1.000	.667	.667	.667	1.000		1.000	1.000	1.000	.667	
N	3	3	3	2	2	2	2	2	3	3	3	3	0	2	3	3	0	3	
QTZ	Correlation Coefficient	-.943**	-.943**	.829*	-.300	-.462	.600	.289	-.800	-.600	-.143	.314	.314	1.000**	1.000**	1.000	1.000**	.314	
Sig. (2-tailed)	.005	.005	.042	.624	.434	.285	.638	.200	.285	.787	.544	.544	.544	1.000**	1.000**	1.000	1.000**	.314	
N	6	6	6	5	5	5	5	4	5	6	6	6	6	1	2	3	6	3	
TC	Correlation Coefficient	1.000**	1.000**	-1.000**	-.400	-.400	-.200	-.316	1.000**	1.000**	.400	-.600	-.400	1.000**			-1.000**	1.000	
Sig. (2-tailed)	.000	.000	.600	.600	.600	.800	.684	1.000**	1.000**	.600	.200	.600	1.000**			.000	.200		
N	4	4	4	4	4	4	4	3	2	4	4	4	4	2	0	0	3	4	
FECB_TOT	Correlation Coefficient	-.040	-.040	-.029	.348	.349	.200	.187	.032	-.300	-.536	1.000**	.750	-1.000	1.000**	.500	.314	-.800	
Sig. (2-tailed)	.872	.872	.905	.157	.155	.425	.459	.906	.624	.215	.052	.052	1.000	1.000	.667	.544	.200	1.000	
N	19	19	19	18	18	18	18	16	5	7	7	7	2	2	3	6	4	19	

** Correlation is significant at the .01 level (2-tailed).

* Correlation is significant at the .05 level (2-tailed).



Relationships addressed in Chapter 2

MAFIC VOLCANIC ROCKS (PAGE 1)

Spearman's rho	MAGSUS	MAGSUS	LOG_MA GSUS	DEN	CHRG	LOG_CHG	RES	LOG_RES	POR	AB	CAL	CLC
Correlation Coefficient	1.000	1.000	1.000	1.000	1.000	1.000	1.000	1.000	1.000	1.000	1.000	1.000
Sig. (2-tailed)	.000	.000	.000	.006	.006	.006	.000	.058	.005	.966	.544	.039
N	217	217	203	18	16	16	16	13	13	6	6	11
Correlation Coefficient	1.000	1.000	1.000	1.000	1.000	1.000	1.000	1.000	1.000	1.000	1.000	1.000
Sig. (2-tailed)	.000	.000	.000	.008	.008	.008	.000	.058	.005	.966	.544	.039
N	217	217	203	18	16	16	16	13	13	6	6	11
Correlation Coefficient	.308**	.308**	1.000	1.000	1.000	1.000	1.000	1.000	1.000	1.000	1.000	1.000
Sig. (2-tailed)	.005	.005	.000	.000	.000	.000	.000	.000	.000	.000	.000	.000
N	203	203	204	16	16	16	16	16	16	16	16	16
Correlation Coefficient	.653**	.653**	-.284	1.000	1.000	1.000	1.000	1.000	1.000	1.000	1.000	1.000
Sig. (2-tailed)	.005	.005	.286	.000	.000	.000	.000	.000	.000	.000	.000	.000
N	18	18	18	18	18	18	18	18	18	18	18	18
Correlation Coefficient	.294	.294	-.284	1.000	1.000	1.000	1.000	1.000	1.000	1.000	1.000	1.000
Sig. (2-tailed)	.005	.005	.286	.000	.000	.000	.000	.000	.000	.000	.000	.000
N	18	18	18	18	18	18	18	18	18	18	18	18
Correlation Coefficient	.000	.000	-.015	1.000	1.000	1.000	1.000	1.000	1.000	1.000	1.000	1.000
Sig. (2-tailed)	.000	.000	.957	.000	.000	.000	.000	.000	.000	.000	.000	.000
N	16	16	16	16	16	16	16	16	16	16	16	16
Correlation Coefficient	.000	.000	-.015	1.000	1.000	1.000	1.000	1.000	1.000	1.000	1.000	1.000
Sig. (2-tailed)	.000	.000	.957	.000	.000	.000	.000	.000	.000	.000	.000	.000
N	16	16	16	16	16	16	16	16	16	16	16	16
Correlation Coefficient	-.537	-.537	.019	1.000	1.000	1.000	1.000	1.000	1.000	1.000	1.000	1.000
Sig. (2-tailed)	.058	.058	.950	.011	.011	.011	.006	.006	.006	.006	.006	.006
N	13	13	13	11	11	11	11	11	11	11	11	11
Correlation Coefficient	.005	.005	-.151	1.000	1.000	1.000	1.000	1.000	1.000	1.000	1.000	1.000
Sig. (2-tailed)	.886	.886	.622	.000	.000	.000	.000	.000	.000	.000	.000	.000
N	13	13	13	12	12	12	12	12	12	12	12	12
Correlation Coefficient	-.314	-.314	-.088	1.000	1.000	1.000	1.000	1.000	1.000	1.000	1.000	1.000
Sig. (2-tailed)	.544	.544	.872	.000	.000	.000	.000	.000	.000	.000	.000	.000
N	8	8	8	5	5	5	5	5	5	5	5	5
Correlation Coefficient	.927**	.927**	.141	1.000	1.000	1.000	1.000	1.000	1.000	1.000	1.000	1.000
Sig. (2-tailed)	.039	.039	.879	.000	.000	.000	.000	.000	.000	.000	.000	.000
N	11	11	11	10	10	10	10	10	10	10	10	10
Correlation Coefficient	.314	.314	-.143	1.000	1.000	1.000	1.000	1.000	1.000	1.000	1.000	1.000
Sig. (2-tailed)	.544	.544	.767	.000	.000	.000	.000	.000	.000	.000	.000	.000
N	8	8	8	5	5	5	5	5	5	5	5	5
Correlation Coefficient	-.442	-.442	-.515	1.000	1.000	1.000	1.000	1.000	1.000	1.000	1.000	1.000
Sig. (2-tailed)	.200	.200	.128	.000	.000	.000	.000	.000	.000	.000	.000	.000
N	10	10	10	9	9	9	9	9	9	9	9	9
Correlation Coefficient	.400	.400	-.400	1.000	1.000	1.000	1.000	1.000	1.000	1.000	1.000	1.000
Sig. (2-tailed)	.600	.600	.600	.000	.000	.000	.000	.000	.000	.000	.000	.000
N	4	4	4	5	5	5	5	5	5	5	5	5
Correlation Coefficient	.700	.700	.500	1.000	1.000	1.000	1.000	1.000	1.000	1.000	1.000	1.000
Sig. (2-tailed)	.188	.188	.391	.000	.000	.000	.000	.000	.000	.000	.000	.000
N	5	5	5	8	8	8	8	8	8	8	8	8
Correlation Coefficient	.024	.024	-.551	1.000	1.000	1.000	1.000	1.000	1.000	1.000	1.000	1.000
Sig. (2-tailed)	.955	.955	.157	.000	.000	.000	.000	.000	.000	.000	.000	.000
N	8	8	8	7	7	7	7	7	7	7	7	7
Correlation Coefficient	.400	.400	.000	1.000	1.000	1.000	1.000	1.000	1.000	1.000	1.000	1.000
Sig. (2-tailed)	.600	.600	1.000	.000	.000	.000	.000	.000	.000	.000	.000	.000
N	4	4	4	4	4	4	4	4	4	4	4	4
Correlation Coefficient	.300	.300	.100	1.000	1.000	1.000	1.000	1.000	1.000	1.000	1.000	1.000
Sig. (2-tailed)	.624	.624	.873	.000	.000	.000	.000	.000	.000	.000	.000	.000
N	5	5	5	5	5	5	5	5	5	5	5	5
Correlation Coefficient	-.800	-.800	-.400	1.000	1.000	1.000	1.000	1.000	1.000	1.000	1.000	1.000
Sig. (2-tailed)	.200	.200	.600	.000	.000	.000	.000	.000	.000	.000	.000	.000
N	4	4	4	4	4	4	4	4	4	4	4	4
Correlation Coefficient	-.315	-.315	.761**	1.000	1.000	1.000	1.000	1.000	1.000	1.000	1.000	1.000
Sig. (2-tailed)	.318	.318	.004	.000	.000	.000	.000	.000	.000	.000	.000	.000
N	12	12	12	11	11	11	11	11	11	11	11	11
Correlation Coefficient	.029	.029	.371	1.000	1.000	1.000	1.000	1.000	1.000	1.000	1.000	1.000
Sig. (2-tailed)	.957	.957	.468	.000	.000	.000	.000	.000	.000	.000	.000	.000
N	6	6	6	8	8	8	8	8	8	8	8	8

** Correlation is significant at the .01 level (2-tailed).

* Correlation is significant at the .05 level (2-tailed).

Relationships addressed in Chapter 2

MAFIC VOLCANIC ROCKS (PAGE 2)

			DOL	CB TOT	HEM	MAG	MC INT	MS	MUS TOT	PY	QTZ	FECB TOT
Spearman's rho	MAGSUS	Correlation Coefficient	.314	-.442	.400	.700	.024	.400	.300	-.800	-.315	.028
		Sig. (2-tailed)	.544	.200	.600	.188	.955	.600	.624	.200	.318	.957
		N	6	10	4	5	8	4	5	4	12	6
LOG_MAGSUS	MAGSUS	Correlation Coefficient	.314	-.442	.400	.700	.024	.400	.300	-.800	-.315	.028
		Sig. (2-tailed)	.544	.200	.600	.188	.955	.600	.624	.200	.318	.957
		N	6	10	4	5	8	4	5	4	12	6
DEN	MAGSUS	Correlation Coefficient	-.143	-.515	-.400	.500	-.551	.000	.100	-.400	-.761**	.371
		Sig. (2-tailed)	.787	.128	.600	.391	.157	1.000	.873	.600	.004	.468
		N	6	10	4	5	8	4	5	4	12	6
CHRG	MAGSUS	Correlation Coefficient	.600	-.750*	.975**	-.714	.286	-.400	-.500	-.800	.055	-.200
		Sig. (2-tailed)	.285	.020	.005	.111	.535	.600	.391	.200	.873	.747
		N	5	9	5	6	7	4	5	4	11	5
LOG_CHG	MAGSUS	Correlation Coefficient	.600	-.750*	.975**	-.714	.286	-.400	-.500	-.800	.055	-.200
		Sig. (2-tailed)	.285	.020	.005	.111	.535	.600	.391	.200	.873	.747
		N	5	9	5	6	7	4	5	4	11	5
RES	MAGSUS	Correlation Coefficient	.500	-.117	.051	-.257	-.250	.400	.100	-.800	-.005	.800
		Sig. (2-tailed)	.391	.765	.935	.623	.589	.600	.873	.200	.989	.104
		N	5	9	5	6	7	4	5	4	11	5
LOG_RES	MAGSUS	Correlation Coefficient	.500	-.117	.051	-.257	-.250	.400	.100	-.800	-.005	.800
		Sig. (2-tailed)	.391	.765	.935	.623	.589	.600	.873	.200	.989	.104
		N	5	9	5	6	7	4	5	4	11	5
POR	MAGSUS	Correlation Coefficient	.868	.294	.000	-1.000**	-.300	-.500	.105	.144	.868	
		Sig. (2-tailed)	.333	.571	1.000	.000	.624	.667	.895	.734	.333	
		N	3	6	3	3	5	3	4	1	8	
AB	MAGSUS	Correlation Coefficient	.179	-.409	.667	-.714	.048	-.700	-.771	.100	-.248	-.357
		Sig. (2-tailed)	.702	.212	.219	.111	.911	.188	.072	.873	.415	.432
		N	7	11	5	6	8	5	6	5	13	7
CAL	MAGSUS	Correlation Coefficient	-1.000	.086	1.000	.600	-.600	.285	.1000	-.300	-1.000	
		Sig. (2-tailed)	1.000	.872	.000	.400	.285	.000	.824	1.000	.000	
		N	2	6	2	4	5	1	1	2	5	
CLC	MAGSUS	Correlation Coefficient	-.700	-.383	.738	-.029	-.143	-.600	-.600	.400	-.055	-.700
		Sig. (2-tailed)	.188	.308	.262	.957	.760	.285	.285	.800	.873	.188
		N	5	9	4	6	7	5	5	4	11	5
DOL	MAGSUS	Correlation Coefficient	1.000	.179	.316	-.500	1.000**	1.000**	.400	-.800	-.450	.643
		Sig. (2-tailed)	.702	.684	.667	.000	.000	.600	.200	.310	.119	
		N	7	7	4	3	3	3	4	4	7	
CB_TOT	MAGSUS	Correlation Coefficient	.179	1.000	-.821	.086	.371	.800	.800	.400	.839**	.607
		Sig. (2-tailed)	.702	.000	.089	.872	.468	.200	.104	.505	.002	.148
		N	7	11	5	6	6	4	5	5	10	7
HEM	MAGSUS	Correlation Coefficient	.316	-.821	1.000	-.316	-1.000	-1.000	-1.000**	.500	-.832	
		Sig. (2-tailed)	.684	.089	.000	.684	1.000	1.000	.000	.391	.368	
		N	4	5	5	4	2	2	3	2	5	
MAG	MAGSUS	Correlation Coefficient	-.500	.086	-.316	1.000	-1.000**	1.000	1.000	1.000	-.200	-.500
		Sig. (2-tailed)	.667	.872	.684	.000	.000	.000	.747	.667		
		N	3	6	4	6	4	2	2	5		
MC_INT	MAGSUS	Correlation Coefficient	1.000**	.371	-1.000	-1.000**	1.000	.000	1.000	.643	1.000**	
		Sig. (2-tailed)	.468	1.000	.000	.000	.119					
		N	3	6	2	4	8	0	0	2		
MS	MAGSUS	Correlation Coefficient	1.000**	.800	-1.000	1.000**	.000	1.000	1.000**	-1.000**	-.100	1.000**
		Sig. (2-tailed)	.200	1.000	.000	.000	.873					
		N	3	4	2	2	0	5	5	3		
MUS_TOT	MAGSUS	Correlation Coefficient	.400	.800	-1.000**	1.000**	.000	1.000	1.000	-1.000**	.257	.800
		Sig. (2-tailed)	.600	.104	.000	.000	.623	.200				
		N	4	5	3	2	0	5	6	3		
PY	MAGSUS	Correlation Coefficient	-.800	.400	.000	1.000**	1.000**	-1.000**	-1.000**	1.000	.800	-.800
		Sig. (2-tailed)	.200	.505	.000	.000	.000	.104				
		N	4	5	2	2	3	3	5	5		
QTZ	MAGSUS	Correlation Coefficient	-.450	.839**	-.500	-.200	.643	-.100	.257	.800	1.000	.054
		Sig. (2-tailed)	.310	.002	.391	.747	.119	.873	.623	.104	.908	
		N	7	10	5	5	7	5	6	5	13	
FECB_TOT	MAGSUS	Correlation Coefficient	.643	.607	-.632	-.500	1.000**	1.000**	.800	-.800	.054	1.000
		Sig. (2-tailed)	.119	.148	.368	.667	.000	.200	.200	.908		
		N	7	7	4	3	3	4	4	7		

** Correlation is significant at the .01 level (2-tailed).

* Correlation is significant at the .05 level (2-tailed).



Relationships addressed in Chapter 2

FELSIC ROCKS - SYENITE INTRUSIVES AND RHYOLITE DIKES

	MAGSUS	LOG_MA GSUS	DEN	CHRG	LOG CHG	RES	LOG RES	AB	DOL	CB TOT	MC INT	MS	MUS TOT	PY	LOG PY	QTZ	FECB TOT	
Spearman's rho	MAGSUS	Correlation Coefficient	1.000	.999**	.399**	.634**	-.223	-.247	-.356	.366	-.438	.738	-.400	-.643	.565	.575	-.770*	.087
		Sig. (2-tailed)		.000	.001	.005	.005	.373	.324	.282	.298	.177	.262	.600	.119	.056	.051	.015
		N	70	70	67	18	18	18	11	10	11	4	4	7	12	9	11	11
LOG_MAGSUS	Correlation Coefficient	.999**	1.000	.394**	.642**	-.216	-.239	-.356	.366	-.438	.738	-.400	-.643	.565	.575	-.770*	.087	
	Sig. (2-tailed)	.000		.001	.004	.004	.390	.339	.282	.298	.177	.262	.600	.119	.056	.051	.015	.800
		N	70	70	67	18	18	18	11	10	11	4	4	7	12	9	11	11
DEN	Correlation Coefficient	.399**	.634**	1.000	.655**	.855**	-.098	-.115	-.462	.494	-.069	.258	.400	.667	.581*	.575	-.731*	.402
	Sig. (2-tailed)	.001	.001		.003	.003	.698	.649	.153	.147	.840	.742	.800	.102	.048	.051	.025	.220
		N	67	67	67	18	18	18	11	10	11	4	4	7	12	9	11	11
CHRG	Correlation Coefficient	.634**	.642**	.655**	1.000	1.000**	-.095	-.109	-.600	.190	-.317	1.000**	-.400	.143	.588	.588	-.679	.267
	Sig. (2-tailed)	.005	.004	.003			.708	.667	.089	.651	.406	.600	.787	.074	.074	.094	.094	.488
		N	18	18	18	18	18	18	9	8	9	4	4	6	10	10	7	9
LOG_CHG	Correlation Coefficient	.634**	.642**	.655**	1.000**	1.000	-.095	-.109	-.600	.190	-.317	1.000**	-.400	.143	.588	.588	-.679	.267
	Sig. (2-tailed)	.005	.004	.003			.708	.667	.088	.651	.406	.600	.787	.074	.074	.094	.094	.488
		N	18	18	18	18	18	18	9	8	9	4	4	6	10	10	7	9
RES	Correlation Coefficient	-.223	-.216	-.098	-.095	-.095	1.000	.999**	.233	.833*	.850*	-.200	-.400	-.600	.091	.091	.107	.833*
	Sig. (2-tailed)	.373	.390	.698	.708	.708			.546	.010	.004	.800	.600	.208	.803	.803	.819	.005
		N	18	18	18	18	18	18	9	8	9	4	4	6	10	10	7	9
LOG_RES	Correlation Coefficient	-.247	-.239	-.115	-.109	-.109	.999**	1.000	.218	.814*	.979*	-.200	-.400	-.600	.036	.036	.162	.828*
	Sig. (2-tailed)	.324	.339	.649	.667	.667	.000		.574	.014	.002	.800	.800	.208	.920	.920	.728	.006
		N	18	18	18	18	18	18	9	8	9	4	4	6	10	10	7	9
AB	Correlation Coefficient	-.356	-.356	-.462	-.600	-.600	.233	.218	1.000	-.018	-.036	-1.000**	-1.000**	-.486	-.355	-.328	.452	-.282
	Sig. (2-tailed)	.282	.282	.153	.088	.088	.546	.574		.960	.915	.000	.000	.329	.285	.325	.260	.401
		N	11	11	11	9	9	9	11	10	11	4	3	6	11	11	8	11
DOL	Correlation Coefficient	.366	.366	.494	.190	.190	.833*	.814*	-.018	1.000	.512	.000	-1.000	-.700	.624	.620	-.476	.964*
	Sig. (2-tailed)	.298	.298	.147	.651	.651	.010	.014	.960		.060	1.000	1.000	.188	.054	.056	.233	.000
		N	10	10	10	8	8	8	10	10	10	4	2	5	10	10	8	10
CB_TOT	Correlation Coefficient	-.438	-.438	-.069	-.317	-.317	.833*	.814*	-.036	.612	1.000	-.800	.500	-.371	.027	.005	.571	.738*
	Sig. (2-tailed)	.177	.177	.840	.406	.406	.004	.002	.915	.060		.200	.667	.468	.937	.989	.139	.010
		N	11	11	11	9	9	9	11	10	11	4	3	6	11	11	8	11
MC_INT	Correlation Coefficient	.738	.738	.258	1.000**	1.000**	-.200	-.200	-1.000**	.000	-.800	1.000	1.000	800	800	500	000	
	Sig. (2-tailed)	.262	.262	.742			.800	.800	.000	1.000	.200			1.000	800	800	.687	1.000
		N	4	4	4	4	4	4	4	4	4	4	0	2	4	4	3	4
MS	Correlation Coefficient	-.400	-.400	.400	-.400	-.400	-.400	-1.000**	-1.000	.500	1.000	.800	-.400	-.400	1.000	.500		
	Sig. (2-tailed)	.600	.600	.600	.600	.600	.600	.600	.000	1.000	.667		.200	.600	.600		.687	
		N	4	4	4	4	4	4	3	2	3	0	4	4	4	2	3	
MUS_TOT	Correlation Coefficient	-.643	-.643	.667	.143	.143	-.600	-.600	-.486	-.700	-.371	1.000**	.800	1.000	-.536	-.536	.400	.371
	Sig. (2-tailed)	.119	.119	.102	.787	.787	.208	.208	.329	.188	.468		.200	.600	.215	.215	.600	.468
		N	7	7	7	6	6	6	6	5	6	2	4	7	7	7	4	6
PY	Correlation Coefficient	.565	.565	.581*	.588	.588	.091	.036	-.355	.624	.027	.800	-.400	-.536	1.000	.998*	-.633	.482
	Sig. (2-tailed)	.056	.056	.048	.074	.074	.803	.920	.285	.054	.937	.200	.600	.215		.000	.067	.133
		N	12	12	12	10	10	10	10	11	10	4	4	7	12	12	9	11
LOG_PY	Correlation Coefficient	.575	.575	.588	.588	.588	.091	.036	-.328	.620	.005	.800	-.400	-.536	.998*	1.000	-.669*	.478
	Sig. (2-tailed)	.051	.051	.051	.074	.074	.803	.920	.325	.056	.989	.200	.600	.215	.000		.049	.137
		N	12	12	12	10	10	10	10	11	10	4	4	7	12	12	9	11
QTZ	Correlation Coefficient	-.770*	-.770*	-.731*	-.679	-.679	.107	.162	.452	-.476	.571	-.500	1.000**	.400	-.633	-.669*	1.000	-.476
	Sig. (2-tailed)	.015	.015	.025	.094	.094	.819	.728	.260	.233	.139	.667		.600	.067	.049		.233
		N	9	9	9	7	7	7	8	8	8	3	2	4	9	9	9	8
FECB_TOT	Correlation Coefficient	.087	.087	.402	.267	.267	.433**	.428*	-.282	.964**	.738*	.000	.500	-.371	.482	.478	-.476	1.000
	Sig. (2-tailed)	.800	.800	.220	.488	.488	.006	.006	.401	.000	.010	1.000	.667	.468	.133	.137	.233	
		N	11	11	11	9	9	9	11	11	4	3	6	11	11	8	11	

** Correlation is significant at the .01 level (2-tailed).

* Correlation is significant at the .05 level (2-tailed).



Relationships addressed in Chapter 2

Appendices on accompanying CD:

**APPENDIX 3A - OBSERVED VERSUS PREDICED DATA FOR SYNTHETIC
INVERSION MODELS**

**APPENDIX 4A - HISLOP 3D MAGNETIC, 3D GRAVITY, 3D DC RESISTIVITY,
AND 3D IP INVERSION RESULTS**

**APPENDIX 4B - 2D DC RESISTIVITY AND INDUCED POLARIZATION
INVERSION RESULTS FOR HISLOP**

**APPENDIX 4C - OBSERVED VERSUS PREDICED DATA FOR HISLOP
INVERSION MODELS**